ABSTRACT

Title of dissertation: COSMIC-RAY ACCELERATION IN CASSIOPEIA A AND GRAZING-INCIDENCE MULTILAYER X-RAY MIRRORS

Frederick Benton Berendse, Doctor of Philosophy, 2003

Dissertation directed by: Dr. Robert Petre and Dr. Peter Serlemitsos
Laboratory for High Energy Astrophysics
NASA Goddard Space Flight Center

This dissertation consists of two separate, but complementary parts. The first part is a search for evidence of cosmic-ray acceleration in the newly-discovered forward shock of the young shell-type remnant Cassiopeia A. Spectra extracted around the entire circumference of the forward shock are best fitted by a two-component model: a nonequilibrium ionization model assuming

nonequipartition between electrons and ions and an additional nonthermal component interpreted as synchrotron radiation. The maximum electron energy is estimated to be ~10 TeV assuming a magnetic field of 0.08–0.16 μG. A population of regions showing very little thermal line emission exists between the forward and reverse shock. These regions can be interpreted either as thermal forward shock emission seen in projection or as synchrotron emission. The search for x-ray synchrotron emission can be facilitated by imaging x-rays above 20 keV where thermal emission is negligible. The focus of the second part of this dissertation is the production of a grazing-incidence multilayer mirror for the *International Focusing Optics Collaboration for μCrab Sensitivity* hard x-ray balloon-borne telescope. The 40-cm diameter, 8 m focal-length mirror is composed of 2040 aluminum foils coated with a platinum/carbon graded multilayer. The mirror consists of 255 concentric shells of a conic approximation to a Wolter Type I geometry. Reflectivity measurements of sample foils give a mean multilayer interface width of 0.5 nm. The on-axis effective area of the mirror is 78 cm^2 at 20 keV to 22 cm^2 at 40 keV. The mirror produces an on-axis image half-power diameter (HPD) of $1.9' \pm 0.5'$. The combined mirror/detector HPD is $2.8' \pm 0.5'$ due to large detector pixels ($54''$). The mirror was tested in-flight using the x-ray binary Cygnus X-1 on 4–5 Jul 2001. The balloon experienced unexpectedly large stochastic motions exceeding the design limits of the pointing system. As a result, an image HPD of $7.2' \pm 1.0'$ was obtained during the flight. An image during a brief time interval with steady pointing has a HPD of $4.0' \pm 0.5'$.

COSMIC-RAY ACCELERATION IN CASSIOPEIA A AND GRAZING-INCIDENCE MULTILAYER X-RAY MIRRORS

by

Frederick Benton Berendse

Dissertation submitted to the Faculty of the Graduate School of the
University of Maryland, College Park in partial fulfillment
of the requirements for the degree of
Doctor of Philosophy
2003

Advisory Committee:

Professor Marvin Leventhal, Chair
Professor Greg Sullivan
Professor M. Coleman Miller
Professor Andrew Wilson
Dr. Robert Petre
Dr. Peter Serlemitsos

UMI Number: 3112488

INFORMATION TO USERS

The quality of this reproduction is dependent upon the quality of the copy submitted. Broken or indistinct print, colored or poor quality illustrations and photographs, print bleed-through, substandard margins, and improper alignment can adversely affect reproduction.

In the unlikely event that the author did not send a complete manuscript and there are missing pages, these will be noted. Also, if unauthorized copyright material had to be removed, a note will indicate the deletion.

UMI®

ProQuest Information and Learning Company
300 North Zeeb Road
P.O. Box 1346
Ann Arbor, MI 48106-1346

PREFACE

This dissertation is composed of two seemingly unrelated subjects, yet there is a connection between the two topics that should not be overlooked. Part I of the dissertation is a search for evidence of acceleration to the observed "knee" of the observed cosmic-ray spectrum at 3000 TeV in the supernova remnant Cassiopeia A. Cosmic-ray electrons at TeV energies emit synchrotron radiation at x-ray energies. Gas passing through the nonradiative shocks of young supernova remnants is heated to 10^7–10^8 K and emits the bulk of its thermal emission also at x-ray energies. Disentangling thermal and nonthermal components is a complication encountered throughout Part I.

Above energies of a few keV, the thermal component drops off rapidly, leaving the nonthermal component dominant at energies above 10 keV. However, current observatories are only capable of observing nonthermal emission in the closest and brightest remnants. The *XMM-Newton* observatory has the capability to image x-rays up to 15 keV, but all other current and past observatories employing focusing optics necessary to observe the faint nebulous emission of supernova remnants do not exceed 10 keV. Part II of this dissertation covers the production and performance verification of a mirror with high effective area between 20–40 keV to observe nonthermal emission from a variety of celestial sources including supernova remnants. The mirror has modest imaging resolution compared to both *XMM-Newton* and *Chandra*, but it is an important step toward the goal of extending imaging optics to 100 keV for the upcoming *Constellation X* mission.

I would like to thank the people who have mentored me while I carried out the research presented in this dissertation: Prof. Marv Leventhal, Dr. Jack Tueller, Dr. Peter Serlemitsos, Dr. Scott Owens, and Dr. Rob Petre. I would also like to thank Dr. Hans Krimm, Dr. Kai-Wing Chan, and Prof. Steve Reynolds for their feedback on parts of this dissertation.

The completion of the InFOCμS telescope would not have been possible without the dedication and hard work of scientists, technicians, engineers and fellow graduate students including: Dr. Scott Barthelmy, Wayne Baumgartner, Steve Derdeyn, Chris Eng, Holly Hancock, Maoling Hong, John Kearney, Dr. Hidyeo Kunieda, Chris Miller, Dr. Ann Parsons, Kiran Patel, Dr. Yasushi Ogasaka, Dr. Takashi Okajima, Larry Olsen, Marton Sharpe, Steve Snodgrass, and Dr. Yang Soong.

I would also like to thank the scientists and support personnel within the Laboratory of High Energy Astrophysics who assisted with various problems I encountered while conducting research.

DEDICATION

To my parents, Fred and Linda. IHS

TABLE OF CONTENTS

PART I: COSMIC-RAY ACCELERATION IN CASSIOPEIA A 1

1 Cosmic-Ray Acceleration in Shell-Type Supernova Remnants 2

1.1 The Observed Cosmic Ray Spectrum 2

1.2 Supernova Remnants 5

1.3 Fermi Acceleration 8

1.3.1 Test Particle Case 9

1.3.2 Effects of Efficient Acceleration 10

1.4 Cosmic-Ray Emission Processes 14

1.4.1 Pion Decay 14

1.4.2 Inverse Compton 16

1.4.3 Synchrotron 17

1.4.4 Bremsstrahlung 18

1.4.5 Total Broadband Emission 19

1.5 Evidence of Cosmic-Ray Acceleration 19

2 The Young Supernova Remnant Cassiopeia A **23**

2.1 History 23

2.2 Optical Observations 24

2.3 Radio Observations 26

2.4 Infrared Observations 27

2.5 X-Ray Observations 28

2.6 Gamma-Ray Observations 31

2.7 The Cosmic-Ray Acceleration Question 31

3 X-Ray Synchrotron Radiation at the Forward Shock of Cassiopeia A **33**

3.1 Observations and Data Reduction 33

3.2 The Forward Shock 34

3.3 One-Component Thermal Models 39

3.4 A Thermal-Thermal Model 40

3.5 A Thermal-Nonthermal Model 46

3.6 Molecular Cloud Interaction 49

3.7 Interpretation of Forward Shock Emission 49

3.8 Summary 57

4 Hard X-Ray Emission in the Postshock Region of Cassiopeia A **60**

4.1 Postshock Emission 60

4.2 Thermal X-ray Interpretation 64

4.3 X-Ray Synchrotron Interpretation 67

4.4 Regions with Strong Line Emission 71

4.5 Summary 71

PART II: GRAZING-INCIDENCE MULTILAYER X-RAY MIRRORS **78**

5 Overview of X-ray Optics **79**

5.1 Physics of X-ray Reflection 81

5.2 Multilayers 85

5.2.1 Reflectivity of Ideal Multilayers 87

5.2.2 The Role of Interface Width 89

5.3 X-ray Telescopes 92

5.3.1 Wolter Systems 93

5.3.2 Image quality in Wolter I systems 93

5.3.3 Conical approximations 96

5.4 Extending Imaging Above 10 keV 97

6 The International Focusing Optics Collaboration for μCrab Sensitivity Telescope **104**

6.1 Telescope Overview 104

6.2 Scientific Potential 106

6.2.1 Supernova Remnants 109

6.2.2 Other Science 110

6.3 Mirrors 112

6.4 Focal Plane Detectors 115

7 Performance of Multilayer Foils 119

7.1 Multilayer Design 119

7.2 The Deposition Process 122

7.3 Reflectometer Measurements 127

7.4 Specular Reflectivity Fits 129

7.4.1 Angle or Energy Offsets 130

7.4.2 Fit Parameters 130

7.5 Thickness Accuracy 133

7.6 Interface Width 135

8 Mirror Performance 155

8.1 Performance Measurement 155

8.2 Effective Area 158

8.2.1 On Axis 158

8.2.2 Off Axis 159

8.3 Image Quality 160

8.4 Scattering Effects 169

9 In-Flight Mirror Verification **174**

9.1 Target Selection 174

9.2 The InFOCμS Flight 175

9.3 Aspect Reconstruction 176

9.3.1 Instruments 176

9.3.2 Determination of the star camera position 176

9.3.3 Euler angles of the x-ray to star camera transformation . . . 177

9.3.4 Determination of the cross-elevation tilt 178

9.3.5 Image reconstruction 179

9.4 Pointing Performance 179

9.5 The Image of Cygnus X-1 180

LIST OF TABLES

3.1 Prominent line transitions observed in x rays from supernova remnants. 42

3.2 Best-fit parameters of the forward shock to a thermal plus synchrotron model. 48

3.3 Best-fit parameters of a double-thermal model fit to the western regions of Cas A. 51

3.4 Break frequencies of the forward shock regions. 54

4.1 Best-fit parameters of a power-law fit to the postshock regions. . . . 69

4.2 Break frequencies of the hard postshock regions if all radio emission is associated with the x-ray emission. 74

4.3 Break frequencies of the hard postshock regions if 10% of the radio emission is associated with the x-ray emission. 75

4.4 Best-fit parameters of thermal regions within the hard postshock filamentary structure. 77

5.1 Space-based x-ray observatories employing grazing-incidence optics. 82

6.1 Instrument characteristics of the InFOCμS telescope. 108

7.1 The number of bilayers deposited on Goddard foils. 123

7.2 Layer thickness ratio mean and thickness accuracy for top and bottom layers. 136

7.3 Results of unimodal and bimodal Gaussian fits to the histogram of interface width. 140

7.4 Statistical summary of the interface width at different mandrel positions within the deposition chamber. 145

7.5 Statistical summary of the difference in interface width between two multilayers deposited in the same deposition run and in two different deposition runs on the same day. 147

8.1 Table of the measured field of view of the InFOCμS mirror. 161

8.2 The half-power diameter of the InFOCμS mirror at different energies. 164

LIST OF FIGURES

1.1 The observed spectrum of primary cosmic rays. 4

1.2 Diagram of a supernova remnant interaction region. 7

1.3 Self-consistent shock structure with efficient particle acceleration. . 12

1.4 Time evolution of the maximum energy accelerated by a supernova remnant. 15

1.5 The contribution of a population of electrons and ions to the non-thermal photon spectrum. 20

2.1 Optical, radio and x-ray observations of the supernova remnant Cassiopeia A. 25

2.2 An x-ray spectrum of the supernova remnant Cassiopeia A. 30

3.1 *Chandra* images of Cas A at 0.5–10 keV and 4–6 keV. 36

3.2 Spectral extraction regions covering the forward shock of Cas A. . . 37

3.3 Sample spectra of the forward shock, intershock, and reverse shock regions. 38

3.4 Fits of one-component thermal plasma models to a sample spectrum of the forward shock. 41
3.5 Fit of a double-thermal model to a sample spectrum of the forward shock. 42
3.6 Temperatures and ionization timescales of the second thermal component derived from a double-thermal model of the forward shock. . 44
3.7 Hardness ratio (4–6 keV/0.5–4keV) of Cas A. 45
3.8 Comparison of silicon equivalent widths measured at the forward and reverse shocks. 47
3.9 Best fit of a thermal plus synchrotron model to a sample forward shock spectrum. 50
3.10 Spectra of the western regions of the forward shock. 50
3.11 Thermal and nonthermal x-ray fluxes of forward shock regions. . . . 55
3.12 Projected flux across the NE and SE shock fronts. 56
3.13 Comparison of the total forward shock nonthermal spectrum extrapolated to 10–25 keV with the measured RXTE spectrum of Cas A. 58

4.1 Extraction regions selected for postshock spectra. 62
4.2 Sample spectra extracted from the postshock region. 63

4.3 Histogram of unabsorbed x-ray surface brightness of forward shock and postshock regions. 65
4.4 Histogram of best-fit parameters of a plane-parallel model fit to the postshock regions. 66
4.5 Fit of a power law plus plane-parallel shock model to a sample postshock spectrum (Region 4). 73
4.6 Spectra of two thermal regions found in hard postshock filamentary structure. 76

5.1 Reflection and transmission off a boundary between two homogeneous media. 84
5.2 Diagram of upward- and downward-propagating wave vectors within a multilayer. 99
5.3 Calculated reflectivity vs. energy for a periodic and graded multilayer. 100
5.4 Illustrations of the contributions of layer interface width: roughness and diffuseness. 101
5.5 The Wolter family of telescopes. 102
5.6 Diagram of effects of low-, mid-, and high-spatial-frequency roughness on image quality. 103

6.1 The continuum sensitivity of InFOCμS and other hard x-ray observatories. 105

6.2 The InFOCμS telescope and gondola. 107

6.3 Quadrant housing and alignment bar grooves of the InFOCμS mirror. 113

6.4 The InFOCμS 20–40 keV mirror. 114

6.5 The CdZnTe focal plane detector of InFOCμS. 118

6.6 The anticoincidence shield of InFOCμS. 118

7.1 Model reflectivity of sample Nagoya and Goddard multilayers. . . . 120

7.2 Diagram of the magnetron sputtering process. 125

7.3 Diagram of the deposition chamber from the side and top. 126

7.4 Diagram of the reflectometer. 128

7.5 Improvements in reflectivity fits with freed parameters. 132

7.6 Effect of layer thickness inaccuracy on multilayer reflectivity. 140

7.7 Sample reflectivity curve at small angles of incidence. 141

7.8 Ratio of fitted to design top layer thicknesses over the foil sampling period. 142

7.9 Comparison of the ratio of fitted to design layer thickness and interface width between a frozen power law index and a thawed power law index. 143

7.10 Fitted carbon thickness power-law index vs. platinum thickness power-law index. 144

7.11 Carbon on platinum interface width vs. platinum on carbon interface width. . . . 148
7.12 Nonspecular scattering measurement of a sample foil. . . . 149
7.13 Interface width vs. design top platinum thickness. . . . 150
7.14 Ratio of carbon on platinum to platinum on carbon interface width vs. platinum on carbon interface width. . . . 151
7.15 Thickness power-law indices vs. carbon on platinum interface width. 152
7.16 Histograms of interface width for foils with 50–60 bilayers. . . . 153
7.17 Interface width vs. mandrel number for four different mandrel diameters. . . . 154

8.1 The x-ray pencil-beam source and beam travel path. . . . 161
8.2 Measured on-axis effective area of the InFOCμS mirror. . . . 162
8.3 Fractional effective area of the InFOCμS mirror. . . . 164
8.4 Normalized off-axis effective area of the InFOCμS mirror. . . . 165
8.5 On-axis calibration image of the InFOCμS mirror obtained from a raster scan. . . . 166
8.6 The encircled energy fraction of the InFOCμS telescope. . . . 167
8.7 The distribution of scattering angles added to the angle of specular reflection off foils in ray-trace simulations. . . . 168

8.8 Focal point positions of the individual InFOCμS quadrants and the complete mirror. 170
8.9 Comparison of single-focus and multiple-focus image simulations to the raster scan image. 171

9.1 Attenuation of photons at InFOCμS float altitude as a function of target elevation. 182
9.2 Diagram demonstrating the two methods used to determine the x-ray axis celestial position from the star camera position. 183
9.3 Difference in cross-elevation tilt between the gyroscope measurement and the value derived by the star camera rotation method. . . 184
9.4 Motion of the InFOCμS gondola in the elevation and cross-elevation directions. 185
9.5 Scatter plot of the calculated x-ray axis position of InFOCμS at 5–7 UT. 186
9.6 Light curve of events detected between 5–7 UT. 187
9.7 Spectrum of events on good pixels between 5–7 UT during the InFOCμS flight. 187
9.8 Image and encircled energy fraction of detected 20–50 keV events on good pixels between 5–7 UT during the InFOCμS flight. 188

9.9 Images without and with exposure time corrections, and the encircled energy function of detected 20–50 keV events on good pixels between 6.56–6.64 UT during the InFOCμS flight. 189

9.10 X-ray mirror distance from Cyg X-1 between 6.56–6.64 UT. 190

9.11 Cross elevation measured by the gyroscope between 6.56–6.64 UT. . 191

ABBREVIATIONS

ACIS	Advanced Charge-coupled device Imaging Spectrometer
AGN	Active Galactic Nuclei
ASCA	*Advanced Satellite for Cosmology and Astrophysics*
ASIC	ASynchronous Integrated Circuit
Az	Azimuth
BBXRT	*Broad Band X-Ray Telescope*
BeppoSAX	*Beppo Satellite per Astronomia X*
BRDF	Bidirectional Reflectance Distribution Function
CALDB	CALibration DataBase
CANGAROO	*Collaboration of Austrailia and Nippon for a GAmma Ray Observatory in the Outback*
Cas A	Cassiopeia A
CAT	*Cerenkov Atmospheric Telescope*
CSM	CircumStellar Medium
CXC	*Chandra* X-Ray Center
Cyg X-1	Cygnus X-1
CZT	Cadmium Zinc Telluide
dec	declination
DWBA	Distorted-Wave Born Approximation
EEF	Encircled Energy Fraction
EGRET	*Energetic Gamma Ray Experiment Telescope*
El	Elevation
EUVE	*Extreme UltraViolet Explorer*
EXOSAT	*European X-ray Observatory SATellite*
FMK	Fast-Moving Knot
FWHM	Full Width at Half Maximum
GOES SXI	*Geostationary Operational Environment Satellite* Solar X-ray Imager

GSFC	Goddard Space Flight Center
HEASARC	High Energy Astrophysics Science Archive Research Center
HEFT	*High Energy Focusing Telescope*
HEGRA	*High Energy Gamma Ray Astronomy*
HERO	*High Energy Replicated Optics*
HETE-2	High Energy Transient Explorer 2
HEXTE	High Energy X-ray Transient Experiment
HPD	Half-Power Diameter
HWHM	Half Width at Half Maximum
InFOCμS	*International Focusing Optics Collaboration for μCrab Sensitivity*
ISAS	Institute of Space and Astronautical Science
ISM	InterStellar Medium
ISO	*Infrared Space Observatory*
ISOCAM	*Infrared Space Observatory* CAMera
KS	Kolmogorv-Smirnov
QSF	Quasi-Stellar Flocculi
RA	Right Ascension
RMS	Root Mean Squared
ROSAT	*ROntgen SATellite*
RXTE	*Rossi X-Ray Timing Explorer*
SMC	Small Magellanic Cloud
SOHO	*Solar and Heliospheric Observatory*
TRA	Transverse Ray Aberration
TRACE	*Transition Region And Coronal Explorer*
UT	Universal Time
VLA	*Very Large Array*
XMM-Newton	*X-ray Multi Mirror - Newton*

PART I

COSMIC-RAY ACCELERATION IN CASSIOPEIA A

Chapter 1

Cosmic-Ray Acceleration in Shell-Type Supernova Remnants

1.1 The Observed Cosmic Ray Spectrum

In 1912, Austrian Victor Hess climbed to an altitude of 5000 m in a hot air balloon carrying an electroscope. He observed a decrease in the amount of ionizing radiation as his balloon ascended, then an increase at about 1500 m.[1] Hess concluded that this radiation must originate from outside the atmosphere. The term "cosmic ray", however, wasn't given to Hess' radiation until 1926 by Millikan.[2] Two years later, Clay discovered that cosmic rays were charged particles deflected by the earth's geomagnetic field. Subsequent cosmic ray research ushered in the birth of elementary particle physics through the discovery of muons by Neddermyer and Anderson in 1939— remaining the sole means of studying elementary particles until the Cosmotron was built at Brookhaven National Laboratory in 1953.[3]

The observed spectrum of primary cosmic rays can be described as a power law over 15 decades in energy with a mean index of $\Gamma = 2.7$ ($dN/dE \propto E^{-\Gamma}$). The fact that a single power law can describe the spectrum over such a large energy range seems to point to a canonical mechanism for accelerating cosmic rays and that this mechanism is nonthermal in nature. When the mean power law index is removed, breaks in the mean power law spectrum can be observed as shown in Fig. 1.1. These breaks are believed to mark changes in the predominant origin of primary cosmic rays. The lowest-energy cosmic rays, up to 10 GeV,[a,b] have fluxes which are modulated by the solar cycle. Cosmic rays with energies between 10 GeV– 3 PeV are believed to originate within our own galaxy.[c] The origin of cosmic rays between the break at 3 PeV (known as the "knee") and the break at 100 EeV (known as the "ankle") is currently unsettled.[d] Observations of the change in cosmic ray rigidity (energy per charge) and composition from extensive air showers seem to favor an astrophysical origin

[a]Energies are typically quoted in terms of energy/nucleon in the cosmic-ray physics community. Because 90% of cosmic rays are composed of protons, the designation "per nucleon" is implied, but not explicitly written, when quoting energies of cosmic rays in this dissertation.

[b]1 GeV = 10^9 eV

[c]1 PeV = 10^{15} eV

[d]1 EeV = 10^{18} eV

of the knee, either due to a change in the source of cosmic rays above the knee or a change in acceleration efficiency.[4] Almost all theories of cosmic rays origins above the ankle of the spectrum are primarily extragalactic in origin.[5]

The origins of most cosmic rays has remained ambiguous despite nearly one hundred years of cosmic ray research. Cosmic rays are deflected by intervening magnetic fields, so any information about the direction of origin is completely lost during propagation to earth. In addition, cosmic rays with the high magnetic rigidity, i.e. high energy, are detectable only indirectly via the air shower of secondary cosmic rays or Cerenkov light produced via interactions with the atmosphere. Cosmic rays with lower energies ($\lesssim$ 300 GeV) must be detected via balloon or space-borne experiments as they do not produce sufficient secondary cosmic rays nor Cerenkov light for detection.

Something can be said, however, about the distances cosmic rays travel before arriving at Earth. The canonical interstellar magnetic field of 1 μG can only confine cosmic rays with a Larmor radius $r_L = \gamma mc^2/(eB)$ smaller than the diameter of our own galaxy. Therefore, the galaxy can only confine protons below $\sim$ 1 EeV. The contribution of extragalactic sources to the overall cosmic ray spectrum must increase above this energy and is believed to dominate the spectrum above the ankle.

A rough estimate of an energy budget of cosmic rays within the galaxy can also shed light into the mystery of the origin of cosmic rays. The lifetime of

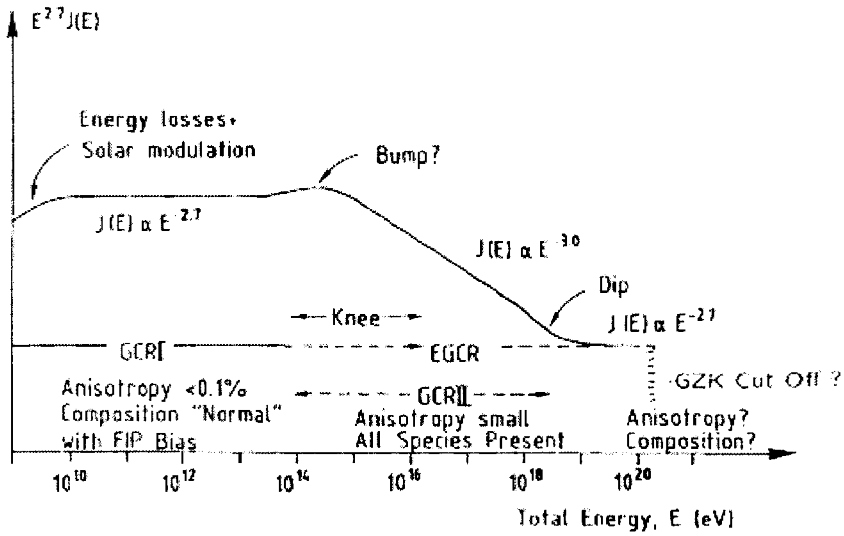

Figure 1.1: The observed spectrum of primary cosmic rays from Axford (1994).[6] The spectrum has been multiplied by $E^{2.7}$ to emphasize the "knee" (3 PeV) and "ankle" (100 EeV) of the spectrum. These features are believed to mark a change in the origin of primary cosmic rays from solar at the lowest energies to galactic and finally to extragalactic at the highest energies.

cosmic rays has been estimated at 10^7 yr based on measured abundances of long-lived radioactive isotopes such as ^{10}Be and ^{26}Al relative to their decay products.[7,8] The measured energy density of cosmic rays within our solar system of ~1 eV/cm^3 generates a total loss of cosmic ray energy within the galaxy of 5×10^{40} erg/s.[9] Therefore, any potential source must be able to deposit this much energy into cosmic rays throughout the galaxy. Supernovae quickly became the most plausible origin— depositing roughly 10^{51} ergs of energy at a rate of one per 50 years into the interstellar medium. Supernovae must therefore deposit roughly 1% of their energy into cosmic rays in order to replenish lost energy. In order to understand the possible mechanisms of acceleration, it is first necessary to describe the physics behind supernovae and their remnants.

1.2 Supernova Remnants

Supernovae were first classified by their observational properties either as Type I or Type II, depending on the absence or presence, respectively, of H Balmer lines in the optical spectrum near maximum brightness. A further delineation separated Type I supernovae into categories Ia, Ib, and Ic based on other spectral and lightcurve characteristics. Spectrally, Type Ib supernovae exhibit strong forbidden lines of O, Si, S, and Ca months after maximum brightness, while Type Ia supernovae show strong Fe and Co lines. The difference between Type Ib and Ic is the presence and absence of He lines, respectively.

It is generally accepted that there exist two mechanisms to trigger a supernova. The first is the detonation or deflagration of a carbon-oxygen white dwarf which has reached Chandresekhar mass (1.4 $M_{\odot}$) through accretion from a binary companion. Reaching this mass, the degenerate white dwarf can no longer support itself against gravitational collapse. This triggers a rebounding shock wave that initiates detonation or deflagration within the white dwarf. This inputs a great amount of thermonuclear energy into the white dwarf in a short time resulting in a Type Ia supernova.[10]

The other mechanism for triggering a supernova is the core collapse of a massive star. Stars prevent self-gravitational collapse by generating internal heat through the fusion of elements. Stars with a pre-supernova mass more than ~ 8 $M_{\odot}$ are incapable of fully supporting gravitational collapse via core electron degeneracy. An increase in the core temperature through this collapse triggers fusion to elements up to iron. Fusion of iron into heavier elements is endothermic, therefore internal heat generation becomes exhausted and the core collapse and becomes neutron degenerate. This releases gravitational energy which then rebounds, supplying $\sim 10^{53}$ erg of energy to the the supernova explosion.[11] Types II, Ib, Ic supernovae are the result of a core collapse occurring at various levels of progenitor mass loss: incomplete or no loss of the H envelope (II), complete loss of the H envelope (Ib), and complete loss of both the H and He envelopes (Ic).

As the ejecta of the supernova expand and sweep up interstellar (ISM) or circumstellar (CSM) matter, an interaction region is created in which two strong shocks form as shown in Fig. 1.2. The first is a blast wave or forward shock consisting of swept-up ISM/CSM. As the remnant sweeps up a substantial amount of ISM/CSM, the shock slows down— allowing ejecta behind the blast wave to enter the interaction region between the ejecta and ISM/CSM. A reverse shock is then created traveling toward the center of the remnant relative in the rest frame of the interaction region. Bounded by these two shocks is the contact discontinuity which marks the boundary between ejecta and swept-up ISM/CSM.

The evolution of a supernova remnant was first qualitatively classified by Woltjer (1972).[12] Four phases describe the radial expansion and velocity of the supernova remnant assuming a symmetric explosion and a homogeneous ambient ISM/CSM density: the free-expansion phase, the Sedov phase, the radiative phase, and the ISM phase. The supernova remnant begins initially in a free-expansion phase as the ejecta expands at a constant velocity unabated by ISM/CSM. The dynamics and expansion rate in this phase depend totally on the physics of the initial explosion, producing velocities on the order of 10^4 km/s. The remnant stays in this phase until the amount of swept-up ISM/CSM becomes comparable with the ejecta.

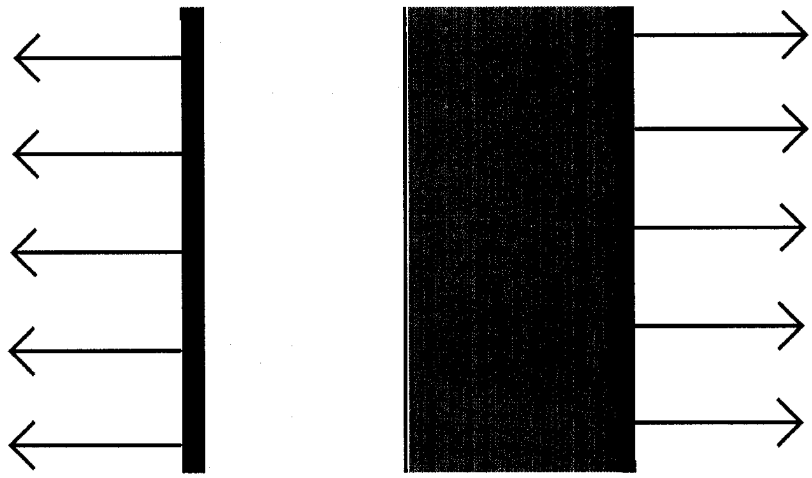

Figure 1.2: Diagram of a supernova remnant interaction region in the rest frame of the contact discontinuity, which marks the boundary between ejecta and swept-up interstellar/circumstellar (ISM/CSM) matter. Propagating outward from the discontinuity is the blast wave or forward shock consisting of swept-up ISM/CSM. The reverse shock propagating toward the explosion origin forms as freely-expanding ejecta catches up to the interaction region which is slowing down in the observer's rest frame.

The second phase occurs when the remnant dynamics are dominated by the amount of swept-up ISM/CSM, but radiative losses are small and therefore energy is conserved in the shock. Sedov (1969) was the first to derive the radial and temperature evolution of the remnant in this phase:[13]

$$\begin{aligned} R_{\text{Sed}} &= 1.17 \left(\frac{E_{\text{SN}}}{n_{\text{ISM}}} \right)^{1/5} t^{2/5} \\ kT_{\text{Sed}} &= \frac{3}{16} \mu m_H V^2 \end{aligned} \tag{1.1}$$

The third phase occurs when the shock has slowed down to a point when the temperature behind the shock is low enough that radiative recombination becomes important, which occurs when the shock velocity slows down to ~ 200 km/s. Shocked material cools quickly providing virtually no pressure in contrast to the Sedov phase. The radial expansion of the remnant now conserves momentum rather than energy as a result:

$$R_{\text{rad}} = R_{\text{rad},0} \left(\frac{8}{5} \frac{t}{t_{\text{rad},0}} - \frac{3}{5} \right)^{1/4} \tag{1.2}$$

where $R_{\text{rad},0}$ and $t_{\text{rad},0}$ are the radius and time at the beginning of the radiative phase. The ISM phase marks the end of the supernova remnant, when the expansion velocity of the shock is comparable to typical ISM thermal velocities (~ 10 km/s) and the supernova remnant becomes indistinguishable from the ISM.

1.3 Fermi Acceleration

Fermi was the first to propose a mechanism to successfully explain the observed power law in the cosmic ray spectrum via interactions with interstellar clouds.[14] He realized that a mechanism which accelerates cosmic rays in proportion to their energy, i.e. $\mathrm{d}E/\mathrm{d}t = \mathrm{E}/\tau_{acc}$, and suffers losses on a timescale of τ_{esc}, will produce a population of cosmic rays that varies as a power law in energy[15]

$$dN/dE \sim E^{-(1+\tau_{acc}/\tau_{esc})}. \tag{1.3}$$

When a relativistic particle collides with an approaching cloud moving at speed u, the net energy gain is $\sim u/c$. Similarly, a collision with a receding cloud results in a net energy loss of $\sim u/c$. Collisions with clouds traveling toward the particle are more frequent than than interactions with clouds traveling away by a factor of $\sim u/c$. Cosmic-ray acceleration in this scenario will take place on a timescale proportional to $\tau_{acc} \sim (c/u)^2$. This dependence on the square of the cloud velocity makes the mechanism inefficient and therefore is known as "second-order" Fermi or stochastic acceleration.

A number of authors independently proposed the currently accepted model of cosmic ray acceleration in supernova remnants via diffusive shock acceleration.[16–19] In this model, accelerated charged particles are confined to the vicinity of the shock by Alfvén waves created by the charged particles themselves.

These waves pitch scatter the charged particles in such a way that a fraction of them are reflected back to the shock front. On average, one complete cycle (upstream to downstream to upstream) gives the particle an energy on average some fraction of u_{sh}/c, where u_{sh} is the velocity of the shock in the observer's frame. This is often referred to as "first-order" Fermi acceleration due to its linear rather than quadratic dependence on the shock velocity.

1.3.1 Test Particle Case

The most simple diffusive shock acceleration models assume that cosmic rays accelerated by the shock do not modify the shock structure. Initial treatments also assumed a magnetic field which is parallel to the shock normal, so there is no magnetic compression across the shock. A particle crossing from the upstream to downstream region at an angle θ_{k1} will increase its velocity from v_{k1} to v_{k2}. A similar boost in energy occurs reflected back upstream at an angle θ_{k2}. In one complete cycle, the particle will increase its energy by

$$\Delta E/E = \left(\frac{1 + v_{k1}(u_1 - u_2)\cos\theta_{k1}/c^2}{1 + v_{k2}(u_1 - u_2)\cos\theta_{k2}/c^2}\right) \tag{1.4}$$

where u_1 and u_2 are the upstream and downstream bulk velocities, respectively. On average the particle will gain energy over each cycle if the distribution of velocity directions is nearly isotropic when crossing the shock front— an assumption which is valid in non-relativistic shocks. If the probability of escape from further acceleration is independent of the energy of the particle, then the differential energy spectrum of cosmic rays will be a power law which depends only on the shock strength in the test particle case.

Accelerated particles are traveling much faster than the Alfvén velocity on both sides of the shock produce Alfvén waves with a wavelength comparable to their gyroradius. The particles are pitch-angle scattered off these Alfvén waves and a fraction of them encounter enough scatterings to be reflected back to the shock. Lagage and Cesarsky (1983) derived the diffusion coefficient of Alfvén waves produced in the test-particle case with a parallel magnetic field and derived a maximum energy of $10^{14}Z$ eV (Z is the charge of the ion) for a typical supernova remnant, which falls short of the observed knee.[20] However, the rate of acceleration, and hence the maximum energy, can be increased when the magnetic field is nearly perpendicular to the shock normal.[21] Drift along the magnetic field allows the particles to cross the shock many times within one mean free path, increasing the rate of acceleration by a factor of 10^2–10^4, depending on the ratio of the gyroradius to mean free path.

Even though shocks are produced in a variety of astrophysical environments, diffusive shock acceleration in the test particle case produces a spectral index which only depends on the ratio of the upstream to downstream bulk velocities

$$dN/dE \sim E^{-\Gamma}\ ;\ \Gamma = \frac{3}{u_1/u_2 - 1} + 1 \tag{1.5}$$

which results in $\Gamma = 2.0$ for a strong shock with a specific heats ratio of $5/3$. In diffusive shock acceleration, a variety of environments produce a ubiquitous spectral index of cosmic rays over many decades in energy. Moreover, after accounting for spallation and transport losses, this is approximately the source spectral index needed to explain the observed the cosmic ray spectrum.[22]

1.3.2 Effects of Efficient Acceleration

If supernova remnants are to account for the cosmic ray spectrum up to the knee, it is necessary for cosmic ray acceleration to be efficient. A significant amount of energy deposited into cosmic rays will affect the shock dynamics nonlinearly in four ways. First, the energy deposited into cosmic rays must come from the kinetic energy of the blast wave. This leaves less energy for the conversion of kinetic energy to thermal energy downstream of the shock and will lower the post-shock electron temperature.[23]

Second, when a significant population of relativistic particles is present, the ratio of specific heats γ decreases, increasing the compression ratio of the shock $\sigma = (\gamma + 1)/(\gamma - 1)$. This increased compression ratio will decrease the distance between the forward and reverse shock due to the higher gas compressibility. The plasma density will also be greatly increased in the more compact interaction region, lowering both the timescale to ionize shocked matter and the growth timescale of Rayleigh-Taylor instabilities. The more compact interaction region could also allow instabilities to mix ejecta all the way to the forward shock.[24]

Third, a significant number of cosmic-ray particles escaping downstream will also increase the compression ratio. If the energy flux of escape downstream is $Q_{\rm esc}$, then the modified compression ratio of a nonradiative shock becomes:[25]

$$\sigma = \frac{\gamma + 1}{\gamma - \sqrt{1 + 2(\gamma^2 - 1)Q_{\rm esc}/(\rho_1 u_1^3)}}. \tag{1.6}$$

Observations of heliospheric shocks show that shocks can be very efficient at converting upstream kinetic energy into cosmic ray energy with efficiencies on the order of 10%–50%.[26–28] With these efficiencies, the shock compression ratio increases to values of σ=4.6–9.1.

Finally, the shock structure downstream is smoothed by the streaming of cosmic rays. This will in turn affect the acceleration of particles. A self-consistent shock structure, shown in Fig. 1.3, consists of a shock precursor which is a discontinuous change in fluid parameters, but the shock itself loses its discontinuity, effectively increasing in thickness. Superthermal particles with shorter diffusion lengths will see only a fraction of the shock compression ratio seen by those accelerated to relativistic energies. The resulting particle spectrum deviates from a power law by becoming slightly concave because particle acceleration has become less efficient at superthermal energies while become more efficient at relativistic energies.[25,29,30]

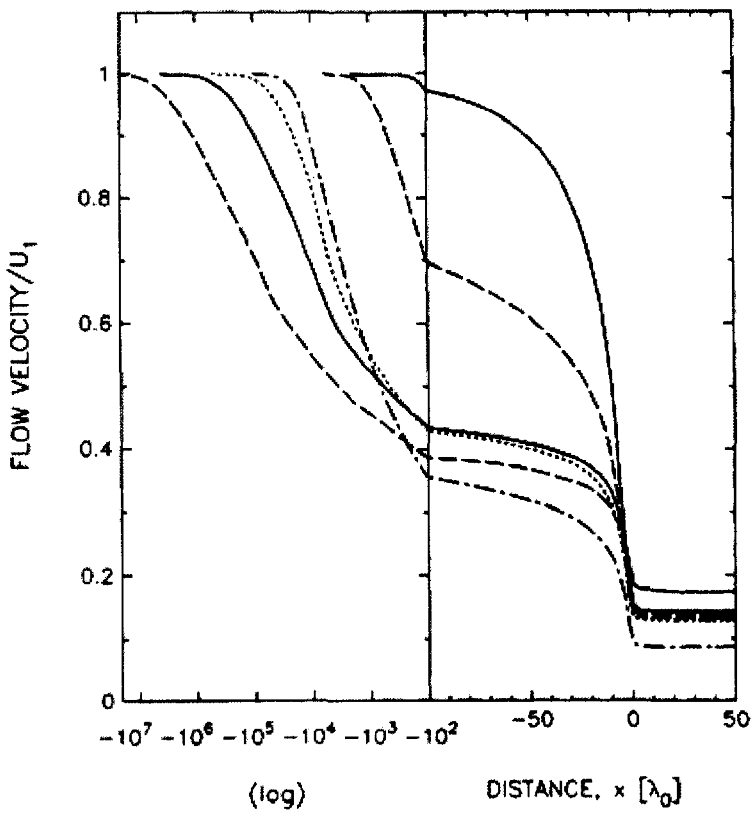

Figure 1.3: Self-consistent shock structure with efficient particle acceleration from Ellison and Reynolds (1991).[30] Efficient particle acceleration creates a small discontinuous subshock followed downstream by a continuous increase in the compression ratio. In this structure, more energetic particles which have larger diffusion coefficients will experience a larger effective shock compression ratio and hence more efficient acceleration. The different lines represent models with an assumed maximum particle energy, increasing from right to left.

The maximum energy of protons and electrons accelerated by diffusive shock acceleration in the presence of efficient cosmic ray acceleration is limited by one of three mechanisms: a finite age of the remnant, radiative losses, or the escape of particles from the shock front.[31] The maximum energy of electrons and protons accelerated by a remnant in the Sedov dynamical phase is

$$E_{\text{age}} = 5E_0 \left[1 - (t/t_{\text{tr}})^{-0.2}\right] \tag{1.7}$$

$$E_0 \approx 71.2 B_{(\mu\text{G})} u_{\text{sh}}/10^9 (\text{cm/s}) \text{ erg}$$

where u_{sh} is the shock velocity. The transition time t_{tr} is the time taken to transition from the free-expansion dynamical phase to the Sedov phase, about 114 years for a typical interstellar density of 1 cm^{-3} and a supernova explosion energy of 10^{51} erg.

When the age of the remnant approaches the half-life of electrons to radiative losses, the maximum energy will transition from age-limited to loss-limited. An electron with energy E_e will lose half its energy to synchrotron radiation in a time

$$\tau_{1/2,\text{synch}} \approx \frac{2 \times 10^5}{B_{\mu\text{G}}^2 E_{e,\text{TeV}}} \text{ yr} \tag{1.8}$$

Assuming that magnetic turbulence approaches the Bohm diffusion limit (i.e. the mean-free path equals the gyroradius) and the shock compression ratio is σ, the maximum energy limited by radiative losses of electrons to synchrotron and inverse Compton radiation (mainly synchrotron if $B \gtrsim 3\ \mu$G) is:

$$E_{\rm rad} \approx 0.32 B_{\mu{\rm G}}^{-1/2} \frac{u_{\rm sh}}{10^8({\rm cm/s})} \left(\frac{\sigma}{\sigma - 1}\right)^{1/2} \text{ erg} \tag{1.9}$$

The third possible limitation of the maximum energy is escape of particles from the shock front. Alfvén waves generated by the accelerated particles only effectively diffuse particles with a gyroradius on the order of the wavelength of the Alfvén wave. If, through a damping mechanism, there is a maximum wavelength of Alfvén waves λ_{max}, then the maximum energy of particles in the escape-limited case is

$$E_{esc} \approx \lambda_{max} e B_{\mu{\rm G}}/4 \text{ erg} \tag{1.10}$$

The power radiated by protons in the same environment is a factor of $(m_e/m_p)^2$ lower, therefore the maximum energy of protons accelerated by a supernova remnant may be significantly higher than that of electrons. Fig. 1.4 shows the time evolution of the maximum energy of cosmic rays accelerated by a remnant. The maximum energy of electrons accelerated by a supernova remnant at any given time peaks when the remnant just enters the radiation loss-dominated era. This occurs on the order of 10^4 yr in a typical remnant environment, therefore historical supernova remnants are the ideal place to search for evidence of cosmic ray acceleration up to the knee of the cosmic ray spectrum.

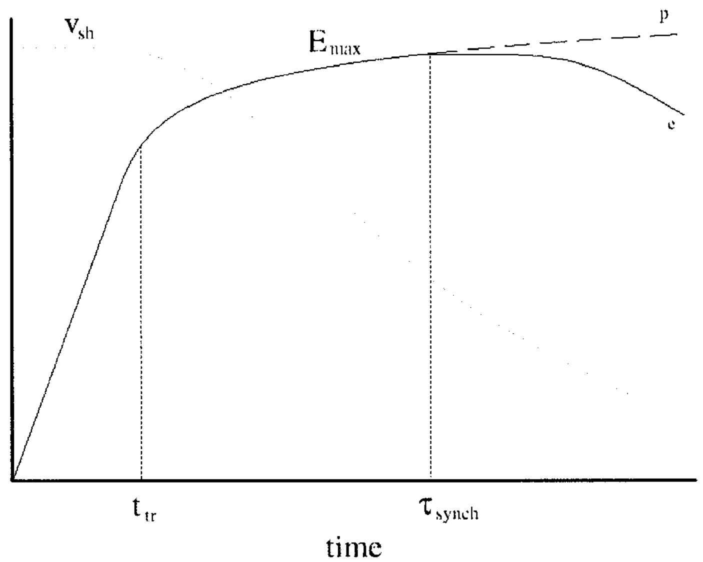

Figure 1.4: Time evolution of the maximum energy accelerated by a supernova remnant E_{max}. The maximum energy increases linearly until the remnant transitions from the free-expansion phase to the Sedov phase at time t_{tr}. The maximum energy remains limited by the age of the remnant until the synchrotron loss time τ_{synch} is comparable to the age of the remnant. Electrons at that point become loss-limited while protons continue to reach higher energies due to much smaller radiative losses. Also plotted is the shock velocity of the remnant v_{sh}.

1.4 Cosmic-Ray Emission Processes

The propagation of cosmic rays in the interstellar magnetic field removes all information regarding their origin. Photons emitted by cosmic rays are the only means by which to ascertain their source. Cosmic ray ions emit via decay of neutral pions produced in ion-ion collisions, while cosmic ray electrons emit via either inverse Compton, synchrotron or bremsstrahlung processes. Photon emission rates of each of these processes are taken from a detailed treatment of cosmic ray emission processes by Baring *et al.* (1999).[32]

1.4.1 Pion Decay

Ion-ion collisions will produce neutral pions which in turn decay to two gamma rays: $p + p \to \pi^0 + p + p$, $\pi^0 \to \gamma + \gamma$. In the center of momentum frame of the colliding protons, the pion will have a momentum four-vector $(\gamma_\pi^* E_{\pi,0}, p_t^*, p_l^*)$ where p_t and p_l are the transverse and longitudinal momenta relative to the protons and asterisks denote measurements in the center of momentum frame. The maximum Lorentz factor available to the pion in a collision occurs when the total energy of both protons is transfered to the pion

$$\gamma_{\pi,\max}^* = [2(\gamma_p - 1) + \mu_\pi^2]\{2\mu_\pi\sqrt{2(\gamma_p + 1)}\} \qquad (1.11)$$

where $\mu_\pi = m_\pi/m_p$. If the pion has a Lorentz factor γ_π^*, then for a given longitudinal momentum there exist two possible values for the Lorentz factor in the observer's frame,

$$\gamma_\pi^\pm = \gamma_{\mathrm{CM}}(\gamma_\pi^* \pm \beta_{\mathrm{CM}} p_l^*), \tag{1.12}$$

where γ_{CM} is the Lorentz factor between the center of momentum and observer's frames.

In the rest frame of the pion, two gamma rays are emitted isotropically and each have an energy equal to half the rest mass of the pion. A Lorentz transformation into the observer's frame produces gamma rays with energies

$$\varepsilon_\gamma^- = \frac{m_\pi}{2}\gamma_\pi\sqrt{1-\beta\cos\phi_1} \tag{1.13}$$

$$\varepsilon_\gamma^+ = \frac{m_\pi}{2}\gamma_\pi\sqrt{1+\beta\cos\phi_2}$$

where ϕ is the angle between the gamma ray trajectory and the pion trajectory. Given the Lorentz-invariant differential cross section for proton collisions $E\ d^3\sigma/dp^3$, the differential production rate of pion-decay gamma rays is

$$
\begin{aligned}
\frac{dn_\gamma}{dt} &= 4\pi n_p c \frac{m_e}{m_\pi} \int_{\gamma_{\rm TH}}^{\infty} d\gamma_p \, \beta_p \, \psi(\gamma_p) \, N_p(\gamma_p) \\
& \times \int dp_l^* d\gamma_\pi \left[\frac{H(\gamma_\pi^+ - \gamma_-)}{(\gamma_\pi^+)^2 - 1} + \frac{H(\gamma_\pi^- - \gamma_-)}{(\gamma_\pi^-)^2 - 1} \right] \\
& \times E \, \frac{d^3\sigma(\gamma_\pi^*, p_t^*)}{d^3 p}. \qquad (1.14)
\end{aligned}
$$

Here the value γ_- is the minimum Lorentz factor of a pion necessary to produce a gamma ray of energy ε_γ and H is the Heaviside step function.

1.4.2 Inverse Compton

Inverse Compton scattering occurs as electrons interact inelastically with low-energy photons. The seed population of low-energy photons is predominantly cosmic microwave background, with infrared and optical photons produced by the remnant only contributing about 10–15% of the seed photons.[22] A cosmic microwave background photon with energy ε_s will be upscattered by the electron to $\varepsilon_\gamma = \varepsilon_s \gamma_e^2$, producing gamma-ray emission. The differential inverse Compton production rate is

$$
\frac{dn_\gamma(\varepsilon_\gamma)}{dt} = c \int N_e(\gamma_e) d\gamma_e \int d\varepsilon_s n_\gamma(\varepsilon_s) \sigma_{\rm KN}(\varepsilon_s, \gamma_e; \varepsilon_\gamma) \qquad (1.15)
$$

where $N_e(\gamma_e)$ is the energy distribution of electrons and $n_\gamma(\varepsilon_s)$ is the energy distribution of seed photons— a blackbody distribution with the CMB temperature of 2.73 K. The Klein-Nishina cross section $\sigma_{\rm KN}$ must be used for electron energies ≥ 30 TeV when the photon energy becomes comparable to the rest mass of the electron in the electron rest frame.

1.4.3 Synchrotron

Synchrotron emission is emitted by electrons of all energies ranging from thermal to the maximum cutoff energy. To a very rough approximation, the energy of a synchrotron photon radiated is $\varepsilon_\gamma \propto \varepsilon_e^2 \nu_L$ where $\nu_L \equiv eB/(2\pi m_e c)$ is the Larmor frequency. Electrons accelerated up to the knee of the cosmic ray spectrum will emit synchrotron radiation at ~ 1 keV in a typical interstellar magnetic field of 1 μG. Electrons in the GeV range will emit photons at radio wavelengths which is the dominant emission mechanism of supernova remnants in that regime. Caution must be exercised in assuming that each electron emits all its power at this energy, because this assumption will underestimate the photons production rate above the characteristic frequency ν_L. An exponential cutoff in the observed electron spectrum will result in a slower-than-exponential cutoff in the observed photon spectrum.

The rate of emission of synchrotron energy from a spectrum of electrons $N_e(\gamma_e)$ is

$$\begin{aligned} \varepsilon_\gamma \frac{dn_\gamma(\varepsilon_\gamma)}{dt} &= \frac{\sqrt{3}}{2\pi} \alpha \frac{eB_\perp}{m_e c} \int_0^\infty N_e(\gamma_e) F(x) d\gamma_e \qquad (1.16) \\ F(x) &\equiv x \int_x^\infty K_{5/3}(z) dz \end{aligned}$$

where $K_{5/3}$ is the modified Bessel function and $x = \varepsilon_\gamma/\varepsilon_c$.[33] The variable $\varepsilon_c = 3/2\,\gamma_e^2\,h\nu_L\,\sin\theta$, where θ is the angle between the magnetic field and shock normal. The synchrotron emissivity of a single electron, $F(x)$, peaks at a value of $x = 0.29$.[34] If the distribution of electrons as a function of energy is a power law, i.e. $N_e \sim \gamma_e^{-p}$, then the distribution of the number of photons scales as

$$\frac{dn_\gamma}{dt} \propto \varepsilon_\gamma^{-(p+1)/2} B_\perp^{(p+1)/2} \tag{1.17}$$

Synchrotron emissivity will increase with the magnetic field, which is important because the maximum energy of electrons in the radiative loss-limited case decreases as the magnetic field increases. Consequently, searching for cosmic-ray acceleration by its synchrotron emission will result in a bias toward remnants which have a large discrepancy between the maximum electron and proton energy. A remnant which is not accelerating cosmic ray electrons to the knee of the spectrum may indeed be accelerating cosmic ray protons to the knee due to this discrepancy.

1.4.4 Bremsstrahlung

Bremsstrahlung emission is also produced by electron-ion and electron-electron interactions. The bremsstrahlung photon production rate is

$$\frac{dn_\gamma(E_e,\varepsilon_\gamma)}{dt} = v_e[(n_p + 4n_{He})\sigma_{e-p}(E_e,\varepsilon_\gamma) + n_e\sigma_{e-e}(E_e,\varepsilon_\gamma)] \tag{1.18}$$

where v_e is the velocity of the electron relative to the target. The cross section is proportional to Z^2, hence the factor of four before the helium density. The electron-proton cross section in the non-relativistic limit and the Born approximation is the Bethe-Heitler cross section:[35]

$$\sigma_{e-p,\mathrm{NR}} \approx \frac{16}{3}\frac{Z^2 e^2 \hbar}{c}\left(\frac{e^2}{m_p c^2}\right)^2 \frac{1}{\beta^2} \ln\left[\frac{(\sqrt{E_e}+\sqrt{E_e-\varepsilon_\gamma})^2}{\varepsilon_\gamma}\right] \tag{1.19}$$

In the ultra-relativistic limit this cross section approaches

$$\sigma_{e-p,\mathrm{UR}} \rightarrow \frac{4r_0^2\alpha}{\varepsilon\gamma}\left[1+\left(\frac{1}{3}-\frac{\varepsilon_\gamma}{\gamma_e}\right)\left(1-\frac{\varepsilon_\gamma}{\gamma_e}\right)\right]\left\{\log\left[2\gamma_e\frac{(\gamma_e-\varepsilon_\gamma)}{\varepsilon_\gamma}\right]-\frac{1}{2}\right\} \tag{1.20}$$

The cross section for electron-electron collisions is much more complicated and is treated by Haug (1975) exactly and Baier *et al.* (1967) in approximation.[36,37] In general, non-relativistic treatments of bremsstrahlung radiation ignore the electron-electron cross section because the dipole term of an e-e collision does not change. In the ultra-relativistic limit, this is no longer the case and the cross section approaches the electron-proton cross section (Eq. (1.20)). The electron-electron contribution to the bremsstrahlung photon spectrum approaches $(n_e = n_p + 2n_{He})/(n_p + 4_n He) \approx 0.86$. Bremsstrahlung emission from thermal electrons and ions produces photons at x-ray energies. The population of accelerated electrons and protons produces emission at gamma ray energies up to their total kinetic energy. Gamma-ray bremsstrahlung is predicted to dominate the gamma-ray flux between MeV to low GeV energies and reach into the TeV range.

1.4.5 Total Broadband Emission

The emission mechanisms just described emit photons across the entire electromagnetic spectrum and can contribute significantly, if not dominate, emission at radio, x-ray and gamma-ray energies. Fig. 1.5 shows how a power-law distribution of electrons and protons translates onto the photon spectrum. The radio emission of all shell-type supernova remnants is dominated by synchrotron radiation from electrons accelerated to GeV energies. Nonthermal x-ray emission is produced by synchrotron emission from TeV electrons, but almost all shell-type supernova remnants are dominated by thermal electron-proton bremsstrahlung and line emission from highly-ionized shocked material. Gamma-ray emission is expected to be dominated by nonthermal bremsstrahlung at MeV energies, then by pion decay and inverse Compton emission at GeV to TeV energies. The relative contribution of these mechanisms depends on the relative number of TeV electrons to protons, which depends on electron synchrotron losses and the relative injection rates of electrons to protons into the acceleration mechanism.

Broadband modeling is important because pion decay is a hadronic process. A definite demonstration that pion decay is occurring within a supernova remnant is the most direct evidence of acceleration of protons in supernova remnants. Conclusions of cosmic ray acceleration based on other emission mechanisms must assume that the protons are accelerated as efficiently as the electrons. There is no known physical reason why this shouldn't be the

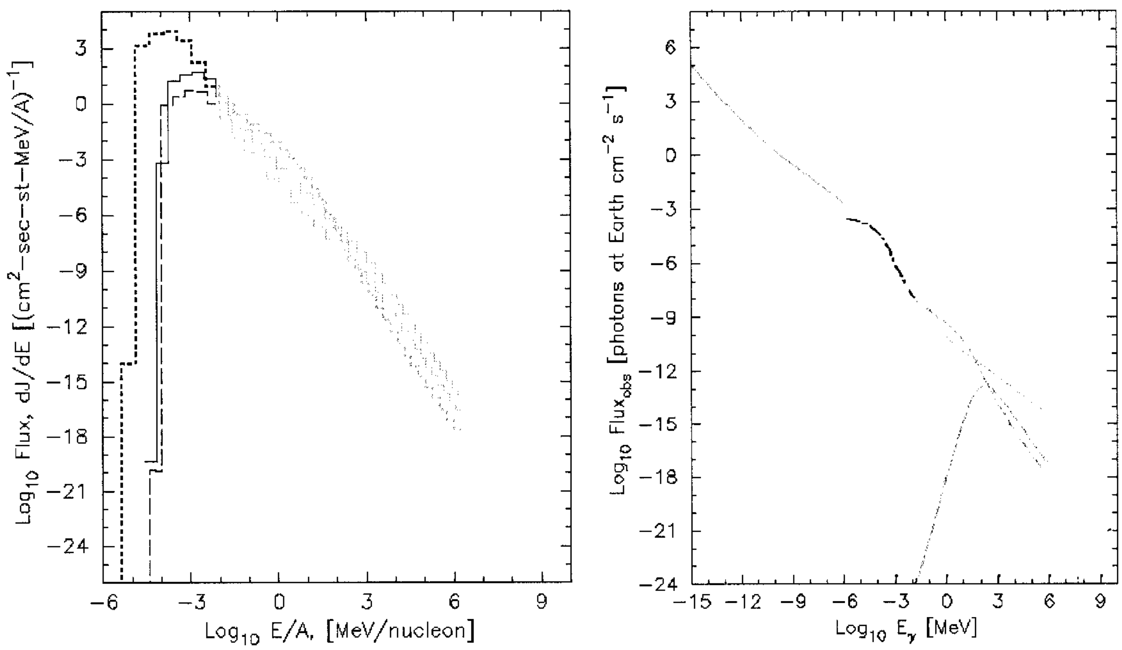

(a) (b)

Figure 1.5: The contribution of a population of electrons and ions to the non-thermal photon spectrum. Both figures are modified versions of Figures 6 and 10 from Baring *et al.* (1999).[32] The particle spectrum in (a) includes electrons (dotted), protons (solid), and fully-ionized He (dashed). The photon spectrum in (b) includes synchrotron (solid), bremsstrahlung (dot-dashed), inverse Compton (dotted) and pion decay (dashed). The three shades represent different particle energy ranges to demonstrate how particles of different energies contribute to the total photon spectrum.

case, yet there is always the possibility of an unknown physical process to change this view.

1.5 Evidence of Cosmic-Ray Acceleration

The power-law radio spectra observed in shell-type supernova remnants provided the first proof that electrons were being accelerated to GeV energies. It was unknown until recently, however, whether or not shell-type supernova remnants are capable of accelerating particles to the knee of the cosmic ray spectrum. In 1995, Koyama *et al.* reported spectral observations of the shell-type supernova remnant SN 1006 with the *Advanced Satellite for Cosmology and Astrophysics* (ASCA) observatory.[38] The outer shell exhibits two opposing shell sections with spectra devoid of line emission, while the interior of the remnant exhibits a thermal spectrum with a range of ejecta elements. This eliminated the possibility of the shell emission being a very underionized thermal emission with strict ejecta stratification,[39] and a synchrotron-dominated spectrum became the favored interpretation in which electrons are being accelerate to energies as high as 100 TeV.[40] This model was confirmed by the successful detection of the northeastern rim of SN 1006 with the CANGAROO TeV gamma ray telescope, interpreted as inverse Compton emission through modeling of the x-ray and gamma-ray spectrum.[41]

Two years after the discovery of x-ray synchrotron in SN1006, a second nonthermal shell was detected by the ASCA observatory in the remnant RX J1713.7-3946.[42,43] This remnant is morphologically similar to SN 1006 and a nonthermal power law with an index of 2.5 was fitted to the observed spectrum. TeV emission from the northwest rim of the remnant was detected by the CANGAROO telescope,[44] but the mechanism responsible for this emission is being debated.[45,46] A third remnant initially discovered by Aschenbach (1998),[47] RX J0852.0-4622, was later shown to exhibit nonthermal emission by Slane *et al.* [48]

Efficient particle acceleration was also inferred through thermal x-ray observations of the supernova remnant 1E 0102.2-7219 in the Small Magellanic Cloud (SMC) by Hughes, Rakowski & Decourchelle (2000).[49] The well-known distance to the SMC allowed for a direct comparison of the ion temperature derived from the proper motion of the remnant's forward shock and the electron temperature obtained from fits to the thermal spectrum. The post-shock electron temperature was much lower than expected even for minimal electron heating only by Coulomb collisions. This can occur only if a significant portion of the shock energy is being deposited into cosmic rays.

Unlike SN 1006, RX J1713.7-3946 and RX J0852.0-4622, most shell-type remnants are dominated at x-ray energies by thermal bremsstrahlung and x-ray lines from highly-ionized elements. However, even physically-based models of thermal emission from shocked plasma often leave excesses at energies above a few keV which are interpreted as nonthermal emission. A combined thermal and nonthermal model has been proposed to explain the spectra of supernova remnants RCW 86, Tycho, and Cassiopeia A (Cas A).[50–52]

There are currently two outstanding problems with the observational scenario of cosmic ray acceleration by supernova remnant shocks. The first is that young supernova remnants ($\lesssim$ 5000 years) are believed to be reaching the age where the maximum particle energy is evolving from age-limited to loss-limited, therefore these remnants should be producing the highest energy particles they will produce over their lifetimes and that their x-ray synchrotron fluxes should be maximized at this age. However, only six young supernova remnants have shown evidence of nonthermal emission and only three are dominated by nonthermal emission.

The second outstanding problem is that no supernova remnant observed to date has shown evidence of accelerating electrons close to the knee of the cosmic ray spectrum at 3000 TeV— falling short by 1–2 orders of magnitude. A study of shell-type remnants by Reynolds and Keohane showed that the maximum x-ray nonthermal emission fell short of the extrapolation of radio emission— evidence that these supernova remnants are not accelerating electrons to energies much greater than 100 TeV if a canonical magnetic field of 10 μG is assumed.[53] This, however does not rule out cosmic-ray proton acceleration to the knee of the spectrum. The question of whether or not cosmic-ray acceleration takes place up to the knee of the spectrum to this day remains unanswered.

Chapter 2

The Young Supernova Remnant Cassiopeia A

2.1 History

In 1948, Ryle and Smith reported bright cosmic radio emission coming from the constellation of Cassiopeia.[54] A subsequent, more accurate determination of the position of this radio emission allowed Baade and Minkowski (1954) to associate this radio emission with an optical nebulosity.[55] Their spectral measurements determined that this nebulosity was moving at very large velocities. What they had discovered was the optical emission from the reverse shock of the supernova remnant now known as Cassiopeia A [$\alpha = 23^{h}23^{m}26^{s}$, $\delta = +58^{\circ}48'$ (J2000)].

Cassiopeia A (Fig. 2.1) is the remnant of a core-collapse explosion of a star that occurred sometime between A.D. 1671–1677 based on expansion rate measurements assuming no deceleration. A suspected historical sighting of Cassiopeia A occurred in A.D. 1680 by the Flemish astronomer J. Flamsteed.[56] The progenitor of this explosion remains uncertain, although it is believed that it experienced significant mass loss as a nitrogen-rich Wolf-Rayet star of type WN7-WN9 before exploding with a mass between 8–15 $M_{\odot}$.[57–60]

Cassiopeia A (Cas A) is the brightest radio source (2720 Jy)[61] and one of the brightest x-ray sources (1.8×10^{-9} erg cm^{-2} s^{-1}, 2–20 keV) in the sky. The most current estimate of the distance of the remnant is 3.4 kpc based on radial and proper motion studies of optical knots.[62] The remnant encompasses an angular diameter of $5'$, corresponding to a linear diameter of 4.9 pc.

2.2 Optical Observations

The optical emission of Cas A is a faint, nebulous ring $2'$ in radius consisting of complex filamentary structures. Spectra of these filaments reveal forbidden line transitions of low-ionization species of oxygen, nitrogen, silicon and sulfur with radial velocities ranging from -4500 to +6000 km s^{-1}.[63] This optical emission spatially coincides with the brightest structures seen in radio and x-rays and is believed to be ejecta heated by the reverse shock.

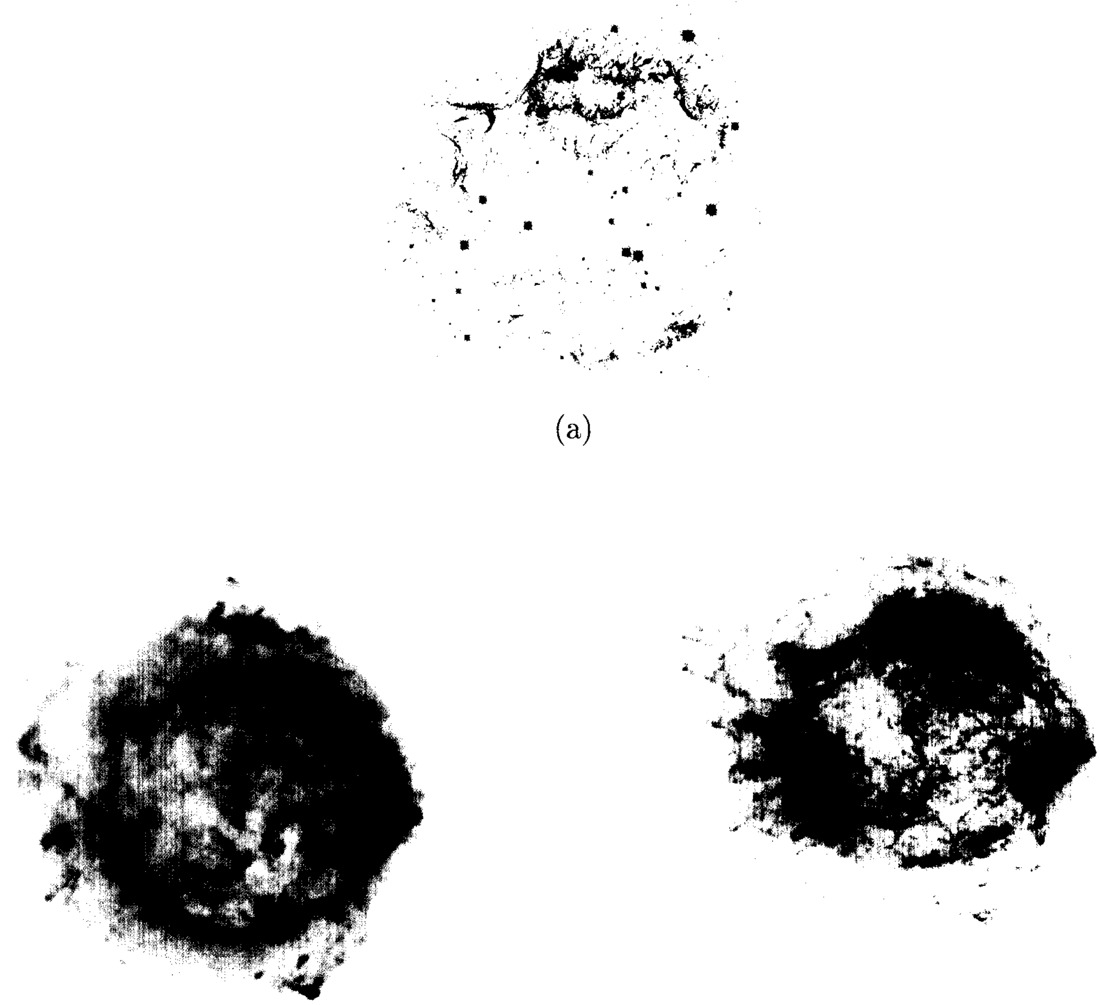

(a) (b) (c)

Figure 2.1: Optical (a), radio (b) and x-ray (c) observations of the supernova remnant Cassiopeia A. The optical observation was taken with the Wide-Field Planetary Camera of the *Hubble Space Telescope*.[63] The radio observation is a 1.4 GHz image from the *Very Large Array*.[64] The x-ray image is a 0.5–10 keV observation from the *Chandra X-Ray Observatory*.

Also seen in optical are a variety of knot-like structures which are distributed similarly to the filamentary structure. These knots are classified into three groups. Fast-moving knots (FMK) are observed with proper motions on the order of 4000–6000 km s−1 and are dominated by oxygen lines with the presence of sulfur and argon lines.[65] The strong presence of oxygen in these knots is not typical of all core-collapse supernovae. Cas A is the prototype of a subclass of core-collapse supernovae known as oxygen-rich supernova remnants. The lack of observed hydrogen and helium and the large expansion velocities are the most convincing evidence that these fast-moving knots are ejecta from the progenitor which lost most, if not all, of its hydrogen envelope prior to the supernova event. The spectra of these fast-moving knots can be modeled as a dense clump of material ionized by a combination of photoionization from photons in the reverse shock and shock heating.[66,67]

The second class of knots seen in optical observations shows evidence of Balmer lines as well as nitrogen. These knots, referred to as quasi-stationary flocculi, have much lower expansion velocities: ≤ 400 km s^{-1}. These flocculi exhibit enhancements of helium and nitrogen over solar composition which suggests these are stellar material lost in a circumstellar wind. When overtaken by the forward shock, this material is heated and produces the observed optical line emission.

The third class of knots are faint knots first termed fast-moving flocculi by Fesen *et al.* (1987).[57] Like quasi-stationary flocculi, they exhibit primarily nitrogen lines. However, these knots are traveling at very large proper motion velocities (7600–8000 km s^{-1}) and are distributed at the very outer edges of the remnant at angular distances of $144'$–$192'$. The presence of nitrogen-rich ejecta at this distance may indicate that not all of the hydrogen envelope was lost prior to the supernova event.

FMKs with the fastest velocities occupy a jet-like feature in the northeast part of the remnant.[57,68] Recent observations of this jet have revealed knots with velocities in excess of 10^4 km s^{-1} both within the NE jet and in its opposite direction,[69] suggesting that this jet is actually bipolar. This jet is the most compelling evidence of Cas A undergoing an asymmetric explosion.

2.3 Radio Observations

Radio observations of Cas A reveal a bright ring of diffuse emission about $4'$ in diameter coming from the reverse shock. Outside of this ring is a fainter plateau of emission that extends to $5'$ in diameter corresponding well with the location of the forward shock. The radio spectrum can be described as a power law with a spectral index ($S_\nu \propto \nu^{-\alpha}$) of $\alpha = 0.77$ due to synchrotron emission.[70] This is the steepest spectrum measured among historical supernova remnants. It appears from measurements of young supernova remnants that there is an evolutionary trend toward flatter spectral indices as a remnant ages.[71] A temporal flattening of the spectral index at the rate of $\Delta\alpha$=+0.00126 yr^{-1} has been observed in Cas A to confirm this trend.[72]

The spectral index of Cas A has been found to vary spatially on scales of 0.15–1.1 pc ($9''$–$66''$) from 0.64 to 0.92.[73] Measurements of radio knots show flatter spectral indices within the bright radio ring ($\langle\alpha\rangle = 0.75$) than the radio plateau ($\langle\alpha\rangle = 0.80$).[74] The spectra of these radio knots are much steeper than the spectral index of $\alpha = 0.50$ expected if the source of synchrotron radiation were ambient cosmic ray electrons. Cas A must be accelerating cosmic-ray electrons somewhere within the remnant. The lack of correlation between spectral index and dynamical properties such as deceleration rate eliminates the knots themselves as a site of acceleration. Rather, the changes in spectral index in these knots are more likely due to changes in the magnetic field from magnetic-field amplification caused by turbulence.

Variations in the radio spectral index on spatial scales at least down to $7''$ are observed into the millimeter radio band.[75] A concavity of the synchrotron spectrum due to the modification of the shock structure by streaming cosmic rays is observed. Unlike the changes in brightness observed in the radio knots at centimeter wavelengths, the fluctuations in the millimeter band are more consistent with actual changes in the efficiency of cosmic-ray acceleration in different regions than changes in the magnetic field strength interacting with a background population of GeV electrons.

Radio polarization signatures are expected to trace the dynamical properties of fluids due to field freezing within the magnetized plasma. Young remnants such as Cas A are expected to exhibit radial polarization out to the reverse shock as a result of ejecta expansion. In Cas A, radial polarization is observed beyond the radio-bright ring of the reverse shock into the radio plateau region attributed to Rayleigh-Taylor instabilities extending from the contact discontinuity.[76] Depolarization due to variable Faraday rotation within the bandwidth of VLA observations is strongly correlated with x-ray thermal emission, suggesting mixing is occurring between thermal and relativistic plasmas.

2.4 Infrared Observations

Mid-infrared imaging and grating spectroscopy of FMKs with the *Infrared Space Observatory* (ISO) reveal the dust environment around Cas A.[77,78] A unique class of silicate dust grains not found in typical interstellar dust is observed in Cas A. A strong correlation between this unique dust emission and that of argon and oxygen lines lead to the conclusion that some of the ejecta of Cas A is being condensed into dust grains.[79] This dust formation will reduce the abundances of elements (except neon) observed in the thermal x-ray spectra of the forward shock.

Ejecta mixing is also evident from mid-infrared observations.[80] [Ar II] and [Ar III], and [S IV] lines are spatially coincident with [Ne II] and [Ne III] lines as well as silicate dust grains. The neon lines, however, are anticorrelated with the silicate dust emission, suggesting that mixing of the argon and sulfur layers was extensive, while very little mixing occurred between the silicon and neon layers.

Mid-infrared observations also show the presence of continuum spectra coincident with the blast wave. These spectra are well fitted by a special class of silicates proposed by Draine and Lee (1984) which are being shock heated.[81] No evidence of synchrotron emission was present in the observations, however the 3σ continuum sensitivity limit of the ISOCAM instrument is roughly 6 times that of the expected synchrotron spectrum at the observation wavelength of 6 μm.

Near-infrared observations (J and K band) reveal faint diffuse emission in a shell morphology.[82] The existence of diffuse emission in the J band precludes thermal dust emission which would need to be emitting at temperatures where grains are expected to be destroyed. The morphology of the diffuse shell is more similar to the radio continuum than to the mid-infrared continuum, indicating the J band emission is most likely synchrotron radiation.

2.5 X-Ray Observations

The x-ray observations of Cas A reveal the bright thermal emission from ejecta heated by the reverse shock. This thermal emission contains line emission from helium-like and hydrogen-like ions of a variety of fusion products from oxygen to iron in supersolar abundances. Expansion velocities of these ejecta based on line centroid measurements show a systematic variation in Doppler velocities on the order of 2000–3000 km s^{-1} toward the observer in the northwest and away from the observer in the southeast.[83–85]

Abundances derived from these thermal emission lines in bright x-ray knots show an enhancement of silicon and sulfur consistent with oxygen-burning nucleosynthesis which took place in the progenitor. Dimmer, more diffuse x-ray emission is consistent with silicon-burning nucleosynthesis which produces iron deeper within the progenitor. This more diffuse component, however, is found to extend beyond the silicon- and sulfur-rich knots which suggests significant mixing of ejecta took place during the supernova explosion.[86]

The jet-like feature originally discovered in optical FMKs in the northeast is prominent in x-ray emission. Ejecta abundances measured in this jet are consistent with explosive silicon burning which took place during the explosion. The protrusion of ejecta beyond the forward shock and faint radial filaments of x-ray emission pointing in the direction of this feature strongly suggests that this feature is a jet of ejecta created by an aspherical explosion. The fastest of optical FMKs in both the jet and in the opposite direction give Doppler velocities exceeding 10^4 km s^{-1}, suggesting the asymmetry originated in the initial supernova event.[69]

A *Rossi X-Ray Timing Explorer* (RXTE) measurement of the spectrum Cas A between 2–50 keV reveals the presence of a nonthermal tail shown in Fig. 2.2.[52] This nonthermal tail was initially interpreted as x-ray synchrotron radiation from TeV electrons, however bremsstrahlung from a population of nonthermal electrons could also explain the spectrum.[87,88]

An increase in the photoelectric absorption of soft x rays points to evidence of an intervening molecular cloud in the western part of the remnant.[89] The velocities of bright radio knots appear anomalous in this region, with some knots actually moving toward the center of the remnant. Absorption of NH_3 and CO toward this regions shows a temperature which is high (≈ 18 K) for its derived molecular hydrogen density (≈ 1000 cm^{-3}).[90] Both the high temperature of the cloud and the anomalous velocities of radio knots suggest an interaction is currently occurring.

One of the most exciting initial findings made with the *Chandra X-Ray Observatory* is the discovery of an x-ray point source near the center of Cas A. This source has a spectrum well-fitted by a blackbody model with a temperature $kT = 0.25 - 0.35$ keV, assuming modification by a neutron-star atmosphere, or a

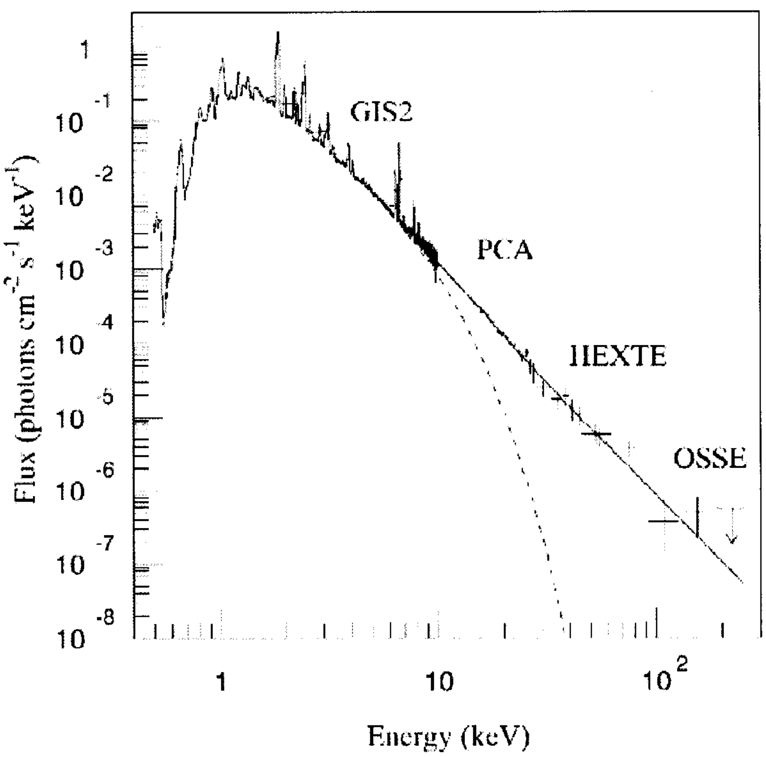

Figure 2.2: An x-ray spectrum of the supernova remnant Cassiopeia A taken from four different instruments, taken from Allen *et al.* (1997).[52] Included are spectra from the GIS2 instrument on ASCA, the PCA and HEXTE instruments on RXTE, and the OSSE instrument on the *Compton Gamma-Ray Observatory.*

power-law model with a photon spectral index ($dN/dE \propto E^{-\Gamma}$) of $\Gamma = 2.8 - 3.6$.[91] The most plausible explanation for this central source is a neutron star with properties more consistent with anomalous x-ray pulsars as opposed to a young Crab-like pulsar. No counterpart to this x-ray source has been discovered at other wavelengths. The point source lies $6.6'' \pm 1.5''$ (6.5 ± 1.5 pc) north of the dynamical center of the remnant derived from optical FMKs.[92]

2.6 Gamma-Ray Observations

An observation of TeV gamma rays would provide very strong evidence that Cas A is accelerating either protons or electrons to TeV energies. A measurement with the *Compton Gamma-Ray Observatory* EGRET instrument gave an upper limit of 2.0×10^{-11} erg cm^{-2} s^{-1} ($E > 100$ MeV).[93] Subsequent measurements with the Whipple Telescope and the *Cerenkov Atmospheric Telescope* (CAT) also resulted in upper limits of $\approx 6 \times 10^{-12}$ erg cm^{-2} s^{-1} ($E > 500$ GeV).[94,95]

A detection of TeV gamma rays from Cas A was finally observed with the HEGRA Cerenkov imaging telescope at the 5σ significance level.[96] The HEGRA telescope detected a flux of $(7.2 \pm 2.0_{\rm stat} \pm 2.0_{\rm sys})\ \times 10^{-13}$ erg cm^{-2} s^{-1} ($E > 1$ TeV) and measured a spectral index of $\Gamma = 2.5 \pm 0.4_{\rm stat} \pm 0.1_{\rm sys}$ between 1 and 10 TeV. The uncertainty in the reconstructed position of the origin of these gamma rays is larger than the diameter of Cas A, leaving the exact location and extent of the gamma-ray emission undetermined.

2.7 The Cosmic-Ray Acceleration Question

The detection of TeV gamma ray emission is unquestionably evidence of cosmic-ray acceleration to TeV energies within Cas A. The question of where this acceleration is occurring is so far unanswered. A hard x-ray nonthermal tail has also been associated with Cas A, but the hardest x-ray imaging to date ($<$ 15 keV) reveals that this emission is diffusely distributed rather than associated with shock structure. How much of this emission is synchrotron emission from TeV electrons must also be answered in order to discern between a hadronic and leptonic origin of the observed gamma-ray emission.

The discovery of the forward shock of Cas A will put the best constraint on how much of this emission is synchrotron emission due to its more favorable conditions for cosmic-ray acceleration in comparison to the reverse shock. Other acceleration sites may also be present within Cas A. Rayleigh-Taylor fingers could produce magnetic inhomogeneities which would be sites of stochastic (second-order) acceleration. Reflection shocks can be formed in the intershock region as the blast wave encounters dense clumps of circumstellar matter. The next two chapters will explore cosmic-ray acceleration at the forward shock and possible sources of postshock acceleration, respectively.

Chapter 3

X-Ray Synchrotron Radiation at the Forward Shock of Cassiopeia A

.

3.1 Observations and Data Reduction

A search for x-ray synchrotron emission at the forward shock of Cas A was conducted using the high-resolution imaging ($\sim 0.5''$ half-power diameter) and modest spectral (110 eV at 1 keV) capabilities of the *Chandra X-Ray Observatory* ACIS instrument.[97] Cas A was observed for 50 ks on 2000 January

30-31 using the backside-illuminated ACIS S3 chip. The observation was conducted in graded mode where each event is assigned a grade based on the neighboring pixels to determine the probability that the event is a photon entering the front aperture of the telescope. The grades assigned are the same as those of the ASCA observatory and only grades 0,2,3,4, and 6 were kept. The light curve showed no significant flaring events during the observation.

The data were reduced with version 2.20 of the *Chandra* calibration database (CALDB) provided by the *Chandra X-Ray Center* (CXC) using their data analysis package CIAO (v. 2.3) and the FTOOLS package (v. 5.2) provided by the High Energy Astrophysics Science Archive Research Center (HEASARC).[98] Known bad pixels and columns were removed based on housekeeping files provided with the data by the CXC. A charge transfer inefficiency correction was also performed during this step. After reduction, two faint bands along the readout direction of the chip were noticed corresponding to the brightest regions of Cas A. These strips are the result of events which occurred during readout of the chip once every 3.2 s. Because the events are not time-tagged, the readout events could not be eliminated from the image, so background spectra were extracted from the source image in regions along the readout direction of the source region. A comparison of data subtracted with same-sky background and blank-sky backgrounds reveals a difference of approximately 10%–20% below 2 keV, but virtually no difference above. This is consistent with a difference due to readout events of the bright emission from the reverse shock which is brightest below 2 keV. Extracted spectra were rebinned to contain a minimum of 20 counts per bin to validate Gaussian statistics and the χ^2 fitting statistic. Spectra were fitted with the latest version of the XSPEC fitting package (XSPEC v. 11.2).[99]

3.2 The Forward Shock

The forward shock of a supernova remnant is preferable to the reverse shock as a location for searching for cosmic-ray acceleration for two primary reasons. First, magnetic fields just behind the forward shock are naturally compressed. If the ambient magnetic field is pointing in a constant direction, it will be very oblique to the shock somewhere on the remnant which will lead to very efficient cosmic ray acceleration. The magnetic field at the reverse shock, on the other hand, is the original magnetic field of the progenitor diluted by the expansion of the remnant. The observed direction of the magnetic field in Cas A from radio polarization studies is primarily radial all the way to the forward shock, therefore no enhancement in the acceleration efficiency is gained due to magnetic field obliquity in the reverse shock. Second, the lower density of the forward shock translates into a lower thermal brightness than that of the reverse shock, therefore it is more likely that a hard excess in the form of synchrotron radiation will be observed in the thermally dominated x-ray emission at the forward shock.

The forward shock of Cas A was first identified by Gotthelf *et al.* (2001) using a first-light *Chandra* observation with an exposure time of 5 ks.[100] The forward shock stands out as wisps tracing a circular pattern in the 4–6 keV image when compared to the 0.5–10 keV image in Fig. 3.1, indicating that the forward shock contains a harder spectrum. This is expected of a forward shock which typically has a higher temperature than the reverse shock and may contain a hard nonthermal component. Gotthelf *et al.* showed that the forward shock spatially corresponds to the dropoff of the radio plateau located outside the bright reverse shock. There is a dramatic change in the radio polarization angle from primarily radial to tangential at the forward shock front. The mean angular distance of the forward shock from the expansion center in their work is $153'' \pm 12''$. There is no presence of a bright radio ring corresponding to the x-ray forward shock emission, which is typically an indication of cosmic ray acceleration. Either cosmic ray acceleration is not taking place within the forward shock, or that this is an atypical example of cosmic ray acceleration.

The forward shock was separated into 15 regions each covering a continuous wisp of bright forward shock emission. The regions encompass all bright forward shock emission which almost encircles the remnant. The

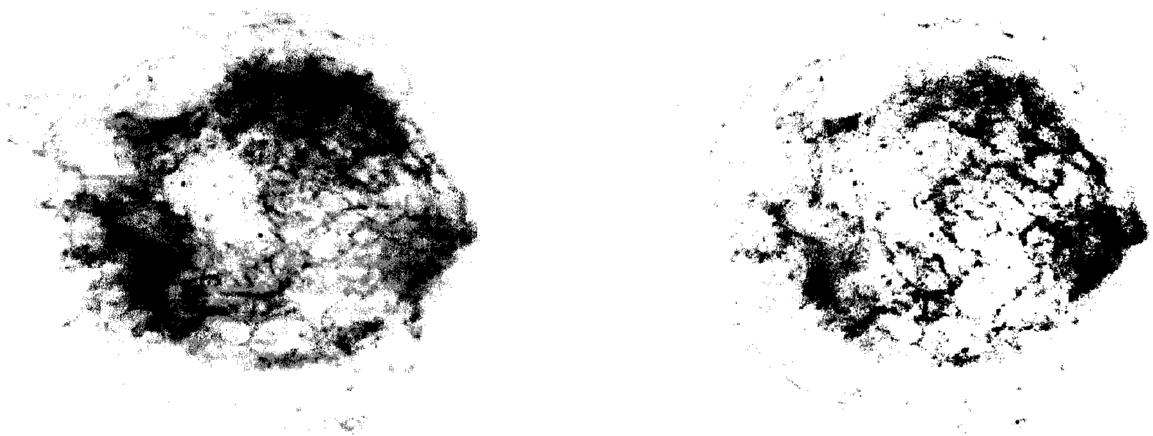

(a) (b)

Figure 3.1: *Chandra* images of Cassiopeia A at 0.5–10 keV (a) and 4–6 keV (b). The thin wisps surrounding the bright inner ring in the 4–6 keV image is the forward shock identified by Gotthelf *et al.* (2001).[100]

extraction regions shown in Fig. 3.2 are each labeled according to their compass position relative to the expansion center.

A qualitative comparison of spectra extracted from the forward and reverse shocks shown in Fig. 3.3 reveals differences between the forward and reverse shocks. The forward shock contains only very weak lines of highly-ionized silicon and sulfur, whereas the reverse shock contains lines of highly-ionized oxygen, neon, magnesium, silicon, sulfur, and iron consistent with ejecta produced by explosive silicon and oxygen burning.[86] The fact that only silicon and sulfur lines are present without the presence of lines of lower Z elements points to the possibility of a second continuum component completely hiding all but the strongest lines. The intershock region seems to be intermediate between these two spectra, showing more prominent silicon and sulfur lines as well as evidence of magnesium lines.

3.3 One-Component Thermal Models

The forward shock spectra were first fitted with a one-component thermal model. The model chosen is the nonequilibrium ionization (NEI) plane-parallel shock model of Borkowski, Lyerly, and Reynolds (2001).[101] It has been well known that supernova remnants do not reach ionization equilibrium until well into the Sedov phase of evolution, therefore nonequilibrium ionization modeling

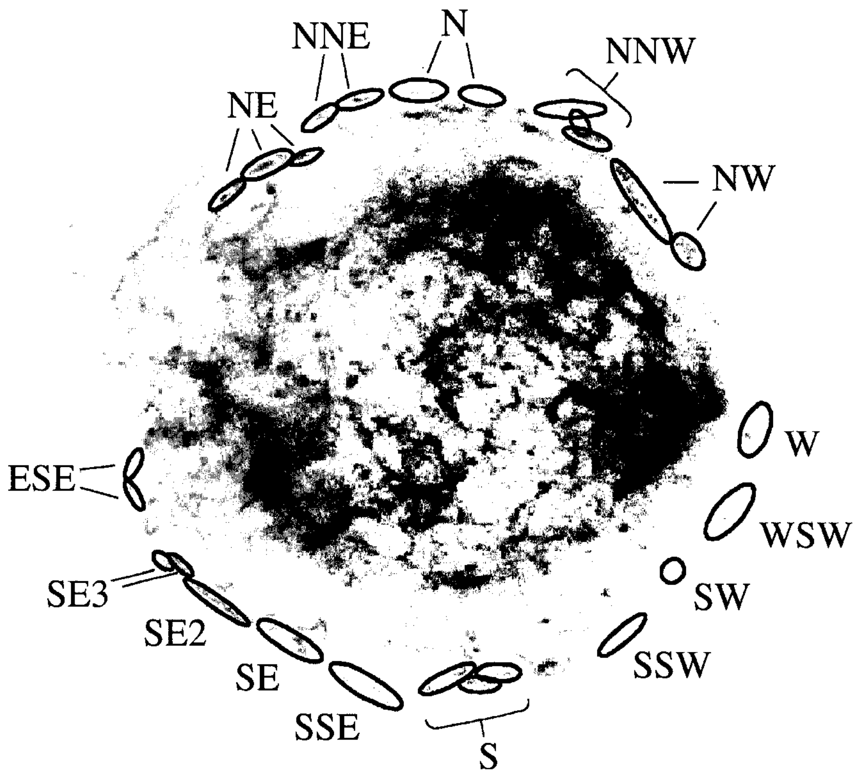

Figure 3.2: Spectral extraction regions covering the forward shock of Cas A.

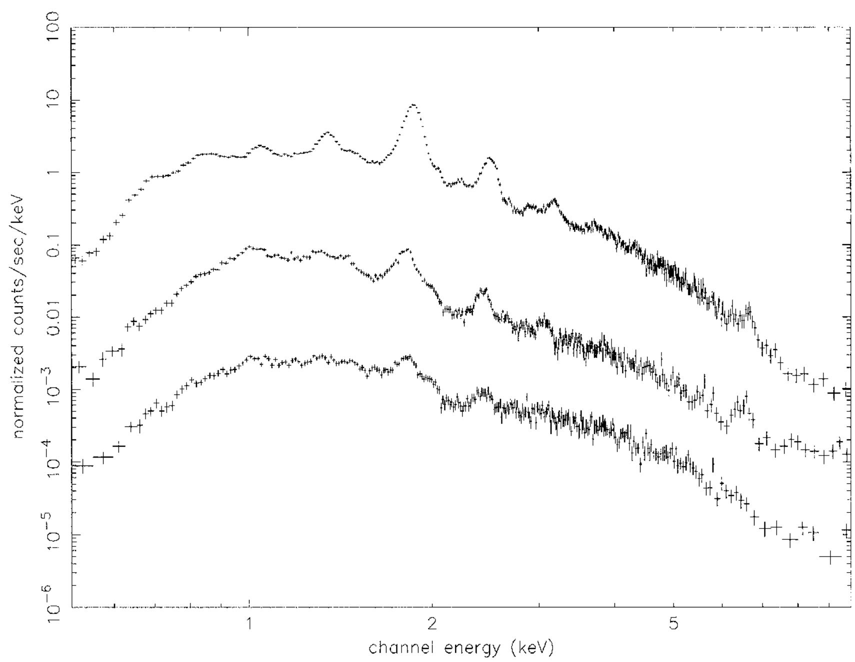

Figure 3.3: Sample spectra of the forward shock (bottom, $\times 0.01$), intershock (middle, $\times 0.1$) and reverse shock (top) regions taken from the northeast of Cas A. The low Si and S equivalent widths in the forward shock, along with the absence of lower Z elements such as Ne and Mg, indicates a second continuum component. Each spectrum is scaled by a factor of 10 above the spectrum immediately below for clarity.

is necessary for all young remnants. While earlier extensive models like those by Hamilton, Sarazin and Chevalier (1983) assume a single ionization state,[102] this model assumes a range of ionization states to reflect the sampling of plasma shocked over a range of times. Unless noted, the particular model used is the *pshock* model available in XSPEC, which assumes that electron temperatures are equilibrated with the ion temperatures at the shock front via some form of collisionless heating.

The parameters for the model are the shock temperature T_s, the maximum ionization timescale $\tau = n_e t$ (cm^{-3} s), and a flux normalization constant $C = 10^{-14}/(4\pi D^2) \int n_e n_H \, dV$ where D is the distance to the source, and n_e and n_H are the electron and hydrogen densities, respectively, in cgs units. With these parameters, the model calculates the ionization states and line emissivities of typical ejecta elements shown in Table 3.1 except argon. At x-ray energies, the dominant lines seen are K transitions from He-like or H-like ionization states with the exception of the Fe L blend at 0.65–1.15 keV. The limited spectral resolution of the ACIS detector does not allow the individual lines in the He-like triplets to be resolved. In addition, the model calculates the thermal bremsstrahlung continuum from a Maxwellian population of electrons at the shock temperature T_s. Photoelectric absorption of soft x rays by intervening interstellar gas is modeled using the cross sections of Morrison and McCammon

(1983),[103] parameterized in the XSPEC *wabs* model by the intervening column density of hydrogen n_H.

The progenitor of Cas A most likely had a stellar wind which expelled most if not all of its hydrogen envelope. High abundances of helium and nitrogen observed optically in QSFs suggests that most if not all of the hydrogen envelope was expelled before the event occurred.[63] The anomalously bright x-ray and radio emission from Cas A can be explained if the supernova is interacting with a dense circumstellar wind. However, the x-ray lines of elements expelled during the stellar wind phase of the progenitor are not prominent in the energy range of *Chandra*.

Models assuming solar abundances [Fig. 3.4(a)] do not provide statistically good fits (*i.e.* $\chi^2/\nu > 2.0$) to any of the forward shock spectra— predicting lines where there are none and vice versa. The centroids of the lines can be shifted by relaxing the constraint of equipartition between electrons and ions at the shock, but this does little to alleviate the poor fit [Fig. 3.4(b)]. Allowing the abundances to vary provides a better fit with a high temperature and low ionization timescale expected of a forward shock with the age of Cas A, however it is evident that this model is too soft at high energies [Fig. 3.4(c)]. Subsolar abundances must be invoked for all elements to explain the very low or nonexistent equivalent line widths. It is physically possible to have subsolar abundances of some elements due to dust formation as has been observed through meteoritic abundances and infrared observations of SN 1987A.[105,106] However, such a model must also explain a very unlikely depletion of neon which is not present in dust grains.

3.4 A Thermal-Thermal Model

A second thermal component added to the model greatly improves the fits, especially to the silicon and sulfur line profiles as shown in Fig. 3.5. This second component could come from either mixing of the reverse shock into the forward shock, or a second population of solar-abundance ions which is being turbulently mixed back toward the forward shock. Two varieties of a second plane-parallel shock model (*pshock*) were used as the second thermal model— one with solar abundances and one with abundances measured at the reverse shock in the same azimuthal direction as the forward shock region. The solar abundances model provided better values of the reduced χ^2 than a component with reverse-shock abundances.

In general, the second component requires a higher ionization timescale, however both the ionization timescale and the temperature of this second component are highly uncertain and change erratically from one region to the next (Fig. 3.6). It is more likely that these changes reflect *ad hoc* model components necessary to obtain good fits rather than actual physical changes

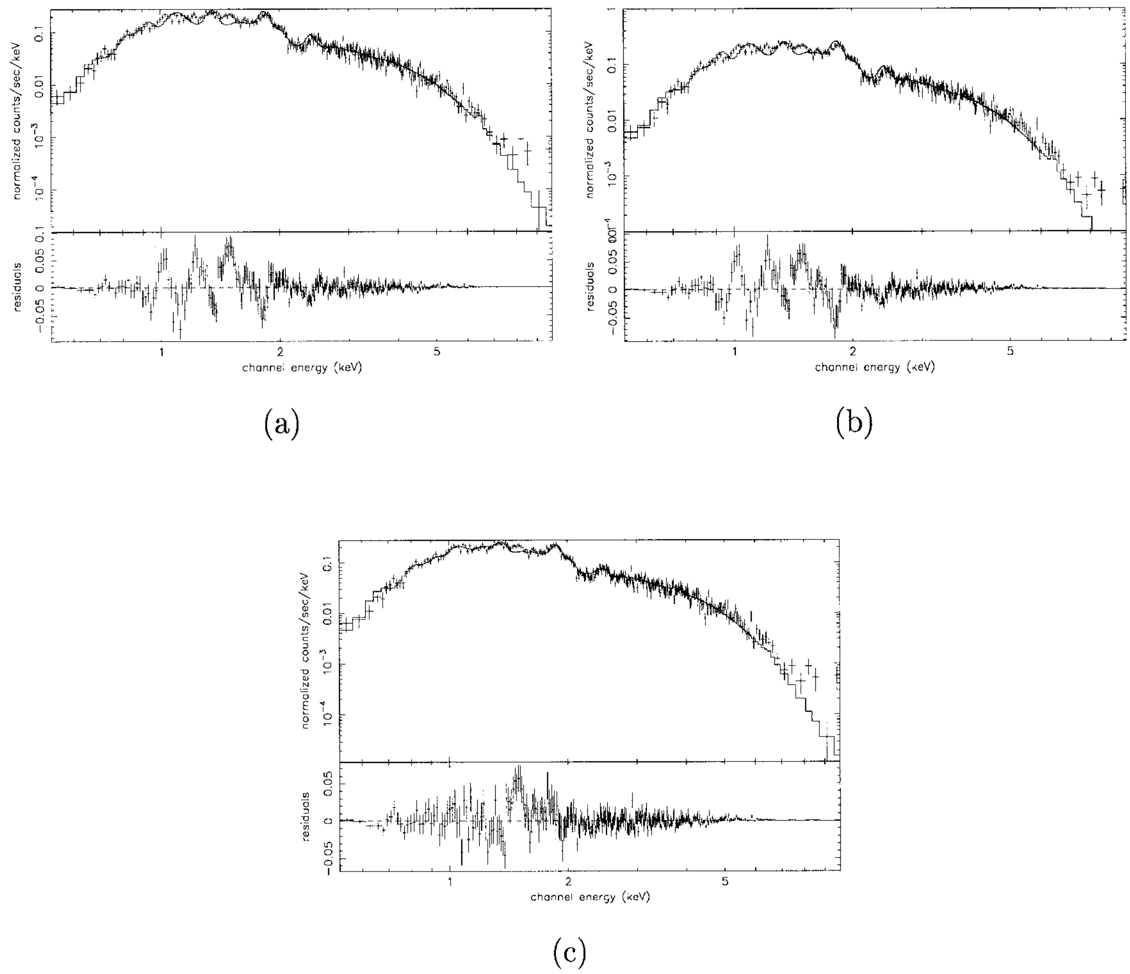

Figure 3.4: Fits of one-component thermal plasma models to a sample spectrum of the forward shock taken from the NE region. Included are models which assumes solar abundances with equipartition between electrons and ions (a), solar abundances with nonequipartition where $T_e = 0.5T_i$ (b), and variable abundances with equipartition (c).

Element	He-α (keV) (average of triplet)	Ly-α (keV)
Oxygen	**0.570**	**0.653**
Neon	**0.916**	**1.016**
Magnesium	**1.34**	1.476
Silicon	**1.86**	2.006
Sulfur	**2.46**	2.622
Argon	3.14	3.315
Calcium	3.90	4.093
Iron	6.70	6.97
Iron L blend	**0.68–1.15**	

Table 3.1: Prominent line transitions observed in x rays from supernova remnants from Petre (1996).[104] Line transitions in bold indicate the strongest lines.

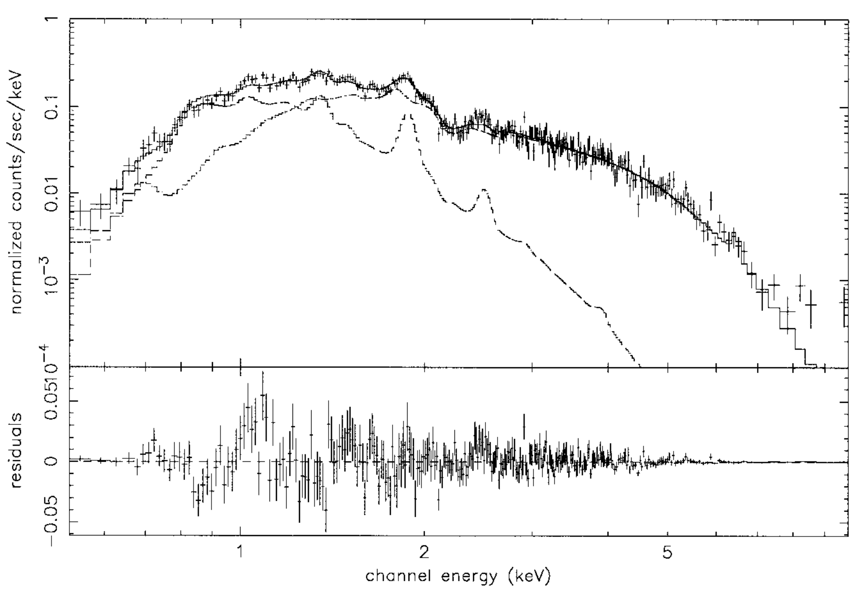

Figure 3.5: Fit of a double-thermal model to a sample spectrum (NE) of the forward shock. The model shown assumes solar abundances for both thermal components. Assuming solar abundances for the second component provided better fits for most regions than assuming reverse-shock abundances.

from one region to the next. Therefore a second thermal component is an unlikely explanation for the forward shock.

There are, however, some parts of Cas A which show bright filamentary structures between the forward and reverse shock regions, especially in the north and south. This bright filamentary structure could either be very bright forward shock structure projected into the interior of the forward shock shell or bright ejecta-dominated material mixed turbulently via Rayleigh-Taylor instabilities toward the forward shock. Most models of Rayleigh-Taylor mixing do not predict the ejecta will reach all the way to the forward shock,[107,108] but it is predicted when either small scale structure in the CSM or efficient particle acceleration is present.[24,109] In the case of particle acceleration, the mixing reaches to the forward shock because the Rayleigh-Taylor instability saturates at larger amplitudes and the distance between the forward and reverse shock decreases due to an increase in the compressibility of the plasma in the presence of streaming accelerated particles.

There are regions where the distance between the forward and reverse shocks is decreased: in the northern and the eastern parts of the remnant. A hardness ratio map (4–6 keV/0.5–10 keV) of Cas A in Fig. 3.7 reveals a softer forward shock in these regions. This coincidence could be interpreted as due to mixing to the forward shock in these regions. If this mixing is due to efficient particle acceleration, it may also give some insight into the difficulty of

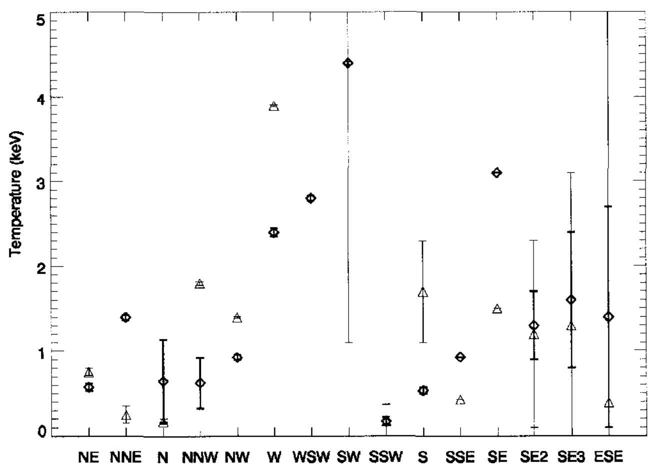

(a)

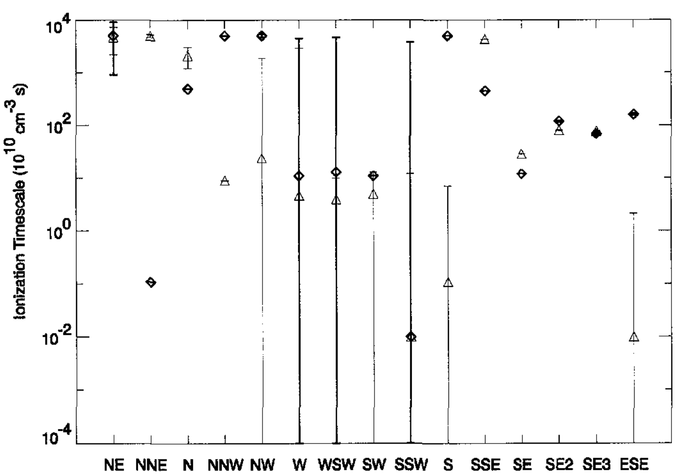

(b)

Figure 3.6: Temperatures (a) and ionization timescales (b) of the second thermal component derived from a double-thermal model of the forward shock. Components assuming solar abundances (diamonds) and reverse shock abundances (triangles) are shown. The erratic behavior from one region to the next is unlikely physical in nature, but rather reflects an *ad hoc* fit to the data.

pinpointing locations of efficient acceleration in most shell-type remnants. Efficient acceleration leads to mixing of ejecta to the forward shock which can mask the nonthermal synchrotron signature indicating efficient acceleration.

To determine whether or not mixing from the reverse shock is reaching the forward shock globally, equivalent widths of the silicon He-α line were extracted from each region of the forward shock and the reverse shock at the same azimuthal position. The continuum used for the equivalent line widths in the forward shock was best-fit double-thermal model with the silicon abundance set to zero. The continuum used for the reverse shock was the best-fit plane-parallel shock model with the silicon abundance set to zero. Significant global mixing from the reverse shock to the forward shock would be expected to manifest itself through a correlation between the equivalent widths at the reverse and forward shocks. Fig. 3.8 shows no such correlation, therefore global mixing to the forward shock is not taking place.

3.5 A Thermal-Nonthermal Model

The next attempt to explain the forward shock spectra is the addition of a power law the *pshock* model. The power-law component ($dN/dE \propto E^{-k}$) models synchrotron radiation emitted by nonthermal electrons— chosen over the maximally-curved *srcut* model by Reynolds (1998).[31] The *srcut* model gives an

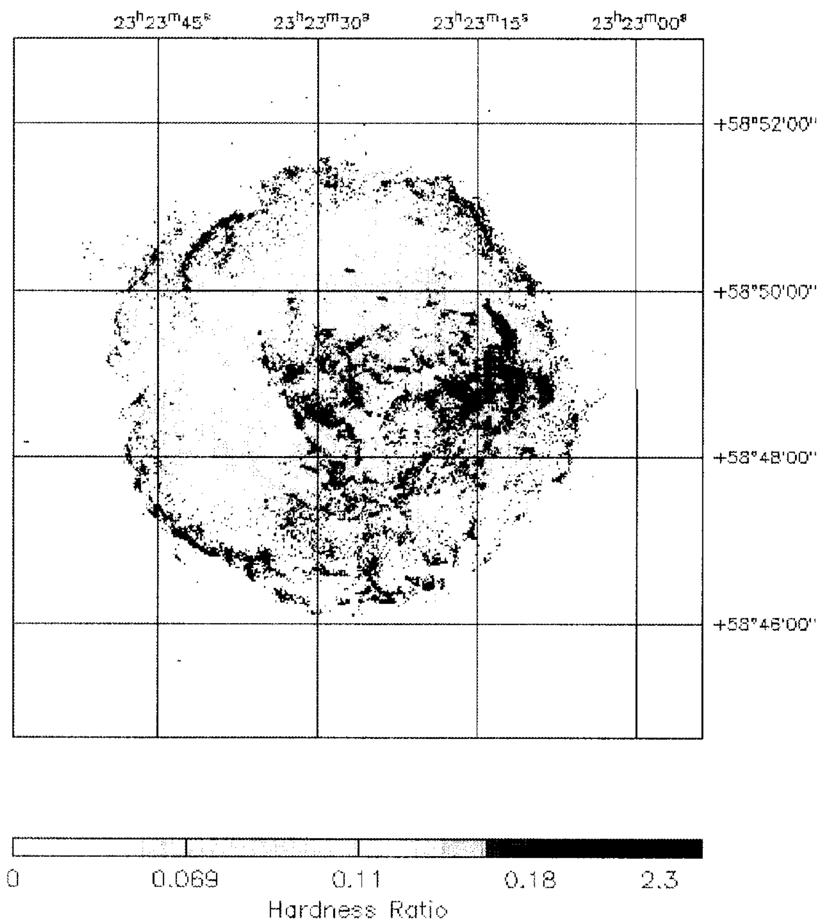

Figure 3.7: Hardness ratio (4–6 keV/0.5–4 keV) of Cas A.

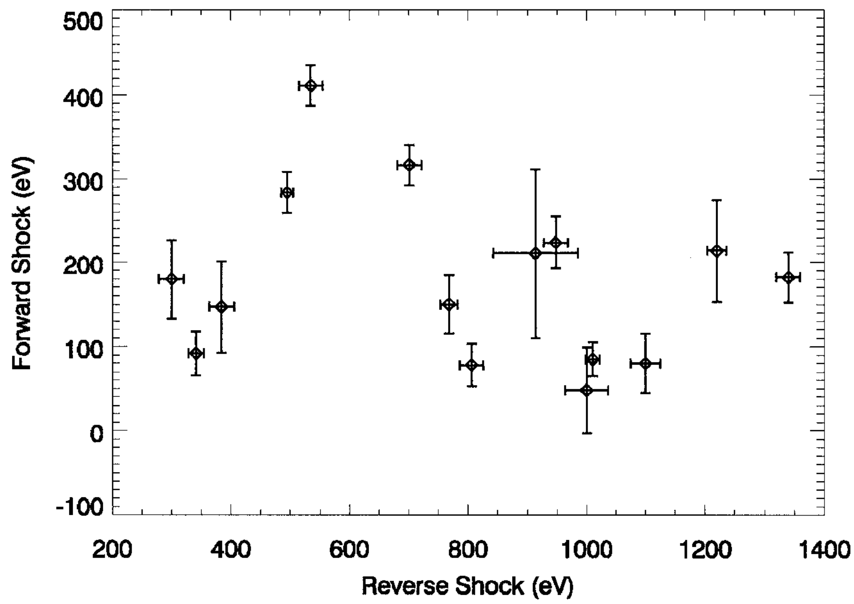

Figure 3.8: Comparison of silicon equivalent widths measured at the forward and reverse shocks. Continua used for measuring equivalent widths in the forward shock were obtained by the best-fit double-thermal model with no silicon abundance. Continua used for the reverse-shock equivalent widths assumed a plane-parallel shock model with no silicon abundance. The lack of correlation between the equivalent widths indicates the lack of global mixing of ejecta all the way to the forward shock.

estimate of the frequency at which the spectrum falls one decade below the extrapolation of the radio spectrum, which then can be used to determine the maximum energy of electrons in a given magnetic field. Therefore, the model requires spatial knowledge of the radio spectrum. A measurement of the radio spectral index at the forward shock would produce large uncertainties due to the dropoff of the radio plateau emission coincident with the x-ray forward shock.

When applied to the forward shock spectra, this model provides a good value of the χ^2/ν fit statistic, but not as good as the double-thermal model assuming solar abundances. Obtaining the best fit to the weak silicon and sulfur line centroids requires nonequipartition between the ions and electrons at the shock front. A fit to the strong lines in the N region gives a ratio of electron to ion temperature of 0.46, which was adapted for the other regions. This degree of nonequipartition is consistent with that found in Kepler's supernova remnant (T_e/T_i=0.5) by Borkowski *et al.* (1994).[110] The thermal plus synchrotron model provides good fits to all regions of the forward shock except those in the western part of the remnant (see Section 3.6). Fits such as that in Fig. 3.9 show that an enhancement of silicon could improve the fit. The best-fit parameters of the model for all forward-shock regions are given in Table 3.2.

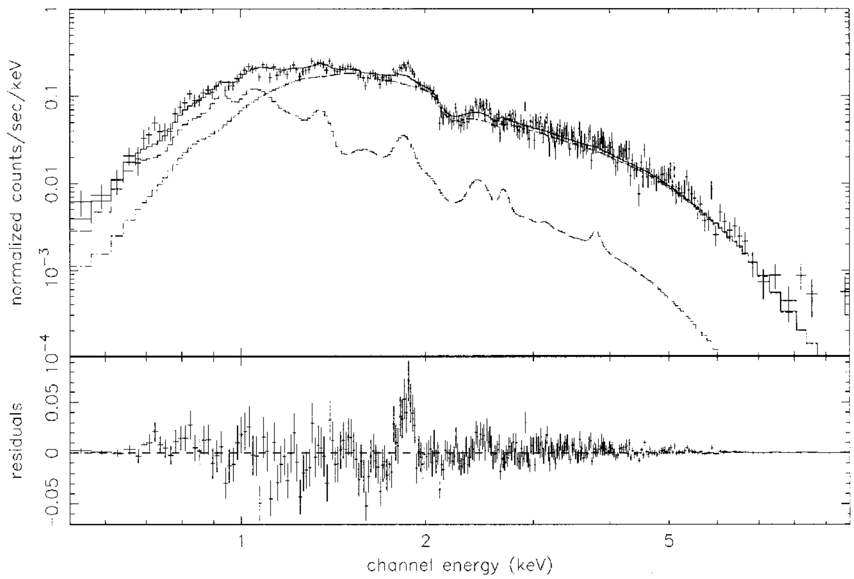

Figure 3.9: Best fit of a thermal plus synchrotron model to a sample forward shock spectrum (NE region). The thermal component of the model is a plane-parallel shock model assuming nonequipartition between electrons and ions ($T_e = 0.46\,T_i$).

Region	n_H (10^{22} cm^{-2})	kT_i (keV)	$\tau = n_e t$ (10^{10} cm^{-3} s)	k	χ^2/ν
NE	1.08 $^{1.06}_{1.09}$	3.0 $^{2.9}_{3.1}$	3.8 $^{3.7}_{4.1}$	2.38 $^{2.34}_{2.42}$	337/281 = 1.20
NNE	1.10 $^{1.07}_{1.13}$	2.4 $^{2.3}_{2.5}$	3.0 $^{2.9}_{3.9}$	2.52 $^{2.46}_{2.57}$	232/226 = 1.02
N	1.24 $^{1.22}_{1.25}$	1.7 $^{1.6}_{1.8}$	3.0 $^{2.9}_{3.1}$	2.87 $^{2.84}_{2.92}$	461/266 = 1.73
NNW	1.08 $^{1.07}_{1.10}$	2.5 $^{2.4}_{2.6}$	3.1 $^{3.0}_{3.2}$	2.55 $^{2.52}_{2.58}$	375/281 = 1.33
SW	1.92 $^{1.77}_{2.04}$	3.2 $^{3.1}_{3.3}$	5.5 $^{5.2}_{5.7}$	2.86 $^{2.73}_{3.07}$	96/97 = 0.99
SSW	1.56 $^{1.51}_{1.68}$	3.0 $^{2.9}_{3.1}$	9.4 $^{8.4}_{9.8}$	2.88 $^{2.78}_{3.00}$	104/107 = 0.97
S	1.75 $^{1.68}_{1.81}$	1.9 $^{1.8}_{2.0}$	5.4 $^{5.2}_{5.9}$	2.74 $^{2.71}_{2.80}$	317/252 = 1.26
SSE	1.77 $^{1.70}_{1.91}$	2.7 $^{2.6}_{2.8}$	2.6 $^{2.4}_{2.9}$	2.55 $^{2.34}_{2.64}$	198/155 = 1.28
SE	1.30 $^{1.21}_{1.32}$	3.7 $^{3.6}_{3.8}$	2.3 $^{2.1}_{2.5}$	2.40 $^{2.37}_{2.47}$	241/209 = 1.15
SE2	1.35 $^{1.30}_{1.44}$	3.4 $^{3.3}_{3.5}$	3.3 $^{3.0}_{3.8}$	2.50 $^{2.41}_{2.58}$	220/167 = 1.32
SE3	1.64 $^{1.56}_{1.74}$	4.3 $^{4.2}_{4.4}$	16 $^{14}_{17}$	2.44 $^{2.33}_{2.50}$	169/143 = 1.18
ESE	1.40 $^{1.38}_{1.45}$	3.0 $^{2.9}_{3.1}$	24 $^{23}_{25}$	2.80 $^{2.71}_{2.87}$	156/121 = 1.29

Table 3.2: Best-fit parameters of the forward shock to a thermal plus synchrotron model. The thermal model is the plane-parallel shock of Borkowski *et al.* (2001) with the electron temperature scaled to the ion temperature: $T_e = 0.46\,T_i$.[101] The nonthermal model is a power law in differential number of photons with an index k. Small numbers indicate the 90% confidence interval.

3.6 Molecular Cloud Interaction

Strong absorption of soft x-rays and peculiar velocities of radio knots in the region indicate that the remnant is interacting with a molecular cloud in the western part of the remnant.[84,74] Forward-shock spectra of the western regions of Cas A are anomalous with respect to the rest of the forward shock. These regions show strong lines of silicon and sulfur and evidence of emission from argon and calcium. The iron Kα line appears in two regions suggesting that there is very little nonthermal emission in these regions. The spectra shown in Fig. 3.10 were best fitted to a double-thermal model with a solar abundance component and a reverse-shock component. The best-fit parameters of this fit are shown in Table 3.3.

3.7 Interpretation of Forward Shock Emission

The shock temperature measured at the forward shock is 2–3 keV, corresponding to a shock velocity ($kT_i = 3/4\, \rho_1/\rho_2\, \mu m_H v_s^2$) of 730–890 km s^{-1} assuming standard a strong nonradiative shock ($\sigma \equiv \rho_2/\rho_1{=}4$) with completely ionized H (65%) and He (35%) comprising most of the material behind the shock. Under these assumptions, the postshock bulk velocity of gas is $3/4\, v_s\ = 540$–670 km s^{-1}. This is lower than the velocities measured in Cas A using Doppler

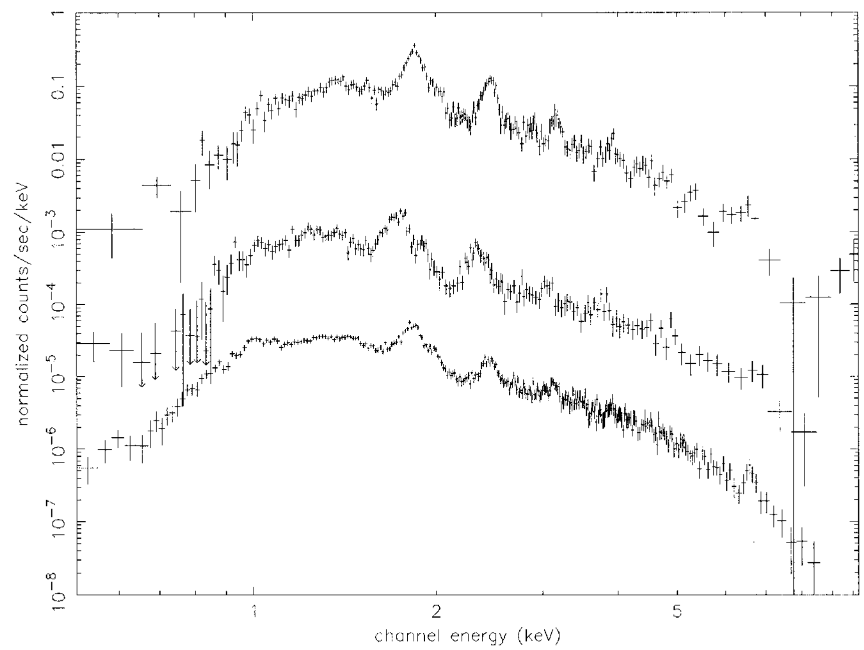

Figure 3.10: Spectra extracted from the western regions of the forward shock, which is interacting with a molecular cloud. The spectra are extracted from the W (top), WSW ($\times 10^{-2}$, middle), and NW ($\times 10^{-3}$, bottom) regions of Fig. 3.2.

	NW		W	WSW	
n_H (10^{22} cm^{-2})	1.31	$^{1.28}_{1.33}$	2.46	2.01	$^{1.87}_{2.06}$
kT_s (keV)	2.0	$^{1.9}_{2.1}$	0.65	0.56	$^{0.46}_{0.65}$
$\tau_s = n_e t$ (10^{10} cm^{-3} s)	0.19	$^{0.18}_{0.22}$	0.88	0.39	$^{0.31}_{0.61}$
Flux$_s$ (10^{12} erg cm^{-2} s^{-1})	2.97	$^{2.80}_{3.14}$	0.58	0.36	$^{0.23}_{0.57}$
kT_r	1.4	$^{1.2}_{2.0}$	3.9	6.0	$^{4.9}_{7.8}$
$\tau_r = n_e t$ (10^{10} cm^{-3} s)	24	$^{12}_{31}$	4.7	4.0	$^{2.9}_{5.0}$
Flux$_r$ (10^{12} erg cm^{-2} s^{-1})	1.01	$^{0.86}_{1.17}$	0.98	0.77	$^{0.66}_{0.89}$
χ^2/ν	$\frac{471}{304} = 1.55$		$\frac{421}{205} = 2.06$	$\frac{266}{178} = 1.49$	

Table 3.3: Best-fit parameters of a double-thermal model fit to the western regions of Cas A. One component assumes solar abundances ("s" subscripts) and the other assumes abundances measured at the reverse shock ("r" subscripts). Both thermal models assume equipartition between the electrons and ions. Fluxes are measured in the range of 0.5–10 keV. The argon line emission at 3.4 keV is not computed by the model. Small numbers indicate 90% confidence interval, which were not calculated for the W region due to the large value of χ^2/ν.

broadening of x-ray lines in the reverse shock ($\approx$ 2000 km s^{-1})[83,84] and of optical [SII] emission from the ejecta ($\langle v \rangle \approx 1800$ km s^{-1}).[63]

There is evidence that Cas A is currently undergoing a transition from the free-expansion phase to the Sedov phase.[100] A remnant with an initial explosion energy of 10^{51} erg from an 8 $M_\odot$ progenitor would produce a shock velocity of 2500 km s^{-1} at the onset of the Sedov phase. The low ion temperature measured at the forward shock would require that the density ratio of the shock be in the range of ρ_2/ρ_1 =20–32. Large density ratios are predicted to occur if efficient shock acceleration is occurring due to the deposition of a significant fraction of energy into cosmic rays.

The measured ionization timescale over the forward shock is on the order of 10^{10}–10^{11} cm^{-3} s. At a distance of 3.4 kpc, the forward shock width of $12''$measured by Vink and Laming (2003, hereafter VL)[111] corresponds to a linear distance of $\sim 6 \times 10^{17}$ cm. This distance is traversed by the downstream plasma in about 10^{10} s, therefore the ionization timescale corresponds to an ambient density of ~1–10 cm^{-3}. This is greater than the canonical interstellar medium density of 1 cm^{-3}— an indication that the forward shock of Cas A interacting with a dense circumstellar medium likely due to mass loss from the progenitor.

The power law indices for the synchrotron component range from k=2.38–2.88 with a mean of $\langle k \rangle = 2.62$. The bright radio knots in the plateau region are believed not to be sites of acceleration, but are bright due to magnetic amplification. The population of electrons responsible for their synchrotron radiation must originate elsewhere. If they originate at the forward shock, then the radio spectrum extrapolated to x-ray energies would result in a photon spectral index of $\langle k \rangle = \langle \alpha \rangle + 1 = 1.80$. The steepening in the synchrotron spectrum at x-ray energies is expected due to synchrotron losses. A continuous injection model assuming a constant (over time) injection of a power law of electrons predicts a steepening of the spectrum to an index of $\langle k \rangle = \langle \alpha \rangle + 1.5 = 2.30$.[34] This is steeper than even the flattest observed spectrum, which can be achieved if the spectrum of injected electrons is steeper at x-ray energies than at radio energies. A cutoff in the maximum energy of electrons injected downstream of the shock by the acceleration process would provide such a steepening in the injected spectrum.

The frequency at which the photon spectrum breaks from the extrapolation of the radio spectrum can be estimated by extrapolating the radio and x-ray spectra and finding where they intersect. Without knowledge of the radio spectral index in each region, however, we estimate the break frequency assuming several reasonable values of the radio spectral index near the observe bright radio spectral index of $\langle \alpha \rangle$=0.80. These break frequencies are an upper limit to the actual break frequency which will be a continuous function rather than a broken power law.

The break frequencies, shown in Table 3.4, are highly dependent on the assumed value of the radio spectral index. Break frequencies which occur in the observed x-ray band (0.5 keV = 1.2×10^{17} Hz) can be ruled out because the observed x-ray spectral index is steeper than all of the assumed radio spectral indices. The mean spectral index of the bright radio knots slightly encroaches on this upper limit, but this is not a problem because the break frequency itself is an upper limit— the actual break frequency could be much lower.

The break frequencies here are not directly comparable to the break frequencies used in the Reynolds *srcut* model— where the break is defined as the frequency where the actual spectrum falls one decade below the extrapolation of the radio spectrum. A spectral index of $\alpha = 0.70$ gives a break frequency of 1.3×10^{16} Hz by extrapolating radio and x-ray spectra in the SE region, while replacing the power-law model with the *srcut* model gives a break frequency of 1.7×10^{17} Hz.

Based on synchrotron loss times and the thickness of the forward shock in the northeast, VL estimate a magnetic field in the range of 0.08–0.16 mG. The peak emitting frequency of a synchrotron spectrum is related to the magnetic field and electron energy by:[112]

$$\nu_{\mathrm{peak}} = 7.0 \times 10^{12}\, B_{\perp}\,(\mu\mathrm{G})\, E^2\,(\mathrm{TeV}) \tag{3.1}$$

Region	Break Frequency (10^{17} Hz)			
	$\alpha = 0.60$	$\alpha = 0.70$	$\alpha = 0.80$	$\alpha = 0.90$
NE	0.011	0.081	1.3	61
NNE	0.023	0.14	1.3	27
N	0.054	0.20	0.97	6.5
NNW	0.031	0.18	1.6	30
SW	0.095	0.38	2.0	14
SSW	0.066	0.25	1.2	8.0
S	0.079	0.36	2.3	23
SSE	0.017	0.091	0.77	13
SE	0.016	0.13	1.9	88
SE2	0.038	0.25	2.8	73
SE3	0.051	0.41	6.4	271
ESE	0.072	0.30	1.7	14

Table 3.4: Break frequencies of the forward shock regions. The break frequencies are defined by the intersection of extrapolations of radio and x-ray spectra. Values of α, the radio spectral index, are assumed in calculating the radio spectra. The x-ray spectra are steeper than the extrapolated radio spectra for all the values of α assumed in the table, therefore break frequencies larger than $\sim 10^{17}$ Hz preclude the assumed value of α.

The forward shock of Cas A cannot be accelerating electrons to energies much higher than those observed in the Chandra band. Assuming a cutoff in the synchrotron spectrum of 10^{17} Hz, the maximum electron energy cannot be greater than $\sim$10 TeV with the magnetic fields derived by VL. This is roughly consistent with the maximum energy of other young remnants— still falling well short of the knee of the cosmic-ray spectrum.

The 4–6 keV continuum is predominantly nonthermal emission, as opposed to the overall x-ray flux which contains more flux from the thermal component (Fig. 3.11). The projected flux in the 4–6 keV band drops off interior to the forward shock more dramatically than in the 0.5–10 keV image (Fig. 3.12), where some thermal emission extends into the intershock region— consistent with the idea that the hard continuum emission is a unique component different from the thermal emission. TeV electrons responsible for 4–6 keV emission are losing significant energy to synchrotron radiation near the forward shock, while GeV electrons responsible for radio emission are allowed to escape into the radio plateau region due to their longer synchrotron lifetimes.

The 20–40 keV x-ray spectrum of Cas A measured with the RXTE by Allen *et al.* (1997) was initially interpreted as synchrotron radiation.[52] However, that interpretation has been questioned by Laming (2001),[87,88] who proposes that the spectrum can be explained by bremsstrahlung emission from a population of nonthermal electrons excited by lower hybrid waves. Reflected shocks are formed

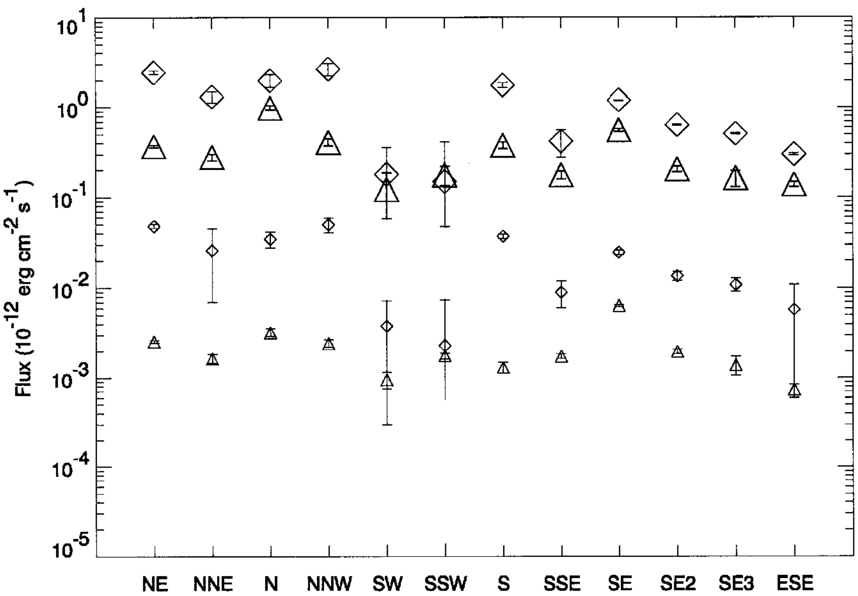

Figure 3.11: Thermal and nonthermal x-ray fluxes of forward shock regions. Plotted are the thermal (large triangles) and nonthermal (large diamonds) fluxes at 0.5–10 keV and the thermal (triangles) and nonthermal (diamonds) fluxes at 4–6 keV. The 4–6 keV fluxes have been scaled by a factor of 0.1 for clarity.

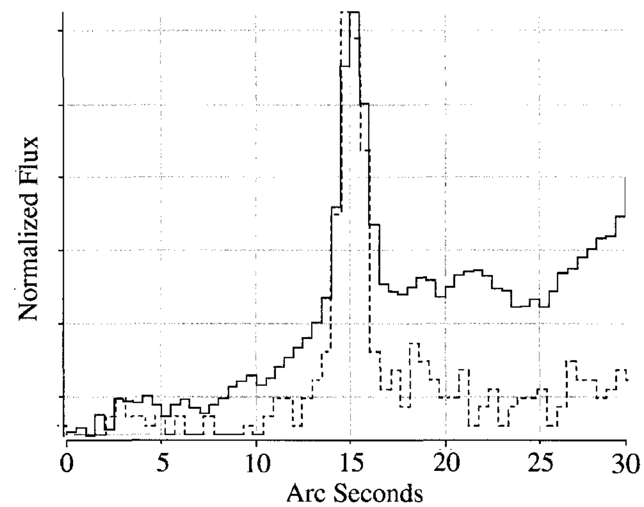

(a)

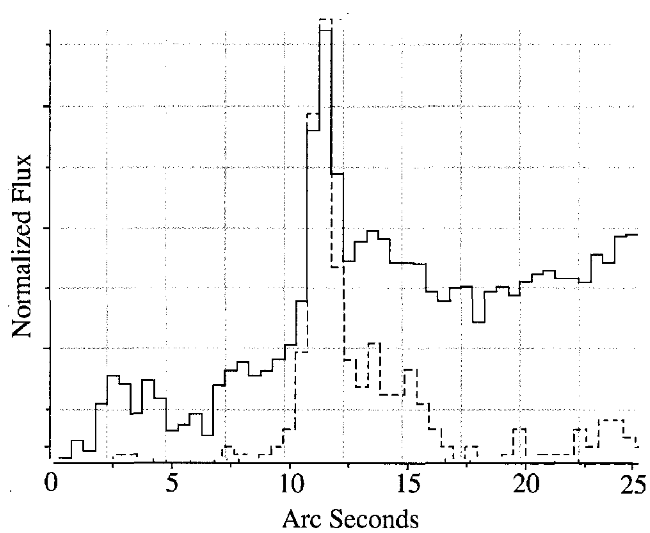

(b)

Figure 3.12: Projected flux across the NE (a) and SE (b) shock fronts. Plotted are the 0.5–10 keV flux (solid) and 4–6 keV flux (dashed). The intershock region is to the right of the shock.

when either the forward or reverse shock interact with a dense clump of material. When a reflected shock reaches high magnetic fields amplified by Rayleigh-Taylor instabilities at the contact discontinuity, lower hybrid waves are formed which accelerate electrons. An *XMM-Newton* observation of Cas A by Bleeker *et al.* (2001) show most of the 10–15 keV x-ray emission is diffusely distributed over the entire remnant rather than constrained near the reverse shock as expected with either synchrotron or nonthermal bremsstrahlung.[113]

An extrapolation of the nonthermal component from the forward shock regions to the 10–25 keV range can be made to determine the fraction of flux in that band attributable to x-ray synchrotron emission at the forward shock. The measured 10–25 keV nonthermal flux from the RXTE observation is 8.5×10^{-11} erg cm^{-2} s^{-1}, while the extrapolated x-ray synchrotron flux is 1.7×10^{-12} erg cm^{-2} s^{-1} (see Fig. 3.13). This difference is nearly two orders of magnitude. Even if the observed forward shock regions are the limb-brightened regions of a shell of forward shock emission, the forward shock can account for no more than $\sim$10% of the observed hard x-ray emission of Cas A.

3.8 Summary

Regions comprising the forward shock were found to be best fitted by a combined thermal and synchrotron model which contribute roughly to the 0.5–10

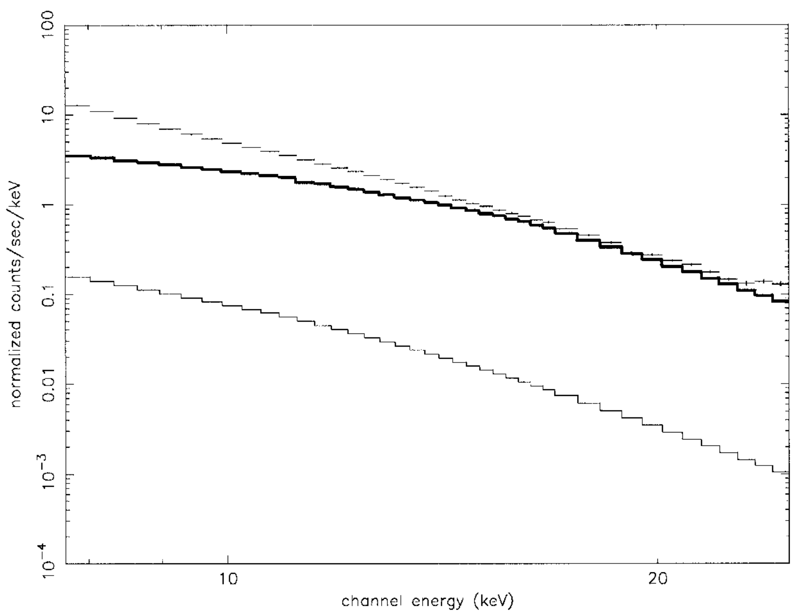

Figure 3.13: Comparison of the total forward shock nonthermal spectrum extrapolated to 10–25 keV (thin solid line) with the measured RXTE spectrum of Cas A from Allen *et al.* (1997).[52] Plotted for reference is the nonthermal component to the Cas A spectrum fitted by Allen *et al.* (thick solid line).

keV flux. Temperatures and ionization timescales, although uncertain, are consistent with the interaction of a shock traveling at 2000–3000 km/s and a dense circumstellar medium. It was necessary to assume the electrons and ions are not in equipartition in order to fit the centroids of the weak line emission observed in the forward shock. The break frequency of the synchrotron component is no greater than 10^{17} Hz, which corresponds to a maximum electron energy of $\sim$10 TeV assuming a magnetic field of 0.08–0.16 mG derived from the thickness of the shock front being due to synchrotron losses. Finally, x-ray synchrotron at the forward shock seems to account for no more than 10% of the observed flux of Cas A above 10 keV.

Chapter 4

Hard X-Ray Emission in the Postshock Region of Cassiopeia A

4.1 Postshock Emission

The postshock region (*i.e.* between the forward shock and contact discontinuity) shows primarily thermal emission with intermediate line strengths between the weak forward shock lines and the strong reverse shock lines. It is consistent with the idea that synchrotron emission is confined to the forward shock and few TeV electrons are traveling very far into the postshock region.

There are filamentary structures in the postshock region which exhibit hard emission as shown in a hardness map (4–6 keV/0.5–4 keV) of Cas A (see Fig. 3.7). This filamentary structure is highly correlated with the 4–6 keV continuum map in Fig. 3.1(b), suggesting an additional hard component is coming from these regions.

Spectra were extracted from 16 postshock filamentary regions labeled in the 4–6 keV image shown in Fig. 4.1. The spectra can be divided into three groups based on the strength of the line emission. Samples of these groups are shown in Fig. 4.2. Most postshock spectra exhibit a very weak silicon line as the only evidence of thermal line emission. These represent a majority of the postshock regions (10 regions). Four regions were statistically consistent with the complete absence of line emission. The remaining two regions near the jet in the northeast of the remnant exhibit strong thermal lines.

The postshock regions are similar to the forward shock regions discussed in Chapter 3 in that they both exhibit weak thermal line emission. In general, however, the postshock regions exhibit much weaker line emission than the forward shock regions. Other differences between the forward shock and postshock regions may be discerned by looking at the x-ray surface brightness. The unabsorbed x-ray surface brightness was determined by calculating the total flux of the observed spectrum (0.5–10 keV) using a best-fit spectral model comprised of a thermal component (*npshock*) plus a power law for the forward shock regions and a power law for the postshock regions. Both models included an absorption component which was subsequently removed to obtain the unabsorbed flux. The areas used in the surface brightness calculation consisted

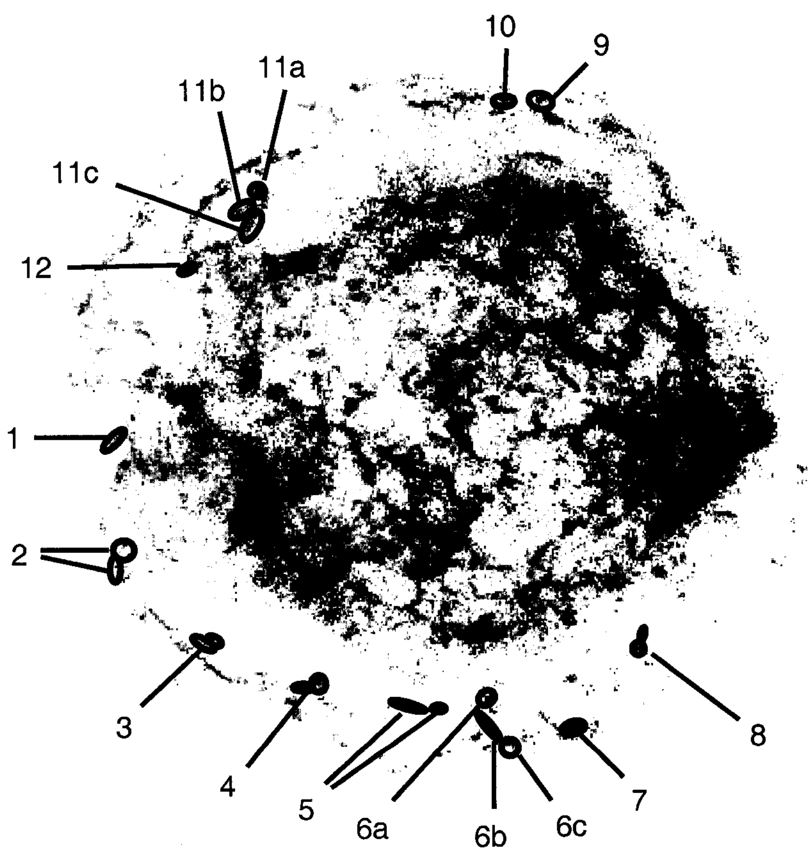

Figure 4.1: Extraction regions selected for postshock spectra, superimposed on the 4–6 keV continuum map of Cas A. The regions selected were those with the highest hardness ratio (4–6 keV flux/0.5–3 keV flux).

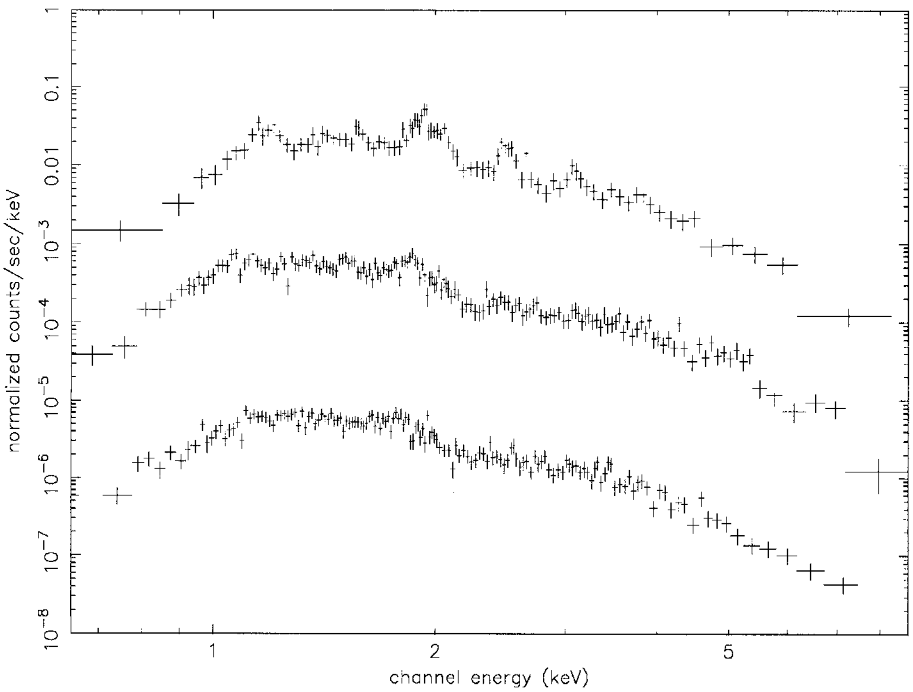

Figure 4.2: Sample spectra extracted from the postshock region. Spectra can be classified qualitatively into three groups: strongly thermal spectra (2 regions, top), weakly thermal spectra (10 regions, middle), and line-free spectra (4 regions, bottom). For clarity, the latter two spectra were scaled by a factor of $10^{-}2$ and 10^{-4}, respectively.

only of pixels within each region that contained fluxes exceeding a set threshold above the mean postshock flux. The unabsorbed flux was scaled by the fraction of flux within these pixels to derive a surface brightness S from the spectrum flux F_{spectrum}

$$S = \frac{\sum_{\text{pixels} > \text{thresh}} C_i}{\sum_{\text{all pixels}} C_i} \frac{F_{\text{spectrum}}}{A_{\text{pixels} > \text{thresh}}} \tag{4.1}$$

where C_i is the photon count rate per pixel (0.5–10 keV) and $A_{\text{pixels} > \text{thresh}}$ is the total area of pixels within the region exceeding the threshold.

The ratio of observed x-ray to radio surface brightness is smaller by about a factor of 10 in the postshock regions compared to the forward shock regions. If the radio plateau between the forward and reverse shocks arises from a volume of GeV electrons which have diffused away from the forward shock region, then one would expect these electrons to fill the volume between the forward and reverse shocks. The total radio emission would then be the sum of the emissivity of this volume over an entire column of radio emission. The x-ray emission, however, appears to be localized to small knots and filaments. Much of the radio emission observed along the line of sight to the postshock x-ray emission could be unassociated with the x-ray emitting region.

The observed x-ray surface brightness in the postshock regions is systematically dimmer than the forward shock regions (Fig. 4.3). This is expected of simple limb brightening from a spherical remnant, but other differences argue against this interpretation. First, the observed forward shock is not perfectly circular— there are parts of the shock which are closer to the remnant center than other regions and there are small scale features in the forward shock. Second, the thin forward shock suggests that it is a very thin shell. Limb-brightening would then drop the emissivity of a simple spherical shell very quickly when moving inward from the tangential circle of the sphere. Some regions of hard postshock emission are found well inside the forward shock highly localized in the form of filaments and knots. Finally, the obviously weaker line emission of the postshock regions also points to a physical difference between these postshock regions and the forward shock. The next two sections discuss two possible physical interpretations of the unique postshock regions.

4.2 Thermal X-ray Interpretation

If the postshock regions are completely thermal emission, they must be regions with very low ionization timescales or very high temperatures in order to account for the very low line emission. Fig. 4.4 shows that a plane-parallel shock model assuming nonequipartition ($kT_e = 0.46\, kT_i$) results in a good fit for all the regions which show little or no evidence of line emission. The models have temperatures which are significantly higher than the forward shocks and ionization timescales which are at most 1.1×10^{10} cm^{-3} s. This number is only an upper limit because there is x-ray emission from the intershock region which

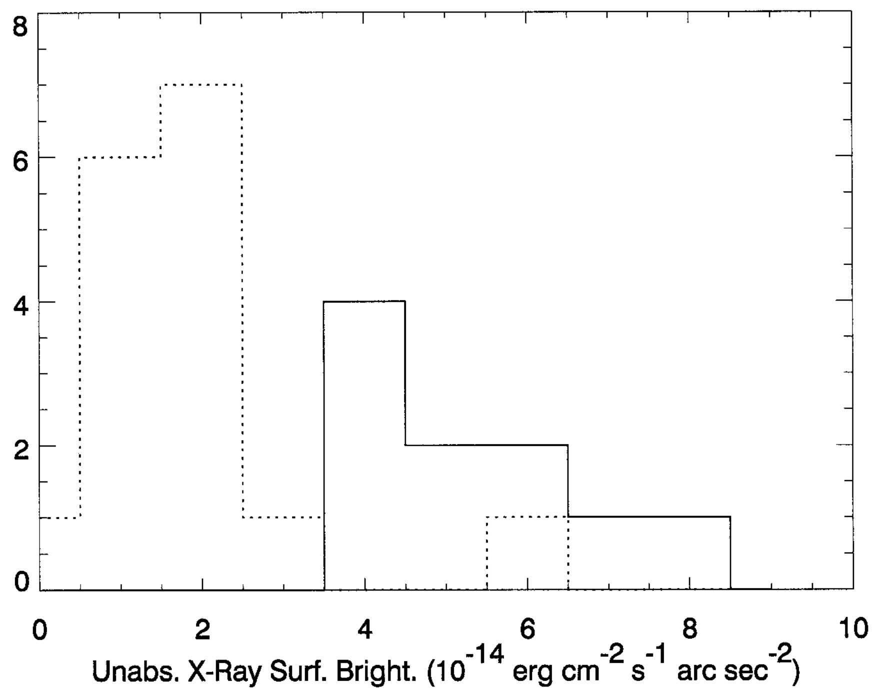

Figure 4.3: Histogram of unabsorbed x-ray surface brightness (0.5–10 keV) of forward shock (solid) and postshock regions (dashed).

has not been accounted for in the fit. The intershock region emission would account for some of the weak line emission which would reduce the fitted ionization timescale or raise the fitted temperature.

The lower ionization timescales ($\tau = n_e t$) eliminate the possibility that these regions are physically behind the forward shock because one would expect higher ionization timescales for material in the postshock region which was shocked at an earlier time. If the thermal interpretation is correct, then the postshock regions must be forward shock emission seen in projection. The combination of lower ionization timescales and higher temperatures suggests that the postshock emission may be projected forward shock emission traveling through a lower density medium.

The very thin nature of the postshock emission features indicates limb brightening from an aspherical remnant if it is indeed forward shock emission seen in projection. Evidence of an asymmetric explosion of Cas A is abundant. Global asymmetries in x-ray Doppler velocities were measured by Hwang *et al.* (2001) showing a systematic redshift toward the eastern part of the remnant.[85] The highest velocity ejecta knots observed by Fesen (2001) have a bipolar distribution along the axis of the jet in the northeast.[69] A three-dimensional map of ejecta mass measured via x-ray Doppler velocities by Willingale *et al.* (2003) could be explained by a an explosion where most of the ejecta are distributed either into an equatorial plane or an axial jet.[114] The postshock x-ray emission

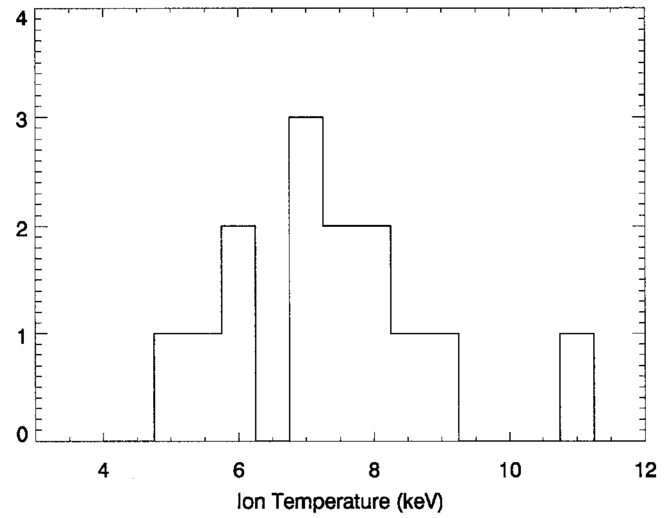

(a)

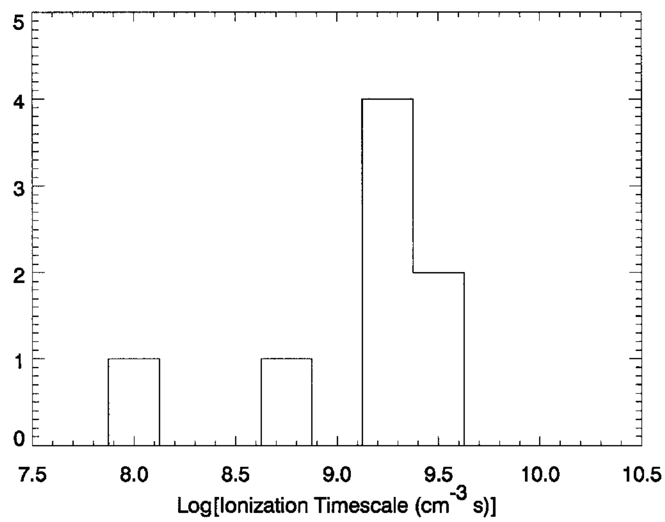

(b)

Figure 4.4: Histogram of best-fit parameters of a plane-parallel model fit to the postshock regions. Shown are the best-fit temperature (a) and ionization timescale (b). The plane-parallel shock model assumes nonequipartition between electrons and ions ($kT_e = 0.46\, kT_i$).

might be forward shock emission from parts of the explosion with less mass or energy than the forward shock regions.

4.3 X-Ray Synchrotron Interpretation

The postshock spectra could also be explained by synchrotron emission with an underlying thermal component. Some regions are fitted very well by a synchrotron model, while others show evidence of line emission.

The radio to x-ray spectral indices of the postshock regions are significantly larger than even the steepest measured radio knots, exhibiting and average spectral index of $\langle\alpha_{\rm RX}\rangle = 1.09$ and a standard deviation of $\sigma_{\alpha_{\rm RX}} = 0.04$. This may be an overestimate because the radio emission is likely filling a volume which is not all associated with the thin filamentary x-ray emission seen in the postshock regions. If only 10% of the radio emission is actually associated with the x-ray emitting region, the spectral index flattens to a value of $\langle\alpha_{\rm RX}\rangle = 0.99$. This value is larger than the average spectral index measured in the radio knots. Over 8 decades of energy, there is a substantial decrease of the x-ray flux below the extrapolation of the radio spectrum— evidence of significant synchrotron losses occuring in the x-ray band. There is no observed correlation between x-ray postshock regions and bright radio knots where magnetic amplification is taking place. This suggests the magnetic field is not changing drastically between the forward shock and postshock regions, therefore the postshock regions are not accelerating electrons to much higher energies than the forward shock.

X-ray emission from supernova remnants is optically thin, therefore the spectra of all the postshock regions should have some component of thermal emission observed between the forward and reverse shocks. The thermal surface brightness in the postshock region is constant to within a factor of 2, so regions without evidence of line emission would necessarily need greater surface brightness in order to mask any line signatures from this underlying thermal component. The line-free regions do not show a systematic increase in x-ray brightness over other regions, which would seem to disfavor a nonthermal interpretation. However, there are only four regions which statistically lack evidence of silicon line emission. One of these regions (Region 11a) has the brightest x-ray surface brightness measured, while the other three regions (Regions 6a-c) all lie in proximity to each other. A lower thermal brightness in that part of the remnant may account for the lack of thermal lines in these three regions.

Postshock regions which show some evidence of line emission can be well-fitted by a combination of a power law model to represent synchrotron radiation and a thermal component (Fig. 4.5). The normalization of this thermal component was allowed to vary but remained consistent with the expected amount of thermal background emission. Most regions show very little thermal emission, so all regions were fitted with only a power law model. Three regions fitted with a thermal plus power law model show a systematic flattening of the fitted power law spectrum by as much as $\Delta k \approx 0.1$.

The best-fit power law parameters to each of the postshock regions are shown in Table 4.1. The fitted power law index in the x-ray band is larger than that of the bright radio knots in the plateau region $\langle \alpha \rangle$=0.80 or $\langle k \rangle$=1.80. However, the x-ray spectral indices are significantly flatter than is observed in the forward shock regions with an average value of $\langle k \rangle$=2.37.

The average spectral index measured in the postshock regions is consistent with the index expected from a continuous injection of a power law of electrons, $\langle k \rangle$=2.30. This is contrary to the forward shock regions where the power law index was steeper than a continuous injection model would predict. The electrons at TeV energies cannot be coming from the forward shock regions because the synchrotron loss times are too small for TeV electrons to escape into the postshock regions. If the postshock regions were reaccelerating electrons, one would expect synchrotron emission to be brighter in the postshock regions not only in x rays, but in the radio as well. No correlation is seen between the x-ray postshock regions and the radio postshock regions, but such a correlation could be disguised by radio emission along the line of sight unassociated with the x-ray emission.

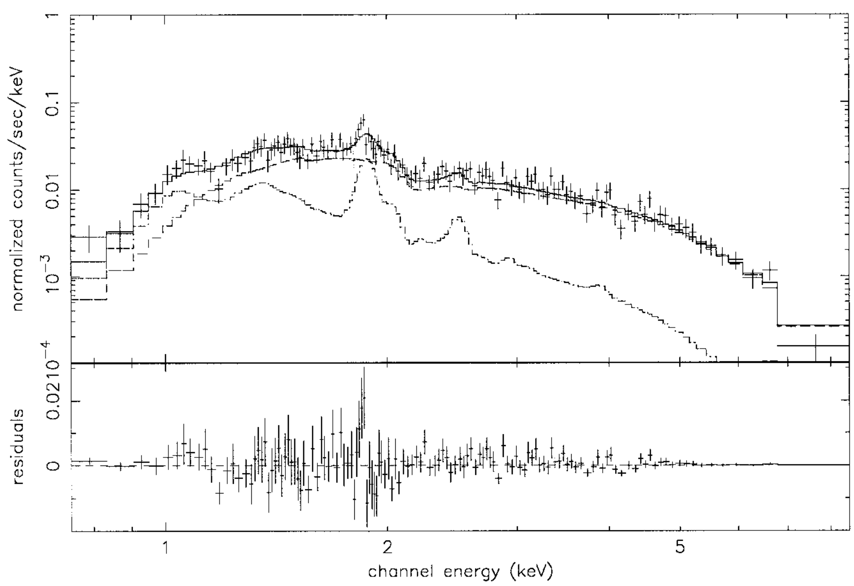

Figure 4.5: Fit of a power law plus plane-parallel shock model to a sample post-shock spectrum (Region 4). The power law component is interpreted here as synchrotron radiation. The thermal component is a best-fit plane-parallel shock model to nearby thermal emission.

Region	n_H (10^{22} cm^{-2})		k		χ^2
1	0.74	$^{0.67}_{0.82}$	2.33	$^{2.26}_{2.50}$	$123/73 = 1.68$
2	0.96	$^{0.91}_{1.01}$	2.45	$^{2.36}_{2.55}$	$217/158 = 1.37$
3	0.84	$^{0.75}_{0.93}$	2.16	$^{2.08}_{2.29}$	$136/90 = 1.51$
4	1.42	$^{1.30}_{1.57}$	2.22	$^{2.09}_{2.37}$	$176/130 = 1.36$
5	1.12	$^{1.01}_{1.26}$	2.46	$^{2.31}_{2.64}$	$144/94 = 1.53$
6a	1.39	$^{1.25}_{1.56}$	2.52	$^{2.36}_{2.69}$	$104/85 = 1.22$
6b	1.44	$^{1.26}_{1.64}$	2.46	$^{2.26}_{2.68}$	$71/65 = 1.09$
6c	1.41	$^{1.26}_{1.57}$	2.24	$^{2.07}_{2.40}$	$85/87 = 0.98$
7	1.35	$^{1.27}_{1.49}$	2.27	$^{2.13}_{2.40}$	$148/157 = 0.94$
8	1.07	$^{0.96}_{1.19}$	2.21	$^{2.06}_{2.36}$	$98/85 = 1.16$
9	0.79	$^{0.73}_{0.85}$	2.30	$^{2.20}_{2.40}$	$187/142 = 1.32$
10	0.77	$^{0.70}_{0.83}$	2.26	$^{2.21}_{2.36}$	$132/101 = 1.31$
11a	1.14	$^{1.08}_{1.21}$	2.66	$^{2.56}_{2.76}$	$198/152 = 1.30$
11b	0.89	$^{0.82}_{0.94}$	2.59	$^{2.47}_{2.69}$	$189/125 = 1.51$

Table 4.1: Best-fit parameters of a power-law fit to the postshock regions. The variable k is the photon spectral index of the power law. Small numbers are the 90% confidence interval for each parameter. Regions 11c and 12, which have high thermal line emission, are not included.

The break frequency at which the extrapolation of the x-ray spectrum meets the extrapolation of the radio spectrum can be calculated for each region as was done for the forward shock. Unlike the forward shock, it is uncertain how much of the radio emission along the line of sight to each region is physically associated with the x-ray emission. Break frequencies for the postshock regions are calculated for the case where all the radio emission is associated with the x-ray emission (Table 4.2) and the case where only 10% of the radio emission is associated with the x-ray emission (Table 4.3). Derived break frequencies are lower by approximately an order of magnitude if all the radio emission is physically associated with the x-ray emission.

It is unlikely that all of the radio emission is physically associated with the x-ray emission due to the thin filamentary nature of the x-ray emission in the postshock regions while the radio emission fills the plateau between the forward and reverse shocks. Associating only 10% of the radio emission with the x-ray emission gives the postshock regions break frequencies close to those of the forward shock regions, but only because this fraction of radio emission gives the postshock regions a radio/x-ray brightness ratio equal to that of the forward shock regions. Whether or not the break frequencies in the postshock regions match those of the forward shock regions depends on the amount of radio emission physically associated with the x-ray emission.

Region	Break Frequency (10^{17} Hz)			
	$\alpha = 0.60$	$\alpha = 0.70$	$\alpha = 0.80$	$\alpha = 0.90$
1	3.9×10^{-4}	2.1×10^{-3}	0.021	0.62
2	2.3×10^{-3}	0.012	0.10	1.9
3	1.4×10^{-5}	6.9×10^{-5}	8.0×10^{-4}	0.062
4	7.5×10^{-5}	4.2×10^{-4}	5.2×10^{-3}	0.32
5	7.8×10^{-4}	3.5×10^{-3}	0.024	0.33
6a	1.9×10^{-3}	8.3×10^{-3}	0.055	0.68
6b	9.0×10^{-4}	4.1×10^{-3}	0.029	0.41
6c	6.3×10^{-4}	4.9×10^{-3}	0.096	11
7	4.6×10^{-5}	2.0×10^{-4}	1.7×10^{-3}	0.043
8	2.2×10^{-5}	9.7×10^{-5}	9.1×10^{-4}	0.036
9	2.4×10^{-4}	1.3×10^{-3}	0.014	0.48
10	1.7×10^{-4}	6.2×10^{-5}	4.2×10^{-4}	8.0×10^{-3}
11a	0.010	0.044	0.26	2.5
11b	1.9×10^{-3}	7.6×10^{-3}	0.042	0.39

Table 4.2: Break frequencies of the hard postshock regions if all radio emission is associated with the x-ray emission, calculated for a range of assumed values of the radio spectral index.

Region	Break Frequency (10^{17} Hz)			
	$\alpha = 0.60$	$\alpha = 0.70$	$\alpha = 0.80$	$\alpha = 0.90$
1	9.1×10^{-3}	0.081	1.6	130
2	0.035	0.26	3.6	130
3	8.7×10^{-4}	0.010	0.48	430
4	3.1×10^{-3}	0.035	1.3	430
5	0.011	0.071	0.78	20
6a	0.023	0.14	1.4	28
6b	0.013	0.084	0.94	25
6c	0.023	0.35	18	9.5×10^{3}
7	1.4×10^{-3}	0.011	0.22	21
8	9.4×10^{-4}	8.9×10^{-3}	0.25	61
9	6.6×10^{-3}	0.061	1.4	152
10	5.4×10^{-4}	3.8×10^{-3}	0.06	4.8
11a	0.091	0.48	3.8	51
11b	0.020	0.10	0.78	11

Table 4.3: Break frequencies of the hard postshock regions if 10% of the radio emission is associated with the x-ray emission, calculated for a range of assumed values of the radio spectral index.

If the postshock regions are interpreted as synchrotron emission, there is no constraint on their location along the line of sight. They could be interior to the forward shock and be sites of cosmic-ray reacceleration: either through first-order Fermi acceleration from reflection shocks formed as Cas A passes through its own inhomogeneous CSM or through second-order Fermi acceleration taking place as turbulence randomizes the velocities of magnetic inhomogeneities capable of scattering cosmic rays. It is also possible that these postshock regions are part of the forward shock which appear interior to the forward shock in projection only. It seems implausible that thin filaments of limb-brightened forward shock emission could appear interior to the forward shock, but by looking at the shape of the forward shock it is easily seen that the forward shock of Cas A deviates from a perfect sphere.

4.4 Regions with Strong Line Emission

Two regions near the northeast jet (Regions 11c and 12) contain line emission from neon, magnesium, silicon and sulfur. The spectra of these regions, in Fig. 4.6 are obviously different from the other regions with their abundant line emission and are considered a separate population. These regions are likely part of the jet in the northeast of Cas A.

Region 11d is best described by a thermal plus synchrotron model assuming nonequipartition between the electrons and ions. The degree of collisionless heating of the electrons is similar to that of the forward shock: $kT_e = 0.46\,kT_i$. The break frequency and radio spectral index are also similar to typical forward shock values.

Region 12 is fitted well by a plane-parallel shock model assuming equipartition between electrons and ions. The spectra contain line abundances which are all subsolar, although the ratios of abundances are consistent with ejecta from explosive silicon nucleosynthesis. The fact that these are subsolar may indicate an underlying continuum component. The underabundance of neon rules out the possibility that this emission is coming from shocked circumstellar matter with subsolar abundances due to adsorption onto dust grains. The best-fit parameters of both regions are shown in Table 4.4.

4.5 Summary

The postshock regions show very weak or no silicon line emission— weaker than the already-weak silicon and sulfur lines evident in the forward shock spectra. These spectra are consistent with either a thermal model with a very high temperature and low ionization timescale or predominantly nonthermal emission. The fact that these regions exhibit a factor of two increase in x-ray

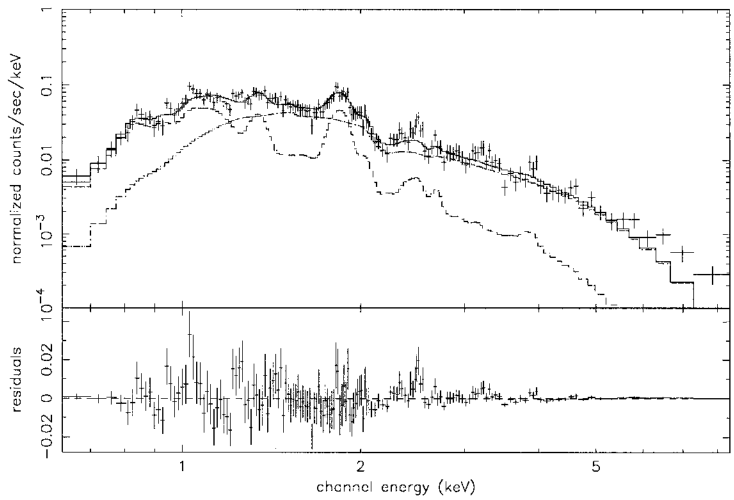

(a)

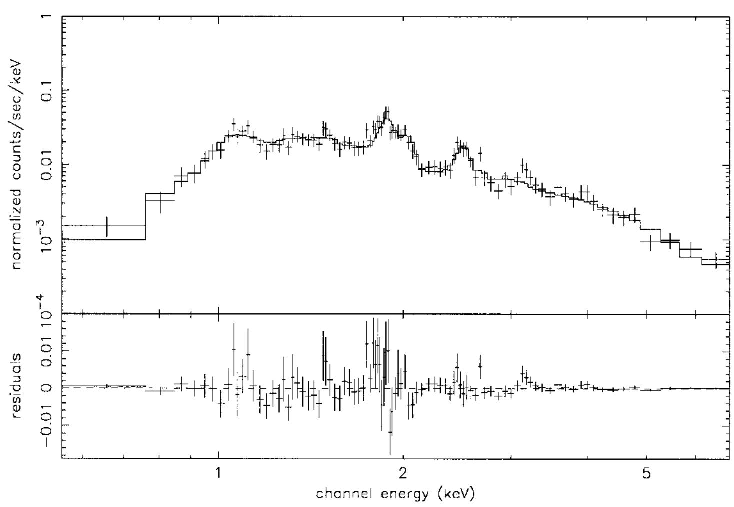

(b)

Figure 4.6: Spectra of two thermal regions found in hard postshock filamentary structure. Regions 11c (a) and 12 (b) of Fig. 4.1 are shown along with the best-fit models for each region. The parameters of the models are in Table 4.4.

Region 11c

Parameter	Value
n_H (10^{22} cm^2)	$1.32\ ^{1.26}_{1.37}$
kT_i (keV)	$2.37\ ^{2.36}_{2.45}$
kT_e (keV)	$1.09\ ^{1.08}_{1.10}$
$\tau = n_e t$ (cm^{-3} s^{-1})	$3.60 \times 10^{10}\ ^{3.46}_{4.05}$
Flux (0.5–10 keV, erg cm^{-2} s^{-1})	$1.71 \times 10^{-03}\ ^{1.59}_{1.90}$
Radio Spectral Index	$0.880\ ^{0.878}_{0.883}$
Break Frequency (10^{17} Hz)	$1.49 \times 10^{17}\ ^{1.40}_{1.56}$
1 GHz Radio Flux (Jy)	42.84 (frozen)
χ^2/ν	$202/153 = 1.32$

Region 12

Parameter	Value
n_H (10^{22} cm^2)	$1.32\ ^{1.28}_{1.36}$
kT (keV)	$3.4\ ^{2.9}_{4.3}$
Ne	< 0.11
Mg	< 0.13
Si	$0.82\ ^{0.71}_{0.93}$
S	$0.96\ ^{0.75}_{1.19}$
Fe	$0.46\ ^{0.40}_{0.52}$
$\tau = n_e t$ (cm^{-3} s^{-1})	$1.4 \times 10^{11}\ ^{1.1}_{1.8}$
Flux (0.5–10 keV, erg cm^{-2} s^{-1})	$4.8 \times 10^{-4}\ ^{4.6}_{5.0}$
χ^2/ν	$82/85 = 0.94$

Table 4.4: Best-fit parameters of thermal regions within the hard postshock filamentary structure. The model used is the plane-parallel shock model of Borkowski *et al.* (2001) assuming equipartition between electrons and ions.[101] The locations of the regions are shown in Fig. 4.1. Small numbers indicate 90% confidence ranges.

surface brightness over the forward shock regions demonstrates that these regions are not a simple spherical projection of the forward shock.

If this postshock emission is thermal in nature, the lower ionization timescales indicate that it cannot be physically behind the forward shock. The favored thermal interpretation is a projection of forward shock emission which interacting with a lower-density environment. If the postshock emission is interpreted as synchrotron, then these regions cannot be accelerating electrons to energies much higher than those derived in the forward shock. The amount of radio emission associated with the x-ray emission in these regions raises an uncertainty in the maximum energy. The break frequency of the photon spectrum in the postshock regions is comparable to value derived from the forward shock if only 10% of the radio emission is physically associated with the x-ray emission coming from the regions.

PART II

GRAZING-INCIDENCE MULTILAYER X-RAY MIRRORS

Chapter 5

Overview of X-ray Optics

X rays are a form of electromagnetic radiation with photon energies between 0.1 keV and 1 MeV, although these boundaries are only loosely defined. Optics in the x-ray band are governed by the same physical laws as optics at visible wavelengths, yet the design of x-ray optics is significantly different. Astronomical applications of visible optics have been in use since the invention of the telescope by either Hans Lippershay or James Metius in 1608, but x-ray focusing optics have only been used in astronomy since the 1960's. While most of this lapse in time can be attributed to the fact that x rays were not discovered until 1895 by W.C. Röntgen,[115] most of the lapse in time after the discovery of x rays can be attributed to two factors. First, astronomical sources of x-rays were not discovered until the 1940's. Second, the properties of materials in the x-ray regime make optics difficult to construct. The refractive index of materials at x-ray wavelengths is very close to unity which makes reflection off materials only possible at very small angles of incidence. As x-ray energies surpass 10 keV, these small angles become problematic for constructing telescopes.

Röentgen's discovery of x rays ushered in an era of high interest in applications of these rays at the beginning of the 20th century. Most of the interest at the time involved possible medical applications— which most likely originated from his demonstration of these new rays by producing a shadowgram of his wife's hand. When von Laue discovered x-ray diffraction in 1912,[116] the application of x rays to determining the lattice structure of crystals came to the forefront of interest. Compton's demonstration of the reflection of x rays off polished surfaces in 1923 led to an exploration of the optical properties of materials and the possibility of creating x-ray optics.[117] However, the interest in x-ray optics focused on exploring the microscopic world rather than the large expanse of the universe— mainly because these x-ray pioneers realized their potential to explore the microscopic world with smaller diffraction limits and deeper penetration into materials before absorption.

X-ray optics were first addressed as early as 1929 by Jentzsch,[118] who explored the problems of constructing x-ray mirrors only six years after Compton's discovery of x-ray reflection from highly polished surfaces. However, the construction of the first two-dimensional x-ray imaging system did not occur until 1948, when Kirkpatrick and Baez used two cylindrical sections arranged orthogonally so each would provide one-dimensional focusing.[119] However, the Kirkpatrick-Baez system suffers from large geometric aberrations. Wolter (1952) proposed three types of optics systems for x-ray microscopes.[120] He showed that it was necessary to have two reflections in order to achieve an image over an extended field of view. Three of his proposed systems used either paraboloid/hyperboloid (types I and II) or paraboloid/ellipsoid (type III) combinations. However, the technology to fabricate such highly aspherical mirrors in grazing incidence applications would not be available for another decade.[121]

The interest in astronomy applications for x-rays did not arrive until Burnight (1948) discovered that the Sun is a source of x rays by exposing photographic film launched on a V2 rocket.[122] The first image of the Sun in x rays was taken by Chubb *et al.* (1960) using a pinhole camera.[123] It was the desire to improve the resolution of the original image of the Sun that piqued interest in x-ray optics for astronomical applications.[124] This interest was advanced by the discovery of the first non-solar celestial source, Sco X-1, with a Geiger counter on a sounding rocket by Giacconi *et al.* (1962).[125] This new demand in creating x-ray telescopes brought about the necessary mirror production technology to make aspherical grazing incidence mirrors possible. Subsequently, Giacconi *et al.* (1963) flew the first Wolter-type design optics on a sounding rocket to observe the Sun.[126] The first extra-solar observations employing x-ray optics did not occur until the Algol triple star system was observed with a Kirkpatrick-Baez telescope by P. Gorenstein *et al.* (1975).[127,128] The first use of a Wolter-type system occurred with an observation of the Cygnus Loop supernova remnant by Rappaport *et al.* (1977).[129]

The launch of the *Einstein* observatory in 1978 ushered in the age of orbital x-ray imaging observatories,[130] a satellite-borne telescope with four concentrically nested, coaligned grazing incidence shells. For a given total collecting area, such a nested configuration has smaller geometric aberrations than a single long shell with the same collecting area. Nested configurations based on Wolter's original design became the optics system of choice for imaging x-ray missions listed in Table 5.

5.1 Physics of X-ray Reflection

The electromagnetic fields in an infinite medium with dielectric constant ϵ, permeability μ and no charge sources can be described by Maxwell's equations:

$$\begin{aligned} \nabla \cdot \mathbf{E} &= 0 \\ \nabla \times \mathbf{E} &= -\frac{1}{c}\frac{\partial \mathbf{B}}{\partial t} \\ \nabla \cdot \mathbf{B} &= 0 \\ \nabla \times \mathbf{B} &= \frac{\mu\epsilon}{c}\frac{\partial \mathbf{E}}{\partial t}. \end{aligned} \tag{5.1}$$

Telescope	Launch	Optics	No. Shells	Energy (keV)
Einstein[130]	1979	Wolter I	4	0.1–4
EXOSAT[131]	1983	Wolter I	2	0.05–2
Tenma[132]	1983	Single Paraboloid	4	0.1–2
ROSAT[133]	1990	Wolter I	4	0.1–2.5
BBXRT[134]	1990	conic Wolter I	118	0.3–12
Yohkoh (*Solar-A*)[135]	1991	modified Wolter I	1	0.3–4
ASCA[136]	1993	conic Wolter I	120	0.1–10
BeppoSAX[138]	1996	conic Wolter I	30	0.1–10
XMM-*Newton*[139]	1999	Wolter I	58	0.1–15
Chandra[140]	1999	Wolter I	4	0.1–10
Astro-E[141]	2000	conic Wolter I	175	0.4–10
GOES SXI[142,143]	2002	modified Wolter I	1	0.2–2
Solar-B[144]	2002	modified Wolter I	1	0.2–6

Table 5.1: Space-based x-ray observatories employing grazing-incidence optics. The term "conic Wolter" means a conic approximation to Wolter optics. The term "modified Wolter" means a modification of the classical Wolter design used to reduce aberrations. Energies listed are operational energies of the focusing optics only.

The solution to these equations is a transverse wave of arbitrary wavelength λ propagating in the direction $\hat{\mathbf{k}}$, which can be expressed in terms of the complex index of refraction of the material $\tilde{n} \equiv n + i\beta = \sqrt{\mu\epsilon}$ as:[35,145]

$$\begin{aligned} \mathbf{E}(\mathbf{x}, t) &= \mathbf{E}_0 \exp[\tfrac{2\pi i}{\lambda}(n\,\hat{\mathbf{k}}\cdot\mathbf{x} - ct)]\exp(-\tfrac{2\pi}{\lambda}\beta\,\hat{\mathbf{k}}\cdot\mathbf{x}) \\ \mathbf{B}(\mathbf{x}, t) &= n\,\hat{\mathbf{k}}\times\mathbf{E} \\ \mathbf{k}\cdot\,\mathbf{B} &= \mathbf{k}\cdot\,\mathbf{E} = 0. \end{aligned} \tag{5.2}$$

The real part of the index of refraction n can be expressed as $1-\delta$. At x-ray wavelengths, both δ and β are small positive values typically in the 10^{-6}–10^{-2} range. A positive value of β indicates that the material absorbs the wave at a characteristic length of $\lambda/(4\pi\beta)$. Even though this characteristic length is much larger than a wavelength, this absorption still plays a significant role in the construction of x-ray optics. The real part of the index of refraction is greater than or equal to unity at optical wavelengths, but at x-ray wavelengths this real part becomes slightly less than unity. This seemingly small, but important difference makes reflection of x-rays off surfaces possible.

At a boundary between two different materials, the EM wave will encounter a discrete change between indices of refraction n_1 to n_2. The boundary conditions between the materials are: 1) the components of $\mathbf{D} \equiv \epsilon\mathbf{E}$ and $\mathbf{B}$ normal to the material surface are continuous and 2) the components of $\mathbf{E}$ and $\mathbf{H} \equiv \mathbf{B}/\mu$ perpendicular to the surface normal are continuous. These boundary conditions give rise to the Fresnel equations (ignoring absorption) describing the reflection and refraction off a boundary. The reflection and transmission coefficients are given for two polarizations of the incident wave— when the electric field is perpendicular to the plane defined by the surface normal and $\mathbf{k}$ (s-polarization) and when the electric field is parallel to this plane (p-polarization). These reflection and transmission coefficients are

$$\left.\begin{aligned} r_{12} \equiv \frac{E_{0,refl}}{E_{0,inc}} &= \frac{n_1 \cos\phi_1 - n_2 \cos\phi_2}{n_1 \cos\phi_1 + n_2 \cos\phi_2} \\ t_{12} \equiv \frac{E_{0,trans}}{E_{0,inc}} &= \frac{2 n_1 \cos\phi_1}{n_1 \cos\phi_1 + n_2 \cos\phi_2} \end{aligned}\right\} \text{s-polarization} \tag{5.3}$$

$$\left.\begin{aligned} r_{12} \equiv \frac{E_{0,refl}}{E_{0,inc}} &= \frac{n_1 \cos\phi_2 - n_2 \cos\phi_1}{n_1 \cos\phi_2 + n_2 \cos\phi_1} \\ t_{12} \equiv \frac{E_{0,trans}}{E_{0,inc}} &= \frac{2 n_1 \cos\phi_1}{n_1 \cos\phi_2 + n_2 \cos\phi_1} \end{aligned}\right\} \text{p-polarization.} \tag{5.4}$$

where the angles ϕ are shown in Fig. 5.1 The fact that these boundary conditions must be satisfied everywhere on the boundary means that the phase factors $n\hat{\mathbf{k}} \cdot \mathbf{x} - \omega t$ of all three waves must be equal at the boundary independent of the nature of the materials comprising the boundary. This requirement gives rise to two important properties of reflected and refracted waves. First, because the index of refraction is the same for the incident and reflected wave, the value of $\hat{\mathbf{k}} \cdot \mathbf{x}$ is also equal between the two— in other words, the angle of reflection must equal the angle of incidence. Second, this requirement also relates the angle of the incident wave to that of refracted wave in the form of Snell's Law:

$$\cos\phi_2 = \sqrt{1 - (n_1/n_2)^2 \sin^2\phi_1}. \tag{5.5}$$

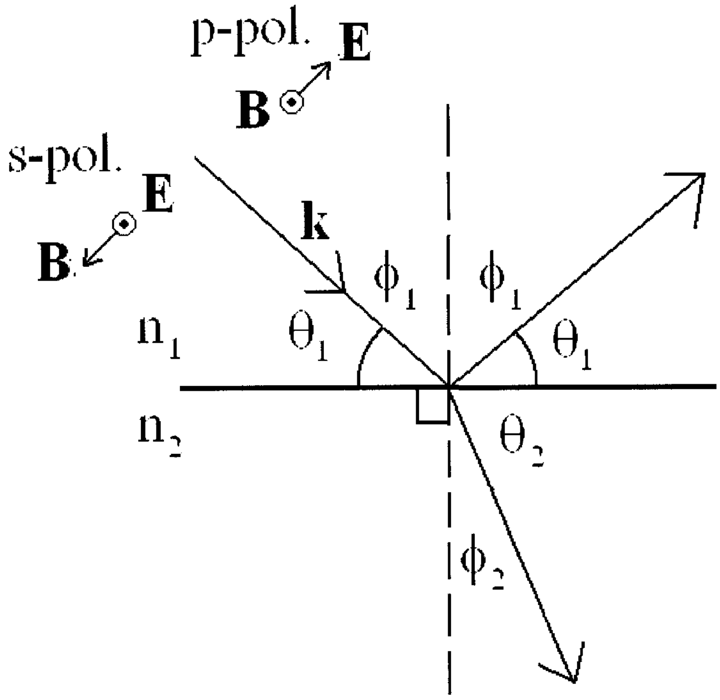

Figure 5.1: Reflection and transmission off a boundary between two homogeneous media with refractive indices n_1 and n_2. The incident wave vector, $\mathbf{k}$, is traveling from medium 1 to 2. The angles ϕ are measured relative to the surface normal, while angles θ are measured relative to the surface. The s- and p-polarizations of the incident wave are also shown.

It is possible for Eq. (5.5) to become imaginary when $n_1/n_2 > \sin\phi_1$. Plugging this imaginary number into either Eqs. (5.3) or (5.4) gives a complex number for the ratio of the reflected to incident electric field whose modulus is one. Therefore, the reflected wave intensity is equal to the incident wave intensity. While at optical wavelengths this is described as total internal reflection, this is total *external* reflection at x-ray wavelengths because the index of refraction is lower in materials than in vacuum. The first observation of total external reflection off a polished surface by Compton in 1923 lead him to deduce the electromagnetic wave nature of x rays.[117] Using Eq. (5.5), it is possible to derive the critical angle measured relative to the surface (not the surface normal) below which total external reflection occurs for an incident wave in vacuum. To a first-order approximation, this critical angle is

$$\sin\theta_c \approx \sqrt{2\delta} \quad \text{for} \quad \delta \ll 1,\ \beta \ll \delta. \tag{5.6}$$

Total external reflection has been successfully applied to the creation of x-ray telescopes operating below 10 keV. All of the telescopes listed in Table 5 utilize total external reflection. These telescopes used polished substrates coated with high-Z materials such as nickel or iridium, which have relatively large values of δ. Above this critical angle, the intensity of the reflected wave decreases very quickly. For incidence angles much greater than the critical angle, the reflected intensity can be approximated as

$$R = \frac{(\delta_2 - \delta_1)^2 + (\beta_2 - \beta_1)^2}{4\sin^4\theta} \tag{5.7}$$

This large decrease in reflected intensity as a function of incidence angle limits the application of single-surface reflection to angles at or below the critical angle.

5.2 Multilayers

There are alternative ways to reflect x rays off a surface efficiently above the critical angle. The first such method is x ray diffraction by crystalline materials. Individual atoms within the crystal scatter x rays with very low efficiency. Constructive interference between successive lattice planes gives a substantial diffracted intensity in specific directions determined by the spacing between lattice planes, the x ray energy, and the angle of incidence. X-ray telescopes typically require broadband reflection over a range of incidence angles in order to create a focused image, so the applicability of crystals to astronomical optics is currently very limited. However, the technology does exist within the semiconductor industry to grow crystal lattices with variable lattice spacings by growing a mixture of silicon and germanium. Such crystals have been applied successfully to create monochromators for synchrotron beams,[146] and may be feasible for x-ray telescope applications at some point in the future.

Multilayers were first proposed for ultraviolet applications by Spiller (1972) although they had been used in optical applications for about 30 years by that time.[147] The primary reason for the delay was that all materials are strong absorbers at wavelengths below 200 nm, so it was believed that materials used for ultraviolet optics would absorb rather than reflect. However, high reflectivity can be achieved by multilayers composed of two materials with a high difference in optical constants, even for strong absorbers. This opened up the possibility of using multilayers to reflect x rays. Multilayers mimic the constructive interference produced by crystals by alternating materials with high and low values of δ in a periodic fashion. The periodic interfaces between the layers are analogous to the lattice planes in crystals, creating substantial reflectivity at a particular angle greater than the critical angle. With the ability to control the periodic spacing of the layers, it became possible to design a surface that would reflect a monochromatic x-ray beam efficiently at a chosen angle of incidence. X ray telescopes with periodic multilayers can be designed with one major limitation— they will only work for a very narrow range of energies.

A modification of periodic multilayers was proposed by Nagel *et al.* (1981) to increase the bandpass of multilayers by grading the spacing between layers as a function of depth in the multilayer.[148] They designed this graded multilayer for use in synchrotron beamlines, but Dhez (1987) later realized its possible application to x-ray astronomy.[149] With the invention of depth-graded multilayers, it became possible to create a telescope which will work within a broad energy bandpass. Graded multilayers have not been used in x-ray telescopes until now— mainly because efficient detectors have not been available at energies above 10 keV where critical-angle telescopes are no longer feasible. The following subsections will describe in detail the physics behind periodic and graded multilayers and their potential application to x-ray astronomy.

5.2.1 Reflectivity of Ideal Multilayers

The simplest calculations of reflectivity from multilayers assume an ideal multilayer which is composed of perfectly smooth boundaries between materials and distances between the boundaries which do not change as a function of position on the surface of the material. The second assumption reduces the problem of calculating reflectivity to a one-dimensional problem. This problem can be solved by accounting for the amplitude of the downward-propagating (i.e. into the material) and upward-propagating waves at each boundary of the multilayer as shown in Fig. 5.2. At the j^{th} boundary, these amplitudes are

$$\begin{array}{llll} a_j = a_{j+1}\exp(i\varphi_j)t_{j+1,j} & + & b_j \exp(2i\varphi_j)r_{j,j+1} & \text{downward-propagating} \\ b_j = a_j r_{j,j-1} & + & b_{j-1}\exp(i\varphi_{j-1})t_{j-1,j} & \text{upward-propagating} \end{array} \tag{5.8}$$

where $r_{j,k}$ and $t_{j,k}$ are the reflection and transmission coefficients of a wave traveling from layer j to k given by the Fresnel equations [Eqs. (5.3,5.4)]. The index j begins with the value 1 at the bottom of the stack. The variable φ_j is the phase delay produced by propagation through the j^{th} layer

$$\varphi_j = \frac{2\pi E}{hc}\tilde{n}\; d_j \cos\phi_j \tag{5.9}$$

where d_j is the thickness of the film immediately above the boundary. The angle ϕ_j can be related to the angle of incidence in vacuum by Snell's law [Eq. (5.5)].

From the reflected and transmitted amplitudes of a single boundary, one can derive the amplitude reflection and transmission of a single film bounded by two boundaries. If the film is illuminated only from the top (i.e., $b_0 = 0$), the reflected and transmitted amplitude of a single film is

$$r_{f1} \equiv \frac{b_3}{a_2} \quad = \quad r_{2,1} + \frac{r_{1,0}\; t_{2,1}\; t_{1,2}\exp(2i\varphi_1)}{1 + r_{2,1}\; r_{1,0}\exp(2i\varphi_1)} \tag{5.10}$$

$$t_{f1} \equiv \frac{a_0}{a_2} \quad = \quad \frac{t_{2,1}\; t_{1,0}\exp(i\varphi_1)}{1 + r_{2,1}\; r_{1,0}\exp(2i\varphi_1)} \tag{5.11}$$

If another film is added on top of this film, one can apply Eqs. (5.10,5.11) to get the reflection and transmission coefficients of the two-film stack by replacing $r_{1,0}$ by the reflection coefficient of the bottom film r_{f1}. Although this second film is illuminated from the bottom by reflected light from the first film, these equations still hold as a good approximation as long as the reflectivity from one film is small enough to ignore any terms of order r^3 or greater. With this

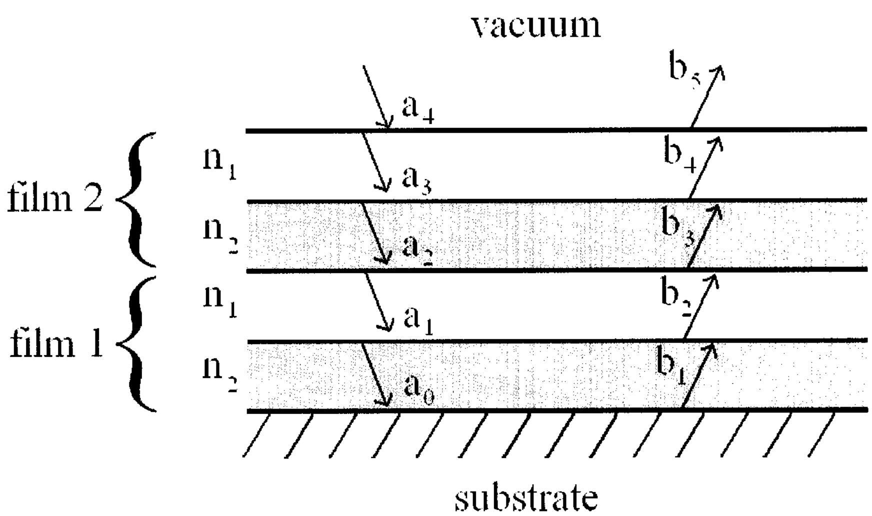

Figure 5.2: Diagram of upward- and downward-propagating wave vectors within a multilayer. The vectors labeled a are propagating down toward the substrate. Vectors labeled b are propagating up toward vacuum.

substitution and the following relation which can be derived from the Fresnel equations,

$$t_{1,0}\, t_{0,1} + r_{1,0}^2 = 1, \tag{5.12}$$

the reflection coefficient of a two-film stack becomes

$$r_{f2} = \frac{r_t + r_{f1} \exp(2i\varphi_2)}{1 + r_t\, r_{f1} \exp(2i\varphi_2)} \tag{5.13}$$

where r_t replaces $r_{3,2}$ as the reflection coefficient of the top boundary of the film. Applying Eq. (5.13) iteratively allows one to derive the reflection coefficient of an arbitrary number of films by starting with the bottom film and working toward vacuum.

A periodic multilayer consisting of two alternating materials with thickness d_1 and d_2 has a maximum reflectivity when the reflection from each film adds in phase, i.e. the phase variation in Eq. (5.13) is an integer multiple of 2π. This condition leads to the Bragg condition

$$m\frac{hc}{E} = 2d \sin\theta_0 \sqrt{1 - \frac{2\delta}{\sin^2\theta_0}}, \quad \delta \ll 1, \beta \ll \delta; \tag{5.14}$$

where $d = d_1 + d_2$ and δ is the thickness-weighted average of δ_1 and δ_2. The term under the radical is a correction for refraction effects added after Bragg's original work.[145,150]

The reflectivity of a periodic multilayer is further optimized by examining the reflection coefficient of an individual boundary in Eqs. (5.3,5.4). One can use

Snell's Law [Eq. (5.5)] to rewrite the s-polarization case, assuming the the grazing angle of incidence is small:

$$r_{12} = \theta_0/2\ (\delta_2\sqrt{1 - 2\delta_2/\theta_0^2} - \delta_1\sqrt{1 - 2\delta_1/\theta_0^2}),\ \ \delta \ll 1, \beta \ll \delta. \tag{5.15}$$

A similar expression can be derived for the p-polarization case. One can maximize r_{12} by maximizing the difference between the two terms in parentheses. For grazing angles much greater than the critical angle, this difference is maximized when the value $\delta_2 - \delta_1$ is maximized. Because x rays are much more energetic than molecular bonding energies of a material, the scattering cross-section depends only on the electron density of the material. Maximizing the reflectivity of a single boundary occurs when there is a large contrast in charge density between the two chosen materials.

A multilayer with periodic layers will produce high reflectivity for a small range of energies at a given incidence angle or vice versa. This is highly undesirable for astronomy applications as it limits the energy bandpass and the field of view of a telescope constructed with such multilayers. Graded multilayers have bilayer thicknesses that change monotonically from layer to layer. Only a few bilayers rather than the entire stack of bilayers are designed to reflect a given energy. Bilayers at the top of the multilayer would be the thickest to reflect the lowest-energy x rays of interest which are absorbed most easily within the multilayer. Consequently, bilayers at the bottom of the multilayer would have thicknesses most appropriate for the highest energy of interest. A comparison of the reflectivity as a function of energy between a periodic and graded multilayer composed of the same two materials is shown in Fig. 5.3. A graded multilayer does not achieve as high a peak reflectivity as a periodic multilayer, but the increased range of angles the multilayer can reflect at a given energy (or *vice versa*) makes multilayer x-ray telescopes a viable alternative to telescopes using critical-angle reflections.

5.2.2 The Role of Interface Width

The derivation above assumes that the boundaries between two layers are perfectly smooth or that the interface width is zero. In reality, of course, this is never the case. With the exception of crystals, whose lattice planes are smooth to within a fraction of an atomic radius, all surfaces have an interface width at x-ray wavelengths. Interface width has two contributions illustrated in Fig. 5.4. Roughness is defined as a well-defined boundary that is not straight, while diffuseness is defined as a boundary with a continuous rather than sharply defined transition from one layer to the other.

Roughness has two important effects on a multilayer. First, it reduces the specular reflectivity of the multilayer i.e. where $\theta_{\rm out} = \theta_{\rm in}$. Second, it gives rise to diffuse scattering of x rays into angles $\theta_{\rm out} \neq \theta_{\rm in}$. The former effect greatly reduces the effective area of the telescope which scales as the reflectivity squared.

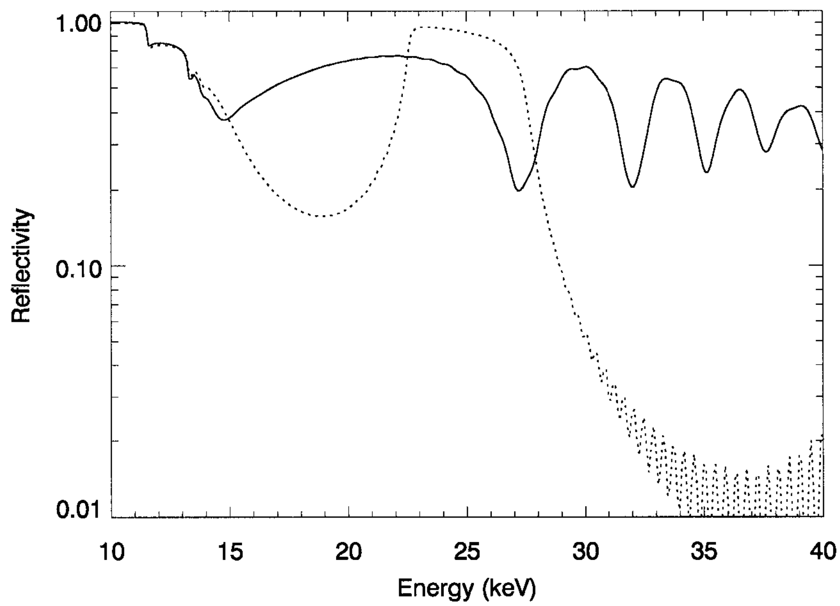

Figure 5.3: Calculated reflectivity vs. energy for a periodic (dotted) and graded (solid) multilayer made of platinum and carbon layers. The graded multilayer has lower peak reflectivity, but provides significant reflectivity over a wide energy range.

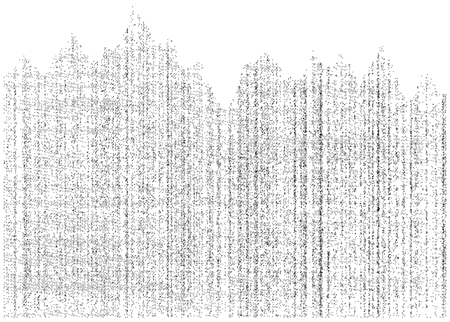

(a)

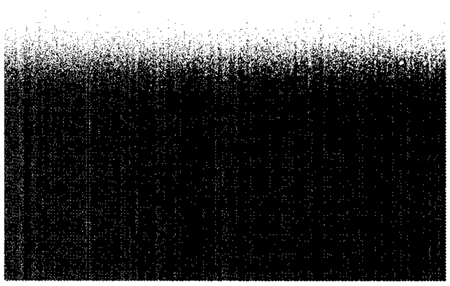

(b)

Figure 5.4: Illustrations of the contributions of layer interface width: roughness (a) and diffuseness (b).

The latter effect reduces the image quality of the telescope by scattering x rays away from the core of a point source image. This can greatly affect the ability of the telescope to properly image faint, diffuse objects.

The effect of roughness on the reduced diffraction intensity of crystals was first investigated by Debye and Waller and can easily be applied to multilayers.[151,152] They found that they could account for the change in d-spacing caused by lattice vibration by splitting the rough lattice plane into a series of small planes each with a contribution to the reflectivity of the plane. They assumed a Gaussian distribution of reflectivity as a function of depth with a width of σ

$$r(z) = \frac{r_0}{\sigma\sqrt{2\pi}}\, e^{-z^2/(2\sigma^2)} \tag{5.16}$$

where r_0 is the reflectivity of a smooth lattice plane or layer boundary. One can determine the reduction from a series of infinitesimal planes by assuming the reflectivity at each boundary and total absorption are small. In this case, the denominator in Eq. (5.13) approaches unity and the reflectivity of the entire boundary becomes a Fourier integral

$$r(q) = \int_0^\infty r(z) e^{iqz_j}\, dz \quad q \equiv \frac{4\pi}{\lambda}\sin\theta. \tag{5.17}$$

The variable q in Eq. (5.17) is commonly referred to as the momentum transfer because it is the amount of momentum in the surface normal direction transferred from the boundary to the photon when reflected. Combining Eqs.

(5.16) and (5.17) results in an expression of the reduction in intensity as a function of incidence angle commonly referred to as the Debye-Waller factor:

$$\frac{R(q)}{R_0(q)} = \exp -(q\sigma)^2. \tag{5.18}$$

A more rigorous investigation of the effects of roughness on multilayer reflectivity by Névot and Croce revealed that the Debye-Waller factor should be modified by accounting for refraction in the materials which is important at small grazing angles.[153] The Névot-Croce factor is

$$\frac{R(q)}{R_0(q)} = \exp -(q_1 q_2 \sigma^2) \quad q_i = \frac{4\pi}{\lambda} n_i \sin\theta \tag{5.19}$$

where the indices {1,2} represent the two materials in the multilayer stack.

The roughness of a boundary also scatters x rays away from the specular peak. The ratio of scattered radiance to incident irradiance is given by the bidirectional reflectance distribution function (BRDF):[a]

$$\frac{1}{I_0}\frac{dI}{d\Omega} = \frac{1}{A}\frac{d\sigma}{d\Omega} \tag{5.20}$$

where A is the area of the boundary sampled by the beam. The differential cross-section, $d\sigma/d\Omega$, can be estimated by a variety of techniques which typically involve an approximation that limits the validity of the technique.[154–158] For

[a]Radiometric terms are used here which differ from traditional astronomical terms. Radiance is defined as power × solid angle^{-1} × projected area^{-1}, which is called intensity in astronomy. Irradiance is the incoming power per unit unprojected area, referred to as flux in astronomy.

scattering at x-ray wavelengths by polished surfaces, the distorted-wave Born approximation (DWBA) is an appropriate method. The Born approximation assumes that the incoming radiation is a plane wave which is weakly scattered by a homogeneous material. It is assumed that the only fields near the scatterer are the incident plane wave. Because it applies only to weak scattering, it is valid only when the scattering angle is much larger than the critical angle. The distorted-wave Born approximation is a perturbation of the Born approximation where the fields near the scatterer are the sum of the incident wave and the reflected wave of a simplified surface in the Born approximation. The DWBA approximation is useful because it is valid even below the critical angle for external reflection. In the case of a smooth surface ($q\sigma \ll 1$), the differential cross-section to scattering off a boundary calculated by DWBA converges to:[159–161]

$$\frac{d\sigma}{d\Omega} = A\frac{q_c^4\, t^2(\theta_{\text{in}})\, t^2(\theta_{\text{out}})}{16\pi^2} P(\mathbf{q}) \tag{5.21}$$

where q_c is the momentum transfer calculated at the critical angle and $t(\theta)$ is the transmission coefficient [Eqs. (5.3,5.4)] calculated at an angle θ. The power spectral density P is the power spectrum of the surface roughness. A beam of x-rays with area A will sample the following two-dimensional power-spectral density:

$$P(\mathbf{q}) = \frac{1}{A}\left|\int_A z(\mathbf{r}) \exp(2\pi i\, \mathbf{q}\cdot\mathbf{r})\, d\mathbf{r}\right|^2 \tag{5.22}$$

where $z(\mathbf{r})$ is the surface height as a function of position and $\mathbf{q}$ is a vector of momentum transfer. When calculating scattering from a surface, one begins by defining the surface structure, then calculating the power spectral density and working back to the BRDF [Eq. (5.20)]. In diffuse scatter calculations from multilayers, it is assumed that the diffuse scatter is weak so that the total diffuse scatter is the sum of the contributions from each boundary.

5.3 X-ray Telescopes

While multilayers have been used in a normal incidence configuration on far ultraviolet observatories such as SOHO and TRACE,[162,163] x-ray telescopes must employ grazing incidence optics either with total external reflection or with multilayers for three reasons. First, much lower values of δ at x-ray wavelengths mean that small angles must be used to achieve high reflectivity. Second, although multilayering can increase the reflectivity of a surface, there is a limit in the gain from using multilayers. When the total thickness of the multilayers approaches the absorption length, no further increase in reflectivity can result from applying more layers. Finally, current thin-film deposition technology is unable to achieve either the layer thickness or the layer roughness needed for large angle reflection. It is for these reasons that x-ray telescopes use a radically different mirror configuration than their optical counterparts. X-ray telescopes designed for non-solar applications, which view low-flux sources, are actually a system of nested, coaligned barrel-like shells where each shell comprises a telescope in itself. However, each individual shell has a very small geometric collecting area due to the small incidence angles necessary to achieve reflection.

5.3.1 Wolter Systems

Wolter devised three types of systems in his first paper on x-ray optical systems.[120] While his aim was primarily a design for microscopes, two of the three designs (Type I and II) in his original work had potential for use in x-ray astronomy (see Fig. 5.5). Both of these designs are a set of a paraboloid primary mirror and a confocal, coaligned hyperboloid secondary mirror. Both designs focus x rays onto one of the foci of the hyperboloid. For a fixed diameter of both primary and secondary mirrors, the type II telescope has a much longer focal length than the type I telescope. Conversely, for a given focal length, the type II telescope will have a much smaller collecting area than a type I system. In extra-solar x-ray astronomy, where signal-to-noise ratios are generally small, this gives the type I system a distinct advantage. The longer focal length of the type II design gives it greater focal plane magnification and makes it easier to place additional instrumentation behind the exit pupil. This makes the type II design quite useful for dispersive spectroscopic applications. A generalization of the type II design to reduce severe off-axis aberrations can also make the high magnification useful in extended field-of-view imaging applications. Generalizations of the type II design have been successfully applied to extreme ultraviolet missions (EUVE, SOHO),[164,165] where high reflectivity can be extended to larger grazing angles, allowing for larger collecting areas and smaller focal lengths. X-ray telescopes, however, have almost exclusively used either the original type I system or a modification thereof.

5.3.2 Image quality in Wolter I systems

The quality of an imaging system is most often tested by how well an imaging system can focus a point source. Real imaging systems do not focus a point source at infinity to a point at the image plane, rather there is some finite size to the image due to three main sources: diffraction effects, geometrical aberrations, and scattering effects.

Diffraction effects are usually neglected in x-ray applications because the diffraction pattern of a circular aperture, which has an angular diameter of $1.22\lambda/D$, is approximately 10^{-8}–10^{-9} at these wavelengths. A grazing-incidence telescope, however, is an annular aperture which produces a series of diffraction rings within groups rather than the Airy function pattern associated with

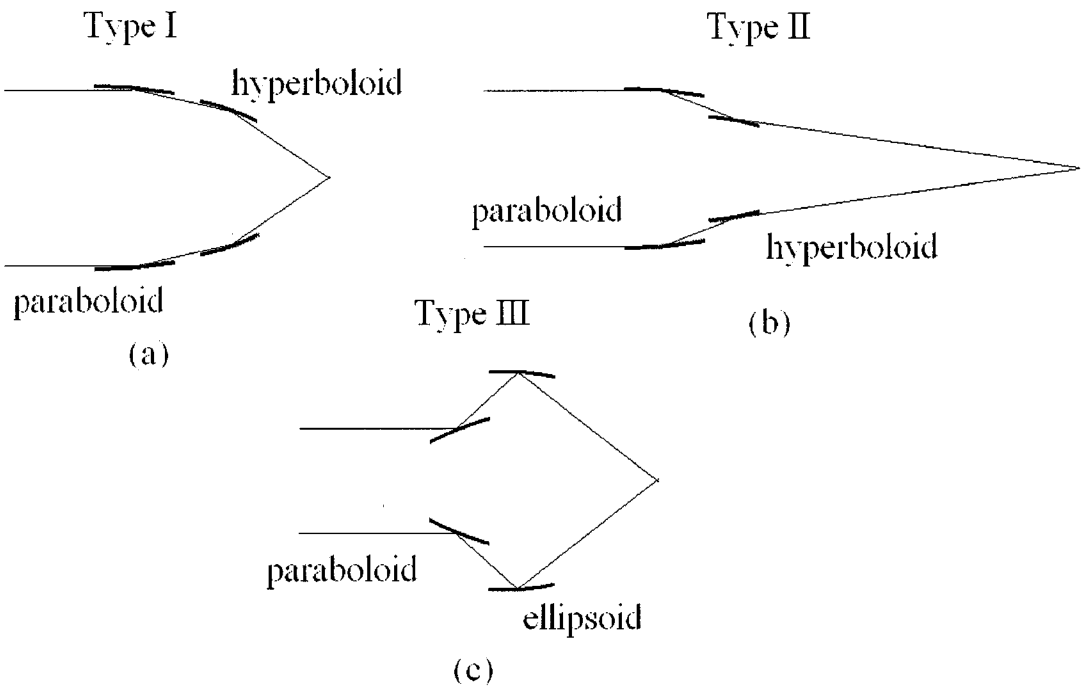

Figure 5.5: The Wolter family of telescopes. The Wolter type I (a) consists of a concave paraboloid primary and a concave hyperboloid secondary. The Wolter type II (b) consists of a concave paraboloid primary and a convex hyperboloid secondary. The Wolter type III (c), which has never been used in astronomy applications, consists of a concave paraboloid primary and a concave ellipsoidal secondary.

circular apertures. The first ring group contains about 95% of the total energy in the diffraction pattern and has an angular diameter of

$$\theta = \frac{1.22\lambda/D}{1-\epsilon}, \tag{5.23}$$

where $\epsilon = D_{\text{in}}/D_{\text{out}}$.[166] Grazing incidence telescopes can have values of ϵ in the range of 10^{-2}–10^{-3}, therefore the diffraction limit is much greater for grazing incidence telescopes compared to normal incidence telescopes of similar size. Typical diffraction-limited angular spot sizes for grazing-incidence telescopes are a fraction of a second of arc. The High Resolution Mirror Array on the *Chandra X-Ray Observatory* approaches its diffraction limit for its lowest design energies,[140] but in general x-ray imaging systems are not diffraction-limited.

Conversely, scattering effects do not play a significant role at optical wavelengths, but are important at x-ray wavelengths. Numerous people have investigated the effects scattering has on the image quality of a grazing incidence system.[167–174] The power spectral density of a given surface can be split into three different spatial frequency ranges based on the source of the surface roughness and its effect on the image quality, shown in Fig. 5.6. Low spatial frequencies, which have correlation lengths on the centimeter or greater scale, are generally due to errors in the overall figure, or shape, of the surface. These errors are typically produced by fabricating a slightly different mirror shape than intended. These figure errors usually transfer a small amount of the energy from the core of the point-spread function (PSF) into higher order diffraction rings without significantly affecting the width of the PSF core. Mid-spatial frequencies, typically on the millimeter scale, are produced typically by polishing imperfections on aspherical surfaces or when applying the reflective thin film(s) to the mirror. These mid-spatial frequencies produce small-angle scatter which widen the core of the image PSF. Such mid-spatial frequency roughness dominated the image quality of the ASCA telescope.[136] A lacquer-dipping technique was used to replace the need to polish the thin aluminum substrates used on the telescope. The lacquer, however, created an "orange peel" effect that introduced mid-spatial frequency roughness. Finally, microroughness has spatial frequencies on the order of micrometers and is either the residual roughness left over after polishing or occurs as a result of the reflective surface deposition process. Microroughness typically greatly reduces the reflectivity of the surface and introduces diffuse scatter into wide angles away from the core of the PSF. Therefore, microroughness also does not change the width of the core of the PSF, but much of the energy is no longer in the core of the PSF. Therefore, for x-ray imaging systems, it is more useful to parameterize image quality by the half-power diameter (HPD), the diameter containing 50% of the energy of the PSF rather than to use the full width at half maximum (FWHM) of the PSF. Microroughness will not change the FWHM of the PSF, but the HPD will certainly increase.

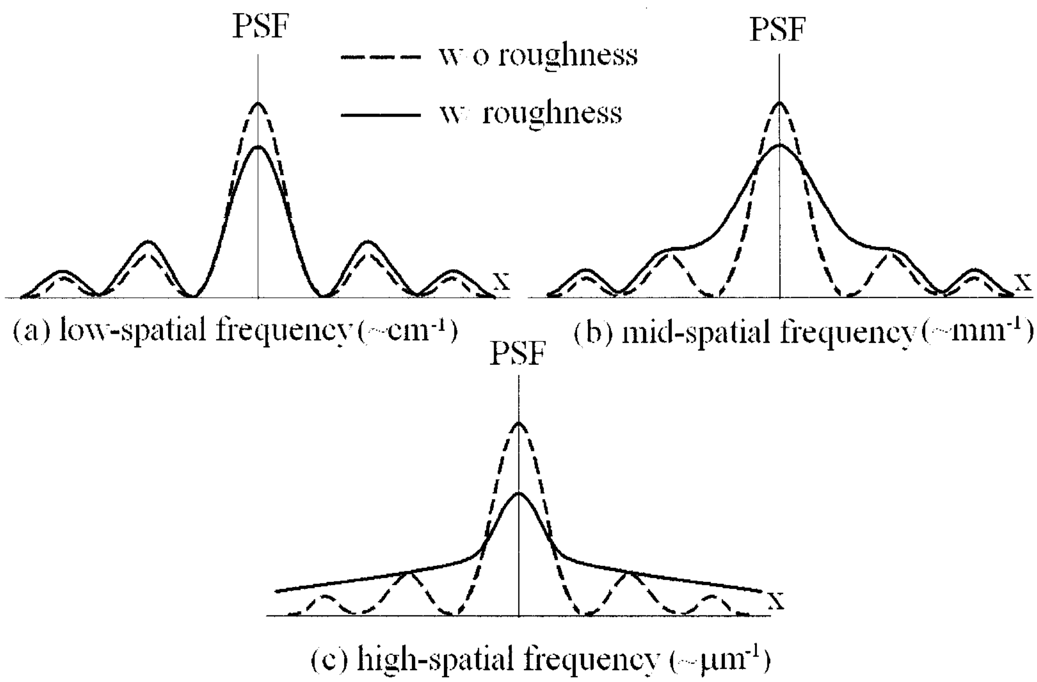

Figure 5.6: Diagram of effects of low-, mid-, and high-spatial-frequency roughness on image quality, based on a figure from Harvey (2002).[137] Shown are a comparison of an ideal image in dashes overlaid on an image affected by low-frequency (a), mid-frequency (b), and high-frequency (c) surface roughness. Note how only the mid-frequency roughness affects the full width at half maximum (FWHM) of the point-spread function (PSF), while both mid- and high-frequency roughness affect the total amount of energy in the core of the PSF without greatly increase the FWHM.

Both optical and x-ray telescopes are affected by geometric aberrations, or degradation in the image caused by the design of the telescope. Geometric aberrations can be calculated by determining the transverse ray aberration.[175,176] This is done by tracing rays arriving from infinity at an off-axis angle θ to the image plane. These rays will intersect the entrance aperture at a polar coordinate position (r, ϕ). The transverse ray aberration (TRA) is defined as the distance on the image plane between a ray intersecting the entrance aperture at (r, ϕ) and a ray entering at (0,0), which is assumed to be where the entrance aperture intersects the optical axis. This distance is often expanded in terms of a power series in r and θ when θ is assumed to be small:

$$\mathrm{TRA} = \sum_m \sum_n a_{mn} r^m \theta^n F_{mn}(\phi) \tag{5.24}$$

TRA changes sign with a rotation of 180°, therefore the value $m + n$ is always odd. Terms with values of $m + n = 3$ are called *third-order* aberrations, terms with $m + n = 5$ are *fifth-order* aberrations, *etc.* Third-order aberrations are given the names *spherical aberration* $(n = 0, m = 3)$, *coma* $(n = 1, m = 2)$, *astigmatism* $(n = 2, m = 1)$, and *distortion* $(n = 3, m = 0)$.

In addition to these transverse ray aberrations, other aberrations also exist which pertain primarily to the focal surface of the telescope. Objects which are off-axis do not have their optimum focus in the same plane as an on-axis object. In other words, the optimum focus for objects off axis does not form a plane, but rather a general surface. The deviation of this general surface from a plane is called *field curvature.* Another form of aberration is *defocus*, which is caused by placing the image plane away from the best focus position along the optical axis. This is often done intentionally to offset other off-axis aberrations, especially in wide-field applications.

No telescope design can ideally produce perfect images over a wide field of view, so often the optimum design depends on the application for which the telescope is intended. To minimize aberrations over the field of view of interest, one can change the design of the telescope to minimize the coefficient a_{mn} in front of the dominant aberration term. In the case of the original grazing-incidence Wolter I telescope, the dominant aberration term at small off-axis angles is coma, but becomes dominated by astigmatism at larger angles.[166,177] Wide-field telescopes used in solar applications use optics modifications to reduce astigmatism at large off-axis angles while sacrificing image quality on-axis. However, for narrow-field extra-solar applications, no significant gain is made by going to an aplanatic (coma-free) system because scattering dominates the geometric aberrations at small field angles.[178] Therefore, the original Wolter type I design is still used in these applications.

5.3.3 Conical approximations

At grazing angles of incidence and large focal lengths, the shape of the paraboloid and hyperboloid approach a conical shape. By using such an approximation, some image quality is sacrificed in return for surfaces which are easier and cheaper to fabricate. This approximation allows thin foils to be used as the reflecting surface rather than thick glass, greatly reducing the weight of the mirror which is important in spacecraft applications. Thin foils also provide high throughput to allow for greater sensitivity to faint objects by tightly nesting foils together.[179,180] Conical thin-foil telescopes were pioneered at Goddard Space Flight Center for the BBXRT telescope and utilized for ASCA, *Astro-E*, and *Astro-E2*. They are ideal for spectroscopic observations of faint point sources, but can also provide imaging capability on the minute-of-arc scale. The image quality of conical foil telescopes is limited by the spherical aberrations introduced by the conical approximation. However, figure errors introduced by stresses on the thin foils and alignment errors have prevented conical foil x-ray telescopes from reaching the geometric aberration limit.[166,181] If these alignment and stress issues can be resolved, it may be possible to produce conical thin-foil x-ray telescopes which can achieve image quality on the order of a few tens of arc seconds.

5.4 Extending Imaging Above 10 keV

X-ray astronomy has experienced a "golden age" within the last 30 years due to advances in x-ray focusing optics and detector technology. However, there is a large disparity in our knowledge of x-ray astronomy above vs. below 10 keV. The energy bandpass above 10 keV is of great interest to astronomers because many classes of celestial objects emit x-rays well above 10 keV. X-rays above 10 keV are typically emitted by nonthermal process while those below can be a combination of thermal and nonthermal processes. Therefore, it is of great interest to astronomers to observe x rays above 10 keV to gain clear insight into nonthermal emission mechanisms. It is quite a coincidence that this transition from thermal to nonthermal emission mechanisms also has been the limit of study for x-ray focusing optics missions. In order to gain greater insight into nonthermal emission mechanisms, it will be necessary to push the current technological limits of focusing x-ray optics.

Focusing optics have been limited to below 10 keV primarily because telescopes to this point have used total external reflection to make highly-reflective surfaces. However, as the real part of the optical constant δ decreases with increasing energy, it becomes necessary to use smaller angles of incidence to achieve high-reflectivity. Such a telescope would necessarily have a lower collecting area. Nesting several telescopes together could counteract this, but the small angles would necessitate a large number of shells which would make mounting such shells difficult and would produce a heavy mirror. A total external reflection mirror above 10 keV would also have a higher focal length or smaller collecting area than present mirrors. Despite these disadvantages, the first focusing optics image between 20–50 keV was taken with a total-external reflection telescope by the HERO collaboration in May, 2001.[182]

The use of graded multilayers to increase reflectivity above the critical angle allows many of the restrictions of total external reflection to be lifted. Larger angles of incidence allow for lighter telescopes with shorter focal lengths. The InFOCμS telescope, described in greater detail in following chapters of this thesis, was the first grazing-incidence multilayer telescope to produce an image at any x-ray energy– an image of the x-ray binary Cygnus X-1 in July, 2001. The HEFT collaboration will also employ grazing-incidence multilayer optics when their telescope will be launched in 2003.[183] Grazing-incidence multilayer optics are seen as a viable technology to extend focusing optics capability up to 100 keV and is a leading choice for the upcoming *Constellation X* mission.[184]

Chapter 6

The International Focusing Optics Collaboration for μCrab Sensitivity Telescope

6.1 Telescope Overview

The *International Focusing Optics Collaboration for μCrab Sensitivity* (InFOCμS) telescope is a balloon-borne hard x-ray telescope built jointly by NASA's Goddard Space Flight Center (GSFC), Nagoya University, Japan's Institute of Space and Astronautical Science (ISAS), and the University of Arizona. It is an 8-m focal length telescope with an elevation-over-azimuth pointing system. The primary goal of InFOCμS is unprecedented sensitivity to faint point sources above 20 keV. InFOCμS is designed to achieve a 3-sigma continuum sensitivity of 100 μCrab in a 12-hour observation. Fig. 6.1 shows a comparison of the sensitivity of InFOCμS to other current and future hard x-ray instruments.

The InFOCμS telescope uses two key technologies to achieve its unprecedented sensitivity. The first technology is graded multilayers, which allows the high reflectivity gained by multilayers to be used in astronomical applications. The second technology is the focal plane detector— a CdZnTe (CZT) detector. CZT is a high-temperature detector which has a quantum efficiency of nearly 100% in the energy range of 20–100 keV. InFOCμS is the first telescope to employ both of these emerging technologies.

The telescope body (Fig. 6.2) is a series of carbon fiber struts arranged to form a truss in order to keep the telescope body light, yet rigid. The telescope is designed to hold four mirrors, one 40-cm diameter mirror with a bandpass of 20–40 keV and three 30-cm diameter mirror with a bandpass of 65–70 keV. The mirrors will have fields of view of $10'$ and $3'$, respectively. The CZT focal plane detectors are pixellated detectors each with a total area of 2.43 cm $\times$ 2.43 cm and a pixel size of 2 mm $\times$2 mm covering an angular area of $54'' \times 54''$. Each detector is surrounded by an active background rejection shield made of cesium iodide.

InFOCμS employs an elevation-over-azimuth pointing system. The elevation drive of the telescope is a long screw threaded through a hole attached

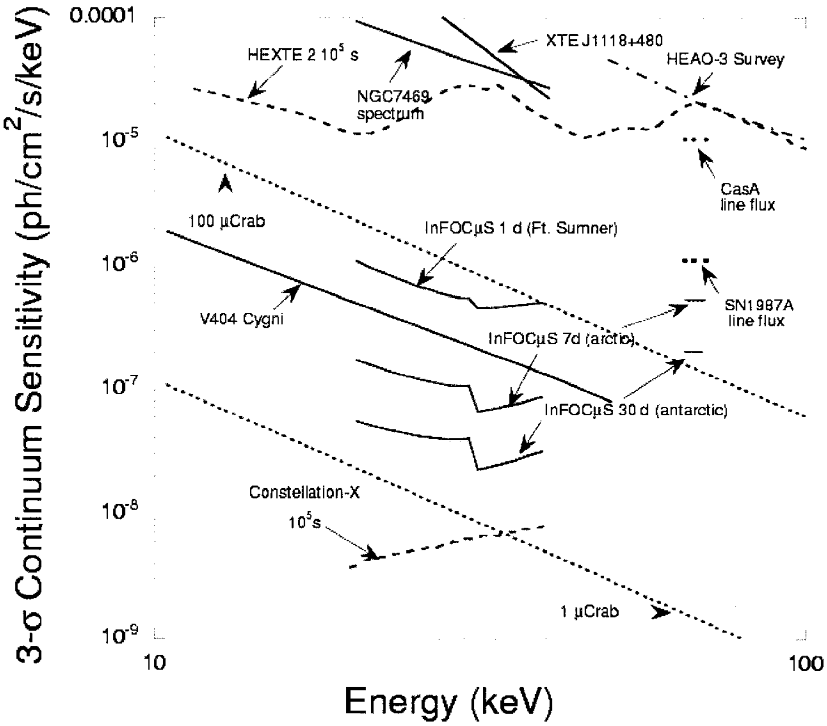

Figure 6.1: The continuum sensitivity of InFOCμS and other hard x-ray observatories. The three InFOCμS lines indicate pointed observations of 1 day (12 hours), 7 days, and 30 days. The continuum sensitivities of the RXTE HEXTE instrument, the HEAO-3 survey, and the projected sensitivity of the Constellation-X hard x-ray telescope are plotted for comparison. Also included are some hard x-ray sources: the ^{44}Ti flux from supernovae Cas A and SN1987A, the continuum flux from the Seyfert 1 galaxy NGC 7469, and the low-mass x-ray binaries XTE J1118+480 and V404 Cygni.

to the truss. The elevation screw is driven by a DC motor on the gondola. The azimuth is controlled by a flywheel which torques the entire gondola. This azimuthal motion of the gondola is decoupled from the balloon.

There are three types of attitude sensors on the gondola. The first is a set of two redundant magnetometers which use the strength and orientation of the earth's magnetic field to determine the azimuth of the gondola. These magnetometers served as feedback for the azimuth pointing servo-loop. The second is a set of inclinometers mounted on the gondola to measure any long-term tilt in either the elevation or cross-elevation directions. The third is two sets of redundant gyros which measure the rate of change in the tilt of the gondola in elevation, azimuth, and cross-elevation. The elevation of the truss relative to the gondola was measured by a synchro-resolver attached to the elevation axis. A summary of the characteristics of the InFOCμS telescope is given in Table 6.1

6.2 Scientific Potential

The hard x-ray sky (i.e. above 20 keV) is a compelling part of the electromagnetic spectrum to study. At this energy, the galaxy begins to become transparent, which allows for exploration of parts of the galactic plane inaccessible to visible-light astronomers. The hottest thermal astrophysical plasmas emit very few hard x rays, but nonthermal emission arising from sources

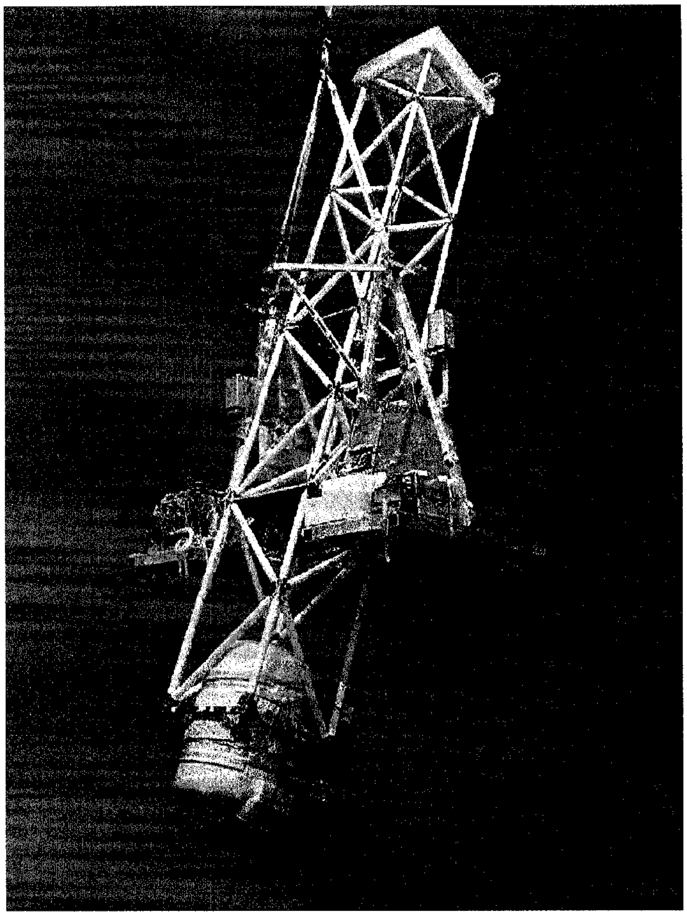

Figure 6.2: The InFOCμS telescope and gondola. The truss is an 8-m long series of carbon fiber struts arranged to provide maximum rigidity at minimum weight. The elevation axis is located 3 m away from the pressure vessel which contains the focal plane detector and detector-related electronics. The mirror is located within a hole on the optical bench at the opposite end of the truss. The gondola contains instrument electronics, the elevation drive, the azimuthal flywheel, gyros and magnetometers for attitude determination, and telemetry electronics.

Mirrors	No. 1 (current)	No. 1 (rebuild)	Nos. 2–4
Focal Length (m)	8	8	8
Energy Bandpass (keV)	20–40	20–40	65–70
Diameter (cm)	40	40	30
On-Axis Effective Area (cm^2, min/max energy)	78/22	120/60	70/70
Field of View (FWHM, arc min)	10	10	3
Resolution (arc min)	2.2	1	1
Half-Power Diameter Size @ Focal Plane (mm)	4.5	2.2	2.2
Detectors			
Detector Material		CdZnTe (CZT)	
Active Volume (cm)		$2.52 \times 2.52 \times 0.2$	
Pixel Pitch (mm)		2 (54″)	
Active Shield		3 cm CsI	
Collimator Field of View (FWHM, deg)		10	
Energy Bandpass (keV)	20–40	65–70	
Energy Resolution (keV)	4.8	5	
Efficiency (%)	100	$\geq$95	
Background Inside Half-Power Diameter (cts/s)	8.2×10^{-4}	3.4×10^{-4}	
3-σ Spectral Sensitivity			
(μCrab in 12 hr)	~ 300	700	
(μCrab in 30 days)	50	90	
Gondola			
Pointing Stability (RMS, arc sec)		30	
Pointing Knowledge (arc sec)		10	

Table 6.1: Instrument characteristics of the InFOCμS telescope. The current 20–40 keV mirror will be replaced by an improved version in the final telescope configuration.

can extend well above this threshold. Therefore, hard x-ray observations can unambiguously reveal the nature of nonthermal sources of x rays and provide constraints on theoretical models of variety of x-ray sources.

There are a few current and near-future space-based observatories designed to observe x rays above 20 keV, such as BeppoSAX, RXTE, INTEGRAL, and HETE-2.[138,185–187] However, the sensitivity of these observatories is far poorer than that of current observatories below 10 keV. The cosmic diffuse background of x-rays greatly limits the sensitivity of hard x-ray observatories, requiring very long observations of only the brightest sources. Focusing optics can greatly enhance the hard x-ray sensitivity by focusing source photons from a large collecting area into a small spot on the focal plane. This leap forward in hard x-ray astronomy, similar to the leap in soft x-ray astronomy taken by the *Einstein Observatory*, will provide serendipitous discoveries of the hard x-ray universe and a new understanding of a variety of celestial objects.

6.2.1 Supernova Remnants

Supernovae are predicted to create radioactive nucleosynthesis products including ^{56}Ni, ^{57}Co, and ^{26}Al. The total yields of such products highly depends on both the nucleosynthesis and ejecta dynamics models used when predicting such yields.[188] One product of particular interest to both observers and theorists is ^{44}Ti. It is of great interest to theorists because it is believed to be formed near the radius differentiating mass expelled as ejecta and mass falling back to form a compact object.[189,190] The total yield is very sensitive to the nucleosynthesis taking place in that region during the explosion, so it will determine the applicability of various nucleosynthesis models. The decay of ^{44}Ti$\rightarrow$^{44}Sc produces inner shell excitation lines at 67.9 keV (100% efficiency) and 78.4 keV (98% efficiency). The lifetime of ^{44}Ti is about 85 years, making it an excellent diagnostic of the dynamics of supernova remnants younger than 1000 years. The high-energy mirrors of InFOCμS will be able to provide for the first time imaging of these decay lines. The low opacity of the galactic plane at these energies will also make ^{44}Ti lines useful in searches for obscured young supernova remnants.

Additionally, the shocks of supernova remnants accelerate cosmic rays via a first-order Fermi mechanism. Although virtually all supernova remnants are believed to accelerate cosmic rays, it is uncertain as to whether or not all supernova remnants accelerate cosmic rays to super-TeV energies. Much of the ambiguity rests in the fact that the soft x-ray spectrum is often dominated by thermal emission from the shock-heated plasma. Searches for evidence of synchrotron radiation at soft x-ray energies look for an excess in thermal model fits to the observed spectrum. This produces an observational bias towards remnants with bright nonthermal emission. Observations at hard x-ray wavelengths would remove this bias because very little thermal emission is produced above 10 keV. The sensitivity of current hard x-ray observatories is too poor to observe the nonthermal emission from all but the brightest remnants. InFOCμS will be capable of opening the observable sky to more galactic supernova remnants, providing a giant leap forward in our understanding of supernova remnants. This may also greatly alter the interpretation of the thermal emission of supernova remnants. Recent evidence shows that the cosmic ray acceleration process can affect the thermal emission from the remnant as well. Therefore, our interpretation of the thermal emission, especially abundances, depends on the amount of energy deposited into cosmic rays.[23]

6.2.2 Other Science

InFOCμS will also provide new discoveries in other areas of astronomy. One of the most compelling questions will be measuring the strength of the intergalactic magnetic field, which has yet to be determined within an order of magnitude. Relativistic jets from active galactic nuclei (AGN) consist of streaming electrons and positrons. At the termini of these jets are radio lobes produced by synchrotron radiation from these particles interacting with the intergalactic magnetic field.[191,192] The luminosity of the radio lobes depends upon both the strength of the magnetic field and the density of the electrons. Without making assumptions about equipartition of energy which may be invalid, neither of these values can be estimated. These same electrons and positrons produce x-ray emission by inverse Compton scattering of the cosmic microwave background. The ratio of x-ray to radio luminosity of the lobes depends only on the energy density of the intergalactic magnetic field and the energy density of the cosmic microwave background. The latter is a well known quantity, therefore combined x-ray and radio observations will be able to place constraints on the value of the intergalactic magnetic field. However, observing the inverse Compton radiation is difficult to do in the soft x-ray band because AGN host galaxies contain hot thermal gas which also produces soft x-rays. InFOCμS will be an ideal instrument to observe the inverse Compton radiation and confine the intergalactic magnetic field.

Our understanding of AGN themselves will also greatly benefit from the sensitive hard x-ray observations InFOCμS can provide. The spectrum of a Seyfert galaxy, a particular class of AGN, has several components.[193,194] The dominant component is a nonthermal power-law spectrum produced by hot accreting matter falling into a supermassive black hole. Several other features can appear in the spectrum. A bump in the power law above 10 keV can appear by Compton scattering of hard photons in the power-law spectrum, referred to as the Compton reflection bump. Resolving these various components will grant x-ray astronomers insight into the nature of these very interesting objects. Attempts to resolve these components with current hard x-ray observatories have met with little success due to their lack of sensitivity and problematic background subtraction. InFOCμS will be able to obtain hard x-ray spectra with sufficient sensitivity to resolve the Compton reflection bump from the exponential cutoff in the underlying power-law spectrum. InFOCμS will also be able to observe AGN which are highly absorbed by the cold torus in the soft x-ray band. Knowing the ratio of absorbed to unabsorbed AGN may give us insight into the nature of the hard x-ray bump observed in the total cosmic x-ray background.

Clusters of galaxies contain hot gas which emits thermal x-ray radiation and have been well-studied by soft x-ray observatories. These clusters also contain relativistic electrons responsible for the diffuse synchrotron emission observed in these objects. These same relativistic electrons will also upscatter the cosmic microwave background to x-ray energies by the inverse Compton process.[195,196] Although this hard x-ray emission has been observed, it is currently unknown whether this emission is diffusely distributed or concentrated within the galaxies of the cluster. If the former picture is correct, then it is possible that the intensity of the hard x-ray component could affect the spectral fits of the thermal soft component— leading observers to infer incorrect dark matter masses within the cluster. InFOCμS will be the first observatory to have the sensitivity and imaging capability to discern the distribution of the hard x-ray emission, perhaps completely changing our understanding of clusters of galaxies.

6.3 Mirrors

The InFOCμS telescope in its final configuration will consist of four 8-m focal length coaligned telescopes— one designed to focus 20–40 keV x rays and three designed for 65–70 keV x rays. Each telescope consists of a set of primary and secondary mirrors in a conical approximation of Wolter I optics. Each mirror consists of 4 quadrant housings, shown in Fig. 6.3, which each hold a set of concentric aluminum foils coated with a Pt/C multilayer. Each foil has a thickness of 155 μm and an axial length of 101.5 mm. The foils are held in the quadrant housing by a series of 26 alignment bars (13 top, 13 bottom) radially spanning each quadrant housing. The alignment bars have trapezoidal-shaped grooves with a minimum width of 170 μm. The radial position of the alignment bars can be adjusted to provide optimum image quality and to hold the foils firmly within the quadrant housing.

The first 20–40 keV mirror, already built and shown in Fig. 6.4, is a 40-cm diameter mirror with 255 concentric rings containing a total of 2040 foils. The reflecting surfaces span radii from 5.88 cm to 19.94 cm. The angle of the primary-mirror foils with respect to the optical axis ranges from 0.105° for the innermost foil to 0.356° for the outermost foil. The angle of the secondary foils is three times that of the primary foils. The total area of exposed reflecting surface of the primary mirror is $\sim$550 cm^2, which is $\sim$ 50% of the total geometric area of the mirror. The second 20–40 keV mirror will feature a similar design with improvements in the alignment bars to decrease stresses on the foils which degrade the image quality and effective area of the mirror. The final design of the 65-70 keV mirror has not yet been determined.

The assembly process for each of the mirrors begins with a flat piece of 155 μm aluminum foil which is mechanically rolled to the approximate desired radius of curvature. The foils are then formed into their final conic shape by fitting them onto a glass forming mandrel and are thermally pressed into shape at a temperature of 140° C for six hours. Foils for four of the eight quadrants were sent to Nagoya University for deposition of the Pt/C multilayer, while multilayers for the remaining four quadrants were deposited at GSFC. Each foil was then fitted into a space between the teeth of the bottom and top alignment bars. The radial position of each alignment bar was then adjusted to obtain the optimum focal plane image of a parallel beam of visible light. Once each quadrant was optimized, the entire mirror was assembled. The position and rotation angle of each quadrant were adjusted to optimize the focal plane image of the entire mirror.

The process for depositing the Pt/C multilayers onto the foils was different for the two facilities performing this task. All foils were shaped into their conical approximation at GSFC. Foils for use in the Nagoya University quadrants were then covered with a 100–200 nm Pt backing before being shipped

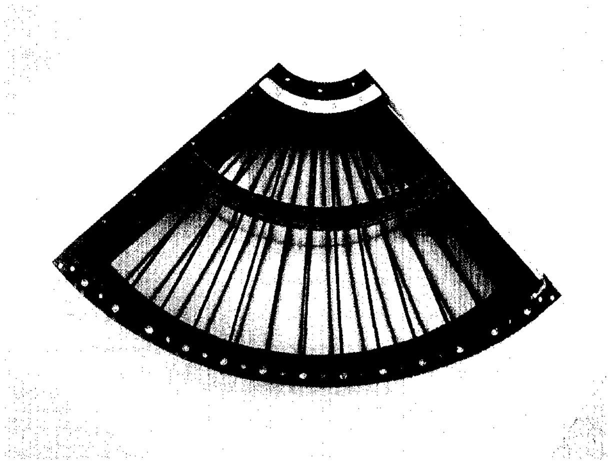

(a)

(b)

Figure 6.3: Quadrant housing (a) and alignment bar grooves (b) of the InFOCμS mirror. Each quadrant holds a series of concentric thin aluminum foils by fitting them in the grooves of the alignment bars. The trapezoidal shape of the alignment-bar grooves has a minimum width of $\sim 170\ \mu$m. The thickness of the aluminum foils is 155 μm.

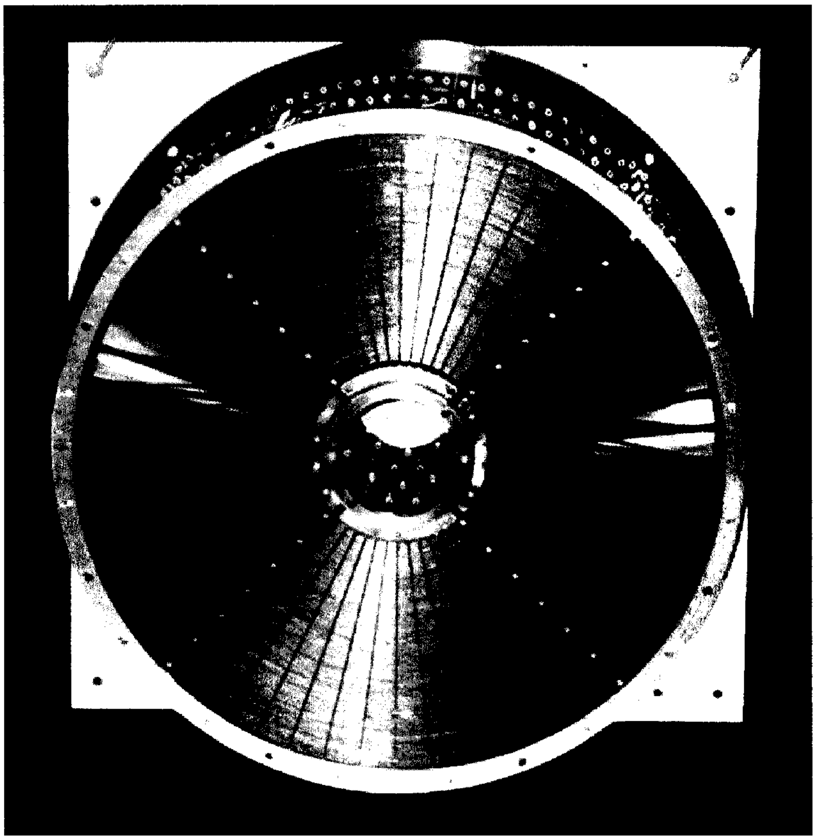

Figure 6.4: The InFOCμS 20–40 keV mirror. The mirror consists of 255 nested shells of aluminum foils in each of eight quadrant housings (four primary, four secondary) for a total of 2040 foils. Each foil was coated with a graded Pt/C multilayer to achieve high reflectivity.

to Nagoya University. The platinum and carbon layers were then sputtered directly onto the foils via DC magnetron sputtering. The multilayers for the GSFC quadrants were deposited onto the foils via a technique called "direct surface replication."[197] In this process, the layers of platinum and carbon are deposited onto a smooth glass mandrel, then transfered to the foil by coating the mandrel and foil with a thin layer of epoxy. The multilayer coatings are described in greater detail in Chapter 7.

6.4 Focal Plane Detectors

The focal plane detectors are pixellated planar CZT detectors. CZT offers a large bandgap energy which makes it usable without cryogenic cooling as is required for germanium crystal detectors. CZT also has nearly 100% quantum efficiency in the energy range of interest to InFOCμS and has superior energy resolution to scintillator detectors used in hard x-ray astronomy such as CsI or NaI. The high electron density in CZT provides a large cross-section for photoelectric interaction which allows for thin wafer with less volume-dependent background. When operated at moderate temperatures ($\sim 0°$ C), CZT also has very low leakage current which reduces noise and permits very sensitive measurements.

The active area of the first CZT detector is 2.52 cm $\times$ 2.52 cm $\times$ 0.2 cm. The pixel size of the detector built for the first flight of InFOCμS is 2 mm $\times$ 2 mm for an angular size of $54''$ at the 8-m focal length of the telescope. The detector has a spectral resolution of $\sim$ 5 keV over the energy range of interest for InFOCμS. The CZT detector is mounted to a one-inch aluminum cube which serves as a coldfinger. An XA-1 ASIC contains a charge-sensitive preamplifier and shaping amplifier for each pixel. The amplified signals are multiplexed to a common discriminator, then an analog-to-digital converter. A bias voltage of -200 V is applied to the detector. The ASIC can only handle 128 channels, whereas the CZT detector has 144 channels, so the four pixels closest to each corner were not connected to the ASIC. The discriminator was set to reject events below 18 keV, but each pixel has a different gain which changes the actual threshold from pixel to pixel. The detector and ASIC were cooled by continually pumping coolant from a thermoelectric cooler into the coldfinger. The focal plane and ASIC are shown in Fig. 6.5.

The detector is surrounded by an active anticoincidence shield comprised of 3-cm thick CsI scintillator, shown in Fig. 6.6. Eight photomultiplier tubes, two on each side of the shield well, collect any scintillation light created in the shield to form a veto signal. The opening at the top of the shield well has an effective field of view of 10° FWHM. The detector sits at the bottom of the shield well.

Focal-plane detectors for the remaining two telescopes will be improved over the current design. These new detectors will feature 1 mm $\times$ 1 mm pixels with an angular size of $27'$ at an 8-m focal length. This new configuration will not greatly increase the amount of charge sharing between pixels. Better spectral resolution will also be possible by a new technique of connecting the detector pixels to the ASIC to eliminate capacitive noise in the current configuration. The background can also be significantly reduced by depth-based background rejection. X rays of energies reflected by the mirrors do not penetrate very far into the CZT detector before being absorbed. The brittleness of CZT precludes making thinner detectors than the current configuration to eliminate noise from other parts of the detector. However, a technique for deducing the depth of interaction by reconfiguring the anode and cathode contacts will make depth-based background rejection possible.

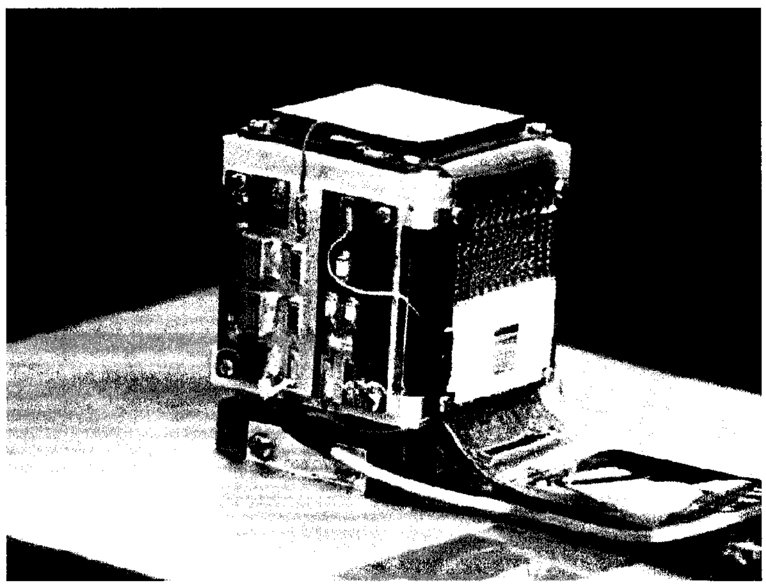

Figure 6.5: The CdZnTe focal plane detector of InFOCμS. The detector sits on top of an aluminum coldfinger cube. On the sides of the cube are the XA-1 ASIC and the bias voltage filter.

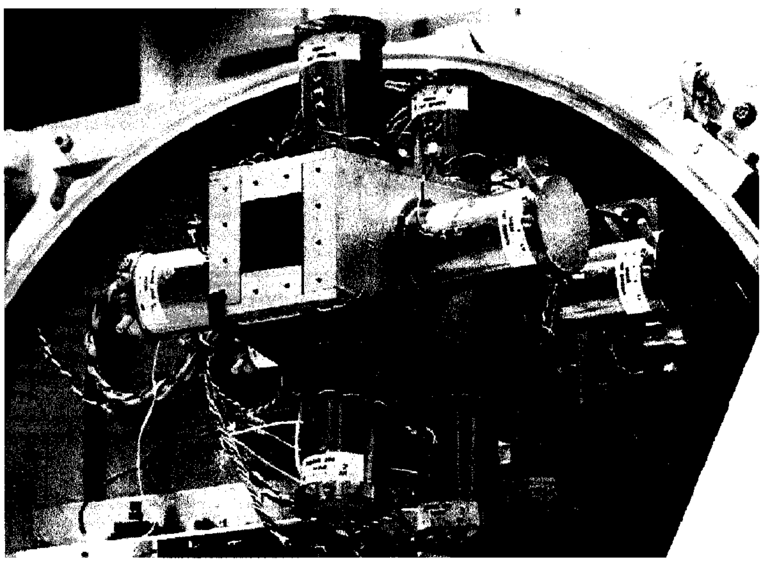

Figure 6.6: The anticoincidence shield (bottom) of InFOCμS. The anticoincidence shield is a 3-cm thick CsI scintillator. The cylinders projecting from the sides of the well are eight photomultiplier tubes which form the veto signal. The effective angular opening of the shield is 10° FWHM.

Chapter 7

Performance of Multilayer Foils

7.1 Multilayer Design

The multilayers of the Nagoya and Goddard quadrants employ two different designs to grade the layer thickness as a function of depth. Both designs employ a power-law design with the thickest layers closest to vacuum for higher efficiency at reflecting lower-energy x rays which do not penetrate as far into the multilayer. The Nagoya quadrants employ a stepwise change in layer thickness as a function of depth; the Goddard quadrants employ a continuous change as a function of depth. Both designs give very similar reflectivity performance as shown in Fig. 7.1. This chapter will focus only on those multilayers produced for the Goddard quadrants.

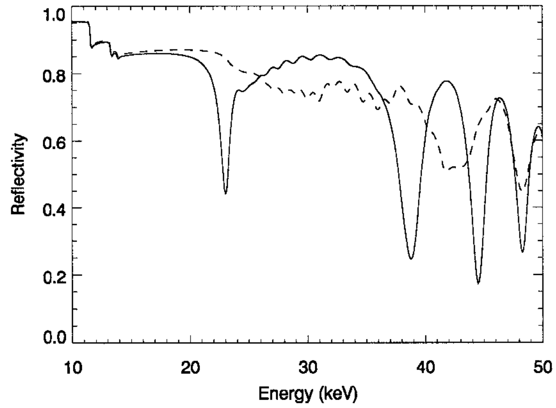

(a)

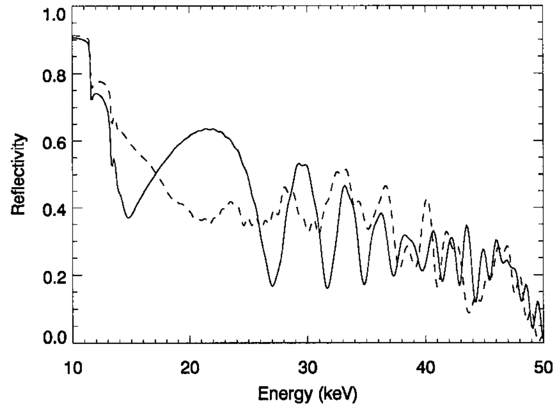

(b)

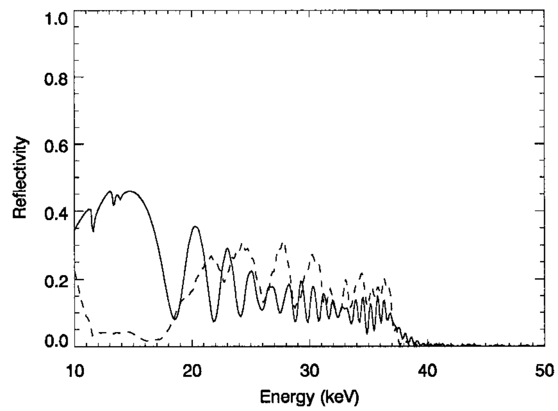

(c)

Figure 7.1: Model reflectivity of sample Nagoya and Goddard multilayers on foils at radius 7.79 cm (a), 12.74 cm (b), and 19.54 cm (c). Both multilayers employ a power-law-like change in layer thickness as a function of depth. The Nagoya multilayers (dashed) employ a stepwise change in thickness, while the Goddard multilayers (solid) employ a continuous change.

The multilayer design for the Goddard quadrants follows the optimization of Joensen *et al.* (1992).[198,199] High reflectivity can be achieved over a broad energy range for a fixed angle of incidence by using a power-law graded bilayer thickness d_i

$$d_i = a/(b+i)^c \tag{7.1}$$

where a, b, and c are free parameters and i is the layer number, starting at 1 nearest vacuum. They empirically find that adopting a value of $c = 0.27$ gives a constant reflectivity over the energy range of interest. This value was adopted for the Goddard multilayers. A combination of the values a and b determine the energy range which the multilayer will reflect at a given angle of incidence.

In the Goddard quadrants, each foil is designed with the middle of its effective energy band at a characteristic energy. It becomes increasingly difficult to reflect the highest-energy x-rays as the angle of incidence is increased, therefore the innermost foil is designed with a characteristic energy of 38 keV. The characteristic energy of each foil varies linearly as a function of radius down to an energy of 20 keV for the outermost foil. This characteristic energy is converted to a thickness d_0 through the Bragg condition for a periodic multilayer [Eq. (5.14)]. We found that adopting a value of $a = 1.5\, d_0$ gives the desired energy range of each foil.

The multilayer can be further optimized by determining the proper value of Γ, the ratio of platinum thickness to bilayer thickness. This is important because constructive interference can occur between successive interfaces (Pt on C and C on Pt) as well as successive bilayer films. Ignoring the effects of absorption, one would normally choose Γ such that the phase delay between two successive interfaces is $\pi/2$— known as a quarter-wave stack. However, this usually leads to very large values of Γ which may be undesirable due to absorption by the platinum layers. Joensen *et al.* determined the optimum value of Γ by balancing constructive interference between successive interfaces with absorption effects

$$\Gamma = \frac{1}{2\pi} \arccos\left(\frac{L^2\mu^2 - 4\pi^2}{L^2\mu^2 + 4\pi^2}\right) \tag{7.2}$$

where L is the total distance the x ray travels through platinum within the multilayer and $\mu \equiv 4\pi\beta_{Pt}/\lambda$. The absorption by carbon layers is small and can be neglected. Eq. (7.2) gives values of Γ ranging from 0.42–0.49 from the innermost to outermost foil assuming 20-keV x rays and an on-axis source. The value of L, and therefore the optimum Γ, changes as a function of off-axis angle. Giving each foil a designated value of Γ is unnecessary— a value of $\Gamma = 0.45$ is assigned to every foil. With this final parameter determined, the expression for the platinum and carbon layer thicknesses becomes

$$\begin{bmatrix} d_{Pt} \\ d_C \end{bmatrix} = \begin{bmatrix} 0.45 \\ 0.55 \end{bmatrix} 1.5\, d_0\, (i - 0.5)^{-0.27}. \tag{7.3}$$

The number of bilayers is also a free design parameter. In general, the reflectivity increases linearly for a low number of bilayers. As the number of bilayers increases, the reflectivity asymptotically approaches unity in a multilayer stack without absorption. With absorption, the reflectivity saturates at a number less than unity when an x-ray within the multilayer has traveled a distance $\sim 1/\mu$. Table 7.1 gives the number of bilayers, chosen to maximize reflectivity, as a function of foil number (1 is the innermost foil).

7.2 The Deposition Process

The platinum and carbon layers are deposited onto the glass mandrel substrate via magnetron sputtering. Sputtering is a process by which a target is bombarded with energetic ions. The energy deposited by the ions is stochastically transferred via collisions to target atoms. Some target atoms are subsequently freed from the target with an angular distribution that goes roughly as the cosine to the target normal. Sputtered atoms propagate either until their kinetic energy is lost in collisions with plasma atoms or adsorbed by other surfaces including the substrate which is placed along the direction of the target normal. The advantages of sputtering over other film deposition techniques such as evaporation are: 1) any substance can be volatilized by sputtering, 2) the energy of the sputtered atoms reaching the substrate is high enough to displace surface atoms which smoothes the layer surface, and 3) deposition rates are

Foil Number	No. Bilayers
1–50	15
51–100	30
101–150	40
151–200	50
201–255	60

Table 7.1: The number of bilayers deposited onto Goddard foils. Foil number 1 is the innermost foil.

stable which allows simple control of layer thickness through timing and greater reproducibility.

Fig. 7.2 shows how magnetron sputtering creates the necessary ions to bombard the target. First, an inert sputtering gas, in this case argon, is introduced to a high-vacuum environment. The target is attached to a cathode held at a negative voltage. The bracket surrounding the target acts as a grounded anode. When the bias on the cathode is large enough and the argon gas pressure is within a certain range, a glow-discharge plasma is created. The pressure of the sputtering gas is important because the electrons must go through a sufficient number of collisions to sustain the plasma, yet be accelerated sufficiently between such collisions. Magnetron sputtering enhances this self-sustaining process by confining the electrons to a toroidal magnetic field. Rather than traveling to the anode where they are lost, they experience an $\mathbf{E}\times\mathbf{B}$ drift in an oval shape around the rectangular target. The magnetic and electric fields prevent electrons from colliding with the target. However the ions, with their larger Larmor radius, will collide with the target and sputter target atoms.

The sputtering gas pressure is also important in the transport to the substrate as well as film growth. Sputtered target atoms initially begin with energies of > 100 eV.[145,200] If the gas pressure is high such that the mean free path is smaller than the target-to-substrate distance, then the sputtered atom can lose a significant amount of energy to collisions before reaching the substrate.

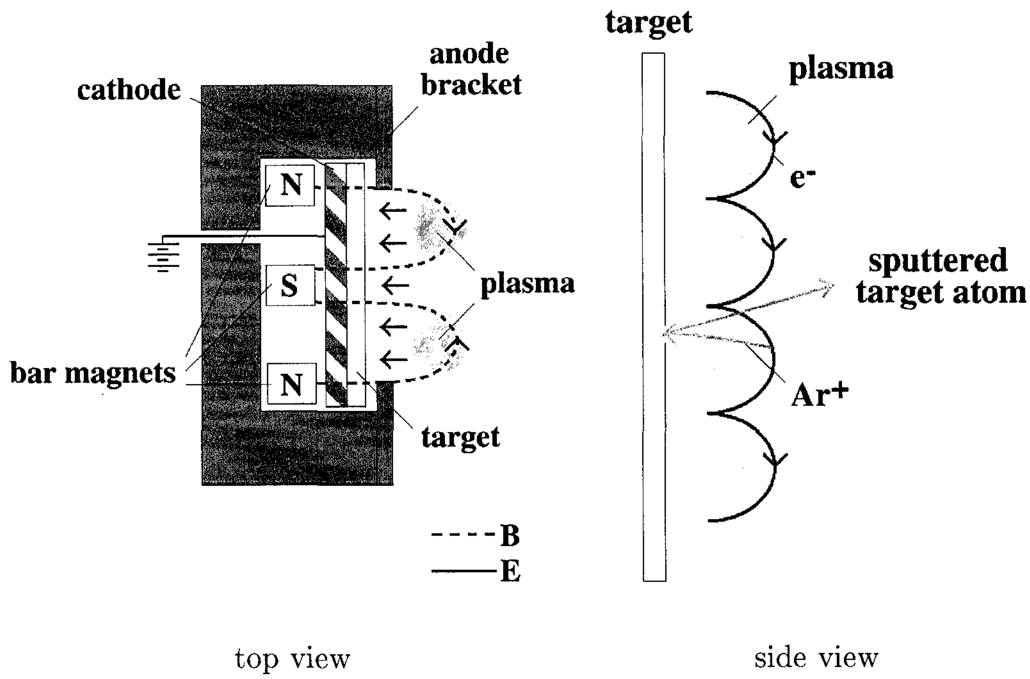

Figure 7.2: Diagram of the magnetron sputtering process. Electrons within the glow-discharge plasma are confined to an area above the target by the electric and magnetic fields. These electrons gain energy from the electric field until they collide and ionize the sputtering gas (argon). The ions, with their larger Larmor radii, collide with the target which sputters target atoms. The residual momentum from the collision carries the target atoms to the substrate. The uniformity of the sputtering process is increased by the cyclic motion of the electrons.

A larger impact energy is advantageous in that it can rearrange surface atoms on the target to produce a smoother surface, but it can also interact up to several tenths of a nanometer below the surface,[201] causing diffusion between layers.

A diagram of the magnetron sputtering chamber used for the InFOCμS multilayers is shown in Fig. 7.3. This chamber can accommodate up to six mandrels for deposition at one time. Each mandrel is placed on a rotation stage controlled by a stepper motor which rotates the mandrel in front of the two targets located at opposite sides of the chamber. The rate of rotation of this stage controls the thickness of the deposited layer. The targets were operated by power control at 57 W for platinum and 500 W for carbon. These powers give a sputtering rate of 0.1 nm s^{-1} for both targets. The entire set of mandrels is on a large rotation table which moves the mandrels from the platinum to carbon targets and vice versa. The distance from the mandrel to the target during sputtering is 7.5 cm. The target dimensions are 20.3 cm $\times$ 5.1 cm. An aluminum mask is placed directly in front of the mandrel to compensate for nonuniformity in sputtering rate in the vertical direction. This mask exposes the rotating mandrel for a longer time in the top and bottom areas of the portion of the mandrel exposed to the target.

The chamber is connected to a cryopump which achieves a pressure of 0.01 mTorr in about 1 hour of pumping time. After the chamber achieves this pressure, the automated process of deposition begins by first introducing the

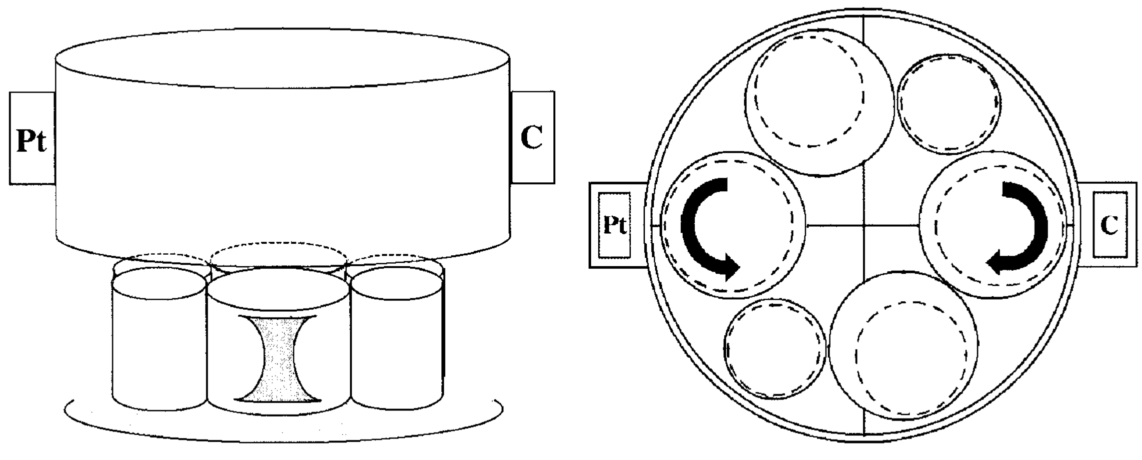

Figure 7.3: Diagram of the deposition chamber from the side (a) and top (b). The deposition chamber can deposit layers onto six mandrels without venting, greatly increasing its production rate. Sputtering takes place simultaneously on two diametrically opposed mandrels placed in front of the targets. The mandrels are rotated in front of the target to control the thickness of the deposited layer. A mask cut into a cylindrical piece of aluminum compensates for nonuniformity in the sputtering rate from the target along the vertical direction.

argon sputter gas at a pressure of 0.75 mTorr. The power on the platinum target is ramped up, then the mandrel in front of the target is rotated at a rate corresponding to the desired layer thickness. It was assumed that the rotation rate is inversely proportional to the deposited layer thickness. When the first layer is finished, the large rotation table rotates 180° to place the mandrel in front of the carbon target. Then the power on both targets is ramped up simultaneously to deposit a layer onto two mandrels at once. After the desired multilayer stack is deposited onto these two mandrels, a final 5 nm layer of platinum is deposited onto both mandrels. The chamber then repeats the deposition process without venting for the remaining sets of diametrically opposed mandrels.

7.3 Reflectometer Measurements

The quality of the multilayer stack is tested by measuring the specular reflectivity of the foil at a range of incidence angles. The shape of this reflectivity curve allows for a precise determination of layer thicknesses and interface width. Because x-rays penetrate well into the multilayer stack, they are an ideal, non-intrusive way to determine the properties of the multilayer.

The reflectometer works by reflecting a monochromatic, well collimated beam of x-rays off a foil sample at an angle θ. A CdZnTe detector positioned at an angle 2θ measures the reflected number of photons resulting from specular reflection. A diagram of the reflectometer is shown in Fig. 7.4. The x-rays are generated by a rotating anode generator which produces x-rays when high-energy electrons collide with a copper target. This generates a spot size of 3 mm$\times$ 0.3 mm with a spectrum composed of a bremsstrahlung continuum and several inner-shell transition lines. The beam is passed through a Ge (111) double-crystal monochromator which is tuned to filter the Cu K-α_1 line at 8.047 keV. Collimation of the beam is limited to the source spot size and a 120 μm tantalum pinhole placed 1 m from the exit of the double-crystal monochromator at the entrance to the main chamber which houses the foil sample and detector. The angular divergence of the beam is 0.012°. The beam is incident with the foil sample at an angle θ which is controlled by a rotation stage in the main chamber. The CZT detector sits at a distance of 780 mm from the rotation axis of the foil and has an area of 3 mm $\times$ 3 mm. Because the x rays are heavily attenuated by air at standard temperature and pressure, the entire system is evacuated to a pressure of less than 5 mTorr.

The system is typically operated in a $\theta - 2\theta$ mode which measures the specular reflectivity over a range of angles. This type of measurement provides information on the reflectivity of the foil and the reduction of specular reflectivity due to interface width. The system can also operate in a fashion that measures the non-specular reflectivity of the foil, which provides information on the

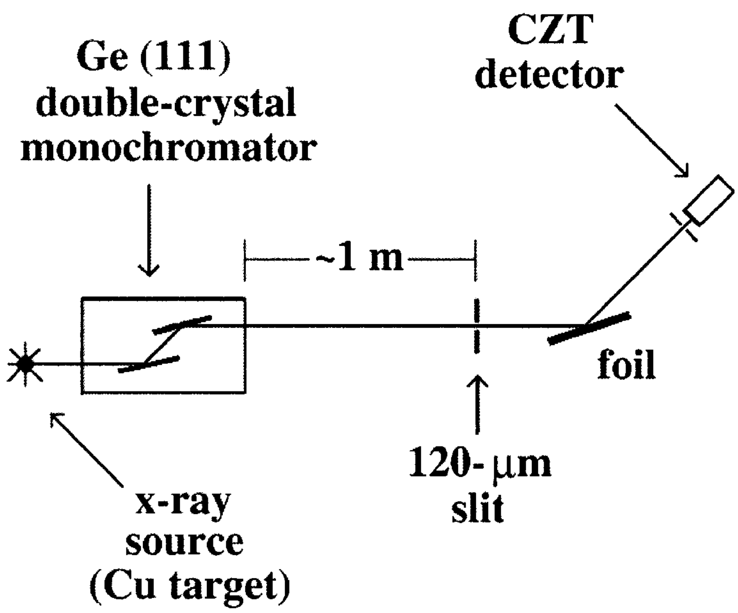

Figure 7.4: Diagram of the reflectometer. X rays are generated by colliding ions with a Cu target, which produces inner-shell transition lines. The Cu K-α_1 line is filtered through a Ge (111) double-crystal monochromator. Collimation is provided by the source spot size and the 120 μm tantalum pinhole at the entrance to the main chamber which houses the foil and CZT detector.

power-spectral density of the roughness between layers. This is done by keeping the sample at a fixed angle while scanning the detector over a range of angles.

7.4 Specular Reflectivity Fits

The specular reflectivity curves measured by the reflectometer were fitted to models calculated by an Interactive Data Language (IDL) program called IMD.[202] This program uses the Fresnel equations [Eqs. (5.3) & (5.4)] to calculate the specular reflectivity of a multilayer stack. The program can accommodate power-law graded multilayers of the form given by Eq. (7.1). It is also very flexible in allowing the user to choose how to parameterize the layer thickness. Using Eq. (7.1) gives the following free parameters: a, b, c, Γ. Monitoring the deposition performance is more straightforward if the layer thickness is reparameterized using the following five parameters: the top platinum and carbon thickness ($d_{Pt,\text{top}}$, $d_{C,\text{top}}$), the bottom platinum and carbon thicknesses ($d_{Pt,\text{bottom}}$, $d_{C,\text{bottom}}$), and the power-law index c. The carbon thickness is proportional to the platinum thickness throughout the multilayer via $d_C = (1-\Gamma)/\Gamma\ d_{Pt}$. In addition to these thickness parameters, the specular reflectivity also measures the mean interface width σ using the Névot-Croce formalism [Eq. (5.19)].

Specular reflectivity measurements were obtained for 78 of the 1040 Goddard foils. These foils were randomly chosen among the foils produced between 2001 Jan 17 and 2001 Apr 17. This sample only covers radii ranging from 7.63 cm–9.16 cm and 12.91 cm–19.54 cm and does not uniformly cover these ranges. Fig. 7.5 shows specular reflectivity measurements for four sample foils with the best-fit model to a power-law graded thickness. The errors associated with the data points are assumed to be the Poisson statistical error in the number of photons received in the detector. Although the fits are qualitatively good for most of the data points, the values of the χ^2_ν statistic are much greater than 1 for all of the foils. Fits for 18 of the 78 foils were qualitatively determined to be poor fits and are excluded from the results given in the rest of this chapter. Before exploring the results of these fits, it is necessary to ensure that the fits cannot be improved by addressing systematic effects.

7.4.1 Angle or Energy Offsets

One possible source of systematic errors is an offset in the measured angle of incidence. Before beginning a reflectivity measurement, the foil must be carefully aligned so the foil begins at a position parallel to the x-ray beam. This is done by scanning both the angular and translational position along the axis orthogonal to the beam and rotation axis. When properly aligned, the foil should occult half of the incident beam and rotating the foil in either direction should occult more than half of the beam. This would translate the reflectivity curve along the angle of incidence axis. A similar shift would occur if the energy of the beam is offset. If such an offset occurs, the resulting thicknesses derived from the fits would be offset. An absolute calibration of the angle or energy offset can be made by examining the critical angle of external reflection. The critical angle only depends on the optical constant δ of the top layer (Pt) [see Eq. (5.6)]. The optical constant δ depends on the electron density of the sputtered material, which could vary because the density of sputtered platinum may be less than its bulk density due to voids created during film growth. However, the critical angle of all of the foils measured lies at the angle corresponding to platinum sputtered at bulk density. It is therefore unlikely that there is both an angle or energy offset and an exactly corresponding change in the density of sputtered platinum.

7.4.2 Fit Parameters

The number of fit parameters can also affect the result of the fits, especially in the case where the fits are very poor (i.e. $\chi^2_\nu \gg 1$). Measurements taken during production of the foils were initially fitted only with the following free parameters: top and bottom platinum thickness, top and bottom carbon thickness, and the width of all interfaces. These fits did well at fitting the first few peaks in the reflectivity curve, but the curve at larger angles of incidence was at best poorly fitted. As a result, the top platinum and carbon thicknesses and the interface width were well-determined, but the bottom layer thicknesses which are responsible for the higher-angle peaks, were not well-determined and were biased by the top layer fits.

Subsequent fits with a greater number of free parameters verified that it was necessary to free more parameters to obtain good fits for the bottom layer thicknesses. A significant improvement in the fit to the reflectivity curve can be seen when each of new parameters are introduced as show in Fig. 7.5. Three changes in the variables fitted during production were made for the following reasons. First, magnetron sputtering produces very reliable sputtering rates which allow for very linear relation between time exposed to the sputtering target and layer thickness. However, this linear relationship is altered significantly by bombardment of the substrate by energetic argon and platinum atoms during platinum sputtering. This can both increase the platinum and reduce the carbon layer thicknesses as these energetic atoms collide and replace carbon atoms as deep as 0.8–1.0 nm within the carbon layer.[201,203–204] Therefore, it is necessary to free the power law indices of the layers to reflect the deviation from this linearity which was assumed during production.

Second, this bombardment also diffuses the interface between the two layers which reduces the reflectivity of that boundary. The yield and kinetic energy of energetic atoms are only significant during the sputtering of platinum due to larger cross-sections for backscattering of argon during the sputtering process which accelerates it toward the substrate and by the larger kinetic energy

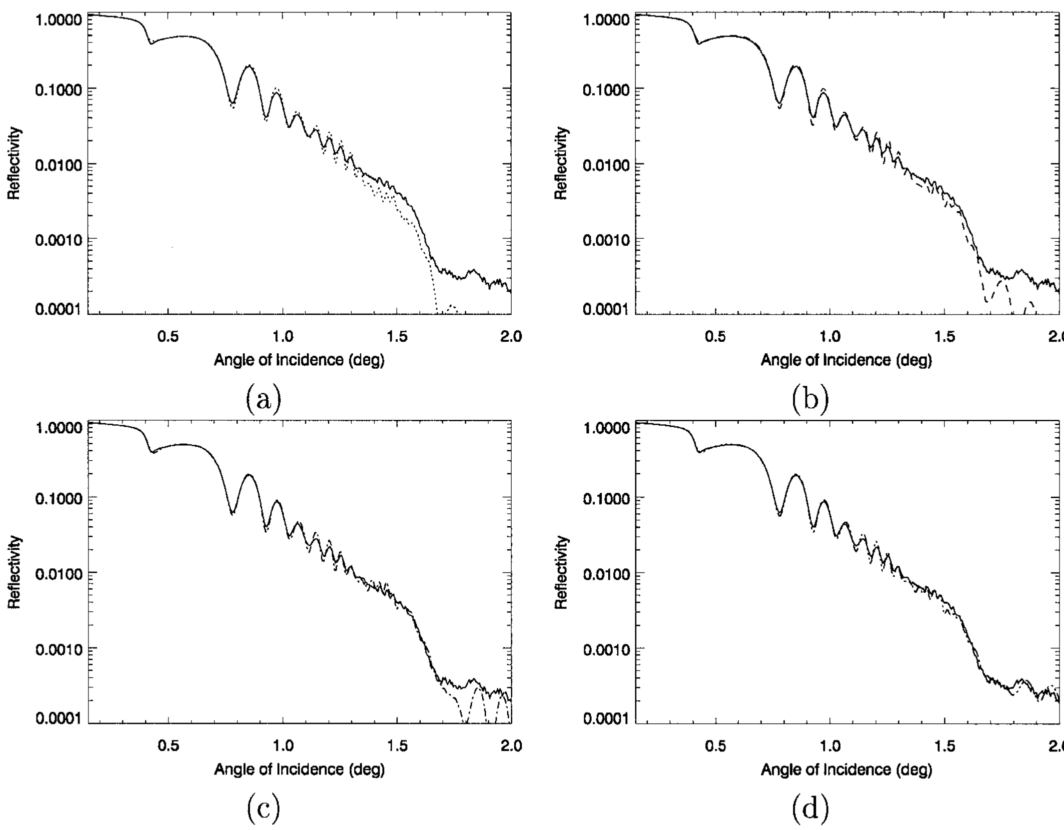

Figure 7.5: Improvements in reflectivity fits with freed parameters. The freed parameters parameters in (a) are the layer thicknesses (top and bottom, Pt and C) and the interface width. In (b), the thickness power law indices of Pt and C are allowed to vary. In (c), the width of each type of interface (Pt on C, C on Pt) is decoupled. An offset in the reflectivity is added to the free parameters in (d).

given to platinum during the sputtering process. Therefore, the diffuseness of interfaces where platinum is sputtered onto carbon is greater than *vice versa* and an improvement in the fits can be realized if these two types of interfaces are allowed to vary independently.

An additive constant to the reflectivity was also included to improve the fit to the reflectivity at large angles of incidence. Nonspecular light scattered into the detector is an unlikely source of this additional photons. The beam size at the detector is ≈ 650 μm, but the slit size in front of the detector is only 500 μm, so photons outside the specular beam do not reach the detector. The measured background of the detector is also too low to account for the additive constant. The additive constant is likely an unknown instrumental effect rather than an intrinsic property of the multilayers. The constant has a negligible effect on the best-fit parameters of the multilayers.

These additional parameters improve significantly the quality of the fits, however the fits are still statistically poor for at least two significant reasons. First, the thicknesses of the layers do not make an ideal power law. Thicknesses can only be produced with an accuracy on the order of 0.1 nm. This inaccuracy affects the position and height of peaks and valleys in the reflectivity curve as shown in Fig. 7.6. In order to significantly improve the fit, the thickness of each individual layer would need to become a free parameter— making the fitting procedure very prone to non-convergence or convergence to a local rather than a global minimum.

Second, the interface roughness varies as a function of depth in the multilayer. Deposition involves the build-up of one layer on top of another layer and the mean interface roughness increases as a function of the number of layers deposited. The direct replication technique was designed to invert the deposited layers so that the smoothest layers would be on the top of the multilayer stack and therefore result in higher foil reflectivity. Evidence of roughness as a function of depth seen in all the foils is shown in Fig. 7.7. The best-fit values of σ result in too low a reflectivity at the smallest angles— likely because the overall roughness is biased toward the roughness of layers further into the multilayer stack, which determine the reflectivity curve at higher angles and are well-fitted by the model. The higher peak reflectivity of these two peaks is consistent with the fact that direct replication places the smoothest layers, which do no suffer from a build-up problem, at the top of the multilayer stack.

7.5 Thickness Accuracy

The ability to deposit layers accurately is important— even crucial in some applications— to achieving the maximum reflectivity of the mirror at the designed energy and angle of incidence. In narrow-band mirrors such as the

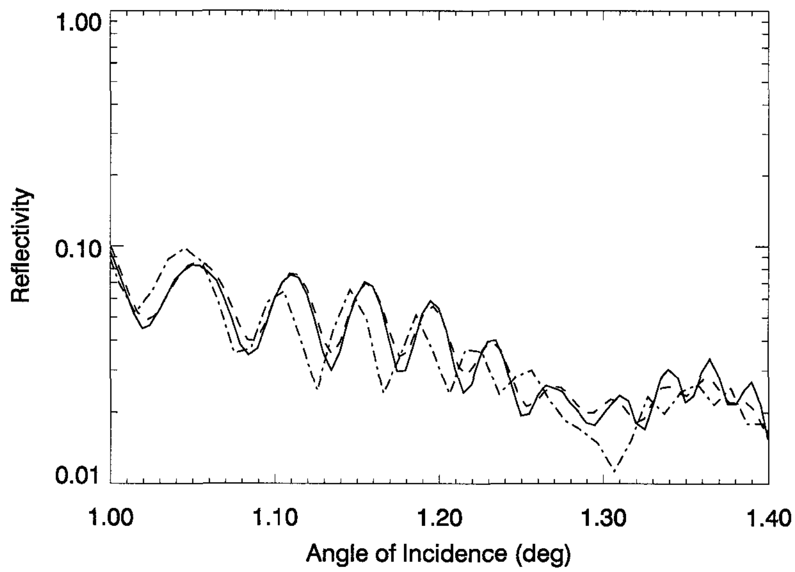

Figure 7.6: Effect of layer thickness inaccuracy on multilayer reflectivity. The solid line is the measured reflectivity of a sample foil. The dashed line represents the best-fit model to the data. The dot-dashed line is the best-fit model modified by a random thickness error of 0.1 nm.

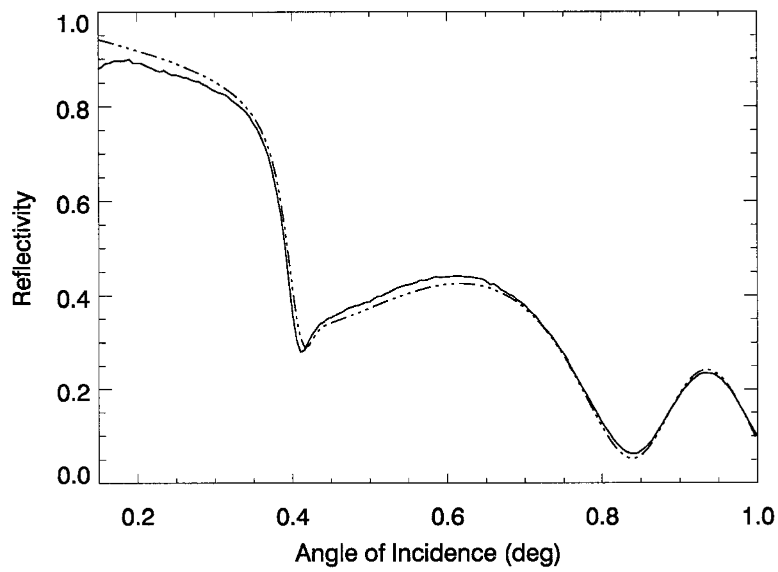

Figure 7.7: Sample reflectivity curve at small angles of incidence. The solid line is the measured reflectivity of a sample foil. Errors in the measurement are less than 4% of the measured reflectivity. The dotted line is the best-fit reflectivity model over the entire range of angles measured (0.0–2.0°). The larger-than-predicted reflectivity at small angles of incidence indicates that the interface width is smaller at the top layers than the best-fit value.

65–70 keV mirrors to be designed for InFOCμS, achieving the desired layer thickness with repeatability to within about 0.1 nm is crucial. A graded multilayer with a broad energy range such as the 20–40 keV mirror has a greater tolerance in layer repeatability. Magnetron sputtering can typically achieve layer repeatability to within 0.1 nm,[201,205,206] but these only involve sputtering onto one substrate in a deposition run, *i.e.* evacuating the chamber, sputtering, and venting the chamber. When multiple substrates are coated in a deposition run, other issues begin to affect repeatability such as the cleanliness of the target anode, which affects the target current and hence the sputtering yield.

The ratio of fitted to designed layer thickness for the top platinum and carbon layers over the sampling time period is given in Fig. 7.8. In these and subsequent figures within this chapter, the sample of foils is divided into foils produced before and after day 50 (2001 Mar 1). This corresponds to a change in the calibration of the rotation rates of the mandrel in front of the platinum target and improved cleaning procedures between deposition runs that stabilized the carbon sputtering rate. A change in the top carbon ratio can also be seen around day 25 (2001 Jan 25), which corresponds to a change in the calibration of the rotation rate in front of the carbon target. Fig. 7.9 shows the failure of monitoring during production to determine the bottom layer thickness of the multilayer. During the production process, the power law index was held frozen at the design value of c=0.27, which biased the bottom-layer thickness to the top-layer thickness value.

The assumption that a fixed power law index was sufficient for monitoring was based on the fact that magnetron sputtering produces a very stable deposition rate, therefore the desired layer thickness depends only on the amount of time the substrate is exposed to the target. This linearity applies well for thick layers but not for thin layers. Energetic bombardment during platinum sputtering replaces previously deposited carbon atoms with platinum atoms. As a result, the platinum layer effectively grows at a greater rate than anticipated because platinum atoms are penetrating into the surface as well as being deposited onto the surface. The carbon does not similarly penetrate into the platinum layer, therefore the interface between the layers is effectively moved into what was the carbon layer. This change in the layer thicknesses is only a function of the penetration depth of the platinum into the carbon layer, therefore each layer should experience a constant offset in thickness. This constant offset will significantly change the bottom layers but will have a much smaller effect on the top layers. The power law index of the platinum layers should decrease and that of the carbon layers should increase as a result.

This very effect is observed in Fig. 7.10. The fitted power-law index of carbon is above 0.27 for most of the foils measured, including all foils measured after day 50. A corresponding decrease is seen in the platinum power-law which

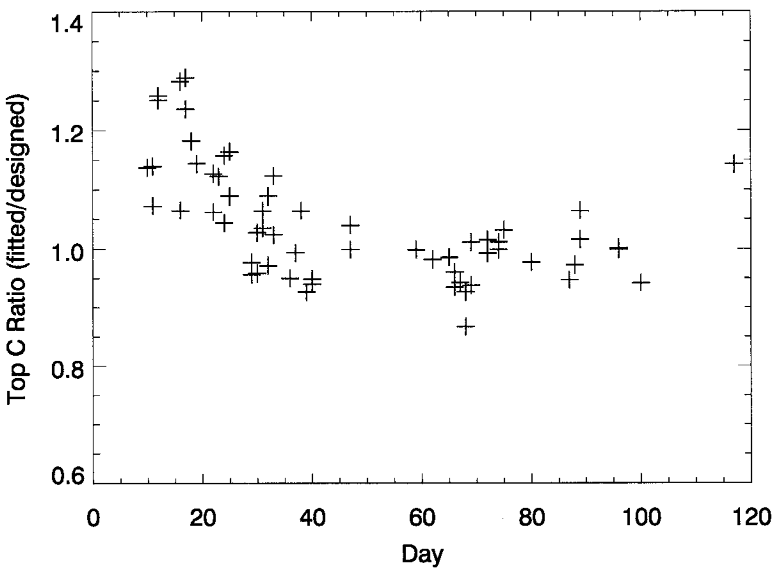

Figure 7.8: Ratio of fitted to design top layer thicknesses over the foil sampling period. The sample is split into two different time periods corresponding to a change in the calibration of the mandrel rotation rate in front of the platinum target and improved cleaning procedures between deposition runs. A change in the average carbon ratio is seen around day 25 which corresponds to a change in the rotation rate in front of the carbon target.

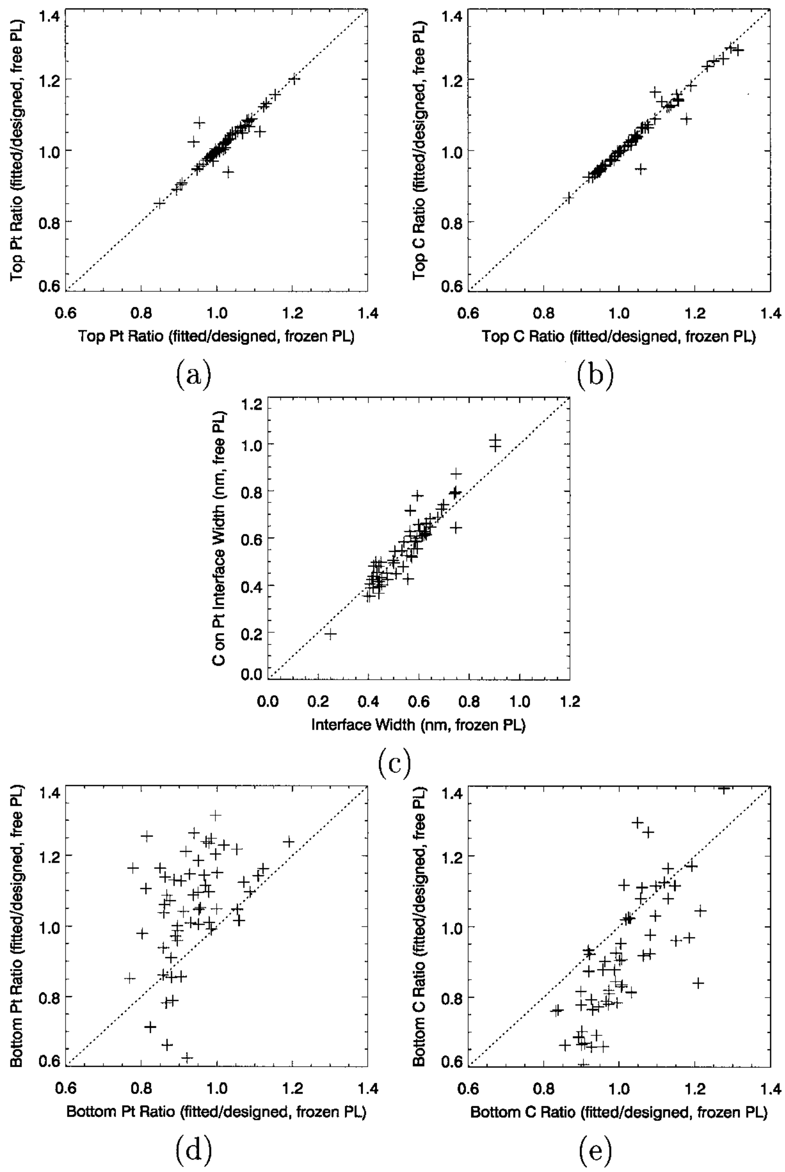

Figure 7.9: Comparison of the ratio of fitted to design layer thickness and interface width between a frozen power law index and a variable power law index. The strong correlation of the top layer thicknesses indicates the frozen power law properly fits the top bilayer thickness (a,b) and interface width (c). However, it is not successful at properly determining the bottom layer thickness (d,e).

is strongly anticorrelated with the carbon power-law index. This strong anticorrelation strongly suggests that energetic bombardment has a significant role in the deposition setup. This is not surprising considering that the deposition is occurring under very low argon pressure. The mean free path length for collisions at the sputtering pressure of 0.75 mTorr is $\sim$30 cm— much longer than the distance between the target and substrate. The sputtered platinum atoms and any reflected argon atoms will arrive at the substrate without losing much energy through collisions with the gas.

The large variation in fitted power law indices seems to indicate that there is an unknown variable affecting the efficiency of energetic bombardment. There are two possible ways to achieve this— either reduce the yield of energetic particles through collisions in the gas or reduce the energy given to energetic particles. Given the mean free path is much longer than the distance between the target and substrate, the former is highly unlikely.

The accuracy of the layer thicknesses is summarized in Table 7.2. The linear thickness accuracy of the deposition chamber is not quite as good as other values reported for magnetron sputtering which are typically less than 0.1 nm. However, those systems are also not mass production systems and are typically thoroughly cleaned between deposition runs— a luxury that cannot be afforded in a mass production setup.

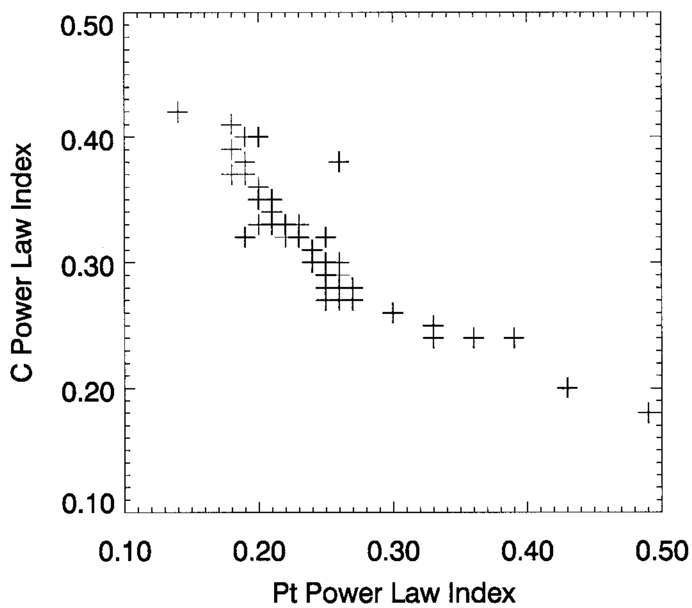

Figure 7.10: Fitted carbon thickness power-law index vs. platinum thickness power-law index. The strong anticorrelation between these fitted values suggests that energetic bombardment during platinum sputtering is effectively decreasing the carbon thickness while increasing the platinum thickness. The large locus of points suggests the efficiency of this energetic bombardment is changing from foil to foil.

Layer Sample	Ratio Mean	Ratio Std. Dev.	Accuracy (nm)
top platinum			
all foils	1.02	0.06	0.3
before day 50	1.04	0.06	0.3
after day 50	0.99	0.05	0.2
top carbon			
all foils	1.04	0.10	0.5
before day 50	1.08	0.10	0.6
after day 50	0.99	0.05	0.3
bottom platinum			
all foils	1.04	0.17	0.3
before day 50	1.00	0.19	0.3
after day 50	1.12	0.10	0.2
bottom carbon			
all foils	0.91	0.19	0.3
before day 50	1.01	0.17	0.3
after day 50	0.76	0.09	0.2

Table 7.2: Layer thickness ratio (fitted/designed) mean and thickness accuracy for top and bottom layers. The large standard deviation of the measured carbon layers of the sample taken before day 50 can be attributed in part to a change in the calibration of rotation rates in front of the carbon target at day 25.

7.6 Interface Width

The interface width of the layer boundaries reduces the reflectivity of the multilayer via the Debye-Waller or Névot-Croce factor [Eq. (5.18) or Eq. (5.19), respectively]. It is important to minimize the width of the boundaries in order to maximize the foil reflectivity and thus the effective area of the x-ray mirror. The best-fit values of the width (σ) of each interface type are shown in Fig. 7.11. The widths range from 0.2–1.0 nm, with most falling in the range of 0.45–0.60 nm. Periodic multilayers composed of Pt/C can typically produce values of σ=0.3–0.4 nm with good reproducibility.[201,207–208] It is likely that any range in derived values of σ arises again from one or more systematic variables during deposition. This section will discuss some of these possible variables.

The specular reflectivity of a foil alone cannot determine whether the interface width is primarily due to roughness or diffuseness. A measurement of nonspecular scattering of x-rays, shown in Fig. 7.12, only depends on properties of the interface roughness and thus can determine the contribution of roughness to the interface width. This measurement was taken by leaving the angle of incidence at a constant angle and placing the detector at five different reflection angles. The incident beam was composed of x rays in the 20–40 keV band. The power spectral density of the interface roughness was assumed to be of the following form:[157]

$$\mathrm{PSD}(q_{\mathrm{par}}) = e^{-z/\xi_{\mathrm{perp}}} \frac{4\pi H \sigma_r^2 \xi_{\mathrm{par}}^2}{[1 + (q_{\mathrm{par}} \xi_{\mathrm{par}})^2]^{(1+H)}} \tag{7.4}$$

A fit to the nonspecular scatter gives the power-spectral density parameters consisting of the roughness σ_r, the correlation length of the roughness along the x-ray beam direction ξ_{par}, the correlation length of the roughness ξ_{perp} as a function of depth ξ_{perp}, and the jaggedness or Hurst parameter H. The small number of scattered x-rays in this measurement precluded deriving anything more than the upper limits of these parameters ($H \leq 1.0$, $\xi_{\mathrm{par}} \leq 10.0$ nm, $\xi_{\mathrm{perp}} \leq 40.0$ nm). These upper limits were derived under the assumption that the interface width is all roughness. No independent determination of the roughness could be made due to the small number statistics of the measurement.

Even though the nonspecular scattering measurement was inconclusive, there is evidence that the interface width is composed of roughness to some extent. Fig. 7.13 shows that σ is significantly smaller for foils with a design thickness of the top platinum layer greater than 5 nm than for those with a design thickness less than 5 nm. All of the foils in the group above 5 nm have 30 bilayers within their multilayer stack, while those in the group below 5 nm have either 50 or 60 bilayers. One possible explanation is that a buildup of layer roughness occurs which increases the mean C on Pt roughness from 0.49 nm for the 30-bilayer group to a mean of 0.58 nm for the 50/60-bilayer group. A Kolmogorov-Smirnov (KS) test gives a probability of 12% that these two groups come from the same parent population. However, there was no statistical difference between the interface width of the 50-bilayer group and the 60-bilayer group— a KS test of these groups gave a 97% probability of coming from the same parent population. While build-up of layer roughness is a well-known phenomenon, there is no reason that such a build-up would exist if the interface width is predominantly diffuseness.

Diffuse interfaces are created by energetic bombardment, which replaces light carbon atoms with heavier platinum atoms, creating an interface where platinum and carbon are mixed. This bombardment only occurs when platinum is being sputtered onto carbon, therefore the value $\sigma_{\mathrm{C/Pt}}$ should be greater than $\sigma_{\mathrm{Pt/C}}$ if diffuseness is a significant contributor— remembering that the replication process reverses the order of the layers within the multilayer stack. Only 41 of the 60 foils in the sample exhibit this characteristic as shown in Fig. 7.14. If the interfaces were completely due to roughness, then there would be little to no difference between $\sigma_{\mathrm{C/Pt}}$ and $\sigma_{\mathrm{Pt/C}}$. However, some of the foils measured show ratios of $\sigma_{\mathrm{C/Pt}}/\sigma_{\mathrm{Pt/C}}$ much less than one— something which is difficult to explain physically.

If the strong anticorrelation of the platinum and carbon power-law indices of the thickness can be attributed to energetic bombardment, then there should be a strong correlation between these power-law indices and the value $\sigma_{C/Pt}$ if the interface is mainly diffuse. Fig. 7.15 shows that there is a correlation between the two above 0.6 nm interface roughness. Additionally, the correlation does change slightly between foils made before and after day 50. Based on this and previous evidence, it is likely that the interface is not predominantly roughness nor diffuseness, but a combination of both.

The high reproducibility of multilayers with magnetron sputtering in other situations seems to indicate that may be a hidden systematic variable which is causing the large range of observed values of σ. Histograms of $\sigma_{C/Pt}$ and $\sigma_{Pt/C}$ reveal what may be a bimodal distribution in the sample of foils with 50 or 60 bilayers in Fig. 7.16. Such a bimodal distribution could indicate that a systematic variable is present. The histogram of $\sigma_{C/Pt}$ can be fitted by a unimodal Gaussian distribution with a value of χ^2_ν close to one. The fits cannot be statistically improved by using a bimodal fit despite the appearance of the histograms— a statistical F-test reveals that there is a non-negligible probability that a random sample would give a similar fit improvement. The fitting, summarized in Table 7.3, was done at two different bin sizes to show that the bin size does affect this probability only in a small manner. There are not enough foils in the sample to make a definitive conclusion that the distribution is bimodal.

If mandrel heating, buildup of material on the target anode, or any other systematic variable is present that changes within a deposition run, then a

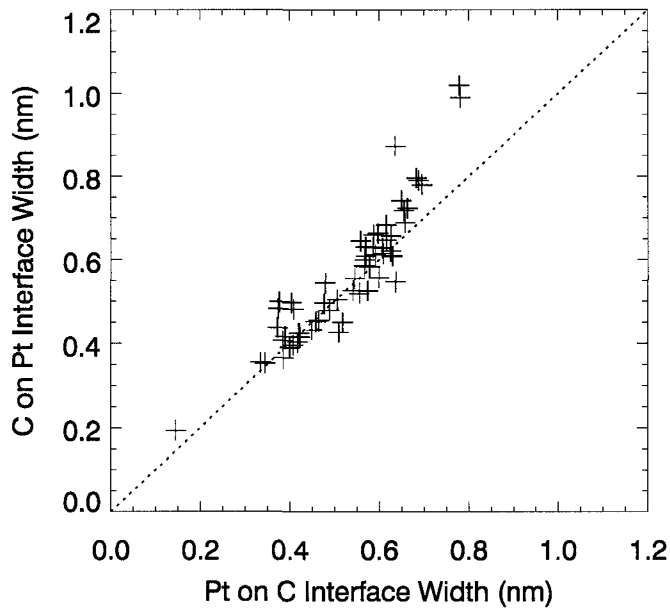

Figure 7.11: Carbon on platinum interface width vs. platinum on carbon interface width.

Interface	Bin Size (nm)	1st Gaussian a_0	a_1	a_2	2nd Gaussian a_0	a_1	a_2	F-Test Prob.
C on Pt	0.04	3.73	0.51	0.16				
		4.90	0.62	0.07	5.13	0.41	0.03	0.64
C on Pt	0.06	6.58	0.54	0.13				
		6.27	0.56	0.13	7.40	0.43	0.003	0.64
Pt on C	0.04	5.69	0.59	0.08				
		8.22	0.60	0.05	5.30	0.41	0.02	0.27
Pt on C	0.06	9.50	0.55	0.07				
		13.00	0.59	0.04	5.69	0.42	0.03	0.42

Table 7.3: Results of unimodal and bimodal Gaussian fits to the histogram of interface width observed in 50–60 bilayer foils. The Gaussian distributions are parameterized as $a_0 \exp\{-[(x-a_1)/(2a_2)]^2\}$. The F-test probability is the probability that a random sample would offer a similar improvement when going from a unimodal to a bimodal fit.

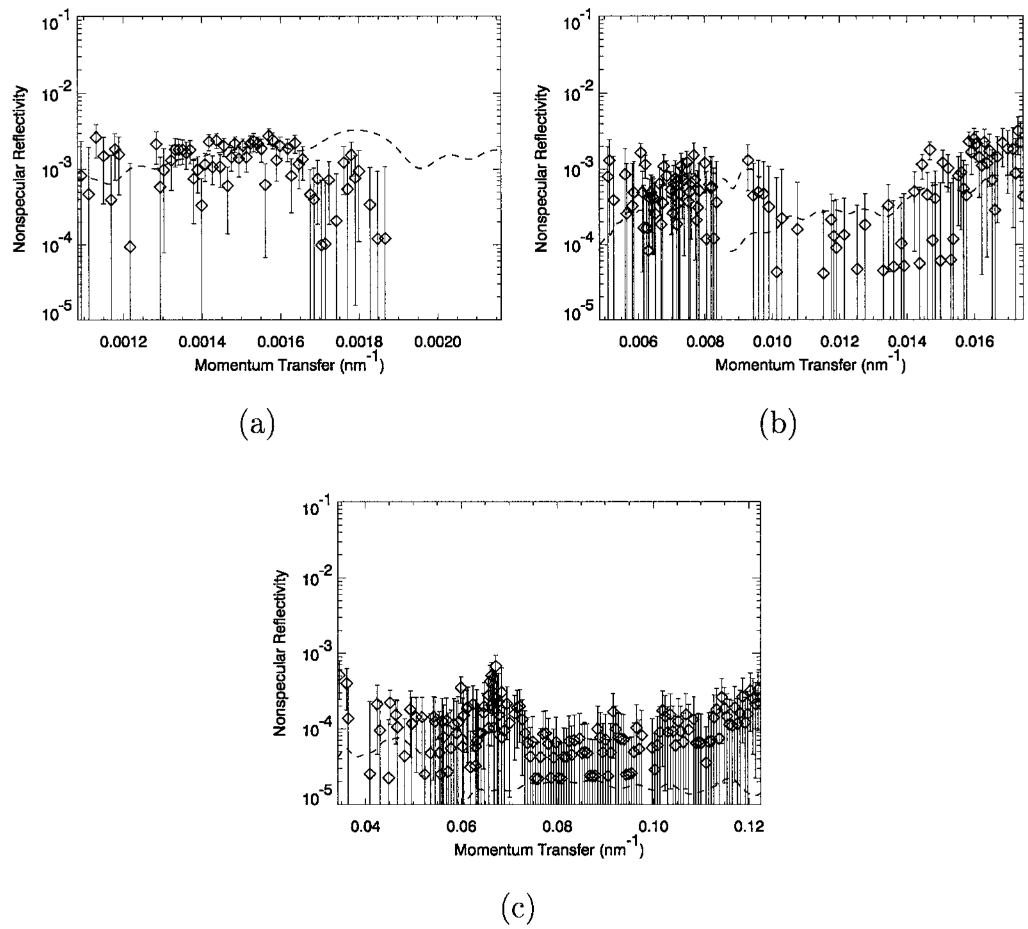

Figure 7.12: Nonspecular scattering measurement of a sample foil. The nonspecular ($\theta_{\text{in}} \neq \theta_{\text{out}}$) scatter seen is due entirely to roughness of the interfaces. The abscissa is given in terms of momentum transfer $q = 4\pi(\sin\theta_{\text{out}} - \sin\theta_{\text{in}})/\lambda$. The measurement was done by setting θ_{in} to 0.195° and setting the detector angle θ_{out} to five different positions. A 20–40 keV x-ray beam was used to provide a continuous range of q values at each θ_{out}. All three plots are the same data plotted in different momentum transfer ranges.

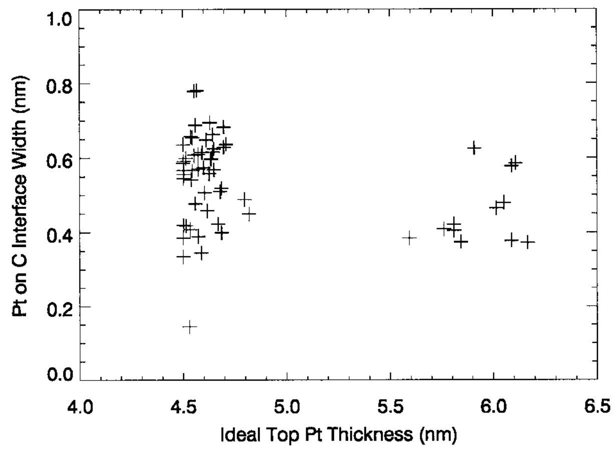

(a)

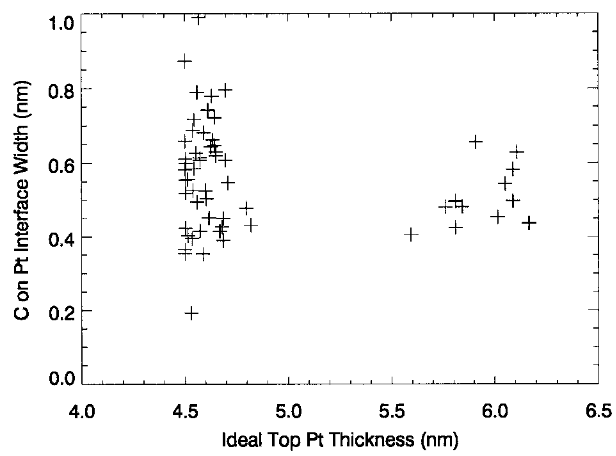

(b)

Figure 7.13: Pt on C (a) and C on Pt (b) interface width vs. design top platinum thickness. The larger interface width on the foils with top thickness smaller than 5 nm is likely due to a buildup of interface roughness as a function of number of layers deposited. The foils with top thicknesses smaller than 5 nm have 50 or 60 bilayers, while those with top thicknesses larger than 5 nm only have 30 bilayers.

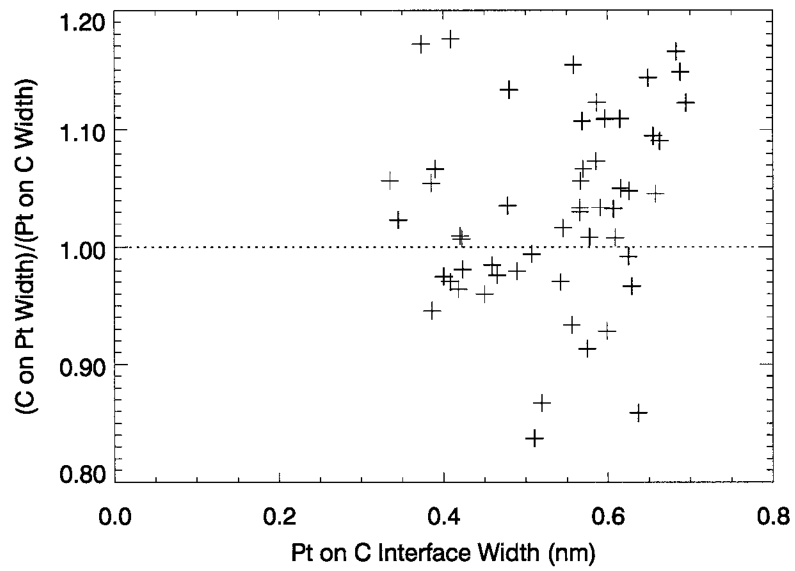

Figure 7.14: Ratio of carbon on platinum to platinum on carbon interface width vs. platinum on carbon interface width. Large positive values of the difference in width can be attributed to the effects of energetic bombardment during platinum sputtering on interface diffuseness. However, only 41 of the 60 foils in the sample exhibit this trait.

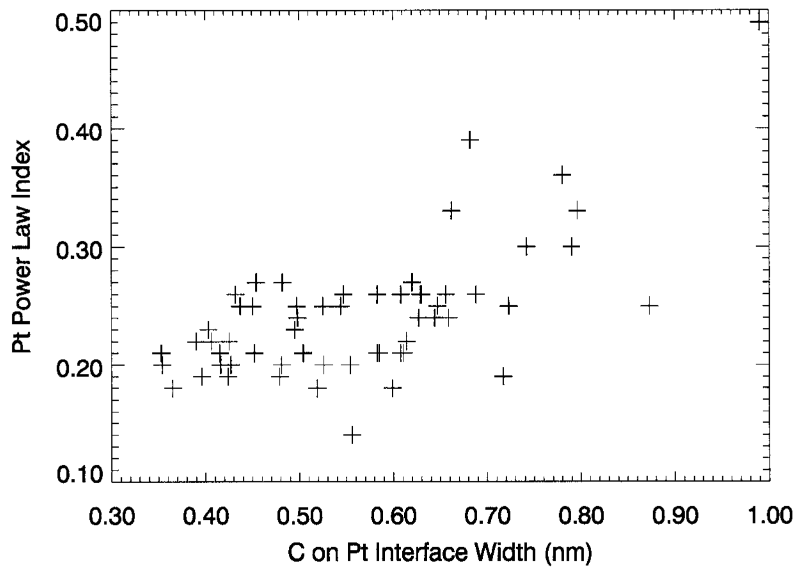

Figure 7.15: Platinum thickness power-law index vs. carbon on platinum interface width. The correlation between the power-law index and measured interface width suggests that diffuseness from energetic bombardment does contribute to the total width.

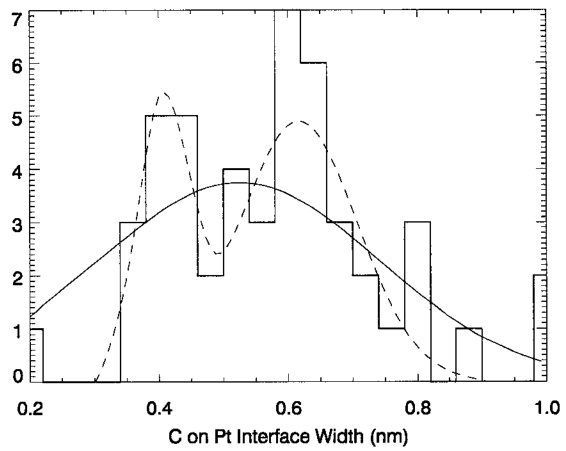

(a)

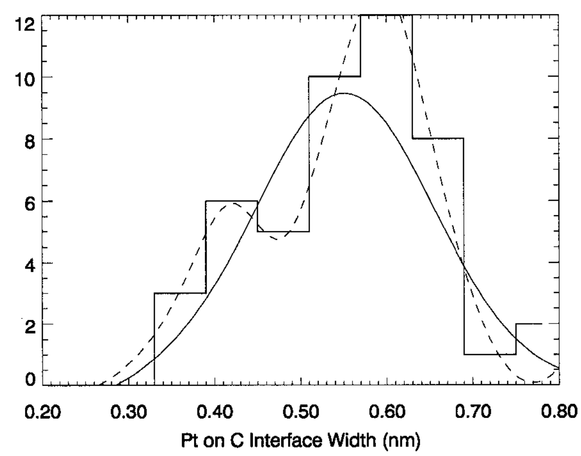

(b)

Figure 7.16: Histograms of C on Pt (a) and Pt on C (b) interface width for foils with 50–60 bilayers. Unimodal and bimodal Gaussian distributions are fitted to the histograms. Bin sizes are 0.04 nm.

systematic increase in interface width should be observable as a function of mandrel position. Mandrels in positions 1 & 4 within the deposition chamber are sputtered first, then those in positions 2 & 5. Positions 3 & 6 were not used during the time period the foil testing took place. Only multilayers with 50 or 60 bilayers are considered to eliminate any bias due to the number of bilayers. For most of the testing period, positions 2 & 5 were used for multilayers with 30 bilayers, so only 4 multilayers were measured with 50-60 bilayers that were in positions 2 or 5. No significant difference in the mean value of σ was detected for either interface type (see Table 7.4).

If there is a systematic variable that remains constant within a deposition run, but changes between deposition runs, then values of σ within a deposition run should be more highly correlated than values between two different runs. The absolute value of the difference in $\sigma_{\mathrm{C/Pt}}$ or $\sigma_{\mathrm{Pt/C}}$ can be used as an indicator of the correlation of interface width between two foils. Seven pairs of foils with multilayers deposited in the same deposition run were compared to 13 pairs of multilayers deposited in two different runs on the same day. The mean difference and standard deviation of this absolute difference is summarized in Table 7.5. The KS probability that the difference in $\sigma_{\mathrm{C/Pt}}$ comes from the same parent population is 23%. The same KS test for the difference in $\sigma_{\mathrm{Pt/C}}$ showed no such possible correlation with a 65% of being derived from the same parent population. If it is true that the differences only in $\sigma_{\mathrm{C/Pt}}$ are lower for two

Interface	Position	Mean Width (nm)	Std. Dev. (nm)	KS Probability
C on Pt	1 and 4	0.58	0.17	
	2 and 5	0.52	0.77	0.69
Pt on C	1 and 4	0.55	0.12	
	2 and 5	0.55	0.96	0.90

Table 7.4: Statistical summary of the interface width at different mandrel positions within the deposition chamber. Only multilayers with 50 or 60 bilayers are considered in these samples– a total of 44 foils for positions 1 & 4 and 4 foils for positions 2 & 5. The KS probability is the probability that the samples of the two positions come from the same parent population.

multilayers deposited within the same run, then it is possible that a hidden systematic variable is affecting the amount of energetic bombardment that is taking place within a deposition run. Physical parameters that could affect the amount of energetic bombardment include the argon gas pressure and the platinum target power.

The mandrel used as a substrate during the deposition process might affect the roughness of the multilayer. Mandrels which are rough will lead to layer interfaces which are also rough. Each mandrel of a particular diameter was given a unique number for tracking purposes. Fig. 7.17 shows the measured interface width as a function of mandrel number for four different mandrel diameters (in mm). If the mandrel roughness is a unique indicator of how rough the interface will be, then there should be a high correlation between the values of σ for two multilayers deposited onto the same mandrel number. No such strong correlation is seen, however it is possible that the diffuseness of the layer interfaces is weakening a strong correlation between σ and mandrel number if one is present.

The fact that both roughness and diffuseness seem to contribute to the interface width may be a significant reason that only very weak correlations at best are found between interface width and parameters such as mandrel position, deposition run, and mandrel number. It is quite possible that there is a combination of physical parameters which determines the interface width. A more robust calibration of the multilayer deposition chamber in its mass-production

Interface	Comparison	Mean Difference (nm)	Std. Dev. (nm)	KS Probability
C on Pt	same	0.10	0.12	
	different	0.21	0.18	0.23
Pt on C	same	0.13	0.12	
	different	0.15	0.12	0.65

Table 7.5: Statistical summary of the difference in interface width between two multilayers deposited in the same deposition run and in two different deposition runs on the same day. Eight pairs of foils are in the same-run sample and 14 pairs of foils are in the different-run sample. A small mean difference indicates that the width is highly correlated to a single variable that changes from one deposition run to the next.

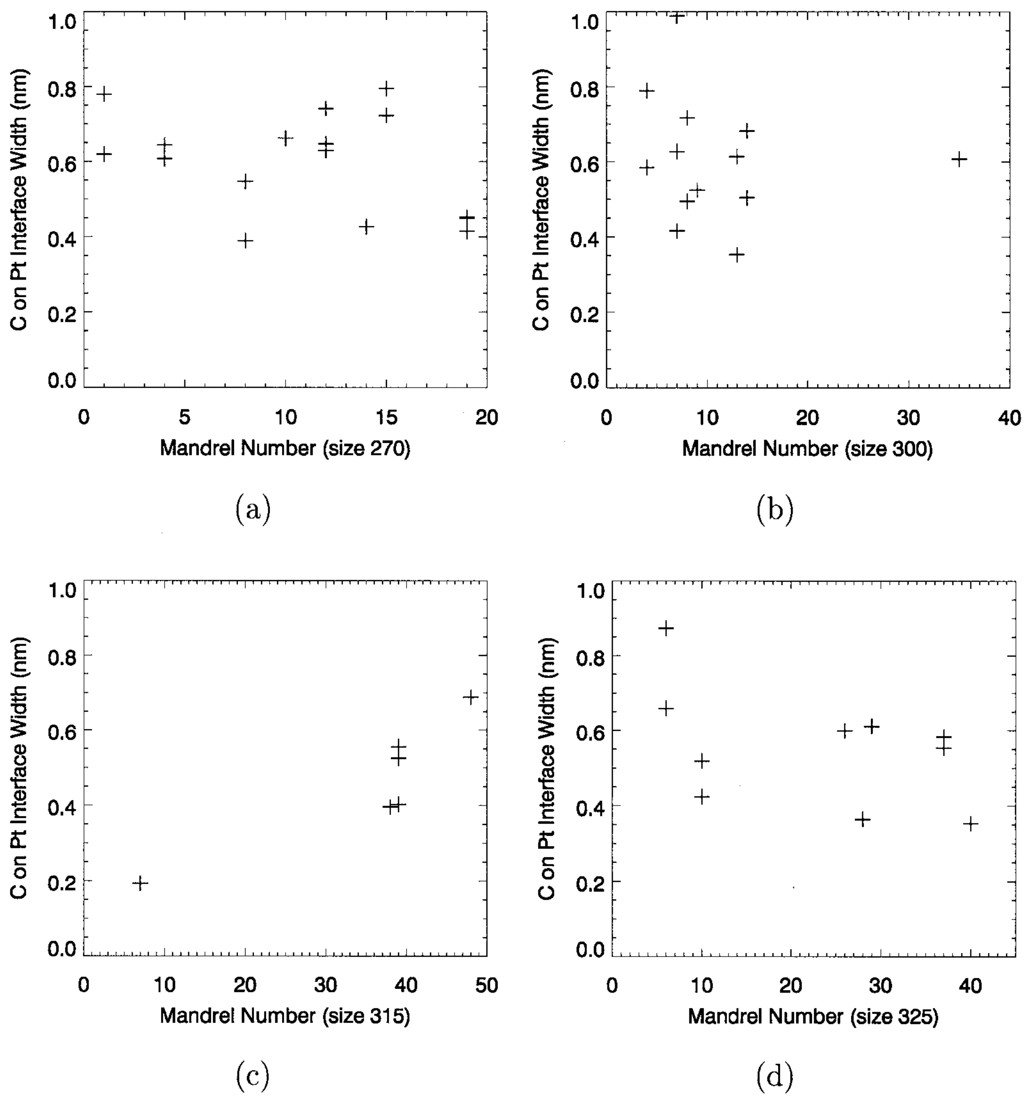

Figure 7.17: Interface width vs. mandrel number for four different mandrel diameters: 270 mm (a), 300 mm (b), 315 mm (c), and 325 mm (d). If the mandrel roughness is a strong contributor to the interface width, then widths of two multilayers deposited onto the same mandrel will be highly correlated. This is doesn't appear to be the case, therefore mandrel roughness is not a strong indicator of interface width.

mode, *i.e.* multiple depositions within a deposition run, will be necessary to produce reliable thicknesses and better interface quality necessary for the next generation of hard x-ray mirrors designed for energies as high as 100 keV.

Chapter 8

Mirror Performance

8.1 Performance Measurement

The effective area and image quality of x-ray mirrors is typically quantified by placing the mirror in a long beamline of nearly-parallel x rays which simulate a point source at an infinite distance. The InFOCμS mirror, however, was not measured this way because the beamline at Goddard Space Flight Center could not accommodate an 8-m focal length mirror. A novel technique consisting of a raster scan of the mirror with a pencil beam was used instead which measures the reflectivity of a small representative sample of the mirror.

The x-ray pencil-beam source used for these measurements is shown in Fig. 8.1. The pencil beam is moved by two large translation stages, each with 60 cm travel and 10 μm resolution. The stages move the source in orthogonal directions. Mounted directly onto the translation stages are two precision tilt stages with $0.1'$ resolution, mounted orthogonally, which control the pitch and yaw of the pencil beam. The x rays are generated by an Oxford 5011 x-ray tube with a tungsten anode which produces a spot size of 105×130 μm. The x rays from the source are collimated by a 70 cm tube and a tungsten pinhole, 100 μm in diameter and 3 mm thick, placed at the opposite end of the collimation tube. The x-ray source produces tungsten L lines at 8.4–10 keV and a hard x-ray bremsstrahlung continuum. A nickel filter 0.135 mm thick was placed immediately behind the collimation pinhole to eliminate the tungsten lines, which produce significant dead time in the detector. The measurements were all completed with the mirror and the flight CZT detector mounted on the telescope in a horizontal position.

The x-ray tube source was operated at a voltage of 50 kV in order to produce a bremsstrahlung spectrum at energies up to 50 keV. All measurements were done at 760 Torr (1 atm) pressure, which results in a fractional attenuation of photons ranging from 0.47 at 20 keV to 0.19 at 40 keV. At a distance of 8.5 m, the photon count rate at 20–50 keV was 4000 photons s^{-1}. A raster scan consisted of moving the pencil beam horizontally across the mirror at a scan rate of 1 or 2 cm s^{-1}. The beam was then moved a vertical distance of 2 mm, and another horizontal scan was done in the opposite direction. This process was repeated until an entire quadrant or mirror was scanned. In a typical raster scan

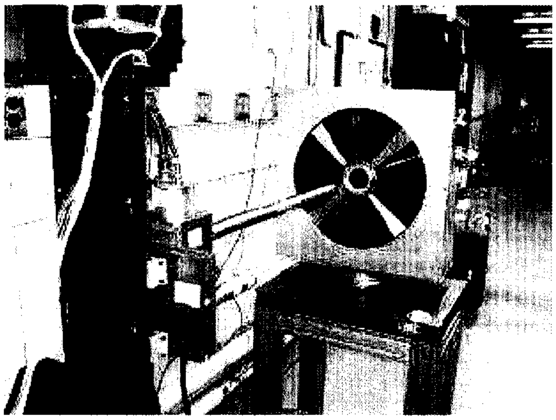

(a)

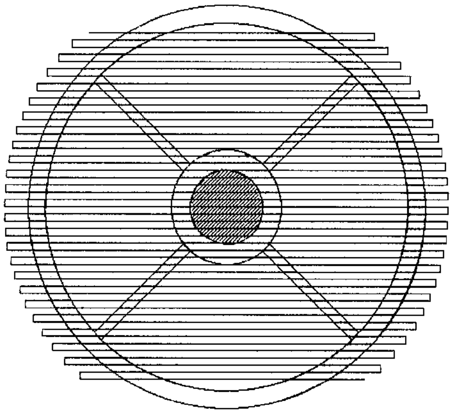

(b)

Figure 8.1: The x-ray pencil-beam source (a) consists of an x-ray source mounted on two translation stages and a tube with a tungsten pinhole at the opposite end which collimates the beam to a divergence of $1'$. The beam scans horizontally across the face of the mirror, steps down, then scans in the opposite direction (b).

of the complete mirror, about 10^5 photons were collected sampling about 5% of the geometric area of the entire mirror.

An important step in using the raster-scan system is aligning the beam with the optical axis of the mirror. The procedure begins with a course alignment by placing a collimating pinhole at the center of the mirror and adjusting the beam to pass through this pinhole and hit the center of the detector. This alignment is refined by scanning the beam along a radius close to the middle of a vertical quadrant, *i.e.* a quadrant in the 12- or 6-o'clock position. The scan could not be done exactly at the center of the quadrant due to the presence of an alignment bar at that position. The pitch was adjusted to maximize the throughput of the beam through the quadrant. This procedure was repeated with a horizontal quadrant to adjust the yaw for maximum throughput. This procedure works because vignetting by adjacent foils is the dominant reason the throughput is reduced when the source is in an off-axis position.

There are three systematic effects that must be accounted for in the raster scan setup in order to determine the mirror performance when viewing a point source at an infinite distance. The first of these effects is the divergence of the raster-scan beam. The divergence is controlled by the collimator pinhole and the spot size of the x-ray source. This produces a beam divergence of $1'$, which is comparable to the expected half-power diameter of the mirror. The image produced by the raster scan will be a convolution of point images over the off-axis angles sampled by the beam. The divergence in the beam also reduces the measured on-axis effective area by 2% at 40 keV (4% at 20 keV) by sampling off-axis angles which have reduced effective area due to vignetting. Such a difference is not expected in off-axis measurements because the mean angle sampled by the beam is nearly the angle at the center of the beam.

The second systematic effect is a smooth change in the pitch or yaw of the collimated beam as the x-ray source travels along the stage. Over the 40 cm diameter of the mirror, the change in pitch/yaw is about $\pm 0.33'$ and varies in a linear fashion between these limits. This change in pitch simulates a point source at a distance of 2 km rather than at an infinite distance.

Finally, detector effects must also be accounted for— namely the comparatively large pixel size of the flight CZT detector, which is $54''$. This is comparable to the image spot size produced by the mirror, complicating any measurement of mirror performance. The efficiency of most pixels was uniform to within a few percent. Pixels which had significantly poorer efficiency were masked as bad. These masked pixels were generally at the edge of the detector. To avoid poor pixels away from the detector edges, the on-axis focus of the mirror was not positioned at the center of the detector.

The image quality of the mirror was determined by comparisons with simulations from Monte-Carlo ray-trace program. This program generates rays from a point source at a given distance and traces their path through the mirror.

At each mirror surface, transmission and reflection coefficients are calculated to determine the probability for reflection. If the ray is reflected, a random scattering angle from an empirical distribution of scattering angles set by the user is added to the angle of specular reflection. Reflection off the untreated backs of foils are ignored because the foil backs are relatively rough and have a low reflection probability at hard x-ray energies. The ideal ray trace simulations account for the beam and detector effects above by setting the source distance at 2 km for all simulations. Focal plane images from the simulations are generated at resolution 5 times better than the pixel size of the detector (2.1 mm). The ray-trace simulation is convolved with a Gaussian with a FWHM of $1.0'$ to simulate the divergence of the pencil beam. The convolved image is then shifted to the center of the actual image and rebinned at the pixel size of the detector.

8.2 Effective Area

8.2.1 On Axis

The small size of the pencil beam relative to the mirror precludes a scan of the entire mirror. It is necessary to keep the beam size small to minimize its divergence. By knowing the vertical distance p between scans and the velocity of the scan v, the effective area of the mirror can be estimated as $A_{\text{eff}} = N_{\text{refl}} vp/I_{\text{inc}}$, where I_{inc} is the count rate of the incident beam and N_{refl} is the reflected total number of photons in the scan. This estimate of the effective area assumes that the ratio of effective area to geometric area is constant within the vertical distance of $\pm p/2$.

The measured on-axis effective area of the mirror is shown in Fig. 8.2, with three different predictions of the effective area. Two of these predictions are a sum of the geometric area of each foil projected along the x-ray axis times the multilayer reflectivity squared (due to two reflections through the mirror) at two different interface widths. Increasing the interface width of the multilayers from 0.4 to 0.5 nm decreases the effective area by approximately 10%. This large difference in predicted effective area would seem to indicate that the systematic change in interface width as a function of top platinum thickness shown in Fig. 7.13 needs to be taken into account. However, an effective area prediction with a linear change in interface width as a function of top platinum thickness differs from the prediction with an interface width of 0.5 nm by at most 5%. Therefore, using a constant interface width model for effective area predictions is valid.

A third prediction of the effective area shown in Fig. 8.2 is based on a ray-trace simulation of the mirror. This simulation adds a random scattering angle chosen from an empirically determined distribution to the specular reflection angle of each mirror surface. The distribution chosen in this case is a double-Gaussian distribution based on simulations of the *Astro-E* mirror image quality. Using the same distribution of scattering angles is valid if the scatter is

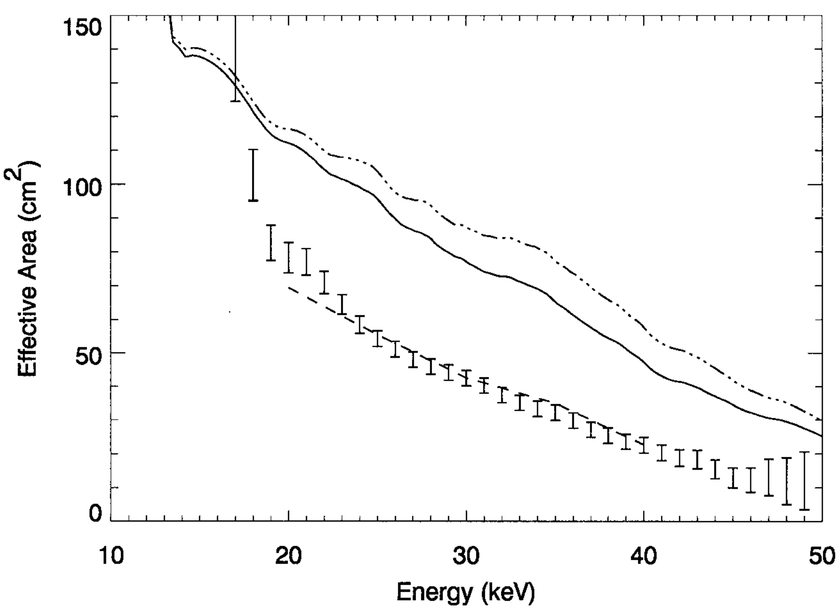

Figure 8.2: Measured on-axis effective area of the InFOCμS mirror. The measured effective area is compared to three predictions. Two predictions are based on the reflectivity and geometric area of each foil with multilayer interface widths of 0.4 nm (dot-dashed) and 0.5 nm (solid). The third prediction (dashed) is based on ray-trace simulations of the mirror assuming a distribution of scattering angles empirically determined in the *Astro-E* mirror and an interface width of 0.5 nm.

primarily from macroscopic figure errors and foil distortions rather than from interface roughness, because the InFOCμS mirror utilizes the same mirror housing, alignment bar design, and foils as *Astro-E.* A ray-trace prediction assuming an interface width of 0.5 nm matches the measured effective area very well.

The measured deficiency in effective area, defined as the fractional difference between measured effective area and the predicted effective area using the sum technique, is typically independent of energy if the scatter is due to figure errors. The reduction in the measured effective area of the *Astro-E* telescope was approximately 25–30% and energy independent over almost a decade of energy.[141] However, Fig. 8.3 shows that this is not the case for the InFOCμS mirror. This does not necessarily rule out figure error as the origin of photon scattering in this particular case. The reflectivity of the mirror at a particular energy is a function of radius— inner foils efficiently reflect photons within the entire bandpass of the mirror while outer foils only reflect the low-energy of the bandpass. The innermost foils are also closer together than the outermost foils in order to prevent stray light from directly traveling through the mirror to the focal plane. Any figure errors which induce scattering into the backs of adjacent foils will preferentially reduce the number of high-energy photons reaching the detector which will manifest itself as an energy dependence in the reduced effective area. Additionally, integrating the nonspecular reflectivity of the sample foil in Fig. 7.12 results in a total reflectivity of a few percent of the specular reflectivity. Therefore the energy-dependent reduction in effective area is most likely due to figure errors rather than interface roughness.

8.2.2 Off Axis

The effective area of the InFOCμS mirror drops as the source is moved off axis due to vignetting by neighboring foils. The reduction in effective area off axis in the azimuth direction can be seen in Fig. 8.4. The field of view of the telescope, defined as the FWHM of the effective area as a function of off-axis angle, is virtually energy independent and is very close to the predicted value of $10'$. The FWHM was derived from a both spline interpolation between the data points and a Gaussian fit. In the elevation direction, there was no measurement at $-6'$, so the field of view in this case is defined as twice the HWHM in the interpolation case. Table 8.1 shows that the spline interpolation systematically gives lower fields of view than the Gaussian fit. Neither fit is an ideal method to determine the field of view of the telescope. the curvature of the spline interpolation, and hence the FWHM, is weighted by points measured nowhere near the half-maximum level. The Gaussian distribution is a poor fit to the data and there is no physical reason for the off-axis effective area to follow a Gaussian distribution. The spline interpolation numbers are favored because the effects of

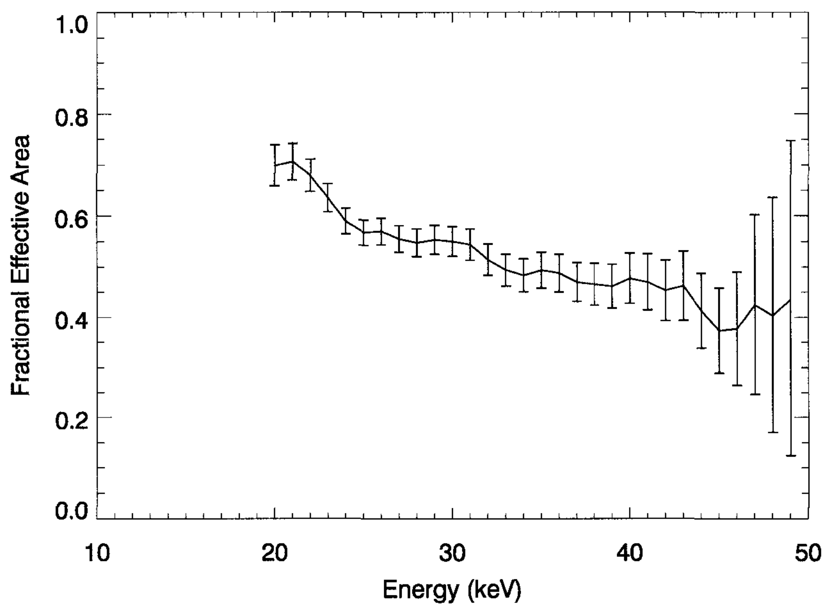

Figure 8.3: Fractional effective area of the InFOCμS mirror. The ordinate axis is the ratio of the measured effective area to the predicted effective area using the sum technique.

curvature are minimized by the measurements which are close to the half-maximum level.

The lack of a large energy dependence in the field of view confirms that vignetting is the dominant source of reduction in effective area despite the fact that the reflectivity of the multilayers will also change as a function of incidence angle. While an individual foil has a reflectivity curve with many reflectivity peaks, the sum of all of these foils smoothes out the reflectivity of the total mirror resulting in a smooth function of energy. When going to off-axis angles, the reflectivity curves of individual foils will change, causing each to be efficient at reflecting other energies. However, the sum of all these foils, again, smoothes out the reflectivity curve which makes it relatively independent of off-axis angle. The quantity that changes going off-axis is not the reflectivity of the mirror, rather it is the amount of geometric area of the mirror not vignetted by neighboring foils.

8.3 Image Quality

A measured on-axis image obtained from the raster scan is shown in Fig. 8.5. Pixel-to-pixel changes in quantum efficiency were small and therefore are not corrected in the image. The 2 keV energy resolution of the detector permits studying changes in the image as a function of energy. Images below 22 keV, however, tend to be unreliable due to an energy threshold used to reduce noise

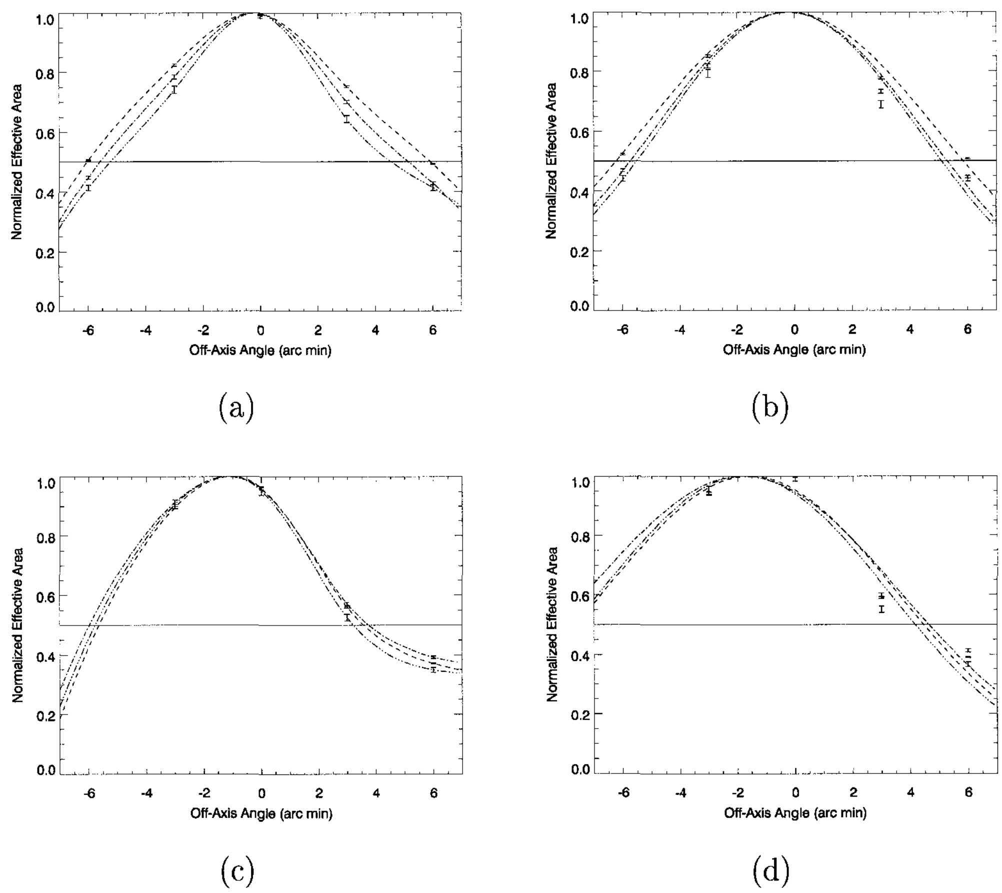

Figure 8.4: Normalized off-axis effective area of the InFOCμS mirror in the azimuth (a,b) and elevation (c,d) directions plotted with a spline interpolation (a,c) and a Gaussian fit (b,d). The lines are the normalized effective area measured at 20 keV (dashed), 30 keV (dot-dashed) and 40 keV (triple dot-dashed). The data were taken during an x-ray axis alignment process, therefore the angles of the abscissa are not centered on the true on-axis position.

events which vary from pixel to pixel. The threshold set point is 18 keV, however individual pixels can have thresholds has high as 22 keV. The centroid of the image does not vary by more than 0.2 pixels over the 24–40 keV energy range.

The intrinsic image quality of the mirror is not straightforward to determine from the raster scan image due to the divergence of the pencil beam and the large size of the detector pixels relative to the size of the image. To account for these effects in determining the image quality, a ray-trace image simulation is convolved by a Gaussian beam of $1'$ to simulate the pencil beam divergence, then rebinned to the pixel size of the InFOCμS detector. The encircled energy fraction (EEF) is used as a quantitative measurement of the image quality, defined as the fraction of energy within a given radius. The measured EEF of the mirror at selected energies is shown in Fig. 8.6 with several EEFs from ray-trace simulations, each performed with a different intrinsic mirror half-power diameter (HPD) before systematic effects of the raster scan are accounted for. Matching the measured EEF to one of these simulations gives an estimate of the true HPD of the mirror. Estimates of the HPD based on these fits are shown in Table 8.2, resulting in a mirror HPD of $1.9' \pm 0.5'$ independent of energy. The error in this measurement is due predominantly to the large pixel size of the detector. This measurement is consistent with a single-quadrant measurement performed at Nagoya University.[209]

Energy (keV)	Azimuthal FOV (arc min)		Elevation FOV (arc min)	
	Spline	Gaussian	Spline	Gaussian
20	12.6	12.0	9.0	12.1
30	10.5	11.0	10.4	12.9
40	9.3	10.6	8.6	11.8

Table 8.1: Table of the measured field of view of the InFOCμS mirror based on spline interpolations and Gaussian fits to the measured data in Fig. 8.4. The azimuth field of view is defined as the FWHM of the effective area at -6$'$–+6$'$. The elevation field of view in the interpolation case is defined as twice the HWHM of the effective area at -3$'$–+6$'$.

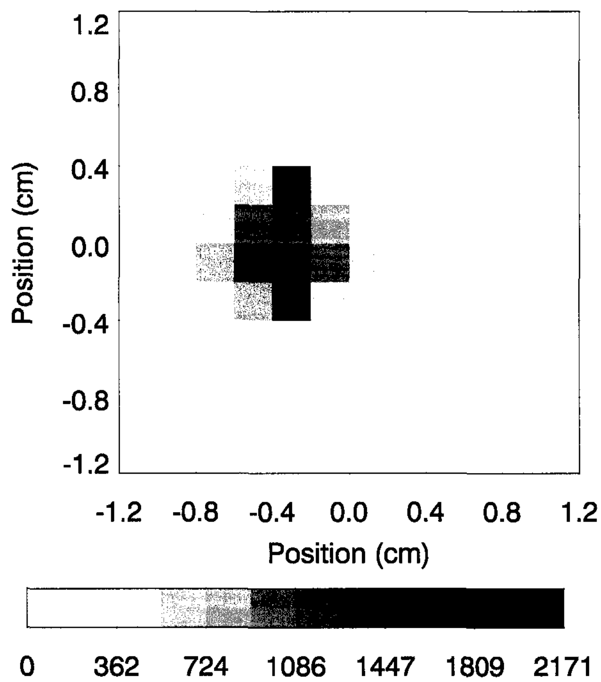

Figure 8.5: On-axis calibration image of the InFOCμS mirror obtained from a raster scan. The image is composed of photons between 20–40 keV.

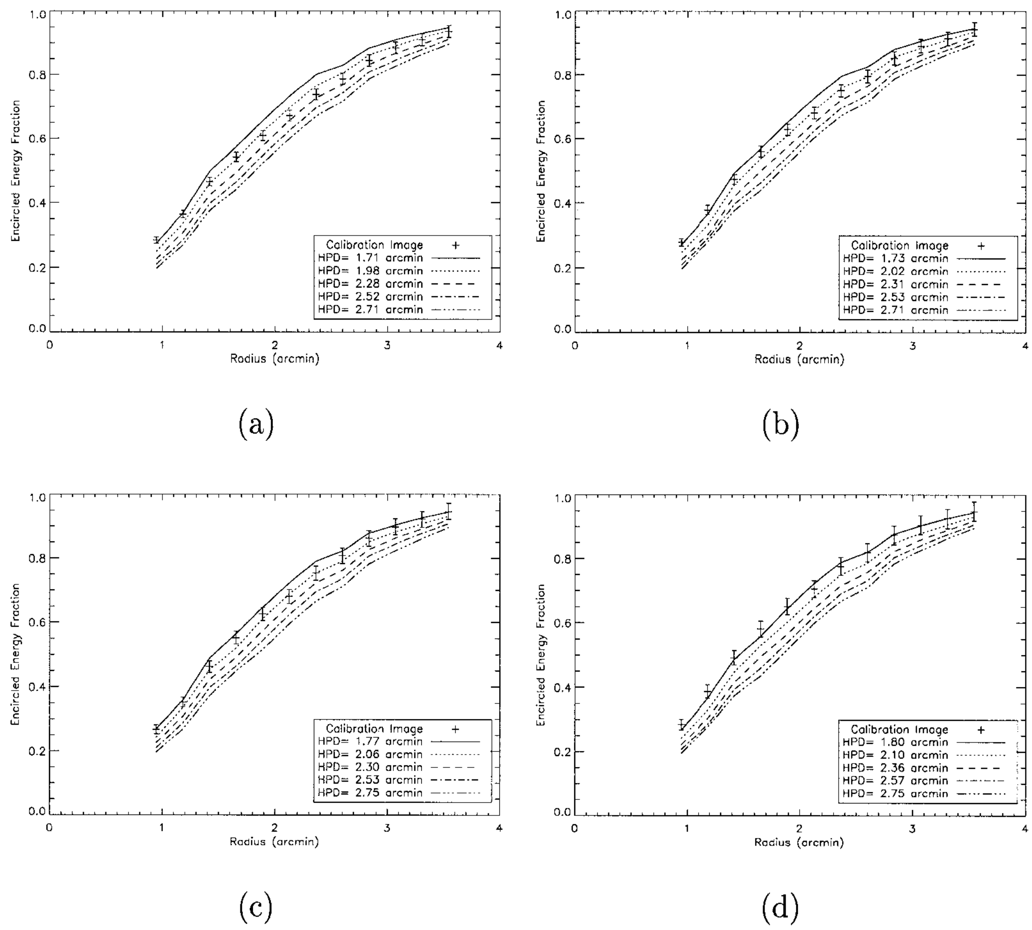

Figure 8.6: The encircled energy fraction (EEF) of the InFOCμS telescope at 24 (a), 28 (b), 32 (c), and 36 keV (d). The lines in each plot are EEFs of ray-trace simulations each with a different assumed mirror EEF. Divergence of the pencil beam and the pixel size increase the size of the observed half-power diameter (HPD) over the inherent HPD of the mirror.

The image quality of the mirror is limited by scattering due to figure errors introduced during the replication process and by stresses induced by foil edges which do not fit properly into the alignment bar grooves. Scattering from interface roughness of the multilayer stack only scatters a few percent of the photons away from the specular peak and therefore plays a minor role in the overall image. These figure errors are simulated in the ray trace programs by adding an offset angle to the specular angle. The distribution of scattering angles is modeled as a double-Gaussian distribution shown in Fig. 8.7. The change in HPD as a function of energy is most likely an indicator that outer foils, reflecting only the lower energies, suffer more from figure errors than inner foils. The outer foils, which are larger in radius of curvature, are more susceptible to strains along the axial direction caused by stresses from a poor fit within the alignment bars.

Scans of the individual quadrants reveal that the centers of the quadrant images are not at the same position as the center of full mirror image. Each quadrant image center, shown in Fig. 8.8, is offset in a direction opposite its position on the full mirror, suggesting that the detector was at a distance greater than the focal length of the quadrants. The offsets in position are as high as one arc minute from the full mirror image center. This offset could be a bias in the centroid fitting technique because the quadrant images are not symmetric, so a fit with a routine which assumes a symmetric spread could bias the centroid position. The focal point of each quadrant was also determined by a second

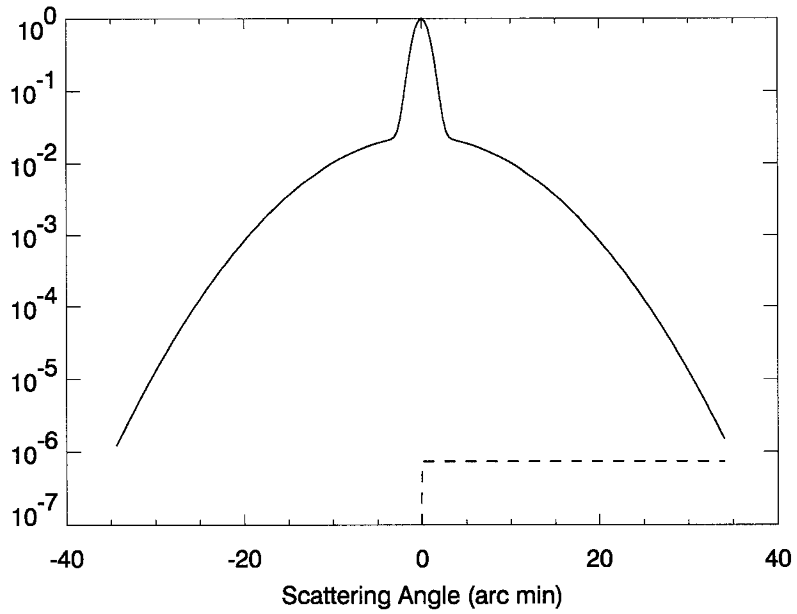

Figure 8.7: The distribution of scattering angles added to the angle of specular reflection off foils in ray-trace simulations. The largest contribution (solid) is a double-Gaussian distribution empirically determined from *Astro-E* image measurements— most likely from figure errors. Interface roughness (dashed) accounts for only a small fraction of the total number of photons.

method based on weighing the counts in bins surrounding the peak of the image. Some differences in quadrant focus position can be seen between the two methods, but both methods show that two of the quadrants have a significantly different focal point than the full mirror.

The difference in quadrant focus positions could be due either to a translation of the quadrants or a deviation of the focal length of each quadrant. Either of these errors will result in a spread in the full mirror image of up to one arc minute between quadrant images and should be visible in images taken with the raster scan. To demonstrate this, a ray-trace simulation of the sum of four quadrants— each with its own focal position— is compared to an image of a full mirror with all quadrants focused on the same position in Fig. 8.9. The separation in quadrant focal points contributes $0.5'$ to the HPD of the full mirror.

The ground calibration image of the full telescope on the ground may not necessarily predict the image quality of the telescope in flight. The InFOCμS mirror housing is a close replica of the *Astro-E* mirror housing, which was designed to operate in a zero-g environment. The InFOCμS telescope operates in a one-g environment, therefore, shifts in elevation of the telescope may shift the position of the quadrants within the housing. Images taken with the InFOCμS telescope in flight will be done at elevations greater than 45°, therefore it is possible that the image will change, perhaps significantly, from the calibration images conducted with the telescope in a horizontal position. No tests were

Energy (keV)	Mirror and Detector HPD (arc min)	Mirror HPD (arc min)
24	3.2	2.0
28	2.8	1.9
32	2.8	1.9
36	2.8	1.9

Table 8.2: The half-power diameter (HPD) of the InFOCμS mirror at different energies. The mirror HPD is defined as the HPD which, when convolved with pencil-beam systematic effects, gives the best fit to the combined mirror and detector HPD. An error of $\pm 0.5'$ is present in all HPD determinations due predominantly to pixel binning effects.

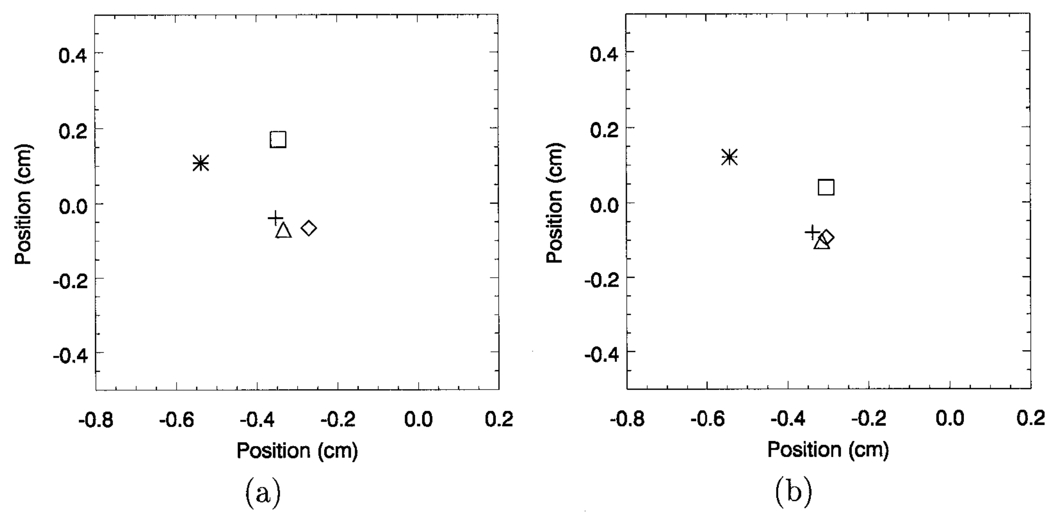

Figure 8.8: Focal point positions of the individual InFOCμS quadrants and the complete mirror. The positions were determined by two methods - a fit to a double-Gaussian distribution (a) and a method which weighs the counts in pixels surrounding the peak of the image (b). In each plot is the focal point of the full mirror image (plus), the right quadrant (asterisk), the left quadrant (diamond), the top quadrant (triangle), and the bottom quadrant (square).

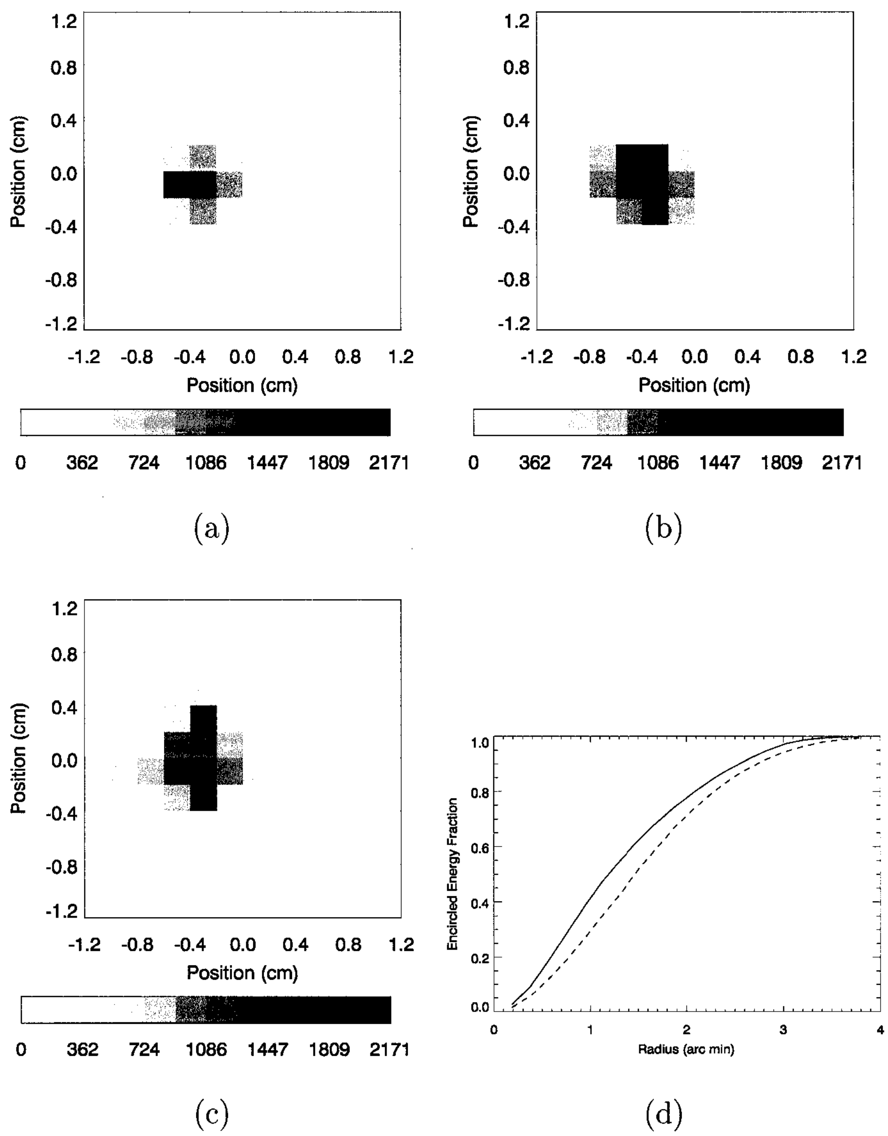

Figure 8.9: Comparison of single-focus (a) and multiple-focus (b) image simulations to the raster scan image (c) of the InFOCμS mirror. The multiple-focus image places the focus of each quadrant at the position given in Fig. 8.8. A comparison of the EEFs of the single-focus (solid) and multiple-focus (dashed) simulations is shown in (d).

available to test the shifting of quadrants, or individual foils within quadrants, as a function of elevation.

8.4 Scattering Effects

The fact that the scattering distribution that best fits the observed images is a double-Gaussian is significant for a few reasons. First, the double-Gaussian suggests there are not one, but two sources of scatter at work within the detector. The narrow Gaussian, with a FWHM of $2'$, controls the observed EEF of the image. The wider Gaussian has a width 9 times that of the narrow Gaussian which controls the effective area because photons scattered more than $5'$ away from the specular angle miss the focal plane detector entirely.

The narrow Gaussian distribution could be caused by figure errors from two significant contributions which have been identified by Soong *et al.* (2001).[181] First, during the replication process multilayers on cylindrical mandrels are replicated onto conical mandrels. In addition, the thickness of the epoxy applied during the replication process varies enough that it introduces stress which changes the figure of the foil. The compressive stress of the multilayers also contributes to this figure error which changes the radius of curvature of the foil. The second contribution derives from the first contribution— deviations in the figure of the foils necessitates a great amount of freedom for the foils to move within the alignment bar grooves. However, the grooves allow too much freedom of movement which causes a blur in the image because the foils are no longer confocal. To correct this, the alignment bars are moved to alternately confine the fronts and backs of foils to reduce freedom of movement within the grooves. The foil figure is unique for each foil, therefore stresses are placed on the foils by the alignment bars which force each foil into a different shape.

The wide Gaussian in the empirical scattering distribution shown in Fig. 8.7 scatters 20% of the total number of photons completely off the focal plane detector. This wide Gaussian distribution only represents photons which are scattered so they do not reach the focal plane of the detector. If this scattering distribution were realistic, it would result in a detectable background outside of the core of the image. A predicted background level of a few percent of the image peak should be detectable within the calibration image, however no such background level is present. Therefore, none of these photons hit the detector and are either all scattered completely away from the detector, but reach the focal plane or never reach the focal plane.

One possible source of the wide-angle scattering is imperfect foil edges, which are used as the standard for aligning the foils and holding them in place. The edges, which can deviate from straightness by as much as 50 μm, could cause some foils to be stressed more than other foils. The scattering angle necessary to cause photons to hit adjacent foils is at least $4'$ and probably close to $5'$ assuming

20% of the photons of a uniformly illuminated foil hit the adjacent foil. This paradigm is consistent with the evidence that there is no detectable background surrounding the core of the image because it preferentially scatters photons close to the edges of the foils which are most likely to be scattered into adjacent foils. The source of this scattering is likely to be stresses on the foils if this paradigm is correct. A linear misalignment of approximately 133 μm would be necessary to create this large a scattering angle. Such a large misalignment is precluded by the 20 μm of free movement available to the foils within the alignment bar grooves.

Chapter 9

In-Flight Mirror Verification

9.1 Target Selection

While it is useful to perform ground calibrations of the mirror and detector in order to gauge their performance, the most useful test to verify how the telescope will behave in flight is to calibrate the telescope with an observation of a well-known celestial x-ray point source. The telescope operates in a different atmospheric temperature and pressure environment than at ground level which may influence any number of variables that affect the whole telescope performance. The influence of gravity on the mirror performance as the truss is raised in elevation also was unknown before flight. Therefore, a bright x-ray point source which would be above 45° elevation (to minimize atmospheric attenuation of x rays) during the date and time of the flight was observed to verify the mirror performance.

Cygnus X-1 (Cyg X-1) is an x-ray binary system at J2000 coordinates α=19^{h}58^{m}21.7^{s} ,δ=35°12′5.78″. It is composed of a supergiant (HDE 226868) and a compact object believed to be a black hole gravitationally bound with an orbital period of 5.6 days.[210–212] Accretion from the supergiant onto the compact object produces a continuum of x rays extending above 100 keV. Cyg X-1 is a variable source in the x-ray to gamma-ray regime which appears to have two states and varies between states on the time scale of several weeks. About 90% of the time is spent is what is called the hard state, where the photon flux above 20 keV can be described by a power law ($dF_\gamma/dE \sim E^{-\Gamma}$) with an index of $\Gamma \approx 1.8$. The less frequent soft state is characterized by an index of $\Gamma \approx 2.3$. Measurements of Cyg X-1 with the *Compton Gamma Ray Observatory* show the hard state produces a variable 20–100 keV flux in the range of 0.2–0.3 cm^{-2} s^{-1}, while the soft state has a lower flux of $\approx$ 0.1 cm^{-2} s^{-1}.[213]

9.2 The InFOCμS Flight

The first flight of InFOCμS took place at the National Scientific Balloon Facility in Palestine, Texas (31°46′47″ N lat, 95°42′23″ W lon). The 1500 kg InFOCμS payload was launched with a 40 million cm^3 polyethylene balloon in order to achieve a minimum float altitude of 38.4 km above sea level. The telescope was launched at 01:10 UT on 2001 Jul 6 (2001 Jul 5 8:10 CDT). Float altitude was reached at 05:15 UT and remained there until the flight was terminated at 08:05 UT for a total float time of 3 hours and 40 minutes. Winds at float altitude were approximately 50 miles per hour from the east. The payload was recovered 15 miles north of Big Spring, Texas (32°13′ N lat, 101°33′ W lon) with minimal damage.

The residual atmosphere of 3.4 g cm^{-2} at float altitude will attenuate most of the hard x-ray flux before it reaches the telescope. This attenuation at the energies of interest to InFOCμS is predominantly due to photoabsorption. To calculate the attenuation as a function of elevation, mass attenuation coefficients of dry air calculated by Hubbell and Seltzer (1997) are adopted.[214] A plane-parallel atmosphere is assumed to derive the change of attenuation as a function of elevation. Under these assumptions, Fig. 9.2 shows that only 10–50% of the photon flux from Cyg X-1 will reach the telescope. The resulting count rate from Cyg X-1 in the hard state is 1–2 cts s^{-1} in the 20–40 keV band for an observation at an elevation of 70°.

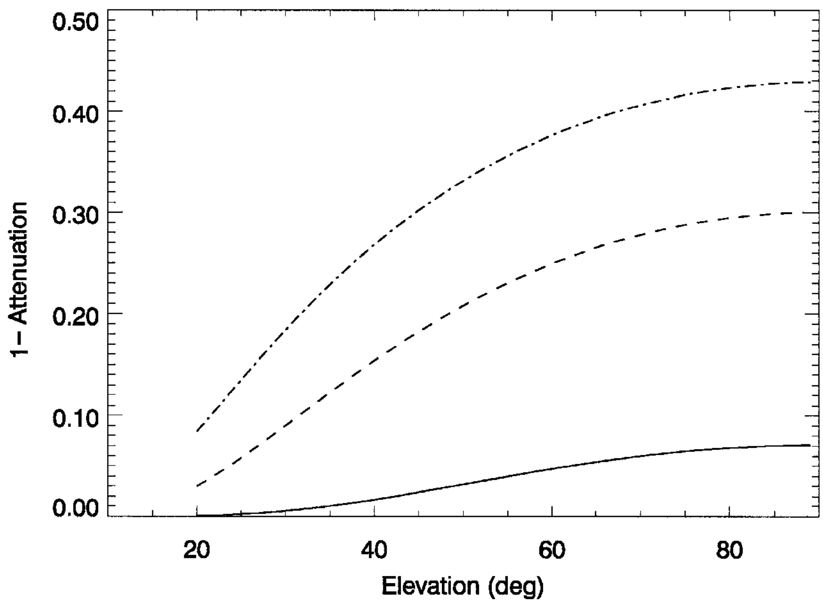

Figure 9.1: Attenuation of photons at InFOCμS float altitude as a function of target elevation. Plotted are the fraction of photons which will reach the telescope at 20 keV (solid), 30 keV (dashed), and 40 keV (dot-dashed).

9.3 Aspect Reconstruction

9.3.1 Instruments

Two instruments are vital for reconstructing the pointing position of the x-ray telescope during the observation. The three-axis gyroscopes mounted on the gondola provide rates of change of the azimuth, elevation, and cross-elevation tilt of the gondola every 80 ms. However, the gyroscopes also have drift, or an offset in the rate, which must be subtracted by fitting the integrated data to a linear trend and subtracting the linear fit. To limit the influence of endpoints in the data, the trend subtraction was iteratively performed by fitting a linear trend and subtracting it from the data. The data between the first and last zero were again fitted and another subtraction performed. This process was repeated until the linear fit slope approached zero. Because the entire gondola is rotated in azimuth while tracking a source, a quadratic function rather than linear was subtracted from the azimuth data in the first iteration. Subsequent iterations involved a linear trend fit.

The second instrument involved in the aspect reconstruction was a star camera with a field of view of $8.5° \times 5.5°$. The star camera produces images once every 12 seconds and tracks the plate position of the two brightest stars in the field every 2 seconds. The process of determining the x-ray axis position is severely complicated, however, by the fact that the star camera was necessarily pointed at an angle of 45° from the x-ray axis in order to avoid occultation by the balloon.

9.3.2 Determination of the star camera position

A complete reconstruction of the x-ray axis aspect consists of using the star camera position to determine the position of the x-ray axis every two seconds and interpolating between star camera points with the gyroscope data. The first step in aspect reconstruction is to determine the aspect of the star camera. The positions of the stars and the known pixel size of ρ_x=34.65$''$ and ρ_y=40.43$''$ in the two CCD chip directions completely determine the position of the star camera center via the following transformations:[215]

$$\begin{aligned}
\xi &= \rho_x x \cos\sigma + \rho_y y \sin\sigma + C_\xi \\
\xi &= \frac{\cos\delta\sin(\alpha-\alpha_0)}{\sin\delta_0\sin\delta + \cos\delta\cos(\alpha-\alpha_0)} \\
\eta &= -\rho_x x \sin\sigma + \rho_y y \cos\sigma + C_\eta \\
\eta &= \frac{\cos\delta_0\sin\delta - \sin\delta_0\cos\delta\cos(\alpha-\alpha_0)}{\sin\delta_0\sin\delta + \cos\delta\cos(\alpha-\alpha_0)}
\end{aligned}$$

where (α, δ) are the right ascension and declination of a star and (α_0, δ_0) are the right ascension and declination of the star camera center. The value ξ is the distance of the star from the camera center along the right ascension direction, η is the distance along the declination direction. The parameters C_ξ,C_η, and σ are free variables in the transformation from plate position (x,y) to (α, δ). The Marquardt-Levenberg χ^2 minimization technique was used to determine the best-fit values of the free parameters including the star camera center right ascension and declination.[216,217]

9.3.3 Euler angles of the x-ray to star camera transformation

The transformation between the star camera position and the x-ray axis position was determined by surveying the Euler rotation angles of the star camera in the gondola frame. If axis 1 points in the direction of the x-ray axis when in a horizontal position, axis 3 points toward zenith, and axis 2 completes the right-handed orthogonal system, then the transformation by rotation about axes 3,2,1 in that order gives Euler angles of (α,β,γ) of ($45°4'9''$, $-0°12'49''$, $0°21'4''$). However, there are two caveats that must be considered. First, these angles could not be verified through preflight pointing tests either using star targets nor using ground markers. The difference in the calculated values of each angle using multiple ground and pointing tests was as high as $6'$. Second, there is no guarantee that the x-ray axis of the telescope is perpendicular to the plane containing the inner ring of the mirror housing. Both the preflight pointing technique and the survey technique use this inner ring as a mounting surface for either a camera or a reference mirror; therefore they assume the x-ray axis is perpendicular to the inner ring plane.

9.3.4 Determination of the cross-elevation tilt

Both the celestial position of the star camera and the angle between the star camera and the x-ray axis do not uniquely determine the x-ray axis position, but rather give a locus of possible points tracing a circle on the celestial sky. There are two possible ways to determine where on this circle the correct x-ray axis position lies as shown in Fig. 9.3.4. The first method employs the cross-elevation tilt obtained by the gyroscopes to convert the sky elevation/azimuth (El,Az) frame to an instrument El,Az frame. The zenith in this instrument frame is the point on the sky where the telescope would point if it were given a command to point at an elevation of 90°. Once in this instrument frame, spherical trigonometry can be used to derive the x-ray axis position in the instrument frame, then a reverse transformation is performed to find the El,Az position of the x-ray axis in the sky frame.

The second method also employs a cross-elevation tilt derived from an angle between two vectors on the star camera: a vector pointing to the zenith and a vector pointing to the north celestial pole. Spherical trigonometry can be used to relate the rotation angle θ to the cross-elevation tilt. However, an analytical expression of this relation would be very difficult to derive. A

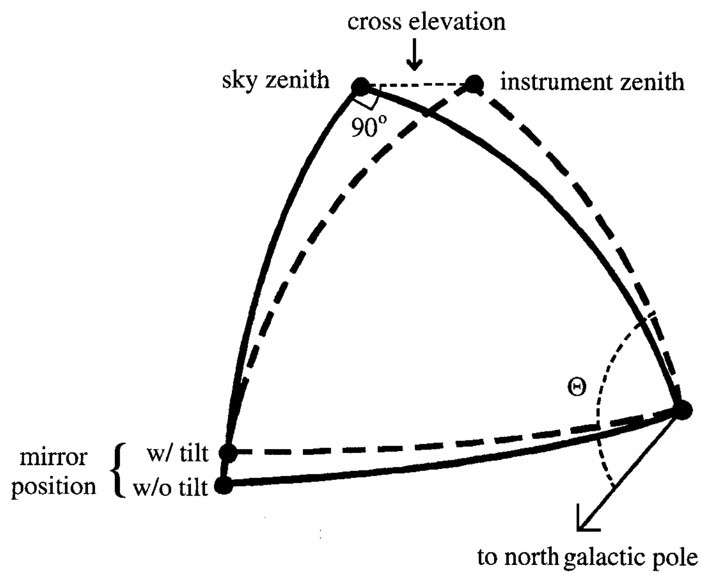

Figure 9.2: Diagram demonstrating the two methods used to determine the x-ray axis celestial position from the star camera position. The star camera position alone gives a possible locus of x-ray axis positions traced by a circle. The position of the x-ray axis on this locus can be determined either by using the cross-elevation tilt derived from the gyroscopes or determining the star camera rotation angle θ between a vector pointing toward the north galactic pole and a vector pointing toward the instrument zenith.

Marquart-Levenburg fit was employed to find the best value of the cross-elevation tilt which gave the rotation angle θ.

There are good reasons that both methods should be employed. First, the gyroscope data does have an integration constant. While in principle this integration constant should be zero when the gondola is properly balanced, in reality it could be nonzero because high-altitude winds could give the balloon load train a non-zero tilt which could vary with time as wind speed increases or decreases. Therefore, the cross-elevation tilt derived from the star camera rotation can serve as a useful check for the gyroscope integration constant. The star-camera determination of the cross-elevation tilt, because it is determined by a fitting method, could also be off because the global minimum is in a flat well. Fig. 9.3.4 shows the difference in cross-elevation tilt derived between the two methods for a short time period. There is a definite linear trend between the two with a slight offset and spurious points far away from the trend due to a poor convergence to the global minimum. This trend was added to the gyroscope data and used as the cross-elevation tilt in determining the x-ray axis position.

9.3.5 Image reconstruction

Once the cross-elevation tilt is determined, the star camera position can be converted to a mirror x-ray axis position using spherical trigonometry. The

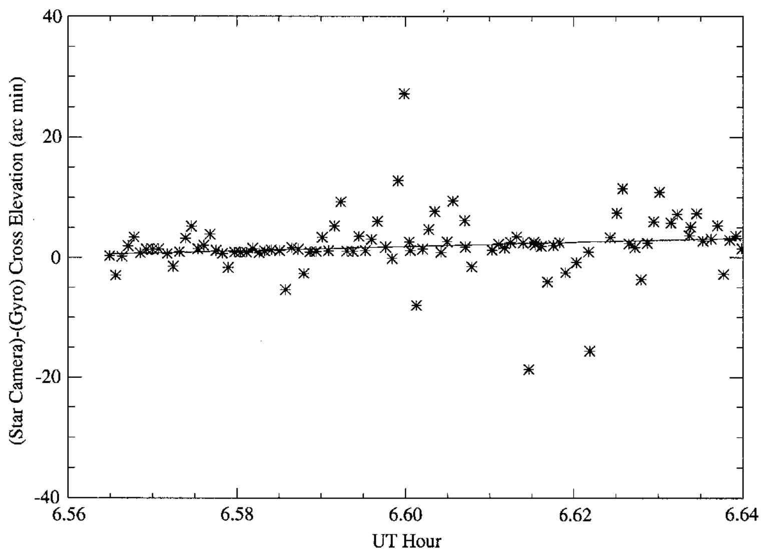

Figure 9.3: Difference in cross-elevation tilt between the gyroscope measurement and the value derived by the star camera rotation method. Spurious points far from the trend are due to a poor convergence of the star camera rotation fitting method.

movement of the x-ray mirror between star camera points was interpolated by the movements in the gondola measured by the gyroscope.

The roll angle of the x-ray mirror must also be known in order to derive the position of each detector pixel on the sky. To accomplish this, a reference point $+10'$ above the mirror in declination is selected and its position is determined in a mirror-centered (X,Y) frame. Once determined, the sky position of every pixel in the detector can be determined. Events which register on a detector pixel at a given time are then assigned to a pixel-sized (RA,dec) bin. This gives a raw image which is smoothed by a convolution with a Gaussian which has the same encircled energy fraction as that of the combined mirror and detector image measured before flight. The image was exposure-corrected by creating an exposure map— summing over time the exposure each (RA,dec) bin received in the time between gyroscope data points. Between points, each detector pixel is exposed for 0.80 ms times the vignetting function, *i.e.* the off-axis effective area divided by the on-axis effective area. This exposure map was also smoothed with the same Gaussian as the image and was divided into the raw image to obtain an exposure-corrected image.

9.4 Pointing Performance

No real-time image of Cyg X-1 was obtained during the flight despite the expected count rate of 1–2 cts s^{-1} on the detector. Unexpectedly large stochastic motions of the entire balloon-gondola system were induced by air turbulence which limited the pointing accuracy of the telescope. The pointing accuracy degraded significantly by turning off the pointing system as shown by three-axis gyroscope data obtained during the flight in Fig. 9.4. Therefore the stochastic motions are attributed to air turbulence rather than the elevation or azimuthal tracking motion of the gondola. The effects of this large stochastic motion can be best seen by plotting the calculated positions of the x-ray mirror pointing position over the time period of 5.0–7.0 UT. Very little time was spent within one field of view of the position of Cyg X-1, as shown in Fig. 9.4. It is not surprising that aspect reconstruction was necessary to obtain an image even of a bright x-ray source such as Cyg X-1.

Several factors contributed to the inability to either dampen or correct for the severe pointing errors incurred during flight. The unexpected magnitude of the stochastic motions precluded any attempts to correct for them using the available pointing correction mechanisms in the elevation and azimuth directions. There was no mechanism to correct or dampen tilt in the cross-elevation direction. In addition, although the star camera was used for fine pointing during

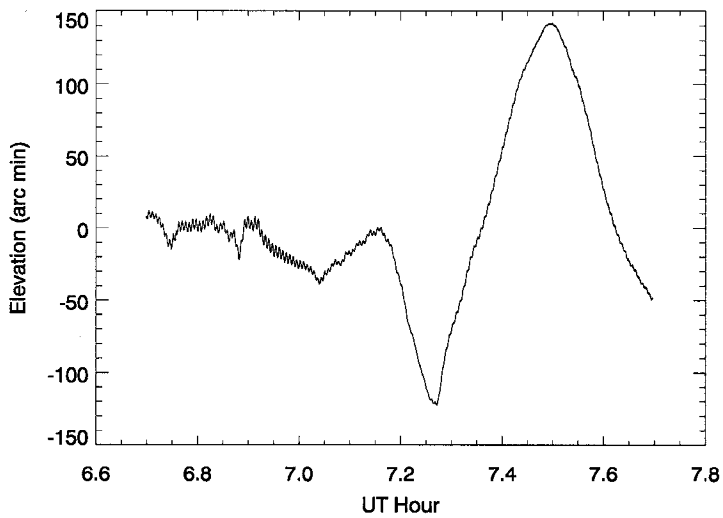

(a)

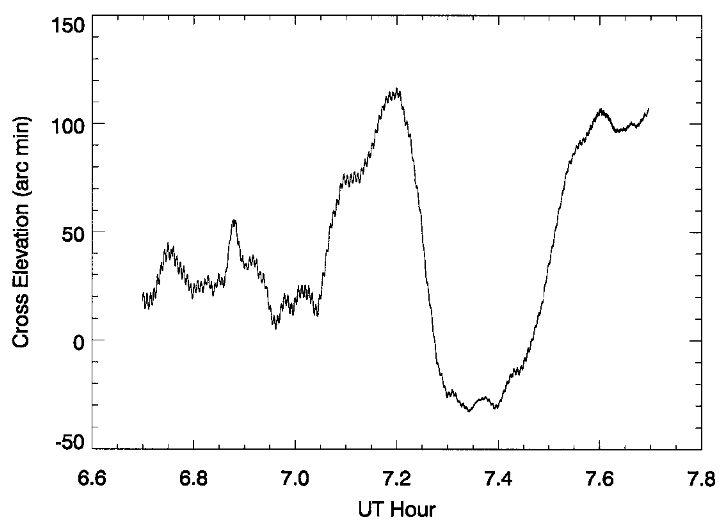

(b)

Figure 9.4: Motion of the InFOCμS gondola in the elevation and cross-elevation directions. The pointing accuracy is much larger than the field of view of the telescope ($10'$). The long-term motion in both directions becomes significantly worse when pointing is turned off at 7.0 UT— indicating the source of the pointing errors is driven by air turbulence rather than pointing corrections.

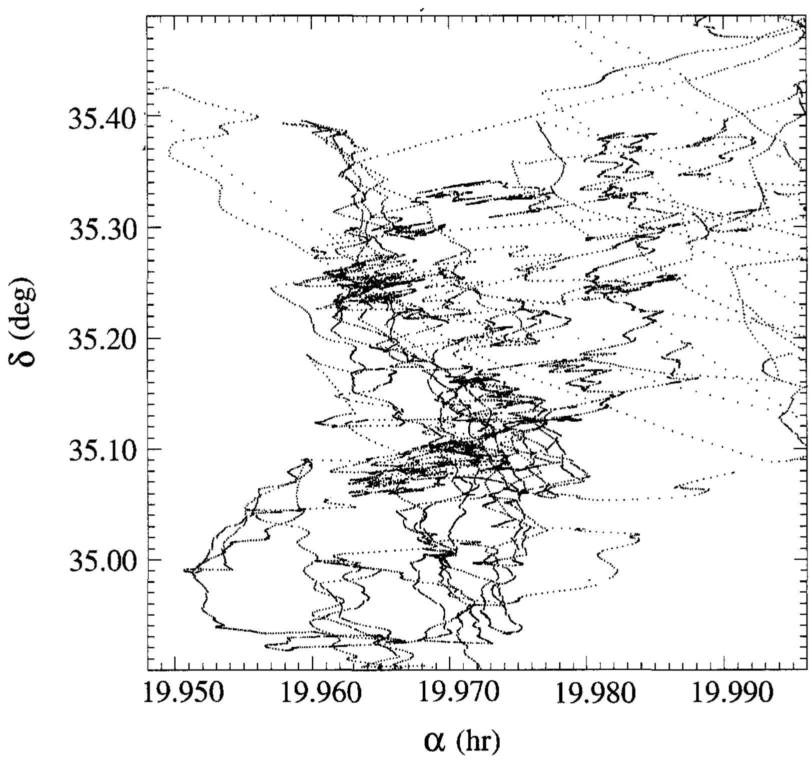

Figure 9.5: Scatter plot of the calculated x-ray axis position of InFOCμS at 5–7 UT. Only a small fraction of the time was spent within one field of view of the Cyg X-1 position, which is at the center of the plot.

flight, the fine pointing updates were done manually rather than incorporating the star camera in the control feedback loop. The manual calculation of the x-ray axis position based on the star camera was complicated by the fact that the star camera was necessarily placed 45° off the x-ray axis. These problems will be fixed on future flights by incorporating active balance weights to keep the gondola level and eliminate elevation and cross-elevation tilt. The star camera will also be incorporated into the control feedback loop for automatic fine-pointing control. There are also plans to improve the alignment procedure between the star camera and the x-ray mirror axis.

9.5 The Image of Cygnus X-1

Despite the severe pointing problems during the flight, Cyg X-1 was detected during the flight. A light curve of events between 5–7 UT reveals several spikes in the light curve once events occurring in good pixels and between 20–50 keV are selected shown in Fig. 9.6. In addition, a spectrum of all events occurring in good pixels, shown in Fig. 9.7, has most events at energies between 20–50 keV, bounded by atmospheric absorption on the low end and low mirror effective area on the high end.

The image resulting from the aspect reconstruction technique for all good events between 20–50 keV occurring between 5–7 UT is shown in Fig. 9.8(a).

The peak count rate in the image is 1.0 cts s^{-1} which is within the range of expected count rates for the Cyg X-1 hard state. The EEF of this image in Fig. 9.8(b) gives a HPD of $7.2' \pm 1.0'$— significantly poorer than the preflight calibration image.

Evidence that the degradation in the image is due to an imperfect aspect solution can be found by taking an image of events that occurred between 6.56–6.64 UT corresponding to the largest peak in the light curve of Fig. 9.6. The image, shown in Fig. 9.9, is a significant improvement in image shape and in the EEF, with a HPD reduced to $4.0' \pm 0.5'$— larger than the calibration image HPD of $2.9' \pm 0.5'$.

The improvement in the image during this brief time is due to a short burst of events that occurred over a very short period in time at the same position; and thus the image quality is determined by the smoothing function used during the image processing rather than an improvement in the aspect solution. Fig. 9.10 demonstrates that the events occurred over several different occasions when the telescope was within one field of view of Cyg X-1. It is likely that the improvement in the aspect solution can be attributed to the fact that the cross-elevation tilt was constant and nearly zero during this time as shown in Fig. 9.11. For this reason, both the real-time and post-flight aspect solutions for the x-ray mirror are relatively straightforward to derive from the star camera position during this brief period of time.

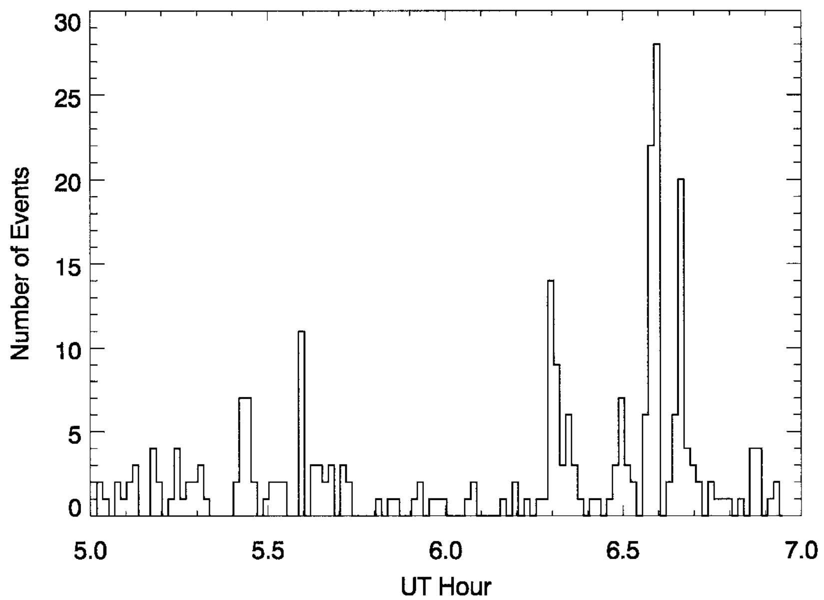

Figure 9.6: Light curve of events detected between 5–7 UT. The events selected are between 20–50 keV occurring in good pixels on the detector.

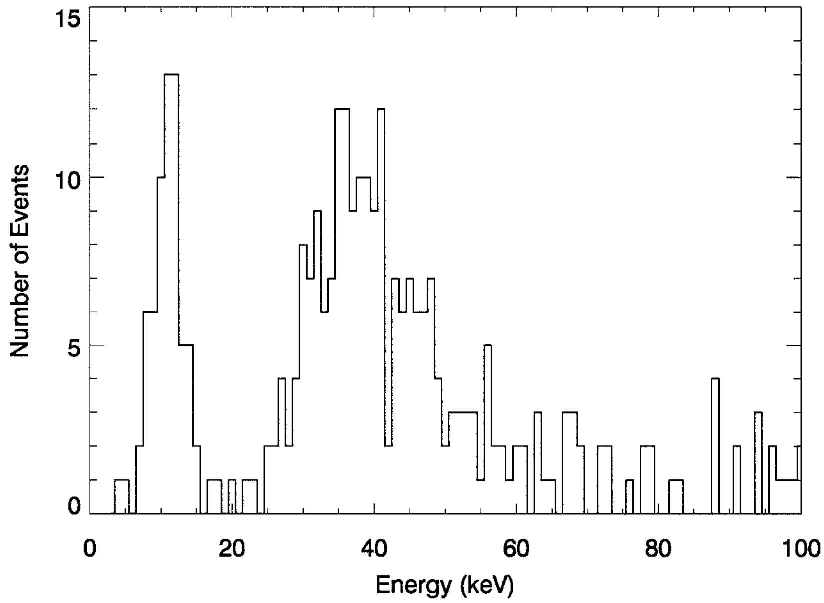

Figure 9.7: Spectrum of events on good pixels during peaks in the count rate observed in Fig. 9.6. The majority of events occur between 20–50 keV, bounded by atmospheric absorption and low mirror effective area, respectively. The events below 20 keV are noise events occurring in pixels with a low noise threshold.

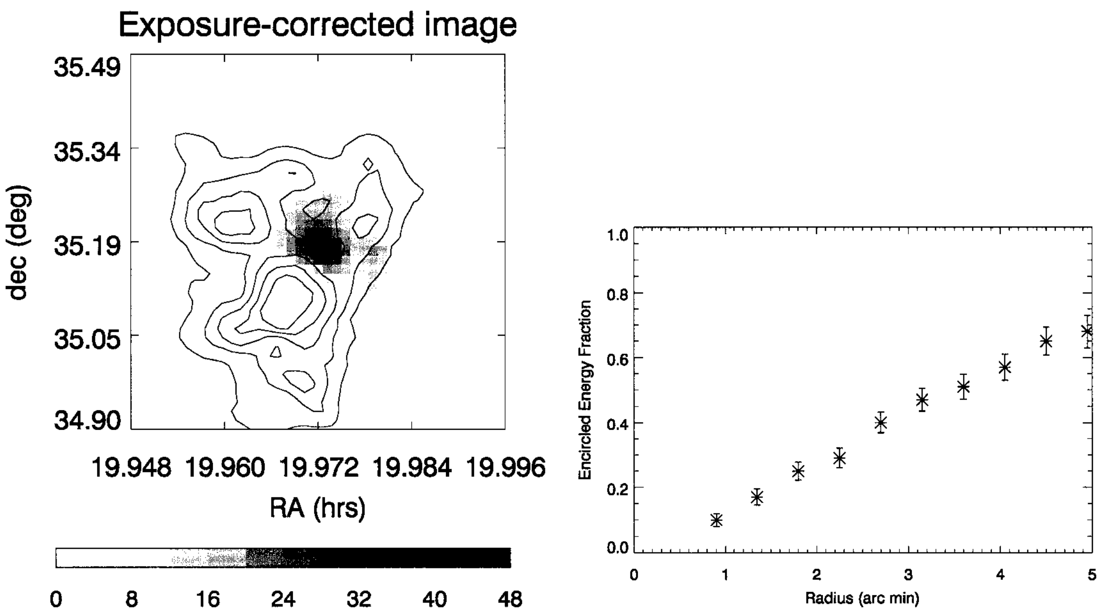

(a) (b)

Figure 9.8: Image (a) and encircled energy fraction (b) of detected 20–50 keV events on good pixels between 5–7 UT during the InFOCμS flight. The contours in the image correspond to an exposure map of the image in increments of 10 s. The gray scale in the image corresponds to the number of counts observed if all pixels are exposed for 48 s. The EEF in (b) does not asymptotically approach unity because noise events occurred while the telescope was pointed away from Cyg X-1.

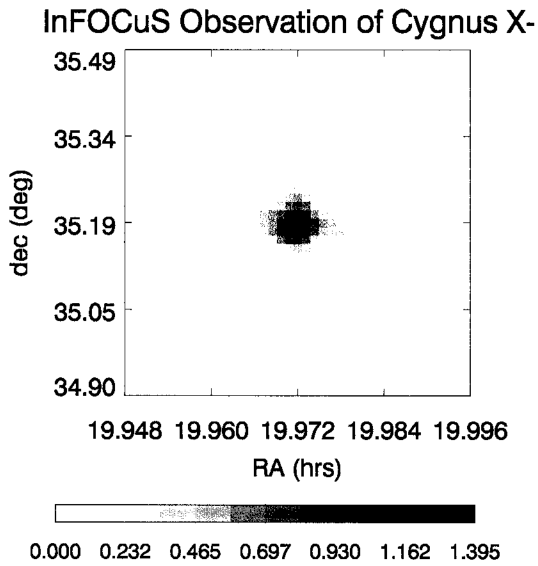

(a)

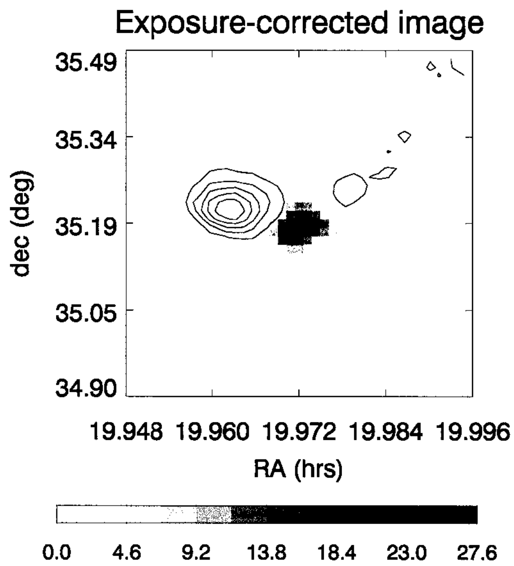

(b)

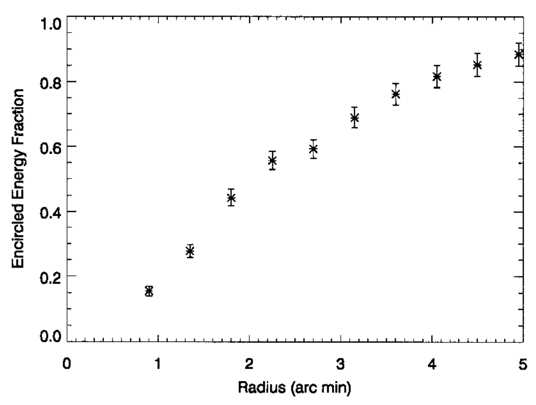

(c)

Figure 9.9: Images without (a) and with (b) exposure time corrections, and the encircled energy function (c) of detected 20–50 keV events on good pixels between 6.56–6.64 UT during the InFOCμS flight. The contours in the image correspond to an exposure map of the image in increments of 5.0 s. The gray scale in the exposure-corrected image corresponds to the number of counts that would be observed in an exposure time of 27.92 s.

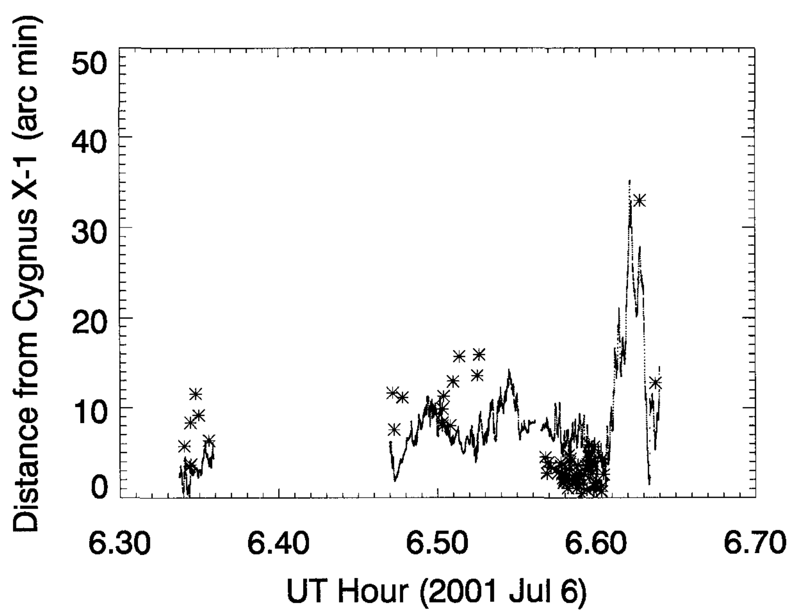

Figure 9.10: X-ray mirror distance from Cyg X-1 between 6.56–6.64 UT (solid line). The asterisks are times and distances from the true Cyg X-1 position when an event between 20–50 keV in a good pixel occurred on the detector.

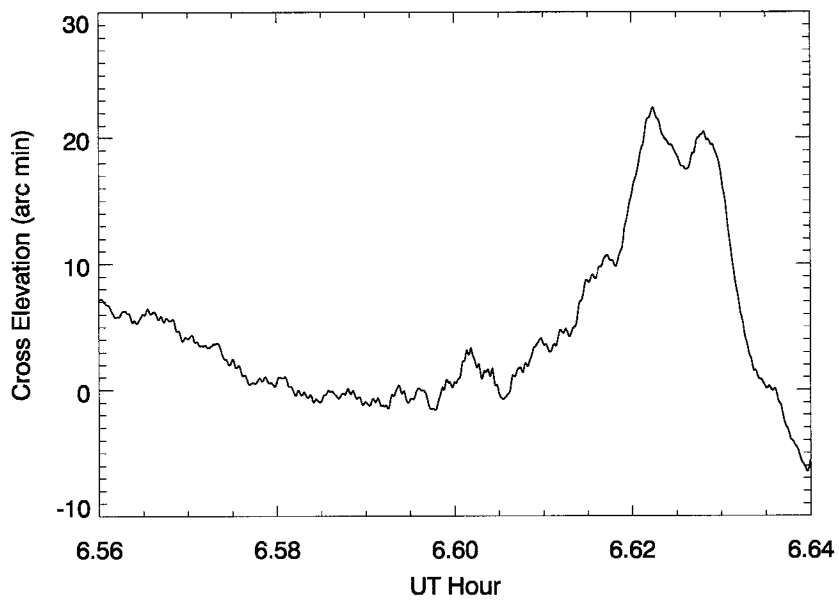

Figure 9.11: Cross elevation measured by the gyroscope between 6.56–6.64 UT. The flat, nearly zero cross-elevation tilt during which most of the events occur indicates that the source of aspect solution errors is the transformation between star camera position and x-ray mirror position which depends heavily on cross-elevation tilt.

BIBLIOGRAPHY

1. V.F. Hess, Phys. Z. **13**, 1084 (1912)

2. R. Millikan, Phys. Rev. **27**, 320 (2002)

3. S.H. Neddermeyer and C.D. Anderson, Rev. Mod. Phys. **11**, 191 (1939)

4. A.D. Erlykin and A.W. Wolfendale, Adv. Space Res. **27**, 803 (2001)

5. P.L. Biermann and G. Sigl, "Introduction to Cosmic Rays" in *Physics and Astrophysics of Ultra-High-Energy Cosmic Rays* Lecture Notes in Physics **576**, M. Lemoine and G. Sigl, eds., (Springer-Verlag, Berlin), 2001

6. W.I. Axford, Astrophys. J. Suppl. Ser. **90**, 937 (1994)

7. J.A. Simpson, "Introduction to the galactic cosmic radiation" in *Composition and origin of cosmic rays; proceedings of the Advanced Study Institute, Erice, Italy, June 20-30, 1982*, M.M. Shapiro, ed., (D. Reidel Publishing, Dordrect), 1 (1983)

8. M.E. Wiedenbeck, "Introduction to the galactic cosmic radiation" in *Composition and origin of cosmic rays; proceedings of the Advanced Study Institute, Erice, Italy, June 20-30, 1982*, M.M. Shapiro, ed., (D. Reidel Publishing, Dordrect), 65 (1983)

9. G. Gloeckler and J.R. Jokipii, Astrophys. J. **148**, L41 (1967)

10. S.E. Woosley, R.E. Taam, and T.A. Weaver, Astrophys. J. **301**, 601 (1986)

11. S.E. Woosley, A. Heger, and T.A. Weaver, Rev. Mod. Phys. **74**, 1015 (2002)

12. L. Woltjer, Ann. Rev. Astron. Astrophys. **10**, 129 (1972)

13. L.I. Sedov, *Similarity and Dimensional Methods in Mechanics*, (Academic Publishing, New York) (1969)

14. E. Fermi, Phys. Rev. **75**, 1169 (1949)

15. R. Blandford and D. Eichler, Phys. Rep. **154**, 1 (1987)

16. G.F. Krymskii, Sov. Phys. - Doklady, **22**, 327 (1977)

17. W.I. Axford, E. Leer, and G. Skadron, "The acceleration of cosmic rays by shock waves" in *International Cosmic Ray Conference, 15th, Plovdiv, Bulgaria, August 13-26, 1977, Conference Papers* **11**, 132 (1978)

18. A.R. Bell, Mon. Not. R. Astr. Soc. **182**, 147 (1978)

19. R.D. Blandford and J.P. Ostriker, Astrophys. J. **221**, L29 (1978)

20. P.O. Lagage and C.J. Cesarsky, Astron. Astrophys. **125**, 249 (1983)

21. J.R. Jokipii, Astrophys. J. **313**, 842 (1987)

22. T.K. Gaisser, *Comsic Rays and Particle Physics* (Cambridge University Press, New York), 155 (1990)

23. A. Decourchelle, D.C. Ellison, and J. Ballet, Astrophys. J. **543**, L57 (2000)

24. J.M. Blondin and D.C. Ellison, Astrophys. J. **560**, 244 (2001)

25. M.A. Malkov and L. O'C. Drury, Rep. Prog. Phys. **64**, 429 (2001)

26. D. Eichler, Astrophys. J. **247**, 1089 (1981)

27. J.T. Gosling, J.R. Asbridge, S.J. Bame, W.C. Feldman, R.D. Zwicki, G. Paschmann, N. Sckopke, and R.J. Hynds, J. Geophys. Res. **86**, 547 (1981)

28. D.C. Ellison, E. Möbius, and G. Paschmann, Astrophys. J. **352**, 376 (1990)

29. U.D.J. Gieseler, T.W. Jones, and H. Kang, Astron. Astrophys. **364**, 911 (2000)

30. D.C. Ellison and S.P. Reynolds, Astrophys. J. **382**, 242 (1991)

31. S.P. Reynolds, Astrophys. J. **493**, 375 (1998)

32. M.G. Baring, D.C. Ellison, S.P. Reynolds, I.A. Grenier, and P. Goret, Astrophys. J. **513**, 311 (1999)

33. G.B. Rybicki and A.P. Lightman, *Radiative Processes in Astrophysics*, (Wiley & Sons, New York) (1979)

34. A.G. Pacholczyk, *Radio Astrophysics*, (W.H. Freeman, San Francisco) (1970)

35. J.D. Jackson, *Classical Electrodynamics* (Second Edition), (Wiley & Sons, New York) (1975)

36. E. Haug, Z. Naturforsch. **30a**, 1099 (1975)

37. V.N. Baier, V.S. Fadin, and V.A. Khoze, Sov. Phys. JETP **24**, 760 (1967)

38. K. Koyama, R. Petre, E.V. Gotthelf, M. Matsura, M. M. Ozaki, and S.S. Holt, Nature **378**, 255 (1995)

39. A.J.S. Hamilton, C.L. Sarazin, and A.E. Szymkowiak, Astrophys. J. **300**, 698 (1986)

40. S. Reynolds, Astrophys. J. **459**, L13 (1996)

41. T. Tanimori, Y. Hayami, S. Kamei, S.A. Dazeley, P.G. Edwards, S. Gunji, S. Hara, T. Hara, J. Holder, A. Kawachi, T. Kifune, R. Kita, T. Konishi, A. Masaike, Y. Matsubara, T. Matsuoka, Y. Mizumoto, M. Mori, M. Moria, H.

Muraishi, Y. Muraki, T. Naito, K. Nishijima, S. Oda, S. Ogio, J.R. Patterson, M.D. Robers, G.P. Rowell, K. Sakurazawa, T. Sako, Y. Sato, R. Susukita, A. Suzuki, R¿ Suzuki, T. Tamura, G.J. Thornton, S. Yanagita, T. Yoshida, and T. Yoshikoshi, Astrophys. J. **497**, L25 (1998)

42. K. Koyama, K. Kinugasa, K. Matsuzaki, M. Nishiuchi, M. Suigizaki, K. Torii, and S. Yamauchi, PASJ **49**, L7 (1997)

43. P. Slane, B.M. Gaensler, T.M. Dame, J.P. Hughes, P.P. Plucinsky and A. Green, Astrophys. J. **525**, 357 (1999)

44. H. Muraishi, T. Tanimori, S. Yanagita, T. Yoshida, M. Moriya, T. Kifune, S.A. Dazeley, P.G. Edwards, S. Gunji, S. Hara, T. Hara, A. Kawachi, H. Kubo, Y. Matsubara, Y. Mizumoto, M. Mori, Y. Muraki, T. Naito, K. Nishijima, J.R. Patterson, G.P. Rowell, T. Sako, K. Sakurazawa, R. Susukita, T. Tamura, and T. Yoshikoshi, Astron. Astrophys. **354**, 57 (2000)

45. R. Enomoto, T. Tanimori, T. Naito, T. Yoshida, S. Yanagita, M. Mori, P.G. Edwards, A. Asahara, G.V. Bicknell, S. Gunji, S. Hara, T. Hara, S. Hayashi, C. Itoh, S. Kabuki, F. Kajino, H. Katagiri,J. Kataoka, A. Kawachi, T. Kifune, H. Kubo, J. Kushida, S. Maeda, A. Maeshiro, Y. Matsubara, Y. Mizumoto, M. Moriya, H. Muraishi, Y. Muraki, T. Nakase, K. Nishijima, M. Ohishi, K. Okumura, J.R. Patterson, K. Sakurazawa, R. Suzuki, D.L. Swaby, K. Takano, T. Takano, F. Tokanai, K. Tsuchiya, H.

Tsunoo, K. Uruma, A. Watanabe, and T. Yoshikoshi, Nature **416**, 823 (2002)

46. Y.M. Butt, D.F. Torres, G.E. Romero, T.M. Dame, and J.A. Combi, Nature **418**, 499 (2002)

47. B. Aschenbach, Nature **396**, 141, 1998

48. P. Slane, J.P. Hughes, R.J. Edgar, P.P. Plucinsky, E. Miyata, H. Tsunemi, and B. Aschenbach, Astrophys. J. **548**, 814 (2001)

49. J.P. Hughes, C.E. Rakowski, and A. Decourchelle, Astrophys. J. **543**, L61 (2000)

50. J. Rho, K.K. Dyer, K.J. Borkowski, and S.P. Reynolds, Astrophys. J. **581**, 1116 (2002)

51. U. Hwang, A. Decourchelle, S.S. Holt and R. Petre, Astrophys. J. **581**, 1101 (2002)

52. G.E. Allen, J.W. Keohane, E.V. Gotthelf, R. Petre, K. Jahoda, R.E. Rotschild, R.E. Lingenfelter, W.A. Heindl, D. Marsden, D.E. Gruber, M.R. Pelling, and P.R. Blanco, Astrophys. J. **487**, L97 (1997)

53. S.P. Reynolds and J.W. Keohane, Astrophys. J. **525**, 368 (1999)

54. M. Ryle and G. Smith, Nature **162**, 462 (1948)

55. W. Baade and R. Minkowski, Astrophys. J. **119**, 206 (1954)

56. W.B. Ashworth Jr., J. Hist. Astron. **11**, 1 (1980)

57. R.A. Fesen, R.H. Becker and W.P. Blair, Astrophys. J. **313**, 378 (1987)

58. R.A. Fesen, R.H. Becker, and R. Goodrich, Astrophys. J. **329**, L89 (1988)

59. G. Garcia-Segura, N. Langer, and M.-M. Mac Low, Astron. Astrophys. **316**, 133 (1996)

60. J. Vink, J.S. Kaastra, and J.A.M. Bleeker, Astron. Astrophys. **307**, L41 (1996)

61. D.A. Green "A Catalogue of Galactic Supernova Remnants (2001 December version)", Mullard Radio Astronomy Observatory, Cavendish Laboratory, Cambridge, United Kingdom (World-Wide Web: http://www.mrao.cam.ac.uk/surveys/srns/)

62. J.E. Reed, J.J. Hester, A.C. Fabian, and P.F. Walker, Astrophys. J. **440**, 706 (1995)

63. R.A. Fesen, J.A. Morse, R.A. Chevalier, K.J. Borkowski, C.L. Gerardy, S.S. Lawrence and S. van den Bergh, Astron. J. **122**, 2644 (2001)

64. T. Dulaney and L. Rudnick, Univ. of MN, private communication

65. T.A. Lozinskaya, *Supernovae and Stellar Wind in the Interstellar Medium*, (New York, American Institute of Physics) (1992)

66. R.S. Sutherland and M.A. Dopita, Astrophys. J. **439**, 381 (1995)

67. A.P. Hurford and R.A. Fesen, Astrophys. J. **469**, 246 (1996)

68. K. Kamper and S. van den Bergh, Astrophys. J. Suppl. Ser. **32**, 351 (1976)

69. R.A. Fesen, Astrophys. J. Suppl. Series **133**, 161 (2001)

70. J.W.M. Baars, R. Genzel, I.I.K. Paulini-Toth, and A. Witzel, Astron. Astrophys. **61**, 99 (1977)

71. D.A. Green "Particle Acceleration in Galactic Supernova Remnants" in *Genesis and Propogation of Cosmic Rays*, M.M. Shapiro and J.P. Wefel, eds., (Dordrecht, Reifel), 205 (1988)

72. W.A. Dent, H.D. Aller, and E.T. Olsen, Astrophys. J. **188**, L11 (1974)

73. M. Anderson, L. Rudnick, P. Leppik, R. Perley, and R. Braun, Astrophys. J. **373**, 146 (1991)

74. M.C. Anderson and L. Rudnick, Astrophys. J. **456**, 234 (1996)

75. M. Wright, J. Dickel, B. Koralesky, and L. Rudnick, Astrophys. J. **518**, 284 (1999)

76. M.C. Anderson, J.W. Keohane, and L. Rudnick, Astrophys. J. **441**, 300 (1995)

77. P.O. Lagage, A. Claret, J. Ballet, F. Boulanger, C.J. Césarsky, D. Césarsky, C. Frannson, and A. Pollock, Astron. Astrophys. **315**, L273 (1996)

78. T. Douvion, P.O. Lagage, and E. Pantin, Astron. Astrophys. **369**, 583 (2001)

79. R.G. Arendt, E. Dwek, and S.H. Moseley, Astrophys. J. **521**, 234 (1999)

80. T. Douvion, P.O. Lagage, and C.J. Césarsky, Astron. Astrophys. **352**, L111 (1999)

81. B.T. Draine and H.M. Lee Astrophys. J. **285**, 89 (1984)

82. C.L. Gerardy and R.A. Fesen, Astron. J. **121**, 2781 (2001)

83. T.H. Markert, C.R. Canizares, G.W. Clark, and P.F. Winkler, Astrophys. J. **268**, 134 (1983)

84. S.S. Holt, E.V. Gotthelf, H. Tsunemi and H. Negoro, Pub. Astron. Soc. Japan **46** L151 (1994)

85. U. Hwang, A.E. Szymkowiak, R. Petre, and S.S. Holt, Astrophys. J. **560**, L175 (2001)

86. J.P. Hughes, C.E. Rakowski, D.N. Burrows, and P.O. Slane Astrophys. J. **528**, L109 (2000)

87. J.M. Laming, Astrophys. J. **546**, 1149 (2001)

88. J.M. Laming, Astrophys. J. **563**, 828 (2001)

89. J.W. Keohane, L. Rudnick, and M.C. Anderson, Astrophys. J. **466**, 309 (1996)

90. R.A. Gaume, T.L. Wilson, and K.J. Johnston, Astrophys. J. **425**, 127 (1994)

91. D. Chakrabarty, M.J. Pivovaroff, L.E. Hernquist, J.S. Heyl, and R. Narayan, Astrophys. J. **548**, 800 (2001)

92. J.R. Thorstensen, R.A. Fesen, S. van den Bergh, Astron. J. **122**, 297 (2001)

93. J.A. Esposito, S.D. Hunter, G. Kanbach, and P. Sreekumar, Astrophys. J. **461**, 820 (1996)

94. R.W. Lessard on behalf of the Whipple Collaboration, Proc. of the 26th ICRC, Salt Lake City **3**, D. Kieda, M. Salamon, and B. Dingus, eds., (Melville, NY, American Inst. Physics) 488 (2000)

95. P. Goret, C. Gouiffes, E. Nuss, and D.C. Ellison, Proc. of the 26th ICRC, Salt Lake City **3**, D. Kieda, M. Salamon, and B. Dingus, eds., (Melville, NY, American Inst. Physics) 496 (2000)

96. F. Aharonian, A. Akhperjanian, J. Barrio, K. Bernlöhr, H. Börst, H. Bojahr, O. Bolz, J. Contreras, J. Cortina, S. Denninghoff, V. Fonseca, J. Gonzalez, N. Götting, G. Heinzelmann, G. Hermann, A. Heusler, W. Hofmann, D. Horns, A. Ibarra, C. Iserlohe, I. Jung, R. Kankanyan, M. Kestel, J. Kettler, A. Kohnle, A. Konopelko, H. Kornmeyer, D. Kranich, H. Krawczynski, H. Lampeitl, M. Lopez, E. Lorenz, F. Lucarelli, N. Magnussen, O. Mang, H. Meyer, R. Mirzoyan, A. Moralejo, E. Ona, L. Padilla, M. Panter, R. Plaga, A. Plyasheshnikov, J. Prahl, G. Pöhlhofer, G. Rauterberg, A. Röhring, W. Rhode, G.P. Rowell, V. Sahakian, M. Samorski, M. Schilling, F. Schröder, M. Siems, W. Stamm, M. Tluczykont, H.J. Völk, C.A. Wiedner, and W. Wittek, Astron. Astrophys. **370**, 112 (2001)

97. M.C. Weisskopf, S.L. O'Dell, and L.P. van Speybroeck, Proc. SPIE **2805**, 2 (1996)

98. J.K. Blackburn, "FTOOLS: A FITS Data Processing and Analysis Software Package" in *Astronomical Data Analysis Software and Systems IV* A.S.P. Conf. Ser. **77**, 367 (http://heasarc.gsfc.nasa.gov/ftools/) (1995)

99. K.A. Arnaud, "XSPEC: The First Ten Years" in *Astronomical Data Analysis Software and Systems V* A.S.P. Conf. Ser. **101**, G.H. Jacoby and J. Barnes, eds., 17 (1996)

100. E.V. Gotthelf, B. Koralesky, L. Rudnick, T.W. Jones, U. Hwang, and R. Petre, Astrophys. J. **552**, L39 (2001)

101. K.J. Borkowski, W.J. Lyerly, and S.P. Reynolds, Astrophys. J. 548, 820 (2001)

102. A.J.S. Hamilton, C.L. Sarazin, and R.A. Chevalier, Astrophys. J. Suppl. Ser. 51, 115 (1983)

103. R. Morrison and D. McCammon, Astrophys. J. **270**, 119 (1983)

104. R. Petre, "X-Ray Spectroscopy of Supernova Remnants" in *Supernova and Supernova Remnants* I.A.U. Colloquium **145**, R. McCray and Z. Wang, eds., (Cambridge University Press, Cambridge), 357 (1996)

105. S. Amari, P. Hoppe, E. Zinner, and R.S. Lewis, Astrophys. J. **394**, L43 (1992)

106. S.H. Moseley, E. Dwek, W. Glaccum, J.R. Graham, and R.F. Loewenstein, Nature **340**, 697 (1989)

107. R.A. Chevalier, J.M. Blondin, and R.T. Emmering, Astrophys. J. **392**, 118 (1992)

108. B.-I. Jun and T.W. Jones, Astrophys. J. **511**, 744 (1999)

109. B.-I. Jun, T.W. Jones, and M.L. Norman, Astrophys. J. **468**, L59 (1996)

110. K.J. Borkowski, C.L. Sarazin, and J.M. Blondin, Astrophys. J. **429**, 710 (1994)

111. J. Vink and J.M. Laming, Astrophys. J. **584**, 758 (2003)

112. D.B. Melrose, "Kinetic Plasma Physics" in *Plasma Astrophysics*, Saas-Fee Advance Course 24 Lecture Notes, A.O. Benz and T.J.-L. Courvoisier, eds., (Springer-Verlag, Berlin), 189 (1994) eitem V.L. Ginzburg and S.I. Syrovatskii, Ann. Rev. Astron. Astrophys. **3**, 297 (1965)

113. J.A.M. Bleeker, R. Willingale, K. van der Heyden, K. Dennerl, J.S. Kaastra, B. Aschenbach, and J. Vink, Astron. Astrophys. **365**, L225 (2001)

114. R. Willinagle, J.A.M. Bleeker, K.J. van der Heyden and J.S. Kaastra, Astron. Astrophys. **398**, 1021 (2003)

115. W.C. Röntgen, "Über eine neue Art von Strahlen," in *Sitzungsberichte Med. Phys. Gesellschaft Würzburg*, 137 (1895)

116. W. Friedrich, P. Knipping, and M. von Laue, "Interferenzersheinungen bei Röntgenstrahlen," in *Sitzb. Math.-Phys. Bayr. Akad. Wiss.* , 303 (1912)

117. A.H. Compton, Philos. Mag. **45**, 1121 (1923)

118. F. Jentzsch, Phys. Z. **30**, 268 (1929)

119. P. Kirkpatrick and A.V. Baez, Bull. Am. Phys. Soc. **23**, 10 (1948)

120. H. Wolter, Ann. Phys. (6th ser., Leipzig) **10**, 94 (1952); *ibid.* **10**, 286 (1952)

121. B. Aschenbach, Rep. Prog. Phys. **48**, 579 (1985)

122. T.R. Burnright, Phys. Rev. **76**, 165 (1949)

123. T.A. Chubb, H. Friedman, R.W. Kreplin, R.L. Blake, and A.E. Unzicker, Mém. R. Sci. Liège 5th ser. **IV**, 235 (1961)

124. R. Giacconi and B. Rossi, J. Geophys. Res. **65**, 773 (1960)

125. R. Giacconi, H. Gursky, F. Paolini, and B. Rossi, Phys. Rev. Lett. **9**, 439 (1962)

126. R. Giacconi, W.P. Reidy, T. Zehnpfenning, J.C. Lindsay, and W.S. Muney, Astrophys. J. **142**, 1274 (1965)

127. P. Gorenstein, H. Gursky, F.R. Harnden, Jr., A. Decaprio, and P. Bjorkholm, IEEE Trans. Nucl. Sci. **22**, 616 (1975)

128. F.R. Harnden, Jr., D. Fabricant, K. Topka, B.P. Flannery, W.H. Tucker, and P. Gorenstein, Astrophys. J. **214**, 418 (1977)

129. S. Rappaport, R. Petre, M.A. Kayat, K.D. Evans, G.C. Smith, and A. Levine, Astrophys. J. **227**, 285 (1979)

130. R. Giacconi, G. Branduardi, U. Briel, A. Epstein, D. Fabricant, E. Feigelson, W. Forman, P. Gorenstein, J. Grindlay, H. Gursky, F.R. Harnden, Jr., J.P. Henry, C. Jones, E. Kellogg, D. Koch, S. Murray, E. Schreier, F. Seward, H. Tananbaum, K. Topka, L. van Speybroeck, S.S. Holt, R.H. Becker, E.A. Boldt, P.J. Serlemitsos, G. Clark, C. Canizares, T. Markert, R. Novick, D. Helfand, and K. Long, Astrophys. J. **230**, 540 (1979)

131. P.A.J. de Korte, J.A.M. Bleeker, S.P. McKechnie, A.J.F. den Boggende, A.C. Brinkman, E.H.B.M. Gronenschild, G. Branduradi-Raymont, J.L. Culhane, and I. Mason, Space Sci. Rev. **30**, 495 (1981)

132. Y. Tanaka, M. Fujii, H. Inoue, N. Kawai, K. Koyama, Y. Maejima, F. Makino, K. Makishima, M. Matsuoka, K. Mitsuda, T. Murakami, J. Nishimura, M. Oda, Y. Ogawara, T. Ohashi, N. Shibizaki, K. Suzuki, I. Waki, T. Yamagami, I. Kondo, H. Murakami, S. Hayakawa, T. Hirani, H. Kunieda, K. Masai, F. Nagase, N. Sato, Y. Tawara, S. Kitamoto, S. Miyamoto, H. Tsunemi, K. Yamashita, and M. Nakagawa, Publ. Astron. Soc. Japan **36**, 641 (1984)

133. J. Trümper, Adv. Space Res. **2** No. 2, 241 (1983)

134. P.J. Serlemitsos, R. Petre, C. Glasser, F. Birsa, IEEE Trans. Nucl. Sci. **31**, 1 (1984)

135. S. Tsuneta, L. Acton, M. Bruner, J. Lemen, W. Brown, R. Caravalho, R. Catura, S. Freeland, B. Jurcevich, and J. Owens, Solar Phys. **136**, 37 (1991)

136. P.J. Serlemitsos, L. Jalota, Y. Soong, H. Kunieda, Y. Tawara, Y. Tsusaka, H. Suzuki, Y. Sakima, T. Yamazaki, H. Yoshioka, A. Furuzawa, K. Yamashita, H. Awaki, M. Itoh, Y. Ogasaka, H. Honda, and Y. Uchibori, Publ. Astron. Soc. Japan **47**, 105 (1995)

137. J.E. Harvey, "Understanding X-Ray Imaging Systems," Short Course Notes (SC 383) of the *International Symposium on Optical Science and Technology: SPIE's 47th Annual Meeting*, (Bellingham, WA, Society of Photo-optical Instrumentation Engineers), p. 72 (2002)

138. G. Boella, R.C. Butler, G.C. Perola, L. Piro, L. Scarsi and J.A.M. Bleeker, Astron. Astrophys. Suppl. Series **122**, 299 (1997)

139. D.H. Lumb, H. Eggel, R. Laine, and A.J. Peacock, " X-ray Multimirror Mission: an overview" in *EUV, X-Ray, and Gamma-Ray Instrumentation for Astronomy VII*, O.H. Siegmund and M.A. Gummin, eds., Proc. SPIE **2808**, 326 (1996)

140. M.C. Weisskopf, H.D. Tananbaum, L.P. van Speybroeck and S.L. O'Dell, "Chandra X-ray Observatory (CXO): overview" in *X-Ray Optics,*

Instruments, and Missions III, J.E. Truemper, and B. Aschenbach, eds., Proc. SPIE **4012**, 2 (2000)

141. H. Kunieda, M. Ishida, T. Endo, Y. Hidaka, H. Honda, K. Imamura, J. Ishida, M. Maeda, K. Misaki, R. Shibata, A. Furuzawa, K. Haga, Y. Ogasaka, T. Okajima, and Y. Tawara, Appl. Opt. **40**, 553 (2001)

142. P.L. Bornmann, D. Speich, J. Hirman, V.J. Pizzo, R. Grubb, C. Balch, and G. Heckman, "GOES solar x-ray imager: overview and operational goals" in *GOES-8 and Beyond,* E.R. Washwell, ed., Proc. SPIE **2812**, 309 (1996)

143. J.E. Harvey and P.L. Thompson, "Generalized Wolter type I design for the solar x-ray imager (SXI)" in *X-Ray Optics, Instruments, and Missions II,* R.B. Hoover and A.B. Walker, eds., Proc. SPIE **3766**, 173 (1999)

144. L. Golub, E.E. DeLuca, J.A. Bookbinder, P. Cheimets, K. Shibasaki, T. Sakao, and R. Kano, "High-resolution grazing incidence telescope for the Solar-B observatory" in *Instrumentation for UV/EUV Astronomy and Solar Missions*, S. Fineschi, C.M. Korendyke, O.H. Siegmund, and B.E. Woodgate, eds., Proc. SPIE **4139**, 313 (2000)

145. E. Spiller, *Soft X-ray Optics* (SPIE Optical Engineering Press, Bellingham, WA, 1994)

146. E.V. Shulakov, V.S. SHekhtman, S.S. Khasanov, and I.A. Smirnova, Nucl. Inst. and Meth. in Phys. Res. Sec. A **448**, 152 (2000)

147. E. Spiller, Appl. Phys. Lett. **20**, 365 (1972)

148. D.J. Nagel, J.V. Gilfrich, and T.W. Barbee, Jr., "Graded-layer-thickness Bragg X-ray reflectors " in *Reflecting Optics for Synchrotron Radiation*, M.R. Howells, ed., Proc. SPIE **315**, 110 (1981)

149. P. Dhez, "Use of X-UV multilayered optics for synchrotron radiation, plasma diagnostics and astrophysical research" in *Soft X-ray optics and technology*, E. Koch and G.A. Schmahl, eds., Proc. SPIE **733**, 308 (1987)

150. W.H. Bragg, Phil. Mag. **27**, 881 (1914)

151. P. Debye, Verh. d. Deutsch. Phys. Ges. **15**, 738 (1913)

152. I. Waller, Z. Physik **17**, 398 (1923)

153. L. Névot and P. Croce, Revue Phys. Appl. **15**, 761 (1980)

154. G.H. Vineyard, Phys. Rev. B **26**, 4146 (1982)

155. S.K. Sinha, E.B. Sirota, S. Garoff, and H.B. Stanley, Phys. Rev. B **38**, 2297 (1988)

156. D.G. Stearns, J. Appl. Phys. **65**, 491 (1988)

157. D.K.G. deBoer, Phys. Rev. B **51**, 5297 (1995)

158. C.L. Vernold and J.E. Harvey, "Modified Beckmann-Kirchoff Scattering Theory for Nonparaxial Angles," in *Scattering and Surface Roughness II*, Z.-H. Gu and A.A. Maradudin, eds., Proc. SPIE **3426**, 51 (1998)

159. E.L. Church and P.Z. Takacs, "The interpretation of glancing incidence scattering measurements," in *Grazing Incidence Optics*, J.F. Osantowski and L.P. van Speybroeck, eds., Proc. SPIE **640**, 126 (1986)

160. P. Croce, L. Névot, and B. Pardo, C.R. Acad. Sci. Paris **274**, 803, (1972); **274**, 855 (1972)

161. A. Steyerl, Z. Phys. **254**, 169 (1972)

162. J.-P. Delaboudiniere, G.E. Artzner, J. Brunaud, A.H. Gabriel, J.F. Hochedez, F. Millier, X.Y. Song, B. Au, K.P. Dere, R.A. Howard, R. Kreplin, D.J. Michels, J.D. Moses, J.M. Defise, C. Jamar, P. Rochus, J.P. Chauvineau, J.P. Marioge, R.C. Catura, J.R. Lemen, L. Shing, R.A. Stern, J.B. Gurman, W.M. Neupert, A. Maucherat, F. Clette, P. Cugnon, and E.L. van Dessel, Solar Phys. **162**, 291 (1995)

163. B.N. Handy, L.W. Acton, C.C. Kankelborg, C.J. Wolfson, D.J. Akin, M.E. Bruner, R. Caravalho, R.C. Catura, R. Chevalier, D.W. Duncan, C.G. Edwards, C.N. Feinstein, S.L. Freeland, F.M. Friedlaender, C.H. Hoffmann,

N.E. Hurlburt, B.K. Jurcevich, N.L. Katz, G.A. Kelly, J.R. Lemen, M. Levay, R.W. Lindgren, D.P. Mathur, S.B. Meyer, S.J. Morrison, M.D. Morrison, R.W. Nightingale, T.P. Pope, R.A. Rehse, C.J. Schrijver, R.A. Shine, L. Shing, K.T. Strong, T.D. Tarbell, A.M. Title, D.D. Torgerson, L. Golub, J.A. Bookbinder, D. Caldwell, P.N. Cheimets, W.N. Davis, E.E. Deluca, R.A. McMullen, H.P. Warren, D. Amato, R. Fisher, H. Maldonado, and C. Parkinson, Solar Phys. **187**, 229 (1999)

164. R.F. Malina, S. Bowyer, M. Lampton, D. Finley, F. Paresce, G. Penegor, and H. Heetderks, Opt. Eng. **21**, 764 (1982)

165. R.A. Harrison, E.C. Sawyer, M.K. Carter, A.M. Cruise, R.M. Cutler, A. Fludra, R.W. Hayes, B.J. Kent, J. Lang, D.J. Parker, J. Payne, C.D. Pike, S.C. Peskett, A.G. Richards, J.L. Culhane, K. Norman, A.A. Breeveld, E.R. Breeveld, K.F. Al Janabi, A.J. McCalden, J.H. Parkinson, D.G. Self, P.D. Thomas, A.I. Poland, R.J. Thomas, W.T. Thompson, O. Kjeldseth-Moe, P. Brekke, J. Karud, P. Maltby, B. Aschenbach, H. Brauninger, M. Kuhne, J. Hollandt, O.H.W. Siegmund, M.C.E. Huber, A.H. Gabriel, H.E. Mason, B.J.I. Bromage, Solar Phys. **162**, 233 (1995)

166. J.E. Harvey and W.J. Gressler, Opt. Eng. **35**, 3037 (1996)

167. E.L. Church, H.A. Jenkinson, and J.M. Zavada, Opt. Eng. **18**, 125 (1979)

168. J.M. Bennett and L. Mattsson, *Introduction to Surface Roughness and Scattering*, Optical Society of America, Washington, DC (1989)

169. J.E. Harvey, "Surface scatter phenomena: a linear, shift-invariant process" in *Scatter from Optical Components*, J.C. Stover, ed., Proc. SPIE **1165**, 87 (1989)

170. J.C. Stover, *Optical Scattering, Measurement and Analysis*, McGraw-Hill (New York) (1990)

171. E.L. Church and P.Z. Takacs, Appl. Opt. **32**, 3344 (1993)

172. V. Holý, J. Kubena, I. Ohlidal, K. Lischka, and W. Plotz, Phys. Rev. B **47**, 15896 (1993)

173. J.E. Harvey, "Scattering effects from residual optical fabrication errors" in *International Conference on Optical Fabrication and Testing*, T. Kasai, ed., Proc. SPIE **2576**, 155 (1995)

174. M. Rauscher, T. Salditt, and H. Spohn, Phys. Rev. B **52**, 16855 (1995)

175. W.T. Welford, *Aberrations of Symmetrical Optical Systems*, Academic Press (New York) (1974)

176. T.T. Saha, "Transverse Ray Aberrations of Wolter Type I Telescopes" in *Grazing Incidence Optics*, J.F. Osantowski and L.P. van Speybroeck, eds., Proc. SPIE **640**, 10 (1986)

177. L.P. vanSpeybroeck and R.C. Chase, Appl. Opt. **11**, 440 (1972)

178. J.E. Harvey, P.L. Thompson, and A. Krywonos, "Hyperboloid-hyperboloid grazing incidence x-ray telescope designs for wide-field imaging applications" in *X-Ray Optics, Instruments, and Missions III*, J.E. Truemper and B. Achenbach, eds., Proc. SPIE **4012**, 328 (2000)

179. P.J. Serlemitsos, App. Opt. **27**, 1447 (1988)

180. P.J. Serlemitsos and Y. Soong, Astrophys. and Space Sci. **239**, 177 (1996)

181. Y. Soong, K.-W. Chan, and P.J. Serlemtisos, "Recent advance in segmented thin-foil x-ray optics" in *X-Ray Optics for Astronomy: Telescopes, Multilayers, Spectrometers, and Missions*, P. Gorenstein and R.B. Hoover, eds. Proc. SPIE **4496**, 54 (2001)

182. B.D. Ramsey, C.D. Alexander, J.A. Apple, C.M. Benson, K.L. Dietz, R.F. Elsner, D.E. Engelhaupt, K.K. Ghosh, J.J. Kolodziejczak, S.L. O'Dell, C.O. Speegle, D.A. Swartz and M.C. Weisskopf, Astrophys. J. **568**, 432 (2002)

183. F.A. Harrison, S.E. Boggs, A.E. Bolotnikov, F.E. Christensen, W.R. Cook, W.W. Craig, C.J. Hailey, M.A. Jimenez-Garate, P.H. Mao, S.M. Schindler and D.L. Windt, "Development of the High-Energy Focusing Telescope (HEFT) balloon experiment" in *X-Ray Optics, Instruments, and Missions III*, J.E. Truemper and B. Aschenbach, eds., Proc. SPIE **4012**, 693 (2000)

184. J.A. Bookbinder, "Constellation X mission and its optics" in *-Ray Optics for Astronomy: Telescopes, Multilayers, Spectrometers, and Missions*, P. Gorenstein and R.B. Hoover, eds., Proc. SPIE **4496**, 84 (2002)

185. H.V. Bradt, R.E. Rotschild, and J.H. Swank, Astron. Astrophys. Suppl. Series **97**, 355 (1993)

186. C. Winkler, Exp. Astron. **6**, 71 (1995)

187. G.R. Ricker, J.P. Doty, S.A. Rappaport, R.K. Vanderspek, M. Matsuoka, K. Nobuyuki, A. Yoshida, E.E. Feinmore, C. Ho, and D. Roussel-Dupre, "The high-energy transient experiment (HETE) - An international multiwavelength mission" in *Gamma-ray bursts - Observations, analyses and theories*, C. Ho, R.I. Epstein, and E.E. Feinmore, eds., (Cambridge Univ. Press, Cambridge, 1992)

188. D.D. Clayton, Astrophys. J. **188**, 155 (1974)

189. S.E. Woosley, D.W. Arnett, and D.D. Clayton, Astrophys. J. Suppl. Ser. **26**, 231 (1973)

190. F.-K. Thielemann, M.-A. Hashimoto, and K. Nomoto, Astrophys. J. **349**, 222 (1990)

191. L.C. Jafelice and R. Opher, Mon. Not. R. Astron. Soc. **257**, 135 (1992)

192. G. Medina-Tanco and T.A. Elßlin, Astropart. Phys. **16**, 47 (2001)

193. P. Guilbert and M. Rees, Mon. Not. R. Astron. Soc. **233**, 475 (1988)

194. A. Lightman and T. White, Astrophys. J. **335**, 57 (1988)

195. R. Fusco-Femiano, D. dal Fiume, L. Feretti, G. Giovanni, P. Gradi, G. Matt, S. Molendi, and A. Santangelo, Astrophys. J. **513**, L21 (1999)

196. J.S. Kaastra, R. Lieu, J.P.D. Mittaz, J.A.M. Bleeker, R. Mewe, S. Colafrancesco, and F.J. Lockman, Astrophys. J. **519**, L119 (1999)

197. Y. Soong, L. Jalota, and P.J. Serlemitsos, "Conical thin foil X-ray mirror fabrication via surface replication" in *X-ray and Extreme Ultraviolet Optics*, R.B. Hoover and A.B. Walker, eds., Proc. SPIE **2515**, 64 (1995)

198. K.D. Joensen, F.E. Christensen, H.W. Schnopper, P. Gorenstein, J. Susini, P. Høghøj, R. Hustache, J. Wood and K. Parker, "Medium-sized grazing incidenc high-energy X-ray Telescopes employing continuously graded multilayers" in *X-ray Detector Physics and Applications*, R.B. Hoover, ed., Proc. SPIE **1736**, 239 (1992)

199. K.D. Joensen, P. Voutov, A. Szentgyorgyi, J. Roll, P. Gorenstein, P. Høghøj and F.E. Christensen, Appl. Opt. **34**, 7935 (1995)

200. D.L. Smith, *Thin-Film Deposition; Principles and Practice*, 1st ed. (McGraw-Hill, Inc., New York, 1995)

201. A. Ivan, R.J. Bruni, P. Gorenstein, and S.E. Romaine, "Influence of deposition parameters on the reflecitivity of multilayer hard x-ray mirrors" in *X-Ray Mirrors, Crystals, and Multilayers*, A.K. Freund, T. Ishikawa, and A.M. Kho, eds., Proc. SPIE **4501**, 142 (2001)

202. D.L. Windt, Comp. in Phys. **12**, 360 (1998)

203. M.M. Hasan, R.J. Highmore, and R.E. Somekh, Vacuum **43**, 55 (1992)

204. D.L. Windt, F.E. Christensen, W.W. Craig, C. Hailey, F.A. Harrison, M. Jimenez-Garate, R. Kalyanaraman, and P.H. Mao, J. Appl. Phys. **88** no. 1, 460 (2000)

205. M.D. Kriese, G. Fournier, J. Rodriguez, and Y.Y. Platonov, "Control of Mo/Si multilayers for soft x-ray performance" in *EUV, X-Ray, and Neutron Optics and Sources*, C.A. MacDonald, K.A. Goldberg, J.R. Maldonado, H.H. Chen-Mayer, and S.P. Vernon, eds., Proc. SPIE **3767**, 242 (1999)

206. V.V. Protopopov, "Graded x-ray multilayer optics for laboratory-based applications" in *Advances in Laboratory-based X-Ray Sources and Optics*, C.A. MacDonald and A.M. Khounsary, eds., Proc. SPIE **4144**, 116 (2000)

207. S.M. Owens, T. Okajima, Y. Ogasaka, F. Berendse, and P.J. Serlemitsos, "Multilayer coated thin foil mirrors for InFOCμS" in *X-Ray Optics,*

Instruments, and Missions III, J.E. Truemper and B. Aschenbach, eds., Proc. SPIE **4012**, 619 (2000)

208. K. Tamura, K. Yamashita, Y. Tawara, Y. Ogasaka, K. Haga, T. Okajima, S. Ichimaru, S. Takahaski, H. Kitou, A. Gotou, K. Nomoto, H. Satake, S. Kato, H. Kunieda, P.J. Serlemitsos, and J. Tueller, "Development of a balloonborne hard x-ray telescope using multilayer supermirror" in *X-Ray Optics, Instruments, and Missions IV*, R.B. Hoover and A.B. Walker, eds., Proc. SPIE **4138**, 111 (2000)

209. T. Okajima, K. Tamura, Y. Ogasaka, K. Haga, S. Takahashi, S. Ichimaru, H. Kito, S. Fukuda, A. Goto, K. Nomoto, H. Satake, S. Kato, Y. Kamata, A. Furuzawa, F. Akimoto, T. Yoshioka, K. Kondo, Y. Haba, T. Tanaka, K. Wada, N. Hamada, M. Hudaverti, Y. Tawara, K. Yamashita, P.J. Serlemitsos, Y. Soong, K.-W. Chan, S.M. Owens, F. Berendse, J. Tueller, K. Masaki, R. Shibata, H. Mori, K. Itoh, H. Kunieda, and Y. Namba, Appl. Opt. **41**, 5417, (2002)

210. W.C. Priedhorsky, J. Terrell, and S.S. Holt, Astrophys. J. **270**, 233 (1983)

211. J.C. Ling, W.A. Mahoney, W.A. Wheaton, A.S. Jacobsen, and L. Kaluzienski, Astrophys. J. **275**, 307 (1983)

212. E.P. Liang and P.L. Nolan, Space Sci. Rev. **38**, 353 (1983)

213. M.L. McConnell, A.A. Zdziarski, K. Bennett, H. Bloemen, W. Collmar, W. Hermsen, L. Kuiper, W. Paciesas, B.F. Phlips, J. Poutanen, J.M. Ryan, V. Schönfelder, H. Steinle, and A.W. Strong, Astrophys. J. **572**, 984 (2002)

214. J.H. Hubbell and S.M. Seltzer, "Tables of X-Ray Mass Attenuation Coefficients and Mass Energy-Absorption Coefficients (version 1.03)," National Institute of Standards and Technology (Gaithersburg, MD), http://physics.nist.gov/xaamdi, (1997)

215. H. Eichorn, *Astronomy of Star Positions*, (Ungar, New York), 68 (1974)

216. D.W. Marquardt, J. Soc. Ind. Appl. Math **11**, 431 (1963)

217. W.H. Press, S.A. Teukolsky, W.T. Vetterling, and B.P. Flannery, *Numerical Recipes in C: The Art of Scientific Computing*, 2nd ed., (Cambridge Univ. Press, New York), 681 (1992)